

# *Engineering Documents*

---

*University of Pennsylvania*

*Year 1995*

---

## Nonlinear Optical Spectroscopy of Gallium Arsenide Interfaces

Jining Qi  
University of Pennsylvania,

University of Pennsylvania, Dissertation, 1995.

This paper is posted at ScholarlyCommons@Penn.  
<http://repository.upenn.edu/seas.docs/5>

NONLINEAR OPTICAL SPECTROSCOPY OF GALLIUM  
ARSENIDE INTERFACES

JINING QI

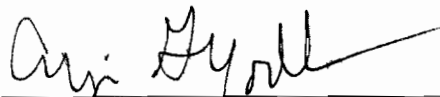
A DISSERTATION

in

PHYSICS

Presented to the Faculties of the University of Pennsylvania in Partial Fulfillment  
of the Requirements for the Degree of  
Doctor of Philosophy.

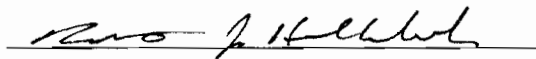
1995



---

Arjun G. Yodh

Supervisor of Dissertation



---

Robert J. Hollebeek

Graduate Group Chairperson

MATH-PHYSICS/OC/001/1995/01

© Copyright 1995

by

Jining Qi

*To: Shan and Sharon*

# Acknowledgements

It is my great pleasure to thank my advisor, Professor A. G. Yodh, for his excellent guidance and for providing me a wonderful research environment. His profound scientific ideas and tireless work have inspired my entire research program. In addition, I fortunately was able to learn from him many other things such as communication and writing.

I must thank Professor G. Mele for guiding me through the theoretical concepts of solid state physics, and Professor A. F. Garito for his generous support and for sharing his equipment with me. I am very grateful to Professor E. Burstein for his guidance in many surface science problems.

I also wish to thank Dr. M. S. Yeganeh for teaching me many of the basic experimental techniques when I first started working in this laboratory, and Dr. L. Campbell and W. Angerer for their critical reading of this thesis. I would like to thank all of my colleagues in the group including D. Boas, J. Culver, A. Dinsmore, M. Kao, P. Kaplan, M. O'Leary, Z. Sun, and R. Verma. I enjoyed working with each of them.

I also thank my parents, who taught me my first science lesson. My deepest thanks goes to my wife Shan and my daughter Sharon for their love, patience, and support.

This work was supported by the ONR through Grant No. N00014-91-J-1867, the NSF through the PYI program Grant No. DMR-9058498, the MRL program Grant No. DMR-8519059, and the Alfred P. Sloan Foundation.

# Abstract

## Nonlinear Optical Spectroscopy of Gallium Arsenide Interfaces

Jining Qi

Arjun G. Yodh

The physics of buried solid/solid interfaces is interesting for both fundamental and technological reasons. In this thesis, second-order nonlinear optical spectroscopy was used to probe the electronic structure of GaAs based interfaces in the near infrared. Second-order nonlinear optical spectroscopy possesses intrinsic interface sensitivity and a long penetration depth. This intrinsic interface sensitivity enables us to suppress spectral contributions from the adjoining bulk media, resulting in more specific assignments of the spectral features.

Our observations provide strong evidence for the existence of atomic displacement-induced defect states at the buried metal:GaAs interface. In particular, in Au:GaAs n-type systems we have observed two resonance features at 0.715 eV and 0.731 eV for the Ga-rich interface and a single resonance feature at 0.715 eV for the As-rich interface. Similar single resonance features at 0.715 eV were observed in As:GaAs n-type samples, but were not present in oxide:GaAs and metal:GaAs p-type systems. After consideration of various three-step optical processes, we conclude that the transitions originate from the midgap states. These resonances differ substantially from what has been observed by other less interface sensitive technologies probing similar system. The origin of these difference is discussed.

In the case of the native oxide GaAs system, we also studied depletion electric field induced effects on second-order nonlinear optical processes. Using a simple three-band model, we calculated the depletion field induced perturbation of the

second-order nonlinear susceptibility of GaAs(001). The field induced modification of the second-order nonlinear susceptibility has been found to add destructively to the unperturbed existing bulk nonlinear second-order susceptibility  $\chi_{yxz}^{(2)}$ . This diminution depends on the square of the near surface depletion electric field. Through studies as a function of dopant type and concentration, we demonstrate that the bulk  $\chi_{yxz}^{(2)}$  is systematically reduced as a result of the depletion field, and that this diminution depends on the square of the near surface depletion field. This is consistent with our theoretical calculations. The sensitivity of the near surface bulk second-order susceptibility to the depletion electric field has also been demonstrated by a photomodulation second harmonic generation (PSHG) technique, by which we measured surface minority trap lifetimes and transverse diffusion of carriers confined near GaAs(001) surfaces.

# Contents

<b>Acknowledgements</b>	<b>iv</b>
<b>1 Introduction</b>	<b>1</b>
<b>2 Second-order nonlinear optical spectroscopy</b>	<b>7</b>
2.1 Introduction to Nonlinear Optics . . . . .	7
2.2 General properties of nonlinear optical susceptibility . . . . .	12
2.2.1 Permutation symmetries of nonlinear susceptibility . . . . .	12
2.2.2 Spatial symmetries of nonlinear susceptibility . . . . .	13
2.3 Nonlinear susceptibility and the band-structure of crystals . . . . .	14
2.4 Second-order Nonlinear Optical Experiments . . . . .	16
2.4.1 SHG from GaAs(001) bulk . . . . .	16
2.4.2 SHG from GaAs(001) surface . . . . .	18
2.4.3 Some concerns about higher-order contributions . . . . .	20
<b>3 Laser systems and experimental implementation</b>	<b>34</b>
3.1 Pumping laser . . . . .	34
3.2 Dye-laser . . . . .	35
3.3 $Ar^+$ ion laser . . . . .	36
3.4 Optical parametric oscillator . . . . .	37
3.5 General optical layouts . . . . .	40
3.6 Electronic data acquisition system . . . . .	43

3.7	Some linear optical experiments . . . . .	44
3.8	Sample cooling system . . . . .	45
<b>4</b>	<b>GaAs and its interfaces</b>	<b>56</b>
4.1	Introduction to GaAs . . . . .	56
4.1.1	Structural and electronic properties . . . . .	56
4.1.2	GaAs bulk defects . . . . .	57
4.1.3	General optical properties of GaAs . . . . .	59
4.1.4	Nonlinear optical properties of GaAs . . . . .	60
4.2	MBE Growth Procedures . . . . .	61
4.2.1	MBE Growth of GaAs(001) . . . . .	62
4.2.2	MBE Growth of Metal:GaAs . . . . .	63
4.3	Linear optical measurements of the metal film thickness . . . . .	64
4.4	General properties of GaAs based surfaces and interfaces . . . . .	65
<b>5</b>	<b>Theory of field induced perturbation on the second-order suscepti-</b>	
	<b>bility</b>	<b>80</b>
5.1	The depletion field . . . . .	81
5.2	Depletion field induced perturbation on second-order susceptibilities .	83
5.2.1	The three band model in GaAs(001) . . . . .	83
5.2.2	The perturbation of the three-bands at the $\Gamma$ point . . . . .	85
5.2.3	The mixture of states at the $\Gamma$ point . . . . .	88
5.2.4	The perturbation of the second-order susceptibility $\chi_{yzx}^{(2)}$ . . . . .	90
5.3	SHG from the depletion region of GaAs . . . . .	93
<b>6</b>	<b>Measurements of depletion electric field effects on SHG</b>	<b>101</b>
6.1	SHG from the depletion region . . . . .	102
6.2	Photomodulation the depletion field . . . . .	104
6.3	Surface trap lifetime . . . . .	106
6.4	Surface minority carrier diffusion . . . . .	108

6.4.1	Spatially separated photoexcitation and SHG experiments . . .	108
6.4.2	Mechanism for surface minority carrier diffusion . . . . .	111
6.4.3	Other possible diffusion processes . . . . .	113
<b>7</b>	<b>Observation of midgap interface states at Metal:GaAs junctions by SHG and SFG</b>	<b>132</b>
7.1	Second-order nonlinear optical spectroscopies from Metal:GaAs interfaces . . . . .	132
7.1.1	SHG spectra from Au:GaAs (n-type) interfaces . . . . .	132
7.1.2	SFG spectra from Au:GaAs (n-type) interfaces . . . . .	133
7.1.3	One-photon resonance paths . . . . .	134
7.1.4	SHG and SFG from Au:GaAs (p-type) interfaces . . . . .	135
7.1.5	SHG and SFG experiments on As:GaAs (n-type) samples . . .	136
7.2	Higher order bulk and Au surface contributions . . . . .	136
7.3	Nature of the midgap interface states . . . . .	137
7.3.1	Atomic displacement induced defect states . . . . .	137
7.3.2	Some concerns about other defects states . . . . .	140
7.3.3	Depletion field effects . . . . .	140
7.3.4	Comparison with interfacial spectra by other techniques . . .	142
<b>8</b>	<b>Conclusion</b>	<b>154</b>
	<b>Appendix</b>	<b>158</b>
<b>A</b>	<b>The transition matrix using dipole operator <math>\vec{Q}</math></b>	<b>158</b>
A.1	$\langle \phi_{\nu}^{(6)}   Q   \phi_{\nu'}^{(7)} \rangle$ . . . . .	159
A.2	$\langle \phi_{\nu}^{(6)}   Q   \phi_{\mu}^{(8)} \rangle$ . . . . .	160
A.3	$\langle \phi_{\nu'}^{(7)}   Q   \phi_{\mu}^{(8)} \rangle$ . . . . .	161
<b>B</b>	<b>Nonzero Electric Dipole Transition Paths</b>	<b>162</b>

C	Depletion field $E\hat{z}$ effects on second-order Susceptibility $\chi_{yxx}^{(2)}$	165
D	Depletion field $E\hat{z}$ effects on second-order Susceptibility $\chi_{zzz}^{(2)}$	169
E	Surface trap lifetime	172
F	Carrier boundary at GaAs surface	174
G	Electrical neutrality assumption	176
H	Effective diffusion model	178
I	Quick reference of computer codes	180

# List of Tables

2.1	Surface $\chi^{(2)}$ elements for several symmetry classes ( $\hat{x} - \hat{y}$ surface plane); 1. $C_n$ represents point group containing one n-fold proper rotation axis; $C_{nv}$ contains $C_n$ plus a $\sigma_v$ reflections. $\sigma_v$ contains a reflection in a plane passing through the axis of the highest symmetry. $C_n$ also requires n of these $\sigma_v$ 's separated by $\frac{\pi}{n}$ . . . . .	22
2.2	Angular dependence of second harmonic polarization $E(2\omega)$ for GaAs(001) bulk $\bar{4}3m$ and surface $mm2$ symmetries. Here $xyz$ , $x'y'z'$ , and $x''y''z''$ represent laboratory frame, bulk $\bar{4}3m$ symmetry frame, and surface $mm2$ symmetry frame, respectively. . . . .	23
2.3	Nonzero fourth-rank tensor elements for $\bar{4}3m$ symmetry media . . . . .	24
4.1	Some physical properties of GaAs at room temperature (300K) . . . . .	67
4.2	Some electronic properties of GaAs at room temperature (300K) . . . . .	67
5.1	Character table of $T_d$ . . . . .	96
5.2	Basis functions of $T_d$ . . . . .	96
5.3	Direct product of $T_d$ . . . . .	97
5.4	Direct product of $\bar{T}_d$ . . . . .	97

# List of Figures

2.1	(a) Phase matching diagram for sum frequency generation. $\hbar\omega_3 = \hbar\omega_1 + \hbar\omega_2$ : energy conservation; $k_3 = k_1 + k_2$ : moment conservation. (b) The tangential momentum conservation of each individual frequencies, $\omega$ and $2\omega$ , at an interface. For the fundamental frequency ( $\omega_1$ ): $k_{  }^i(\omega) = k_{  }^R(\omega) = k_{  }^T(\omega)$ . For the harmonic wave ( $2\omega$ ): $2k_{  }^T(\omega) = k_{b2,  }^T(2\omega) = k_{f2,  }^T(2\omega) = k_{f1,  }^R(2\omega)$ . The subscripts “f” and “b” refer to free and bound waves respectively. ‘i’, ‘R’, and ‘T’ refer to incident, reflected and refracted waves respectively.    represents the tangential component. . . . .	25
2.2	Schematic diagram of three-wave mixing processes. (a) Three-wave mixing in a two level system. An intraband transition ( $ n \rangle$ to $ n \rangle$ ) is involved. (b) Three-wave mixing in a three level system. . . . .	26
2.3	Second harmonic generation in GaAs(001) crystal. $XYZ(X'Y'Z')$ represents the laboratory (crystal) frame. $\phi$ is the angle between the crystalline [100] axis with the plane of the incidence. The fundamental SH generating light $\hbar\omega$ is p-polarized, at a incident angle $\theta$ with the $Z$ axis. SHG light is s-polarized. . . . .	27
2.4	In p-in/s-out configuration, a typical bulk GaAs(001) SHG ( $\chi_{xyz}$ ) output are plotted as a function angle $\phi$ . The fundamental photon energy is at $\hbar\omega = 1.41$ eV. The solid line is fitting by using formula $I_{SHG} = I_0 \cos^2(2\phi)$ . . . . .	28

2.5	In p-in/s-out with $\phi = 0$ configuration, SHG signals from GaAs(001) bulk ( $\chi_{xyz}$ ) are plotted as a function of fundamental (one-photon) and SHG photon (two-photon) energies. . . . .	29
2.6	$ \chi_{xyz}^{(2)} $ as a function of one and two-photon energy for GaAs. $E_0$ and $E_1$ represent two resonance features which are related to GaAs $E_0$ transition and $E_1$ transition. . . . .	30
2.7	Three different frames at GaAs(001) surface. $XYZ$ , $X'Y'Z'$ and $X''Y''Z''$ represent laboratory frame, GaAs crystal bulk frame ( $\bar{4}3m$ symmetry), and GaAs surface frame ( $mm2$ symmetry), respectively (see figure 2.7). . . . .	31
2.8	Microscopic view of surface $mm2$ symmetry axis with respect to the bulk $\bar{4}3m$ symmetry axis at GaAs(001) surface. . . . .	32
2.9	SHG signals from GaAs(001) surface are plotted as a function of fundamental (one-photon) and SHG photon (two-photon) energies. The crystalline axis $[100]$ is in the plane of incidence, i.e. $\phi = 0$ . In p-in/p-out, SHG signal arose from the contributions of $\chi_{zzz}^{(2)}$ , $\chi_{xzx}^{(2)}$ and $\chi_{yzy}^{(2)}$ . In s-in/p-out, SHG signals arose from the contributions of $\chi_{xzx}^{(2)}$ and $\chi_{yzy}^{(2)}$ , and were much smaller than the p-in/p-out surface signals. More details are in text. . . . .	33
3.1	PDL-2 dye-laser layout. . . . .	46
3.2	A typical dye-laser output power spectra for LDS867 dye. . . . .	47

3.3	Schematic drawing of optical parametric oscillator OPO and optical parametric amplifier OPA. A, B, C, and E are high reflective mirrors for the pumping beams. D is beam-dumper for 1064 nm pumping light; H, I are transparent for IR light, but are highly reflecting at 532 nm. G is highly reflective at 1064 nm, but is transparent for IR light; J is transparent for signal beams at the OPO stage, but not for the idler beams; $T_1$ and $T_2$ are telescopes. Inlet shows reflected spots of pumping beam 532 nm (1064 nm) on mirror C (E), and two reflected spots correspond to two crystals in OPO (OPA) stage. . . . .	48
3.4	Top view of OPO or OPA stage. Walk-off effect is canceled in this configuration. C: optical axis; $\theta$ : surface cutting angle; $TA_1$ , $TA_2$ : Crystal rotation axis with opposite direction. . . . .	49
3.5	A typical Mirage3000 OPO output power spectrum while the pumping power of 532 nm (1064 nm) was at 70 mJ/pulse (280 mJ/pulse). . . . .	50
3.6	Schematic diagram of optical setups in SHG and SFG experiments. . . . .	51
3.7	The transmitted SH intensity of a wedged quartz plate as a function of the translation distance. . . . .	52
3.8	Linear reflectivity spectroscopy experimental setup. . . . .	53
3.9	Experimental setup for the linear reflectivity as function incident angle experiments. . . . .	54
3.10	Schematic drawing of sample cooling system. . . . .	55
4.1	GaAs crystal structure. Lattice constants see table 4.1. . . . .	68
4.2	First Brillouin zone for the GaAs lattice. . . . .	69
4.3	The electronic band structure of GaAs. . . . .	70
4.4	An isolated As antisite ( $As_{Ga}$ ) defect structure. . . . .	71
4.5	Theoretical calculations of the atomic displacement-induced defect state energy levels in GaAs bulk (from reference 6). . . . .	72

4.6	(a) Linear electric dipole transition at the direct band gap of GaAs. The dipole operator is represented by $\Gamma_5$ . (b) Linear reflectivity $R$ as function of the incidence photon energy from GaAs crystal. The light incident at angle $45^\circ$ . The solid line is the theoretical calculation. . . . .	73
4.7	Schematic diagram of MBE growth chamber. . . . .	74
4.8	(a) One of the proposed $2 \times 4$ reconstructions at GaAs surface. As atoms form the first layer; (b) One of the proposed $4 \times 2$ reconstruction at GaAs surface. Ga atoms form the first layer. . . . .	75
4.9	Linear reflection from two-slab system. . . . .	76
4.10	Linear reflectivity $R$ as function of the incident angle for a Au:GaAs system. The solid line is the best fit to the Au layer thickness, which is $80\text{\AA}$ . Incident light is at $632.8nm$ . . . . .	77
4.11	Linear reflectivity $R$ as function of the incident angle for a As:GaAs system. The solid lines (a) and (b) represent two different As overlayer thicknesses in the theoretical calculation, i.e. $d_a \sim 100\text{\AA}$ , and $d_b \sim 50\text{\AA}$ . Since the As overlayer is amorphous, the film is expected to be nonuniform. . . . .	78
4.12	Fermi level pinning positions at different solid:GaAs interfaces. Circles represent n-type GaAs based interfaces; Triangles represent p-type GaAs based interfaces (from reference 95). . . . .	79
5.1	Schematic drawing of the band-bending profile for an n-type semiconductor within the depletion region. $E_c$ , $E_v$ , and $E_f$ represent conduction band, valence band, and Fermi level respectively. $N_s$ , $\rho$ refer to surface charge density and ionized doping density respectively. More details are in text. By assuming the depletion approximation and a uniform doping density, the magnitude of the depletion electric field and the potential energy for electrons are plotted as a function of the distance from the surface. . . . .	98

5.2	Schematic diagram of the second harmonic process at the $\Gamma$ point of the Brillouin zone in GaAs. The fundamental photon energy is near the band gap energy, i.e. $\hbar\omega \sim E_{\Gamma_6} - E_{\Gamma_8}$ . . . . .	99
5.3	Schematic drawing of the electric dipole elements ( $Q_x, Q_y, Q_z$ ) with respect to the crystal orientation and light polarizations. . . . .	100
6.1	Schematic of the SHG experiment in p-in/s-out polarization configuration with crystalline [100] direction in the plane of incidence. The output SHG intensity is dominated by the contributions from $\chi_{yxz}^{(2)}$ . . . . .	115
6.2	The variation of SH intensity at two-photon energy of 2.68 eV as a function of doping density. Both n- and p-type (see inset (a)) samples exhibit a reduction in SHG intensity as a function of increasing doping density. The solid lines are our theoretical fit to the data. . . . .	116
6.3	The plot of $\log(I_0^{2\omega} - I^{2\omega}(E))$ as a function of $\log(\rho)$ with SH fundamental photon energy at 2.68 eV. It clearly can be seen that the relationship between the SHG intensity and dopant density (electric field) is linear (quadratic) at the low dopant densities. . . . .	117
6.4	Schematic drawing of photomodulation second-harmonic generation (PSHG) experiment. In such PSHG experiments, light from an $Ar^+$ ion laser illuminates the sample and modulates the band bending in the depletion region while the SHG experiment is in progress. . . . .	118
6.5	The enhancement of normalized SHG intensity at two-photon energy of 2.68 eV for two typical n-type ( $n=10^{16}/cm^3$ ) and p-type ( $p=10^{16}/cm^3$ ) samples as a function of the photoexcitation intensity. The solid lines are the theoretical fit to the data. The photon energy of the photomodulation light was 2.72 eV. . . . .	119

6.6	Schematic photomodulation of band-bending near surface. The linear photoexcitation creates electrons and holes in the depletion region. These carriers are separated by the built-in field and partly neutralize the surface charge. This in turn decreases the depletion electric field and the band bending. . . . .	120
6.7	Enhancements of SHG ratio as a function of fundamental SH photon energies. The profile is same in n- and p-type samples. $E_0$ refer to the GaAs band gap. The photon energy of the photomodulation light was 2.72 eV. . . . .	121
6.8	SH intensity from a typical p-type ( $\rho_p = 10^{16}/cm^3$ ) sample as a function of time after photomodulation light was turned off. From our theoretical fitting (solid line), the discharging time, $\tau$ , of the surface traps is $\sim 25 \pm 1$ seconds. . . . .	122
6.9	SH intensity from a typical n-type ( $\rho_n = 10^{16}/cm^3$ ) sample as a function of time after photomodulation light was turned off. From our theoretical fitting (solid line), the discharging time, $\tau$ , of the surface traps is $\sim 24 \pm 1$ seconds. . . . .	123
6.10	Schematic drawing of energy band profile at $Ga_2O_3 : GaAs$ n-type interface. . . . .	124
6.11	A 10 Hz Nd:YAG pumped dye laser, with $\sim 50 \mu m$ sample spot size, was used as the fundamental probe light for the SHG measurements. An $Ar^+$ ion laser was used as a cw photocarrier excitation beam, and its transverse beam profile on the sample was a narrow rectangle ( $\sim 2.5 cm$ long, $\sim 4 mm$ wide) with sharp ( $\leq 50 \mu m$ ) edges on all sides. The long edge of the excitation beam was made parallel to the sample [010] axis. The photoexciting beam edge is at $x = 0$ , and a schematic drawing of the photoexcited surface minority carrier density with diffusion length, $L$ , is plotted as a function of the distance, $x$ . . . . .	125

6.12 A typical digram of the variation of SHG output from n-type (p-type) GaAs plotted as a function of distance,  $x$ , from the photoexciting beam edge,  $x = 0$  at room temperature.  $I_{on}(2\omega)$  ( $I_{off}(2\omega)$ ) represents the SHG intensity when the photoexciting beam is on (off). The solid lines are our best fits. The error represents the standard deviation of multiple measurements on multiple samples. The hole (electron) diffusion length,  $L_h$  ( $L_e$ ), is  $2.83 \pm 0.09 \text{ mm}$  ( $7.01 \pm 0.13 \text{ mm}$ ). . . . 126

6.13 A schematic diagram of the energy and position of a minority carrier (p-type sample) that is excited, diffuses, and is then captured again. 127

6.14 Schematic of the mean square displacement  $\langle \delta r^2 \rangle$  of the minority carrier as a function of time. The solid line indicates the carrier diffusion process with a free carrier diffusion coefficient  $D_{free}$  (large positive slope) and the carrier capture by traps for a time  $\tau_e$  (flat line). The dashed line (with relatively small positive slope) represents the effective diffusion process (with effective diffusion coefficient  $D_{eff}$ ) that we observed. Here  $\tau_c$  is the trapping time for the free carrier, and  $\tau_e$  is the time required for the carrier to become reexcited out of trap. Figures are intended to convey ideas and are *not* drawn to scale. . . 128

6.15 A typical SHG results at two different temperatures for n-type GaAs samples. . . . . 129

6.16 Diffusion coefficients as a function of temperature for a typical n-type GaAs sample. The solid line is our fitting according to activated free carrier diffusion model(see Figure 6.13). . . . . 130

6.17 (a) shows  $\ln(D_{eff})$  as a function of  $T^{-1/3}$  for n-type GaAs. The solid line is a linear fit according to VRH model. Inset(b) shows  $\ln(D_{eff})$  as a function of  $T^{-1}$  for n-type GaAs. The solid line is a linear fit according to FRH model. . . . . 131

- 7.1 In p-in/p-out with  $\phi = 0$  configuration, (a) SHG spectrum from As-rich Au:GaAs n-type sample. The solid line is a guide for the eye; (b) SHG spectrum from Ga-rich Au:GaAs n-type sample. The two solid lines are fits using two Lorentzian line shape functions, and the dashed line is the combination of the two lines. The peak positions are estimated to be  $0.708 \pm 0.014$  eV and  $0.731 \pm 0.014$  eV respectively. 144
- 7.2 In p-in/p-out with  $\phi = 0$  configuration, SFG spectrum from an As-rich interface sample. The solid line is a guide for the eye; In the Ga-rich interface sample, the SFG spectrum was shown below. The two solid lines are fit using two Lorentzian line shape functions, and the dashed line is the combination of both lines. The peak positions are estimated to be  $0.713 \pm 0.014$  eV and  $0.730 \pm 0.014$  eV respectively. 145
- 7.3 Bulk SHG spectra from the Au:GaAs n-type sample; the solid line is a guide for the eye. Both As-rich and Ga-rich interface samples have the same bulk spectra. No resonance features have been observed in the bulk SHG contribution. The SHG contribution from the linear combinations of higher-order bulk  $\gamma$  and surface  $\chi_{\parallel\parallel\perp}^{(2)}$  term was near the noise levels in both n- and p-type systems. . . . . 146
- 7.4 Schematic diagram of two probable three-step optical processes  $1 \rightarrow 2 \rightarrow 3$ . Here  $E_v$ ,  $E_I$ , and  $E_c$  represent energies of the valence band maximum, interface states, and conduction band minimum respectively. (a) The transition starts from valence band maximum. The three-step process is represented by  $E_v \xrightarrow{\hbar\omega} E_I \xrightarrow{\hbar\omega} E_c \xrightarrow{2\hbar\omega} E_v$ . (b) The transition starts from interface states. The three-step process is represented by  $E_I \xrightarrow{\hbar\omega} E_c \xrightarrow{2\hbar\omega} E_v \xrightarrow{\hbar\omega} E_I$ . . . . . 147
- 7.5 Interface SHG and SFG spectra from Au:GaAs p-type system, no resonance features were observed. . . . . 148

7.6	Interface SHG and SFG spectra from native oxide GaAs surface, no resonance features were observed. . . . .	149
7.7	Interface SHG spectra from the As capped GaAs n-type sample; the solid line is a guide for the eye. The SHG from thick Au surface was at our noise level. . . . .	150
7.8	Schematic of As and Ga displacement defects. . . . .	151
7.9	In comparison to cathodoluminescence spectra from 10 Å Au on GaAs (from reference 24), Our SHG reveals much sharp resonance feature. . . . .	152
7.10	In comparison to ultraviolet-photoemission measurements at very low Au coverages on GaAs surfaces from reference 23, the interface states became broadened when Au coverage increases from 0.1 monolayer to 0.35 monolayer . . . . .	153

# Chapter 1

## Introduction

Some interesting properties of semiconductor interfaces arise from the existence of interface states. For instance, Fermi level pinning and Schottky barrier heights are determined by these interface states[1, 2]. Furthermore, a charging of the interface results in the formation of a space-charge layer which affects the lineup of the energy bands of the two adjacent materials[3, 4]. For these reasons the physics of buried semiconductor interfaces is both interesting and important, since it contributes to the technological development of electronic devices.

The various electronic and structural properties of interface states originate in many ways. The interface states can be associated with native defects[5, 6, 7], metal-induced states[8, 9, 10], new bonds[11, 12, 13], new band profiles[14, 15, 16, 17], and strain[18, 19]. All of these interface features can influence the properties of the interface. Probing of these *buried* interface states are needed in order to understand their nature. These are challenging problems.

The metal:semiconductor interface has been studied extensively since these interfacial systems form the heart of electronic devices[20]. The alignment of the band structures at such contacts influences carrier transport and photoconductivity in these systems. Improved crystal growth and calibration techniques have resulted in dramatic increases in our understanding and control of interface properties[21, 22].

Buried interfaces are difficult to analyze however; the interface features are produced with a spatial region that is a few atomic layers thick, and is generally covered by a thick overlayer. Surface electric diagnostics are generally limited by the electron penetration depth[7, 10, 23]. For example, inverse photoemission spectra (IPS)[10] and ultraviolet-photoemission spectra (UPS)[23] can only probe buried interface properties under a few monolayers. Optical methods offer long penetration depths, however linear optical spectroscopies lack interface specificity. For instance, cathodoluminescence spectra (CLS)[24] exhibit no intrinsic sensitivity to the buried interface, and contributions from the bulk are not eliminated. This lack of clean spectra from the buried interface makes it difficult to challenge microscopic models of growth and defects in these systems.

Second-order nonlinear optical spectroscopies possess long penetration depths characteristic of most optical methods and intrinsic interface specificity characteristic of second-order optical processes[25]. This technique has attracted considerable attention in probing buried interfacial features[13, 16, 26, 27, 28, 29]. Since the first successful second-order nonlinear optical spectroscopy of  $CaF_2 : Si$  interface systems[13], in which bonding and antibonding states transition of interfacially localized Ca (4s) and Si (3p) hybridized orbitals were observed, second-order nonlinear spectroscopies have been successfully used recently to probe buried interfacial features associated with new band profiles in a ZnSe:GaAs heterostructure[16], new bonds at a  $SiO_2 : Si$  interface[30, 31], and strain at Si based interfaces[19, 32]. In the ZnSe:GaAs work, a virtual cross-over transition between the ZnSe valence band and a *resonance state* of a quantum well located *across* the junction in the GaAs conduction band was observed. Such a virtual coupling was shown to be very sensitive to interfacial lattice relaxation[17] and electronic traps at the heterojunction[33].

This thesis is focused on the investigation of electronic properties of GaAs based interfaces and surfaces by means of second-order nonlinear optical spectroscopy. GaAs is an important material in integrated circuits and optoelectronics[34]. For

instance, the GaAs based heterostructures  $Al_xGa_{1-x}As/GaAs$  are useful for electro-optic device applications, e.g. laser diodes and solar-cells[35, 36]. On the other hand, the remarkable electronic and optical performances of GaAs based devices are influenced by growth conditions, defects, and reconstructions. For example, laser diodes degrade when the defects act as non-radiative recombination centers[37]. As many as fifteen (twelve) electron (hole) traps have been identified in GaAs[38]. However, their nature is only partially understood.

By comparison to recent interface second-order nonlinear optical spectroscopies[13, 16, 30, 31, 19, 32], our results explicitly reveal the existence of defect states near the interface. Our experiments exhibit interface midgap states at metal:GaAs junctions and demonstrate that these states are sensitive to interface preparation[39]. In contrast to the UPS and CLS measurements[10, 23, 24], however, *sharp* resonant features were observed. The intrinsic interface sensitivity of second-order nonlinear optical spectroscopies enables us to suppress spectral contributions from the adjoining bulk media, resulting in more specific assignment of the interfacial spectral features. Further studies of Oxide:GaAs systems reveal the sensitivity of second-order nonlinear optical processes to the depletion electric field which arises from the charging of the surface state[40]. Our observations introduce a new class of nonlinear optical phenomena at interfaces which provides useful information about defect states[39], depletion fields[40], and carrier diffusion along the surfaces[41].

This thesis is organized as follows. First, a brief introduction to second-order nonlinear spectroscopy is presented in chapter 2. The symmetry dependence of the second order susceptibility and the azimuthal angular dependence of the nonlinear polarization configurations are discussed. Some concerns about higher order contributions are explored, and two typical SHG spectra from the bulk and surface of GaAs(001) crystal are illustrated.

In chapter 3, the experimental implementations and laser systems are described in detail, and some concerns about signal processing are addressed. We also discuss

some useful linear optical reflectivity experiments.

In chapter 4, general electronic and optical properties of GaAs are reviewed, and the MBE growth conditions of our samples are presented. We also discuss some properties of our samples, such as the Fermi level pinning and surface reconstruction.

In chapter 5, we present a theoretical analysis of second-order nonlinear optical processes in the presence of the depletion electric field. Our main interest is to elucidate the relationship between the macroscopic susceptibility  $\chi_{ijk}^{(2)}$  and the depletion electric field. The field induced modification of the second-order nonlinear susceptibility has been found to add destructively to the unperturbed existing bulk nonlinear second-order susceptibility  $\chi_{yxz}^{(2)}$ . This diminution depends on the square of the near surface depletion electric field.

In chapter 6, the SHG experimental results in Oxide:GaAs systems are presented and compared to our theoretical analysis in chapter 5. Experiments reveal that the near surface second-order nonlinear optical susceptibility,  $\chi_{yxz}^{(2)}$ , is significantly affected by the depletion electric fields in GaAs(001). With increasing depletion fields, both n- and p-type GaAs samples exhibit a reduction of the bulk second-order susceptibility  $\chi_{yxz}^{(2)}$ , independent of the electric field direction. This picture is in agreement with our theoretical expectations. Our experiments demonstrate the *quadratic* relationship between the SHG intensity and the electric field at low dopant concentrations.

The sensitivity of the near surface bulk second-order susceptibility to the depletion electric field has also been demonstrated using a photomodulation second harmonic generation (PSHG) technique. In such PSHG experiments, light from a Tungsten-lamp-monochromator illuminates the sample to modulate the band bending in the depletion region while the SHG experiment is in progress. An *enhancement* of the second-harmonic intensity has been observed for both n- and p-type samples as a result of a modulation light induced reduction of the depletion fields. We have performed time dependent measurements to follow the *decrease* of the SHG intensity

after the photomodulation light is turned off. This is a direct measurement of the surface state (trap) *discharging* time[33]. Although samples with different doping densities have much different depletion widths, all of our samples exhibit approximately the same discharging time ( $\sim 25$  seconds).

Furthermore, spatially separated second-harmonic generating and photomodulation light beams were employed to study the transverse diffusion of carriers confined near GaAs(001) surfaces. Carrier transport was found to be isotropic and diffusive with small effective diffusion coefficients compared to those of carriers in the bulk. The effective diffusion coefficient is  $2 \times 10^{-2} \text{ cm}^2/\text{second}$  ( $3 \times 10^{-3} \text{ cm}^2/\text{second}$ ) for electrons (holes). It is proposed that these differences arise through the effects of charge traps and near surface charge recombination. Temperature dependent measurements further confirm that charge traps play a prominent role in the diffusion of both holes and electrons.

In chapter 7, we describe how second-order nonlinear optical spectroscopy was used to probe the interface electronic structure of GaAs based thin films and interfaces. The interface spectra from Au:GaAs n-type systems exhibit two resonance features at 0.715 eV and 0.731 eV in Ga-rich interface and a single resonance feature at 0.715 eV in As-rich interface. A similar single resonance feature at 0.715 eV was observed in As:GaAs n-type samples, but were not present in Oxide:GaAs and metal:GaAs p-type systems. All of the observed resonance features are sharp one-photon resonances. Our results suggest that the one photon resonances from metal:GaAs n-type samples are due to a resonant transition from the occupied midgap states to the conduction band minimum. As a result of the lower occupied midgap electron density in p-type and oxide systems, the resonance process originating from these midgap states was too weak to be detected.

The similar resonance at 0.715 eV in As-rich Au:GaAs and As:GaAs n-type samples suggests that this common interface state may be related to As atoms. On the other hand, the interface state at  $\sim 0.731 \text{ eV}$  was only found at the Ga-rich interface

in Au:GaAs n-type systems. This indicates that this interface state is related to the presence of excessive Ga atoms at the interface. We suggest that the interfacial resonance features may arise from the existence of atomic displacement-induced defect states near the junction. In such cases, the formation of As (Ga) atom displacement-induced defect states near the As-rich (Ga-rich) interface is expected as a result of the relative concentrations of As and Ga atoms during growth. Qualitatively the two resonance peaks (peak height or integrated area) can be related to the ratio of As:Ga at the interface. In comparison to the broadened interface states observed in photoemission at very low Au coverages on GaAs surfaces[23], the very sharp observed spectra suggest that overlayer metal atoms displace the As or Ga, and that the detected atomic displacement defects occur in bulk GaAs just far enough from the interface so that their interaction with the metal overlayer free electron states is weak. Possible origins of the dramatic spectral differences observed by our non-linear optical techniques and other no interface sensitive surface techniques will be considered.

Finally, a summary and discussion of future directions are presented in chapter 8.

# Chapter 2

## Second-order nonlinear optical spectroscopy

Second-order nonlinear optical process has inherent sensitivity to the buried interfaces. Because of broken bulk symmetry at the interface, interface second-order susceptibilities have different symmetry properties as compared to the bulk substrate[25]. In this chapter, we present a brief review of nonlinear optical processes, especially the second-order nonlinear process. Two typical second harmonic generation (SHG) spectroscopies from GaAs(001) bulk and surface are demonstrated.

### 2.1 Introduction to Nonlinear Optics

When the optical dielectric constants and magnetic permeabilities become functions of the electromagnetic fields in the media, nonlinear optical processes arise[42]. For instance, the Pockels effect, in which an applied DC electric field changes a crystal's dielectric constants, was observed long before the advent of lasers. However in many cases, nonlinear optical effects require intense electromagnetic fields for observation. Many interesting nonlinear optical phenomena have been observed since the invention of lasers[25]. When two intense light beams (with frequencies  $\omega_1, \omega_2$ ) propagate

inside a nonlinear media, new optical fields at different frequencies, such as  $2\omega_1$ ,  $2\omega_2$ ,  $\omega_1 + \omega_2$ ,  $\omega_1 - \omega_2$ ,  $3\omega_1$ , and  $3\omega_2$ , etc., can be generated under certain circumstances.

The interaction between electromagnetic waves and a medium is governed by the Maxwell equation. The general description of waves propagation in a nonlinear media is[42]

$$[\nabla \times \nabla \times + \frac{1}{c^2} \frac{\partial^2}{\partial t^2}] \mathbf{E}(\mathbf{r}, \mathbf{t}) = -\frac{4\pi}{c^2} \frac{\partial^2}{\partial t^2} \mathbf{P}(\mathbf{r}, \mathbf{t}). \quad (2.1)$$

The polarizations  $P(r, t)$  are expressed in terms of the fields and also serve as sources for the fields. When two waves at frequencies  $\omega_1$  and  $\omega_2$  incident into a nonlinear media ( $E_1 e^{i(\omega_1 t - k_1 \cdot r)}$  and  $E_2 e^{i(\omega_2 t - k_2 \cdot r)}$ ), the solution of fields  $\mathbf{E}(\mathbf{r}, \mathbf{t})$  and polarizations  $\mathbf{P}(\mathbf{r}, \mathbf{t})$  is typically expanded into a set of infinite plane waves:

$$\mathbf{E}(\mathbf{r}, \mathbf{t}) = \sum_n E(k_n, \omega_n) = \sum_n E_n e^{i(\omega_n t - k_n \cdot r)} \quad (2.2)$$

$$\mathbf{P}(\mathbf{r}, \mathbf{t}) = \sum_n P(k_n, \omega_n) = \sum_n P_n e^{i(\omega_n t - k_n \cdot r)}. \quad (2.3)$$

For linear optical processes, only the  $n = 1$  and  $n = 2$  terms are nonzero[43]. For instance,

$$\begin{aligned} [\nabla \times \nabla \times + \frac{1}{c^2} \frac{\partial^2}{\partial t^2}] E_1 e^{i(\omega_1 t - k_1 \cdot r)} &= -\frac{4\pi}{c^2} \frac{\partial^2}{\partial t^2} P_1(r, t) \\ &= -\frac{4\pi}{c^2} \frac{\partial^2}{\partial t^2} \chi^{(1)} E_1 e^{i(\omega_1 t - k_1 \cdot r)}. \end{aligned} \quad (2.4)$$

The more general solution,  $\omega_n = l\omega_1 + m\omega_2$  ( $l, m$  are integers), represents higher-order nonlinear optical processes,

$$\begin{aligned} [\nabla \times \nabla \times + \frac{1}{c^2} \frac{\partial^2}{\partial t^2}] E(k_n, \omega_n) &= -\frac{4\pi}{c^2} \frac{\partial^2}{\partial t^2} P(k_n, \omega_n) \\ &= -\frac{4\pi}{c^2} \frac{\partial^2}{\partial t^2} \chi^{(l+m)}(\omega_n = l\omega_1 + m\omega_2, \underbrace{\omega_1, \dots, \omega_1}_l, \underbrace{\omega_2, \dots, \omega_2}_m) : E^l(k_1, \omega_1) E^m(k_2, \omega_2). \end{aligned} \quad (2.5)$$

In this case, the nonlinear susceptibility  $\chi^{(l+m)}(\omega_n, \underbrace{\omega_1, \dots, \omega_1}_l, \underbrace{\omega_2, \dots, \omega_2}_m)$  couples the incident fields at  $\omega_1$  and  $\omega_2$  to produce a field at  $\omega_n = l\omega_1 + m\omega_2$ .

In the case of harmonic generation ( $\omega_1 = \omega_2$ ) under the electric dipole approximation, the general form of the polarization can be written as

$$\mathbf{P} = \chi_{ij} : \mathbf{E}(\omega) + \chi_{ijk}^{(2)} : \mathbf{E}_j(\omega) \mathbf{E}_k(\omega) + \chi_{ijkl}^{(3)} : \mathbf{E}_j(\omega) \mathbf{E}_k(\omega) \mathbf{E}_l(\omega) + \dots \quad (2.6)$$

Here the indices  $i, j, k$  refer to the cartesian components of the fields. The first, second, and third terms represents the linear polarization, second-order nonlinear polarization, and the third-order nonlinear polarization, respectively. Under nonresonant conditions,  $\chi_{ijk}^{(2)}$  is usually 6 to 7 orders of magnitude smaller than  $\chi_{ij}$ , and  $\chi_{ijkl}^{(3)}$  is 12 to 14 orders of magnitude smaller than  $\chi_{ij}$ [25, 43]. The  $n$ th-order susceptibility is roughly  $7n$  orders of magnitude smaller than the linear susceptibility  $\chi_{ij}$ .

Many nonlinear optical experiments involve second-order nonlinear optical processes. Typical experiments are sum frequency generation SFG ( $\omega_3 = \omega_1 + \omega_2$ ) and difference frequency generation DFG ( $\omega_3 = \omega_1 - \omega_2$ ). Since our research work focused on second-order nonlinear optical phenomena, the following discussion concentrates on second-order nonlinear optical processes. The second-order polarization  $P^{(2)}(\omega_3)$  can consist of electric dipoles, magnetic dipoles, electric quadrupoles, or even higher order multipole contributions[42]. In the plane wave approximation, the second-order nonlinear optical wave equation is written as[42]

$$\nabla \times \nabla \times \mathbf{E}(k_3, \omega_3) + \frac{\epsilon}{c^2} \frac{\partial^2}{\partial t^2} \mathbf{E}(k_3, \omega_3) = -\frac{4\pi}{c^2} \frac{\partial^2}{\partial t^2} \mathbf{P}^{(2)}(k_3, \omega_3). \quad (2.7)$$

With

$$P_i^{(2)}(\omega_3 = \omega_1 + \omega_2) = \chi_{ijk}^{(2)} : E_j(\omega_1) E_k(\omega_2) + \Gamma_{ijkl}^{(3)}(\omega_3) \mathbf{E}_j(\omega_1) \nabla_k \mathbf{E}_l(\omega_2) + \dots$$

$\chi_{ijk}^{(2)}$  ( $\Gamma_{ijkl}^{(3)}$ ) is a third rank tensor (fourth rank tensor). The first term represents the electric dipole contribution, and second term represents the magnetic dipole and electric quadrupole contributions. Generally the dominant contribution is from the electric dipole term  $\chi_{ijk}^{(2)}(\omega_3) : \mathbf{E}_j(\omega_1) \mathbf{E}_k(\omega_2)$ . Only in media for which the electric dipole transition is forbidden, will the electric quadrupole and magnetic dipole contributions dominate the nonlinear process. The magnetic dipole and electric quadrupole contributions are usually  $10^5$  or  $10^6$  times smaller than the electric dipole[25]. Therefore we mainly consider second-order nonlinear optical processes in the electronic dipole transition approximation. Discussions of higher-order terms are presented in references 45, 46, and 47.

In the consideration of electric dipole contribution, the incident wave produce a second harmonic source polarization,  $P^{(2)}$

$$P^{(2)} = \chi(2\omega, \omega, \omega) : EE e^{i(k_b \cdot r - 2\omega t)}.$$

with

$$k_b = 2k = \sqrt{\epsilon(\omega)} \frac{2\omega}{c}.$$

Therefore the exact solution to equation 2.7 is

$$\mathbf{E}^{(2\omega)} = \mathbf{E}_f^{(2\omega)} e^{i(k_f \cdot r - 2\omega t)} - \frac{4\pi(4\omega^2/c^2)P}{k_f^2 - k_b^2} \left[ \hat{p} - \frac{k_b(k_b \cdot \hat{p})}{k_f^2} \right] e^{i(k_b \cdot r - 2\omega t)}, \quad (2.8)$$

$\hat{p}$  represents a unit vector in the direction of  $\mathbf{P}^{(2\omega)}$ . The first term of Eq. (2.8) is the solution of the homogeneous part of nonlinear wave equation 2.7. This wave propagates in the direction of  $k_f$ , i.e.,

$$k_f = \sqrt{\epsilon(2\omega)} \frac{2\omega}{c}.$$

The second term is a particular solution of the inhomogeneous nonlinear wave equation 2.7. This field is bound to the fundamental wave, and propagates with wavevector  $k_b$ . The subscripts “f” and “b” refer to free and bound waves respectively.

In general, the nonlinear optical radiation could appear in all directions; However the the radiation pattern is strongly peaked in a certain direction due to the so called phase matching condition. For instance, in the case of sum frequency generation (SFG) experiments, energy conservation requires  $\omega_3 = \omega_1 + \omega_2$ , while the momentum conservation requires  $k_3 = k_1 + k_2$ . Therefore the most effective SFG is along the phase matching direction  $k_3$  (see figure 2.1(a)). In the case of second harmonic generation at an interface boundary, the tangential momentum conservation of each individual frequencies,  $\omega$  and  $2\omega$ , must be satisfied. For the fundamental frequency,  $\omega_1$ , it is linear Snell’s law, i.e.,

$$k_{\parallel}^i(\omega) = k_{\parallel}^R(\omega) = k_{\parallel}^T(\omega).$$

Here ‘i’, ‘R’, and ‘T’ refer to incident, reflected and refracted waves respectively.  $\parallel$  represents the tangential component. To satisfy this condition for the harmonic wave at  $2\omega$ , we get the boundary conditions

$$2k_{\parallel}^T(\omega) = k_{b2,\parallel}^T(2\omega) = k_{f2,\parallel}^T(2\omega) = k_{f1,\parallel}^R(2\omega).$$

$k_{fi}$  ( $k_{bi}$ ) represents the magnitude of the free (bound) wavevector in medium-i (see figure 2.1(b)).  $k_{\parallel}^T(\omega)$  is the linear refracted wave. In the case of vacuum/solid interface, the angles of reflection and refraction of the second harmonic waves are derived as

$$\sin\theta_1^R = \frac{k_{f1,\parallel}^R(2\omega)}{|k_{f1}^R(2\omega)|} = \frac{k_{\parallel}^T(\omega)}{|k^R(\omega)|} = \frac{k_{\parallel}^R(\omega)}{|k^R(\omega)|} = \sin\theta^i,$$

$$\sin\theta_f^T = \frac{k_{b2,\parallel}^T(2\omega)}{|k_{b2}^T(2\omega)|} = \sqrt{\epsilon(2\omega)}^{-1} \sin\theta^i,$$

$$\sin\theta_b^T = \sqrt{\epsilon(\omega)}^{-1} \sin\theta^i.$$

Here  $\theta^i$  is the fundamental wave incident angle. The reflected second harmonic wave propagates in the same direction as the reflected fundamental wave. The bound wave propagates in the same direction as the refracted fundamental wave, and whereas the free wave in general goes in a different direction. In the case of solid-1/solid-2 interface, the above equation is

$$\sqrt{\epsilon_1(2\omega)} \sin\theta_1^R = \sqrt{\epsilon_1(\omega)} \sin\theta^i,$$

$$\sqrt{\epsilon_2(2\omega)} \sin\theta_f^T = \sqrt{\epsilon_1(\omega)} \sin\theta^i,$$

$$\sqrt{\epsilon_2(\omega)} \sin\theta_b^T = \sqrt{\epsilon_1(\omega)} \sin\theta^i.$$

More complicated cases such sum frequency generation is presented in reference 42.

## 2.2 General properties of nonlinear optical susceptibility

The nonlinear optical susceptibility depends on the character of the media that supports the polarization. For example, it depends on properties such as symmetry, band-structure, etc.. In this section, we briefly describe some general properties of the nonlinear optical susceptibility.

### 2.2.1 Permutation symmetries of nonlinear susceptibility

The  $n$ th-order nonlinear optical process arises from the interaction of  $n$  optical fields through a  $n$ th-order nonlinear optical susceptibility  $\chi_{i,j,k,\dots,t}^{(n)}(\omega, \omega_1, \omega_2, \dots, \omega_n)$ . Because those  $n$  fields are simultaneously interacting, a variation in their orders should not change the final field strength. Thus there exist an intrinsic permutation symmetry in the nonlinear susceptibility  $\chi_{i,j,k,\dots,t}^{(n)}(\omega, \omega_1, \omega_2, \dots, \omega_n)$  such that the Cartesian indices can be permuted together with their frequencies, i.e,  $n$  total  $(j, \omega_1), (k, \omega_2), \dots, (t, \omega_n)$  pairs can be permuted among the tensor elements  $\chi_{i,j,k,\dots,t}^{(n)}(\omega, \omega_1, \omega_2, \dots, \omega_n)$ , without changing its value. In the case of second-order nonlinear susceptibility, the intrinsic symmetry permutation is simply,

$$\chi_{ijk}^{(2)}(\omega, \omega_1, \omega_2) = \chi_{ikj}^{(2)}(\omega, \omega_2, \omega_1) \quad (2.9)$$

As a result, the original 324 complex elements of  $\chi^{(2)}$  elements reduce to 81 independent parameters.

If the media is optically lossless, a full permutation symmetry exists[47], i.e., all  $n+1$   $(i, \omega), (j, \omega_1), (k, \omega_2), \dots, (t, \omega_n)$  pairs can be permuted among the tensor element  $\chi_{i,j,k,\dots,t}^{(n)}(\omega, \omega_1, \omega_2, \dots, \omega_n)$  without changing its value. In particular, the second-order nonlinear susceptibility, with the full symmetry permutation, is simply,

$$\chi_{ijk}^{(2)}(\omega, \omega_1, \omega_2) = \chi_{ikj}^{(2)}(\omega, \omega_2, \omega_1) = \chi_{jik}^{(2)}(\omega_1, \omega, \omega_2) = \dots \quad (2.10)$$

Under the full symmetry conditions, all elements of  $\chi^{(2)}$  are real, and all 81 parameters of  $\chi^{(2)}$  reduces to 27 independent elements. Furthermore, in the absence of dispersion, the nonlinear susceptibility is essentially independent of frequency, and  $\chi_{i,j,k,\dots,l}^{(n)}(\omega, \omega_1, \omega_2, \dots, \omega_n)$  remains constant when only the Cartesian indices are permuted. This is called Kleinman's symmetry. If all of the above conditions are satisfied, the number of independent tensor elements can be greatly reduced. For example, the total number of independent elements of  $\chi^{(2)}$  reduces to 10.

### 2.2.2 Spatial symmetries of nonlinear susceptibility

The spatial symmetries of nonlinear susceptibility depends solely on the properties of the crystal and must be consistent with the physical properties of the crystal. Such symmetry constraints are expressed in a very general form by Neumann's principle, which states that a crystal point group must be either the same or a subgroup of the symmetry group inherent in the physical property considered [48]. For example, under the electric dipole approximation, a second-order susceptibility is forbidden in a media such as Si which possesses an inversion symmetry. On the other hand, GaAs carries a single nonzero bulk second-order susceptibility  $\chi_{yxz}^{(2)}$  based on its zinc-blende crystal structure[47]. Moreover, at surfaces or interfaces, the bulk symmetry is broken and some of the bulk forbidden second-order nonlinear susceptibilities may be allowed.

In many cases, the interface or surface has a rather well-defined structural symmetry. The interface  $\chi_{ijk}^{(2)}$  will have symmetry properties related to the interface structures [28]. In GaAs(001) case, the bulk symmetry  $\bar{4}3m$  is reduced to  $mm2$  at the surface. The allowed surface second-order susceptibilities are  $\chi_{zii}^{(2)}$ ,  $\chi_{iiz}^{(2)}$ ,  $\chi_{izi}^{(2)}$ , instead of a single element  $\chi_{xyz}^{(2)}$  inside the bulk, where the surface plane [001] is chosen in the  $\hat{x} - \hat{y}$  plane and  $\hat{x} - \hat{z}$ ,  $\hat{y} - \hat{z}$  are the two mirror planes. This can be explained as follows. Consider reflection operations through two mirror planes

$$x \longrightarrow -x$$

$$y \rightarrow -y.$$

These spatial symmetry operations do not change the values of the surface  $\chi_{ijk}^{(2)}$ . Since  $\chi_{ijk}^{(2)}$  transforms as a cartesian tensor,  $x$  or  $y$  must appear evenly in the  $i, j, k$  indices. As a result, the nonvanishing elements of  $\chi_{ijk}^{(2)}$  are  $\chi_{xxz}^{(2)}$ ,  $\chi_{xzx}^{(2)}$ ,  $\chi_{zxx}^{(2)}$ ,  $\chi_{yyz}^{(2)}$ ,  $\chi_{yzy}^{(2)}$ ,  $\chi_{zyy}^{(2)}$ , and  $\chi_{zzz}^{(2)}$ . According to the intrinsic symmetry permutation,  $\chi_{xxz}^{(2)} = \chi_{xzx}^{(2)}$  and  $\chi_{yyz}^{(2)} = \chi_{yzy}^{(2)}$  must be satisfied. Generally, surface second-order nonlinear optical susceptibilities  $\chi_{ijk}^{(2)}$  with different symmetries can be calculated under the same rules, and the results are shown in Table 2.1. Some higher-order nonlinear optical susceptibilities are also presented in reference 47.

## 2.3 Nonlinear susceptibility and the band-structure of crystals

Microscopically the nonlinear susceptibility arises from the dipole transitions among the electronic states of the medium. The most general phenomenological form of  $n$ -th order susceptibility is,

$$\chi^{(n)} \sim N \frac{e^{n+1}}{\hbar^n} \sum_{g,e,e',\dots} \frac{\langle g|\vec{r}|e\rangle\langle e|\vec{r}|e'\rangle\dots\dots\langle f|\vec{r}|g\rangle}{(\omega_1 - \omega_{eg} + i\Gamma_{eg})(\omega_2 - \omega_{e'g} + i\Gamma_{e'g})\dots\dots(\omega_n - \omega_{fg} + i\Gamma_{fg})} \quad (2.11)$$

Here  $|g\rangle$  represents ground state, and  $|e\rangle, |e'\rangle, \dots$  are any excited states of the medium.  $N$  is the number of atoms(molecules) per volume. There are a total of  $n$  frequencies  $(\omega_1, \omega_2, \dots, \omega_n)$ , all of which are coupled with the energy levels of the medium through the  $n$ th-order nonlinear susceptibility. Clearly the spectrum of the nonlinear susceptibilities should reveal the correlation between the electronic structure and the nonlinear optical interactions. Whenever the optical field energy  $\hbar\omega_n$  equals the transition energy between two states (e.g.  $\hbar\omega_{fg}$ ), the nonlinear susceptibility is resonantly enhanced. The most interesting features of the nonlinear optical spectroscopy involve those resonance terms and reveals electronic structure informations

about the system. In contrast, the nonresonance terms only contribute a constant background.

There are many detailed calculations of nonlinear second-order susceptibilities based on perturbation theory [25, 42, 47, 49, 50]. In the case of second-harmonic generation, the  $\chi_{ijk}^{(2)}$  can be written as

$$\begin{aligned} \chi_{ijk}^{(2)} = & N \frac{e^3}{\hbar^2} \sum_{g,n,n'} \langle g|r_i|n'\rangle \langle n'|r_j|n\rangle \langle n|r_k|g\rangle \\ & \times [(2\omega - \omega_{ng} + i\Gamma_{ng})^{-1}(\omega - \omega_{n'g} + i\Gamma_{n'g})^{-1} \\ & + (2\omega + \omega_{ng} + i\Gamma_{ng})^{-1}(\omega + \omega_{n'g} + i\Gamma_{n'g})^{-1} \\ & + (\omega + \omega_{ng} + i\Gamma_{ng})^{-1}(\omega - \omega_{n'g} + i\Gamma_{n'g})^{-1}] \end{aligned} \quad (2.12)$$

Here  $|g\rangle$  represents the ground state, and  $|n'\rangle$  and  $|n\rangle$  are two excited states of the medium. From the view of the electric dipole transition approximation, we can also see why the second-order susceptibility in an inversion symmetric medium is zero. The states  $|g\rangle, |n'\rangle, |n\rangle$  must have definite parity in the inversion symmetric medium and  $\vec{r}$  can only connect states with opposite parity in the dipole transition approximation. Since  $\vec{r}$  occurs an odd number of times in the transition matrix, the second-order nonlinear susceptibility vanishes. Furthermore, we can roughly estimate the magnitude of the second-order susceptibility of a crystal.  $\chi^{(2)}$  scales as  $\frac{Ne^3}{\omega^2} r^3$ , and with a typical atomic length  $r \sim 10^{-8} \text{cm}$ ,  $\omega \sim 10^{15} \text{Hz}$ , and  $N \sim 10^{22} \text{cm}^{-3}$ , one obtains  $\chi^{(2)} \sim 10^{-8} \text{esu}$ .

The second-order nonlinear optical process involves three-wave mixing. The interband or intraband transition starts from ground state  $|g\rangle$ , passes through a first excited state  $|n\rangle$ , to a second excited state  $|n'\rangle$ , and finally returns to the ground state (see figure 2.2). Such processes are virtual transitions in which no population transfer occurs. The value of  $\chi$  includes a summation over all possible excited states. The resonance could be a one-photon resonance, in which the incident photon energy  $\hbar\omega$  equals an energy transition between two states involved, or a two photon

resonance in which the second-harmonic photon energy  $2\hbar\omega$  equals the energy transitions of two states involved. The summation over all states makes the problem complicated and unsolvable. Fortunately experiments only deal with resonances or near resonances, and the dominate terms of second-order susceptibilities mainly arise from those resonance states. For example, in direct band gap materials, if the fundamental SH generating photon energy is near the energy band gap of the system, the second-order-susceptibility is dominated by the transitions between the valence band maximum and conduction band minimum [50]. Thus, we only need to consider resonance states in our theoretical analysis.

## 2.4 Second-order Nonlinear Optical Experiments

Second-order nonlinear optical spectroscopy attracts specific attention due to its long penetration depths and intrinsic interface specificity[25]. Many successful second-order nonlinear optical (SHG or SFG) experiments have been performed to probe different interfacial properties, such as surface adsorption/desorption[51], interface structures[28, 52, 53], electronic dynamics at interfaces[54], and interface states[13, 16]. In this section, we describe two typical second-harmonic generation experiments in GaAs(001) systems. The surface signals from the GaAs(001) samples were separated from the bulk signals by proper choice of sample orientation and light polarizations.

### 2.4.1 SHG from GaAs(001) bulk

GaAs has a zinc-blende crystal structure ( $\bar{4}3m$ ) and carries a single nonzero bulk second-order susceptibility  $\chi_{xyz}^{(2)}$ . In the laboratory frame, the surface was in the  $\hat{x} - \hat{y}$  plane, and the  $\hat{z}$  axis was normal to the surface [001] plane. The crystal axes were  $\hat{x}'$ ,  $\hat{y}'$ , and  $\hat{z}'$ . The  $\hat{z}'$  axis is the same as  $\hat{z}$ , and the  $\hat{x}' - \hat{y}'$  plane sits in the  $\hat{x} - \hat{y}$  plane with a relative angle  $\phi$  between the  $\hat{x}'$  and  $\hat{x}$  (see figure 2.3). The symmetry of

GaAs bulk  $\chi_{ijk}^{(2)}$  can be measured by rotating the crystal with respect to the laboratory frame. If a p-polarized (polarization in the plane of incidence, i.e., in  $\hat{x}$  direction) fundamental light propagates in the GaAs(001) crystal, the generated s-polarized (perpendicular to the plane of incidence, i.e., in  $\hat{y}$  direction) second-harmonic light can be derived as follows. The fundamental incident light fields in the crystal frame are related to the fields in the lab frame as follows,

$$E_{z'}(\omega) = E_z = E_0 \cos(\theta) \quad (2.13)$$

$$E_{x'}(\omega) = E_0 \sin(\theta) \cos(\phi) \quad (2.14)$$

$$E_{y'}(\omega) = -E_0 \sin(\theta) \sin(\phi) \quad (2.15)$$

Here  $E_0$  is the incident optical field at frequency  $\omega$ , and  $\theta$  is the incident angle with respect to the  $\hat{z}$  axis. Therefore the output SHG field in the crystal frame can be written as

$$E_{y'}(2\omega) = 2\chi_{y'x'z}^{(2)} E_{x'} E_{z'} \quad (2.16)$$

$$E_{x'}(2\omega) = 2\chi_{x'y'z}^{(2)} E_{y'} E_{z'} \quad (2.17)$$

As a result, the s-polarized SHG output field is

$$E_y(2\omega) \sim \chi_{x'y'z}^{(2)} E_0^2 \sin(2\theta) \cos(2\phi) \quad (2.18)$$

Therefore in the p-in/s-out polarization configuration, the output SHG signal exhibits a  $\cos^2(2\phi)$  functional dependence on the rotation angle  $\phi$ . This rotation symmetry of  $\cos^2(2\phi)$  is the same whether one detects SHG signal in reflection or transmission geometry. The bulk SHG output field as a function of the rotation angle  $\phi$  and polarization has been calculated in table 2.2.

It is worth noting that both the probing light and the SHG output must propagate through the boundary between the air and the GaAs(001) crystal. The effect of this can be taken into account using the Fresnel coefficients which depend on the linear optical properties of the medium and the incident angle  $\theta$ . Nevertheless, the

boundary condition effects do not change the SHG signal rotation symmetry with respect to angle  $\phi$ . More detailed calculations of the boundary effects is presented in reference [55]. Our SHG signal from undoped GaAs(001) as a function of the rotation angle in a reflection geometry has been plotted in figure 2.4. The  $\cos^2(2\phi)$  relationship has been successfully demonstrated. By selecting  $\phi = 0$ , we maximized the sensitivity to the bulk SHG contribution. A typical bulk GaAs SHG spectrum is plotted in figure 2.5. After considering linear factor [55], we determined  $|\chi_{xyz}^{(2)}|$ , and our spectra indicate a one-photon resonance at  $E_0$  and a two photon resonance at  $E_1$  in GaAs crystal (see figure 2.6) [56].

### 2.4.2 SHG from GaAs(001) surface

The separation of bulk and surface GaAs signals in second-order nonlinear optical experiments is achieved by choosing certain light polarization configurations. At the surface, the bulk symmetry is broken and some bulk forbidden second-order susceptibilities are allowed in the surface symmetry frame. Moreover, the surface symmetry axes will not necessarily be the same as the bulk symmetry axes.

At the GaAs(001) surface, the bulk symmetry  $\bar{4}3m$  is broken, and the new symmetry for the surface is  $mm2$ . In the  $mm2$  symmetry frame  $(\hat{x}'', \hat{y}'', \hat{z}'')$ , the symmetry axis  $\hat{x}''$  ( $\hat{y}''$ ) in which the two mirror planes  $(\hat{x}'' - \hat{z}'', \hat{y}'' - \hat{z}'')$  sit is rotated  $45^\circ$  about the  $\hat{z}$  axis ( $\hat{z}'' = \hat{z}$ ) with respect to the crystal axis  $\hat{x}'$  ( $\hat{y}'$ ) (see figure 2.7). Microscopically GaAs surface  $mm2$  symmetry frame and bulk  $\bar{4}3m$  symmetry frame are plotted in figure 2.8.

When an s-polarized fundamental wave is incident on the sample, the incident field in the laboratory frame is

$$\vec{E}(\omega) = E_y(\omega)\hat{y} \quad (2.19)$$

In the  $mm2$  frame, the fields are

$$E_{x''}(\omega) = E_y(\omega)\sin(\phi + 45^\circ)\hat{x}'' \quad (2.20)$$

$$E_{y''}(\omega) = E_y(\omega)\cos(\phi + 45^\circ)\hat{y}'' \quad (2.21)$$

$$E_{z''}(\omega) = 0 \quad (2.22)$$

The nonvanishing second-order susceptibilities in the  $mm2$  symmetry are given in table 2.1. Finally, the second harmonic output fields in the  $mm2$  symmetry frame are

$$E_{x''}(2\omega) = 0 \quad (2.23)$$

$$E_{y''}(2\omega) = 0 \quad (2.24)$$

$$E_{z''}(2\omega) = [\chi_{z''x''x''}\sin^2(\phi + 45^\circ) + \chi_{z''y''y''}\cos^2(\phi + 45^\circ)]E_y^2\hat{z} \quad (2.25)$$

The only nonzero surface SHG field is polarized along the  $\hat{z}$  direction. Thus, the above function exhibits a p-polarized SHG output field as a function of the rotation angle  $\phi$ . All possible rotation angle dependences of the SHG field from a GaAs(001) surface are calculated in table 2.2. With  $\phi = 0$  for such an s-in/p-out configuration, the measured SHG signal arises only from the surface  $\chi_{z''x''x''}$  and  $\chi_{z''y''y''}$  contributions, while the bulk contribution is zero (see table 2.2).

According to table 2.2, in p-in/p-out with  $\phi = 0$  configuration, one can also observe pure surface SHG contributions. A typical SHG spectrum with surface contributions is plotted in figure 2.9. These surface SHG signals arises mainly from surface second-order susceptibility  $\chi_{z''z''z''}$ ,  $\chi_{x''z''x''}$ ,  $\chi_{y''z''y''}$ ,  $\chi_{z''x''x''}$  and  $\chi_{z''y''y''}$ . According to the full symmetry permutation,  $\chi_{x''z''x''}$  ( $\chi_{y''z''y''}$ ) is equal to  $\chi_{z''x''x''}$  ( $\chi_{z''y''y''}$ ). However, our SHG experiments in s-in/p-out configuration indicate that the surface SHG signals from  $\chi_{z''x''x''}$  and  $\chi_{z''y''y''}$  contributions were two orders of magnitude smaller than surface signal in p-in/p-out configuration. (see figure 2.9). It suggests that the surface second-order susceptibility elements  $\chi_{z''x''x''}$  and  $\chi_{z''y''y''}$  are much weaker than the element  $\chi_{z''z''z''}$ . Under such circumstances, the above surface SHG signals in p-in/p-out configuration arise mainly from  $\chi_{z''z''z''}$ . In the s-in/s-out polarization configuration, all surface and bulk second-order nonlinear optical processes are forbidden in the electric dipole approximation, the SHG signal was below our

noise level.

### 2.4.3 Some concerns about higher-order contributions

There exist two kinds of higher-order contributions to the second-order nonlinear optical processes. One arises from the nonlocal response of the system which carries the electric quadrupole and magnetic dipole contributions  $(\Gamma_{ijkl}^{(\omega_3)} \mathbf{E}_j^{(\omega_1)} \nabla_k \mathbf{E}_l^{(\omega_2)})$ [55]. The other arises from the higher-order electric dipole effect under a strong external field. For example, the third-order susceptibility under an external  $E_l^{DC}$  field results in an effective second-order susceptibility  $\chi_{ijk}^{(\omega_3)} = \chi_{ijkl} : E_l^{DC}$ [57, 58, 59, 60]. The fourth-rank tensors  $\Gamma_{ijkl}$  and  $\chi_{ijkl}$  have exactly the same symmetry. For  $\bar{4}3m$  symmetry media (GaAs, ZnSe), the nonzero elements for  $\Gamma_{ijkl}$  and  $\chi_{ijkl}$  are shown in Table 2.3. Theoretically these elements are much smaller than the second-order electric dipole susceptibility by a factor of  $10^5$  to  $10^7$ [25].

Generally it is conventional to divide the nonlocal effects from the electric quadrupole and magnetic dipole into isotropic and anisotropic contributions with respect to the orientation of the crystal:

$$P_i^{(2\omega)} = (\delta - \beta - 2\gamma)(\mathbf{E} \cdot \nabla)E_i + \beta E_i(\nabla \cdot \mathbf{E}) + \gamma \nabla_i(\mathbf{E} \cdot \mathbf{E}) + \zeta E_i \nabla_i E_i. \quad (2.26)$$

Here  $\delta, \beta, \gamma,$  and  $\zeta$  are phenomenological constants. The first three terms are isotropic, and the last term is anisotropic with respect to the orientation of the crystal. The relationships among  $\delta, \beta, \gamma, \zeta,$  and  $\Gamma_{ijkl}$  has been discussed in reference[55]. These higher-order contributions to second-order nonlinear processes can be calculated in specific polarization configurations. For media with  $\bar{4}3m$  symmetry, in the s-in/p-out configuration, the results are[55]

$$P_x = -2\zeta E_y^2 k_x \sin^2 \phi \cos^2 \phi + 2\gamma E_y^2 k_z (\sin^4 \phi + \cos^4 \phi) \quad (2.27)$$

$$P_z = \Gamma_{zyiy} E_y^2 k_i = \Gamma_{zyxy}^{(L)} E_y^2 + \Gamma_{zyzy}^{(L)} E_y^2 k_z = \Gamma_{zxzx}^{(C)} E_y^2 k_z = \frac{\gamma}{2} E_y^2 k_z \quad (2.28)$$

If we set  $\phi = 0$ , the output SHG contributions are determined by the tensor element

$\gamma$ . In addition, the surface dipole contributions to SHG also exist at  $\phi = 0$  in the s-in/p-out polarization configuration (see Table 2.2). Therefore, we can only measure the linear combination of  $\gamma$  and the surface tensor elements  $\chi_{zxx}, \chi_{zyy}$ ,

$$P_z = \frac{\gamma}{2} E_y^2 k_z + \frac{1}{2} [\chi_{z''x''x''} + \chi_{z''y''y''}] E_y^2 \quad (2.29)$$

On the other hand, in the s-in/s-out configuration, the surface SHG radiation is zero. The SHG signal arises from the higher-order bulk nonlinearity  $\zeta$ .

$$P_y = \zeta \frac{\sin 4\phi}{4} E_y^2 k_x. \quad (2.30)$$

Therefore the possibility of higher-order bulk contributions can be examined in the s-in/s-out and s-in/p-out polarization configurations. All of our experimental results show that these higher-order contributions were too weak to be detected (see last section discussions).

In addition, higher-order bulk contributions can also be brought out with an externally applied DC electric field. Macroscopically such a field creates effective second-order susceptibilities through the coupling of the external field  $E$  and the third-order susceptibility or even higher-order susceptibilities,

$$\chi_{ijk}^{(2)} = \chi_{ijkl}^{(3)} : E_l + \chi_{ijklm}^{(4)} : E_l E_m + \dots$$

Here the  $l, m, \dots$  are the external fields directions. Physically this can be understood as follows. The external fields break the bulk symmetry, and perturb the electronic states of the medium. As a result it leads to the enhancement of otherwise forbidden second-order nonlinear optical processes. For example, external-field-induced second-harmonic generation (DCSHG) have been observed in gases[57, 58] and crystals[59, 60]. In the case of GaAs(001), the coupling of the field  $E$  normal to the surface and third-order susceptibilities ( $\chi_{ijk}^{(2)} = \chi_{ijkz}^{(3)} : E_z$ ) could result in the nonzero elements,  $\chi_{zzz}^{(2)}, \chi_{yzy}^{(2)} = \chi_{xzx}^{(2)}, \chi_{yyz}^{(2)} = \chi_{xxz}^{(2)}, \chi_{zyy}^{(2)} = \chi_{zxx}^{(2)}$  (see table 2.3). Furthermore, the field also induces perturbations to the original bulk second-order susceptibility  $\chi_{xyz}$ . Such field induced effects are discussed in chapter 5 and demonstrated in our experiments.

Symmetry <sup>1</sup>	Mirror Plane	Nonvanishing Elements
$C_1$	No Mirror	$xxx, xxy = xyx, xyy, yxx,$ $xyy = yyx, yyy, xxz = xzx, xyz = xzy,$ $yxz = yzx, yyz = yzy, zxx, zxy = zyx,$ $zyy, xzz, yzz, zxx = zzx,$ $zyz = zzy, zzz$
$C_{1v}$	$\hat{y} - \hat{z}$	$xxy = xyz, yxx, yyy, xxz = xzx,$ $yyz = yzy, zxx, zyy, yzz,$ $zyz = zzy, zzz$
$C_2$	No Mirror	$xxz = xzx, xyz = xzy, yxz = yzx,$ $yyz = yzy, zxx, zyy,$ $zxy = zyx, zzz$
$C_{2v}$	$\hat{x} - \hat{z}, \hat{y} - \hat{z}$	$xxz = xzx, yyz = yzy, zxx, zyy, zzz$
$C_3$	No Mirror	$xxx = -xyy = -yxy = -yyx,$ $yyy = -yxx = -xxy = -xyx,$ $xxz = xzx = yyz = yzy,$ $xyz = xzy = -yxz = -yzx,$ $zxx = zyy, zzz$
$C_{3v}$	$\hat{y} - \hat{z}$	$yyy = -yxx = -xxy = -xyz,$ $xxz = xzx = yyz = yzy,$ $xxz = xzx = yyz = yzy,$ $zxx = zyy, zzz$
$C_4, C_6$	No Mirror	$xxz = xzx = yyz = yzy,$ $xyz = xzy = -yxz = -yzx,$ $zxx = zyy, zzz$
$C_{4v}, C_{6v},$ isotropic	$\hat{x} - \hat{z}, \hat{y} - \hat{z}$	$xxz = xzx = yyz = yzy,$ $zxx = zyy, zzz$

Table 2.1: Surface  $\chi^{(2)}$  elements for several symmetry classes ( $\hat{x} - \hat{y}$  surface plane); 1.  $C_n$  represents point group containing one n-fold proper rotation axis;  $C_{nv}$  contains  $C_n$  plus a  $\sigma_v$  reflections.  $\sigma_v$  contains a reflection in a plane passing through the axis of the highest symmetry.  $C_n$  also requires n of these  $\sigma_v$ 's separated by  $\frac{\pi}{n}$ .

Polarization	Surface $C_{2v}$ Contribution
$S_{in}/S_{out}$	0
$S_{in}/P_{out}$	$[\chi_{z''x''x''}\cos^2(\phi + 45^\circ) + \chi_{z''y''y''}\sin^2(\phi + 45^\circ)]E_y^2\hat{z}$
$P_{in}/S_{out}$	$(\chi_{x''z''x''} - \chi_{y''z''y''})E_xE_z\cos(2\phi)\hat{y}$
$P_{in}/P_{out}$	$[\chi_{z''z''z''}E_z^2 + \chi_{z''x''x''}E_x^2\cos^2(\phi + 45^\circ)$ $+ \chi_{z''y''y''}E_y^2\sin^2(\phi + 45^\circ)]\hat{z}$ $+ [\chi_{x''z''x''}\cos^2(\phi + 45^\circ)$ $+ \chi_{y''z''y''}\sin^2(\phi + 45^\circ)]E_xE_z\hat{x}$
	Bulk $\bar{4}3m$ Contribution
$S_{in}/S_{out}$	0
$S_{in}/P_{out}$	$\chi_{z'x'y'}E_y^2\sin(2\phi)\hat{z}$
$P_{in}/S_{out}$	$\chi_{y'x'z'}E_xE_z\cos(2\phi)\hat{y}$
$P_{in}/P_{out}$	$-\chi_{x'y'z'}(2E_xE_z\hat{x} + E_x^2\hat{z})\sin(2\phi)$

Table 2.2: Angular dependence of second harmonic polarization  $E(2\omega)$  for GaAs(001) bulk  $\bar{4}3m$  and surface  $mm2$  symmetries. Here  $xyz$ ,  $x'y'z'$ , and  $x''y''z''$  represent laboratory frame, bulk  $\bar{4}3m$  symmetry frame, and surface  $mm2$  symmetry frame, respectively.

$\Gamma_{ijkl}$	$\Gamma_{xxxx} = \Gamma_{yyyy} = \Gamma_{zzzz},$ $\Gamma_{yzzy} = \Gamma_{zyyz} = \Gamma_{zxxx} = \Gamma_{xzzx} = \Gamma_{xyyx} = \Gamma_{yxxy},$ $\Gamma_{yzyz} = \Gamma_{zxxz} = \Gamma_{xzzz} = \Gamma_{yxxy} = \Gamma_{xyxy},$ $\Gamma_{yyzz} = \Gamma_{zzyy} = \Gamma_{zzxx} = \Gamma_{xxzz} = \Gamma_{xxyy} = \Gamma_{yyxx}$
$\chi_{ijkl}$	$\chi_{yyzz} = \chi_{zzyy} = \chi_{zxxx} = \chi_{xzzz} = \chi_{xxyy} = \chi_{yyxx},$ $\chi_{xxxx} = \chi_{yyyy} = \chi_{zzzz},$ $\chi_{yzyz} = \chi_{zxxz} = \chi_{xzzz} = \chi_{yxxy} = \chi_{xyxy},$ $\chi_{yzzy} = \chi_{zyyz} = \chi_{zxxx} = \chi_{xzzz} = \chi_{xyyx} = \chi_{yxxy}$

Table 2.3: Nonzero forth-rank tensor elements for  $\bar{4}3m$  symmetry media

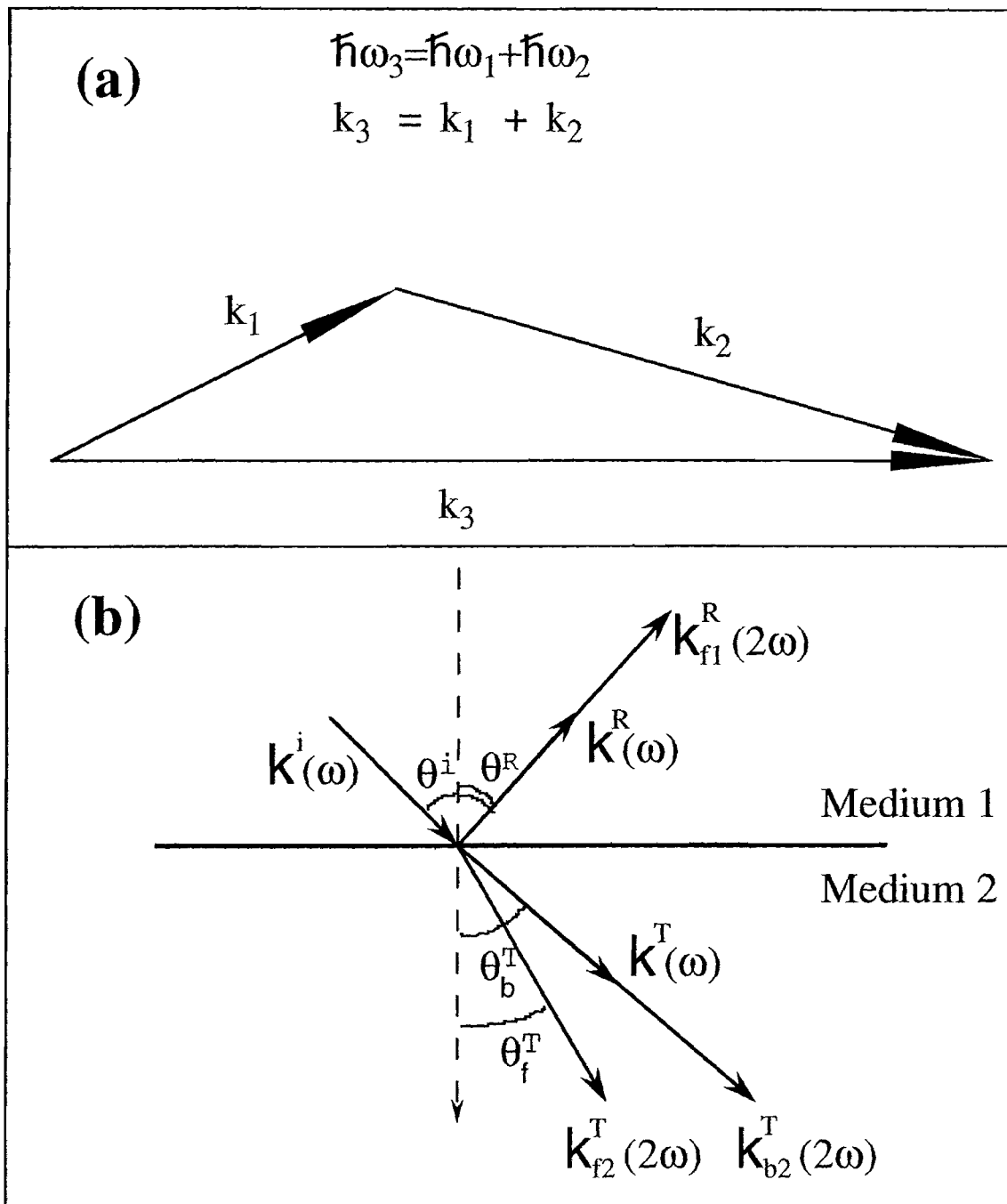
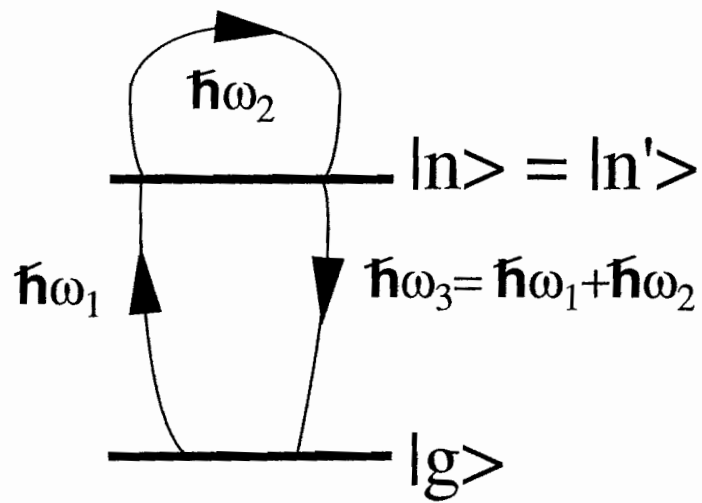
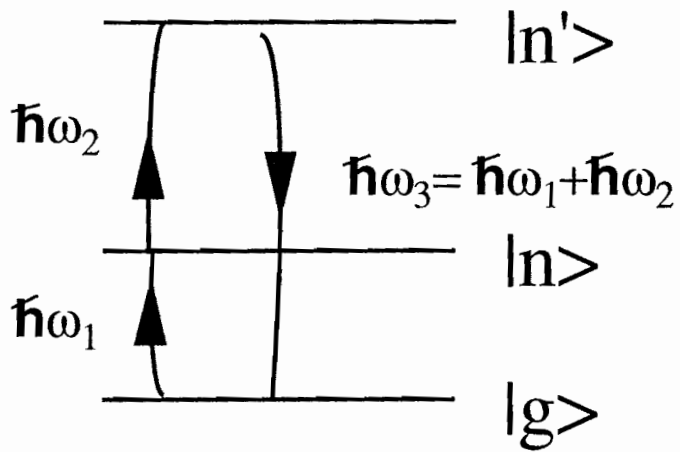


Figure 2.1: (a) Phase matching diagram for sum frequency generation.  $\hbar\omega_3 = \hbar\omega_1 + \hbar\omega_2$ ; energy conservation;  $k_3 = k_1 + k_2$ : moment conservation. (b) The tangential momentum conservation of each individual frequencies,  $\omega$  and  $2\omega$ , at an interface. For the fundamental frequency ( $\omega_1$ ):  $k_{\parallel}^i(\omega) = k_{\parallel}^R(\omega) = k_{\parallel}^T(\omega)$ . For the harmonic wave ( $2\omega$ ):  $2k_{\parallel}^T(\omega) = k_{b2,\parallel}^T(2\omega) = k_{f2,\parallel}^T(2\omega) = k_{f1,\parallel}^R(2\omega)$ .



(a) Three-wave Mixing in Two -level system



(b) Three-wave Mixing Process in Three-level System

Figure 2.2: Schematic diagram of three-wave mixing processes. (a) Three-wave mixing in a two level system. An intraband transition ( $|n >$  to  $|n >$ ) is involved. (b) Three-wave mixing in a three level system.

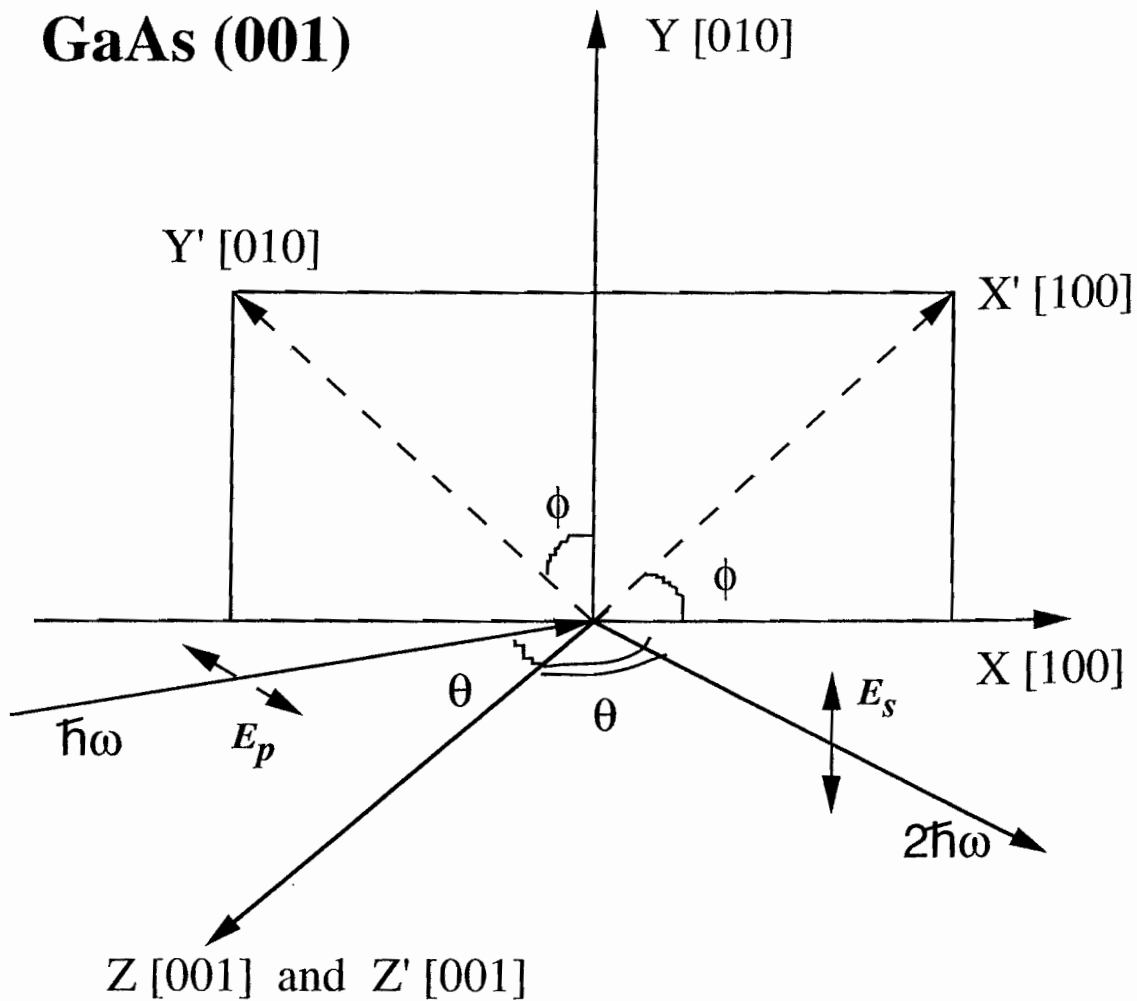


Figure 2.3: Second harmonic generation in GaAs(001) crystal.  $XYZ(X'Y'Z')$  represents the laboratory (crystal) frame.  $\phi$  is the angle between the crystalline [100] axis with the plane of the incidence. The fundamental SH generating light  $\hbar\omega$  is p-polarized, at a incident angle  $\theta$  with the Z axis. SHG light is s-polarized.

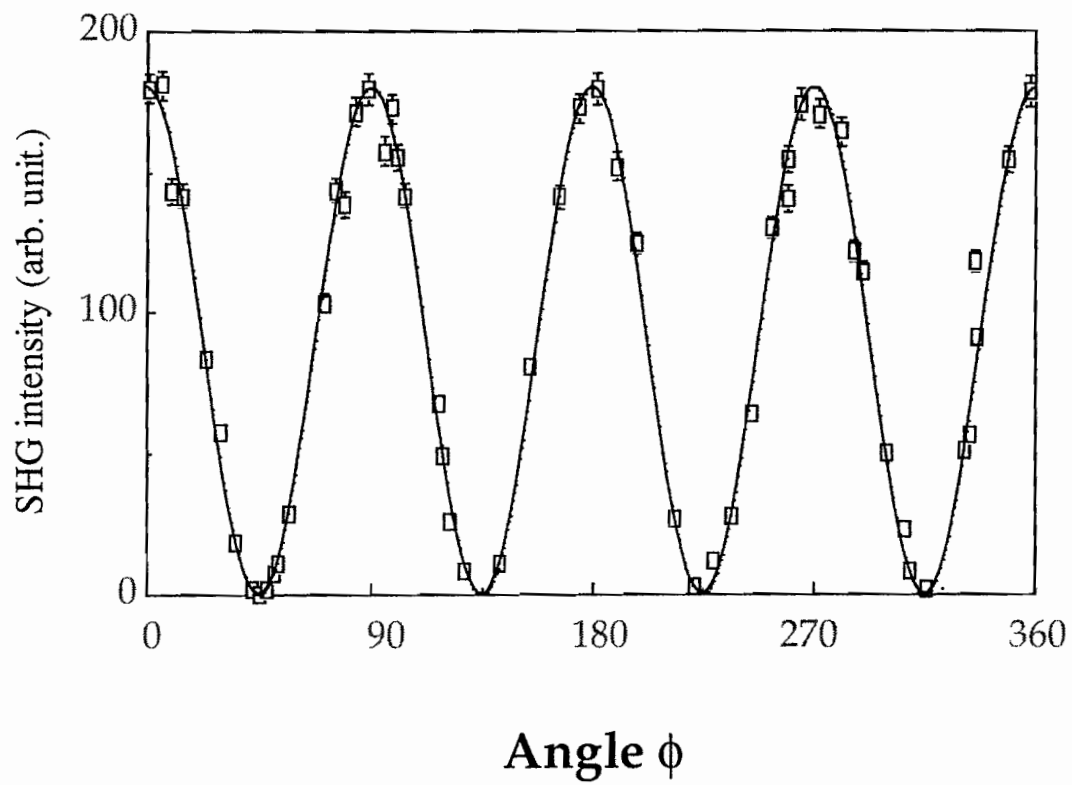


Figure 2.4: In p-in/s-out configuration, a typical bulk GaAs(001) SHG ( $\chi_{xyz}$ ) output are plotted as a function angle  $\phi$ . The fundamental photon energy is at  $\hbar\omega = 1.41$  eV. The solid line is fitting by using formula  $I_{SHG} = I_0 \cos^2(2\phi)$ .

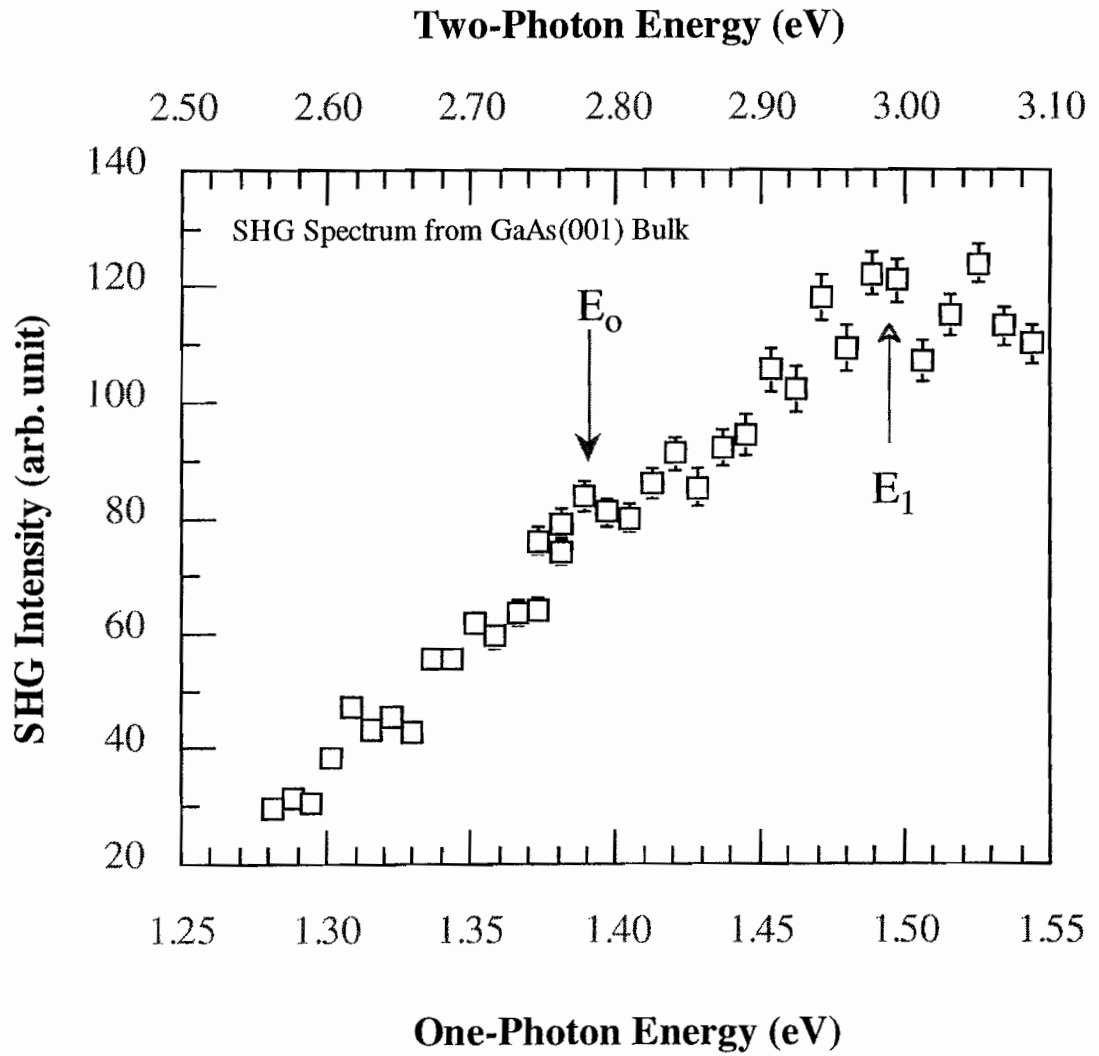


Figure 2.5: In p-in/s-out with  $\phi = 0$  configuration, SHG signals from GaAs(001) bulk ( $\chi_{xyz}$ ) are plotted as a function of fundamental (one-photon) and SHG photon (two-photon) energies.

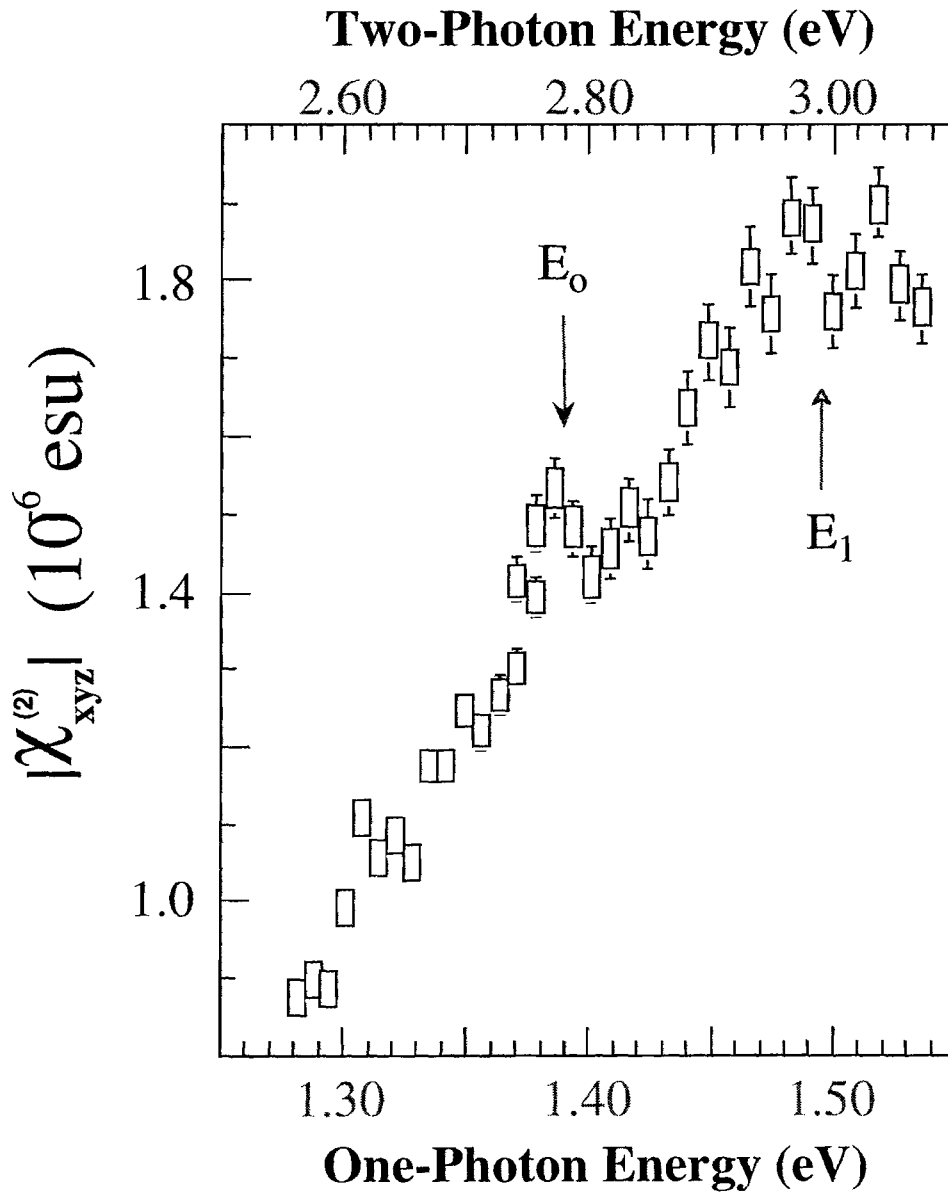


Figure 2.6:  $|\chi_{xyz}^{(2)}|$  as a function of one and two-photon energy for GaAs.  $E_0$  and  $E_1$  represent two resonance features which are related to GaAs  $E_0$  transition and  $E_1$  transition.

# GaAs(001) Surface

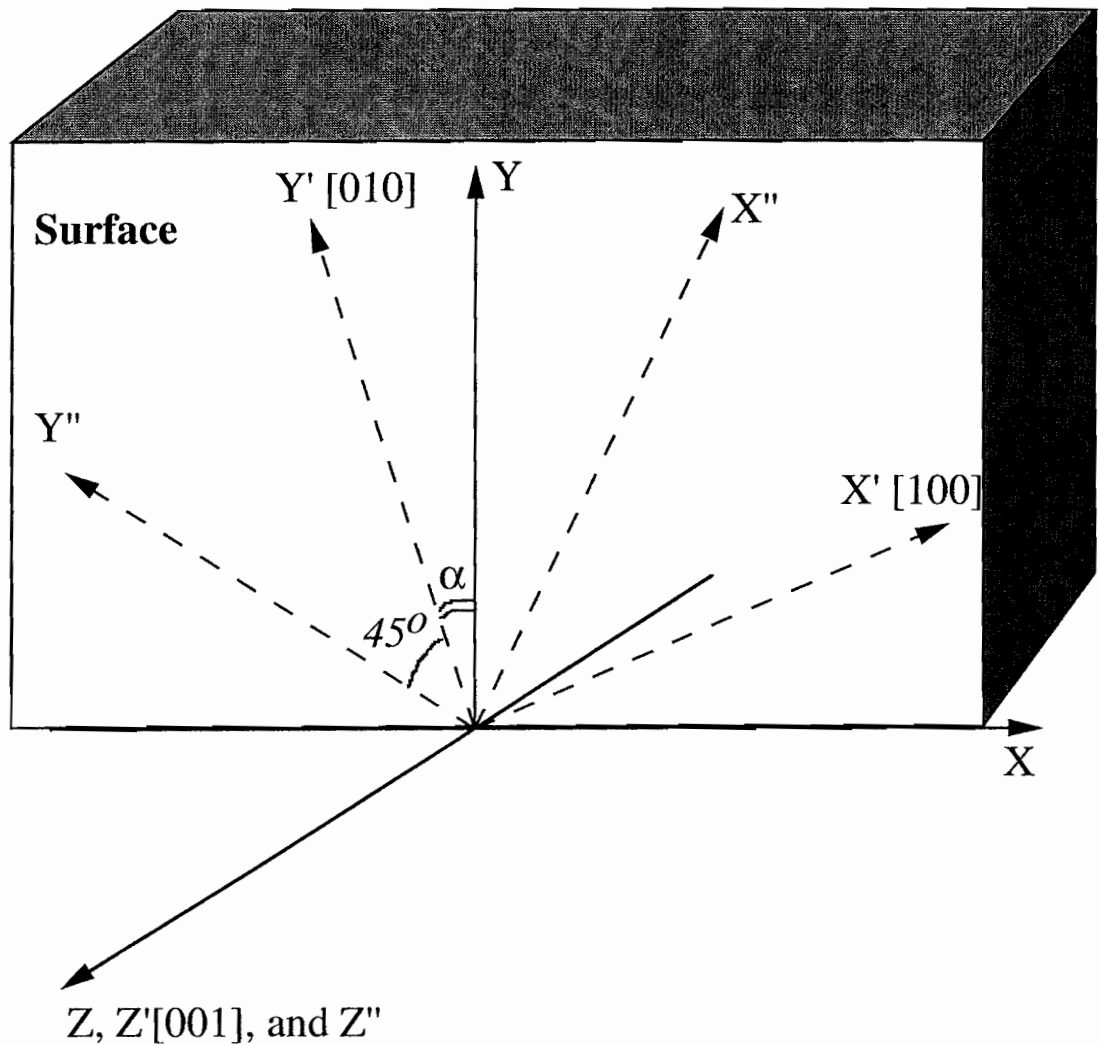
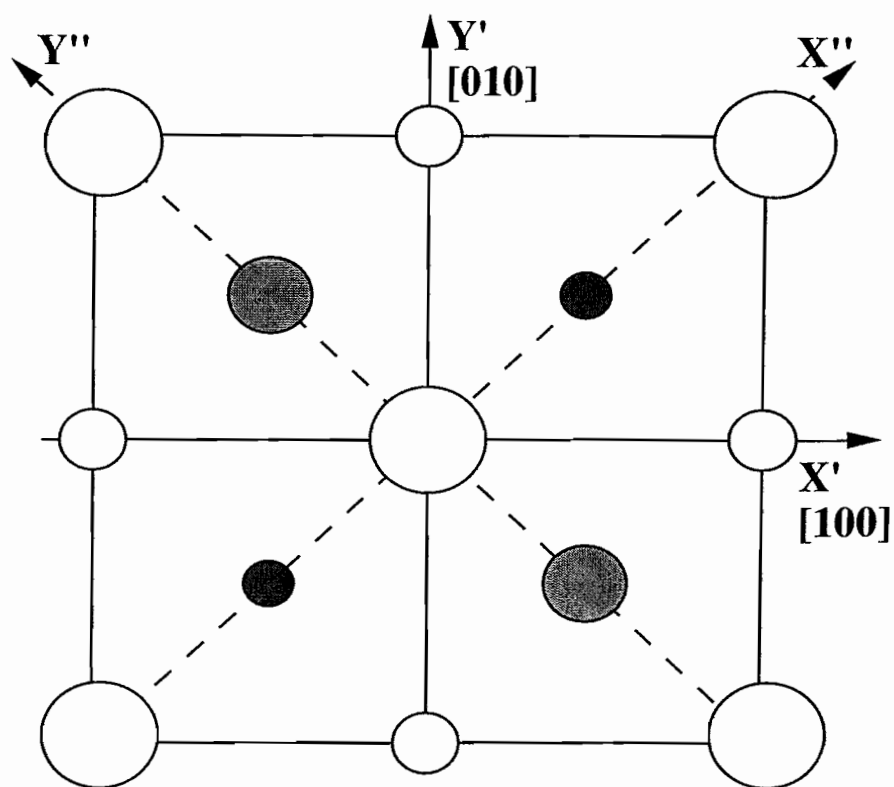


Figure 2.7: Three different frames at GaAs(001) surface.  $XYZ$ ,  $X'Y'Z'$  and  $X''Y''Z''$  represent laboratory frame, GaAs crystal bulk frame ( $\bar{4}3m$  symmetry), and GaAs surface frame ( $mm2$  symmetry), respectively (see figure 2.7).



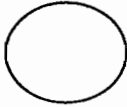
-  **First Layer As Atoms**
-  **Second Layer Ga Atoms**
-  **Third Layer As Atoms**
-  **Forth Layer Ga Atoms**

Figure 2.8: Microscopic view of surface  $mm2$  symmetry axis with respect to the bulk  $\bar{4}3m$  symmetry axis at GaAs(001) surface.

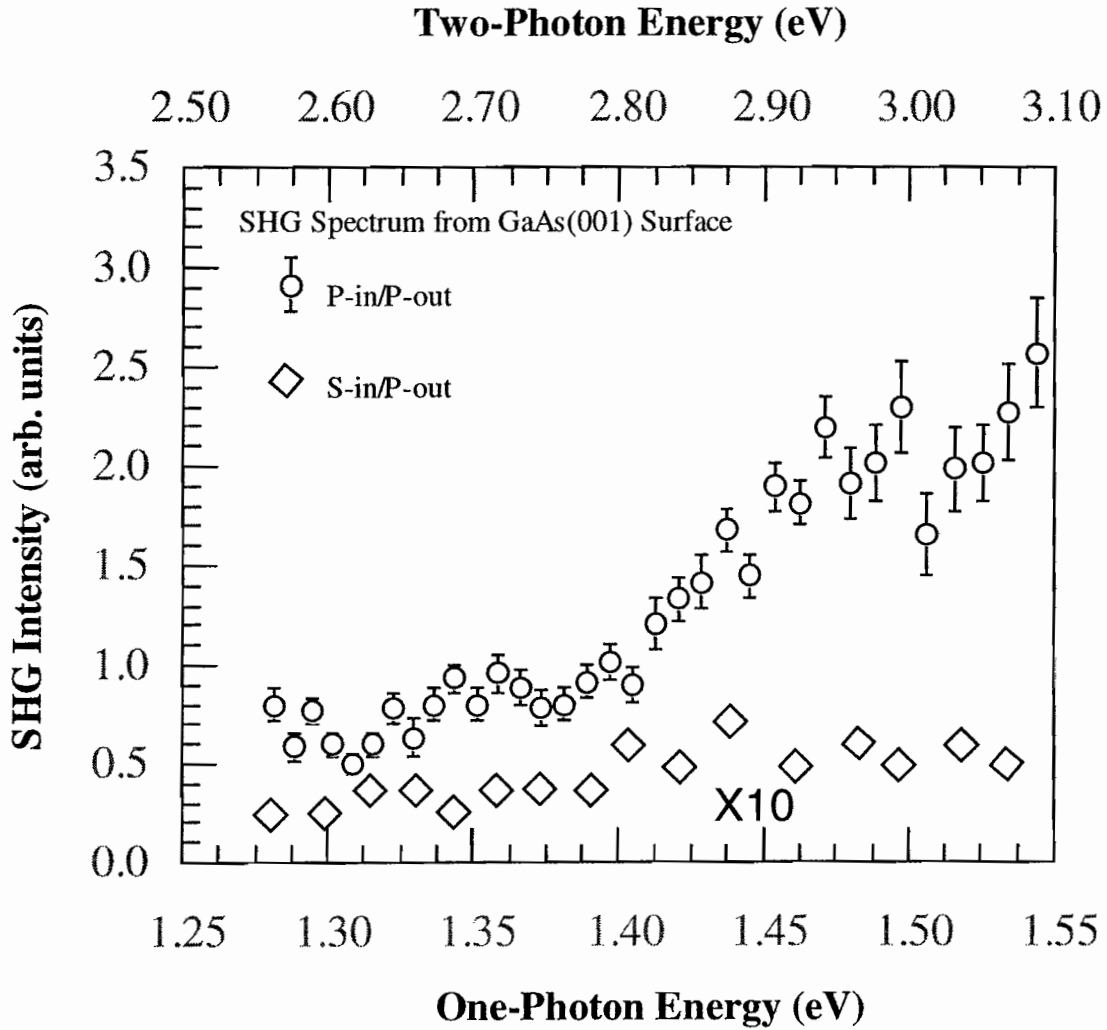


Figure 2.9: SHG signals from GaAs(001) surface are plotted as a function of fundamental (one-photon) and SHG photon (two-photon) energies. The crystalline axis [100] is in the plane of incidence, i.e.  $\phi = 0$ . In p-in/p-out, SHG signal arose from the contributions of  $\chi_{zzz}^{(2)}$ ,  $\chi_{xxx}^{(2)}$  and  $\chi_{yzy}^{(2)}$ . In s-in/p-out, SHG signals arose from the contributions of  $\chi_{xxx}^{(2)}$  and  $\chi_{yzy}^{(2)}$ , and were much smaller than the p-in/p-out surface signals. More details are in text.

# Chapter 3

## Laser systems and experimental implementation

In this chapter, we give a brief overview of our laser systems, which provide us with tunable probing light sources from visible to mid-infrared spectral regions. General optical implementations and electronic data acquisition systems are also presented.

### 3.1 Pumping laser

All of our tunable laser systems (dye-laser or optical parametric oscillator OPO) are pumped by a *Spectra Physics* GCR-3 Nd:YAG Q-switched laser. The laser produces p-polarized (horizontally polarized) pulses, with a time duration of 10 *nanoseconds* and a repetition rate of 10 *Hz*, at a fixed wavelength of 1064 *nm*. The average pulse energy of the 1064 *nm* light pulse reaches  $\sim 1$  *J/pulse*. A frequency doubler (SHG) stage containing a temperature controlled, phase-matched KDP ( $KH_2PO_4$ ) doubling crystal is pumped by the 1064 *nm* laser pulses to generate s-polarized (vertical polarization) pulses at 532 *nm* wavelength. The phase matching in the KDP crystal can be either type-I or type-II [25]. Therefore two kinds of KDP crystals can be used in the frequency doubler stage. A type-II (type-I) KDP crystal has a

high (low) power conversion efficiency at  $\sim 45\%$  ( $\sim 30\%$ ). As a result of different phase velocities of the ordinary and extraordinary lights in the KDP crystal, the pumping light will not be linearly polarized after a type-II KDP crystal. On the other hand, a type-I KDP crystal preserves the linear polarization of the pumping light ( $1064nm$ ). Therefore the type-I KDP frequency doubler is the best choice for the optical parametric oscillator OPO system which strictly requires *linearly* polarized pumping beams.

## 3.2 Dye-laser

The dye-laser is based on the principle that many organic compounds absorb strongly in a certain region of the visible spectrum, and fluoresce efficiently over a large wavelength range to the red of this absorption. If the intensity of the pumping light is very high, a population inversion between two molecular states can be attained. Light amplification by the stimulated emission of radiation is possible over almost the entire fluorescence band. By incorporating various pumping schemes, the dye-laser can provide tunable coherent light from near ultraviolet to the near infrared.

In order to achieve a tunable narrow bandwidth output, one mirror of the normal laser cavity is replaced by a diffraction grating. The grating normal makes an angle  $\theta$  with the axis of the cavity, and the light reflected back along the the cavity axis must satisfy

$$2d\sin\theta = m\lambda \quad m = 1, 2, 3, \dots$$

Here  $\lambda$  is the oscillating wavelength of the laser and  $d$  is the grating space. As a result, oscillation is prevented for the other wavelengths, which are not reflected back along the cavity axis. Thus narrow bandwidth output is obtained and wavelength tuning can be accomplished by varying grating angle  $\theta$ .

Our dye laser is a Spectra-Physics PDL-2, pumped by the  $532 nm$  light from the Nd:YAG laser. A schematic drawing of the dye-laser layout is plotted in figure 3.1.

Wavelength tuning is achieved by rotating the grating inside the pressure box. Figure 3.2 shows a typical dye laser output spectrum (LDS-867 Exciton dye). Such a dye laser system contains an oscillator, pre-amplifier, and amplifier. In our experiments, the amplifier was longitudinally pumped, and the oscillator was transversely pumped. Generally this dye-laser system provides a photon energy range from  $1.38 \text{ eV}$  ( $900 \text{ nm}$ ) to  $2.22 \text{ eV}$  ( $560 \text{ nm}$ ). After further modification of the grating system to 1200 grooves/mm with efficiency  $\sim 75\%$  in near-infrared, we can extend the dye-laser range to  $970 \text{ nm}$  by using LDS925 Exciton dye[55]. All of the dye-laser output light was s-polarized (vertically polarized).

### 3.3 $Ar^+$ ion laser

In the  $Ar^+$  ion laser, the population inversion is achieved by a two step process. First, a large number of ground state ions are created in the high current discharge; Second, collisions with fast electrons excite these ions to very high metastable levels ( $\sim 20\text{eV}$  above the  $Ar^+$  ground state).

Our  $Ar^+$  ion laser is a *Coherent* model 52. The laser provides 6 cw visible lines

<i>Wavelengths</i>	<i>Power(W)</i>	(3.1)
$\lambda_1 = 514.5\text{nm}$	1.2	
$\lambda_2 = 496.5\text{nm}$	0.7	
$\lambda_3 = 488.8\text{nm},$		
$\lambda_4 = 488.0\text{nm}$	1.1	
$\lambda_5 = 476.5\text{nm}$		
$\lambda_6 = 457.9\text{nm}$	0.55	

All powers were measured at current of 30 A without intracavity etalon. This  $Ar^+$  ion laser is roughly 25 years old, The laser tube was rebuilt by Holo-Spectra Corp.,

high-current operations ( $> 30A$ ) are not recommended.

### 3.4 Optical parametric oscillator

The optical parametric oscillator is a device which produces intense optical radiation with a high degree of spatial and temporal coherence. It generally involves at least one three-wave mixing nonlinear optical process. Typically, a strong high-frequency electromagnetic wave, called the *pump light* with a frequency  $\omega_p$ , interacts via the nonlinear properties of the medium (difference frequency generation) with two lower frequency waves (starting from quantum noises), termed the signal ( $\omega_s$ ) and idler ( $\omega_i$ ) waves, to produce amplification at these two frequencies

$$\omega_p = \omega_s + \omega_i.$$

The only difference between the parametric amplification process and difference frequency generation is that the parametric process is initiated by a single pumping beam, while difference frequency generation is initiated by two pump beams of more or less comparable intensity. In a laser, the gain is provided by a population inversion between two states; in parametric oscillator the gain is produced by the interaction between electromagnetic fields in a nonlinear medium. The parametric interaction arises from the second-order nonlinear optical process based on  $\chi_{ijk}^{(2)}$ .

Our optical parametric generation system was a Mirage 3000 made by STI Optonics. Type-II phase matching KTP ( $KTiOPO_4$ ) crystals are used as the nonlinear media. The system was pumped by both the 532 nm and 1064 nm outputs of a Nd:YAG, GCR-3 laser. The Mirage 3000 is packaged as a single integrated unit that is fully automated and controlled by a 386/33MHz computer supplied as an integral part of the system. All the phase matching angles of the type-II KTP crystals were controlled by a finely tuned stepper motor ( $\sim 10^{-3}$  rad/step). The software that controls the rotation stages is based on Windows 3.0.

A schematic drawing of the Mirage 3000 OPO system is shown in figure 3.3. It includes two successive stages, each stage containing two KDP crystals ( $7 \times 7 \times 15 \text{ mm}^3$ ) with same surface-cut angle. The crystal surface was coated with an anti-reflection film for pump light and generated light.

One of the mechanisms which limits parametric generation in anisotropic crystal is the extraordinary wave “walk-off” effect. This effect arises from the different propagation directions of phase (k wave vector) and energy flow (Poynting vector). In the type-II phase matching conditions, the energy flow of the extraordinary beam and the ordinary beam do not overlap everywhere for beams of finite cross sections. As a result, the nonlinear conversion efficiency is lowered. Since the crystals are angle tuned in our OPO/OPA system, the “walk-off” of the output beams from the OPO stage will further result in low conversion efficiency when these beams pass through crystals in the subsequent OPA stage. In addition, the walk-off angles are different for different wavelengths, variation of output beam directions will induce systematic errors in optical spectrum obtained in our experiments.

The “walk-off” effect is eliminated in our OPO/OPA system. This is advised as follows: In each stage, the two identical crystals are placed on separated rotation mounts, and each of them is set to the phase matching angle  $\theta$  corresponding to the desired output wavelength (see figure 3.4). The two crystals are arranged with their respective optic axes at an angle of  $2\theta$  relative to one another (see figure 3.4). In this configuration, the extraordinary beam walks off the ordinary beams in the first crystal and then walks back on them in the second crystal. Tuning of the wavelength is performed by rotating the two crystals about their tuning axes  $TA1$  and  $TA2$  in opposite directions. Thus the walk-off effects can be eliminated over the whole tuning wavelength region. A typical OPO output power spectra is plotted in figure 3.5.

The first stage (parametric oscillator stage) is pumped by s-polarized  $532 \text{ nm}$  light, with a pulse energy of  $60 \sim 90 \text{ mJ/pulse}$  and a beam diameter  $\phi \sim 5 \text{ mm}$ . It produces a p-polarized signal (s-polarized idler) from  $710 \text{ nm}$  to  $840 \text{ nm}$  (from  $1450$

$nm$  to  $2100\text{ nm}$ ). The signal output is used to calibrate the entire range of OPO wavelength settings.

The second stage (optical parametric amplifier stage) is pumped by the p-polarized  $1064\text{ nm}$  light which amplifies the s-polarized idler output ( $1450 - 2100\text{ nm}$ ) from the first stage and generated a p-polarized idler output (from  $2100\text{ nm}$  to  $4000\text{ nm}$ ) at the second stage. The  $1064\text{ nm}$  light source has a pulse energy at  $250 \sim 300\text{ mJ/pulse}$  and a beam diameter  $\phi \sim 7\text{ mm}$ . Normally the operating power is around one and one half times of the gain threshold power for both OPO and OPA stages. Finally an s-polarized signal (p-polarized idler) beam is amplified (generated) with a tunable wavelength from  $1450\text{ nm}$  to  $2100\text{ nm}$  (from  $2100\text{ nm}$  to  $4000\text{ nm}$ ).

The general alignment procedures are follows:

- (1) After the telescopes ( $T_1$  And  $T_2$ ), both pump beams are extracted out of the OPO box and sent far away ( $\sim 5\text{ feet}$ ). Then the spatial pump beam profiles are checked to get rid of any hot spots, while the YAG laser is operating at full power.
- (2) During the alignment of OPO/OPA, the  $523\text{ nm}$  ( $1064\text{ nm}$ ) pump beam power must be set at low pulse energy , i.e.  $\sim 10\text{ mJ/pulse}$  ( $\sim 25\text{ mJ/pulse}$ ).
- (3) All the centers of the pump beams are  $50\text{ mm}$  above the optical bases and centered through all mirrors and irises. All mirrors may need to be tuned several times.
- (4) Crystals surfaces are normal to the incident pumping beams during the alignments. In the OPO stage, this is achieved by reflecting  $532\text{ nm}$  pump light back to overlap with the incident  $532\text{ nm}$  beam outside the OPO box, and then finely tunig the crystal rotation stages to let the reflected spots on the mirror C in a vertical line (see inlet of figure 3.3). In the OPA stage, this is achieved by reflecting  $1064\text{ nm}$  pump light back to overlap with the incident  $1064\text{ nm}$  beam outside the OPO box, and then finely tunig the crystal rotation stages to let the reflected spots on the mirror E in a horizontal line (see inlet of figure 3.3).
- (5) Generally increasing pump intensity to find lasering thresholds for each stages. In OPO stage, the thresholds for  $532\text{ nm}$  pump light is around  $25 \sim 30\text{ mJ/pulse}$ ;

In OPA stage, the threshold for 1064 nm pump light is around  $100 \sim 120 \text{ mJ/pulse}$ . (6) In OPO stage, one needs to tune mirror H, J, I to maximize the output signal light, then recheck the threshold. It is very important to find the correct threshold to determine the normal operation pumping power. In OPA stage, one needs to tune mirror H, J, I, G to maximize the output signal and idler light, then recheck the threshold. All these procedures may need to be repeated several times.

### 3.5 General optical layouts

Our second-order nonlinear optical experiments were performed within different spectral regions. A standard PDL-2 dye laser covers a range of 1.28 eV (970 nm) to 2.22 eV (560 nm), and the Mirage 3000 OPO covers a range of 0.88 eV (1450 nm) to 0.31 eV (4000 nm). Both the dye laser and the OPO were pumped by a single Nd:YAG laser, and can be used independently or simultaneously (see figure 3.6). In the case of SHG experiments, we used either dye laser or OPO as our fundamental light source. In SFG experiments, we mixed output beams from the dye-laser and the OPO simultaneously, or used the residue 1064 nm light beam from Nd:YAG laser after a certain delay line in order to overlap in time with either dye laser output or OPO output.

All nonlinear optical experiments were performed in air. The optical lenses and prisms have no optical absorption in the wavelength region  $300 - 2200 \text{ nm}$ . A beam splitter takes  $\sim 10\%$  of the laser beam to a y-cut wedged-quartz as a reference, and the other  $\sim 90\%$  to the sample line. The wedged quartz plate has an apex angle of  $0.8^\circ$ .

In order to achieve a good signal to noise ratio and eliminate any false spectral structures, we need to consider fluctuations in several areas, such as intensity, space, and time. Because the nonlinear properties of quartz have been well studied and its second-order nonlinear optical susceptibility has no optical features in the visible and

near-infrared[61], it is ideally suited as a reference material. Our optical configuration enables us to measure sample and reference signals simultaneously. Therefore we could minimize the effects of spatial and temporal fluctuations in the fundamental beams.

Long-pass spectral filters were placed in front of the sample and reference quartz to remove background light which might overlap the second-order nonlinear optical signals. Short-pass spectral filters were placed after the sample and reference quartz to block the incident fundamental laser light. All of the optical settings were the same in both lines to minimize systematic errors. The light was incident on the sample at a  $75^\circ$  angle, and thus  $> 50\%$  incident light transmitted into the sample. Normally the collimated beam was  $2 \sim 3\text{mm}$  in diameter and had a fluence of  $\sim 5\text{ mJ/cm}^2$ [55]. However, in carrier diffusion measurements described later in chapter 6, the beam size could be as small as  $50\mu\text{m}$  in diameter.

In the reference line, the light was incident normal to the surface of the wedged quartz crystal. Due to phase matching and interference, the output SHG or SFG from quartz oscillates as a function of frequency and incident angle. However by utilizing y-cut wedged quartz, we can achieve a flattened fringe envelope function by translation of the crystal slab normal to the incident beam direction[55]. The formula describing such fringes can be written as

$$I^{(2\omega)} = C_1^2 + C_2^2 + 2C_1C_2 \cos(d\Delta\phi) \quad (3.2)$$

with

$$C_1 = Q \frac{-2\sqrt{\epsilon_f}[1 + \sqrt{\epsilon_b}]}{[\sqrt{\epsilon_f} + 1]^2}, \quad (3.3)$$

$$C_2 = Q \frac{\sqrt{\epsilon_f} + \sqrt{\epsilon_b}}{\sqrt{\epsilon_f} + 1}, \quad (3.4)$$

$$\Delta\phi = (k_{f,z} - k_{b,z}), \quad (3.5)$$

$$Q = \frac{P}{\epsilon_b - \epsilon_f}. \quad (3.6)$$

$$(3.7)$$

Here the subscripts  $f$  and  $b$  refer to free and bound waves respectively, and  $k_f$  ( $k_b$ ) represents the magnitude of the free (bound) wavevector in the quartz.  $d$  is the thickness of the quartz plate, and  $P$  is the second-order nonlinear polarizability. The maximum peaks were equal in such a configuration, and the minimum of the SHG intensity can reach zero with an infinitely small beam size. More details about finite size beam effect are discussed in reference 55. In figure 3.7, a typical SH intensity with beam cross section at  $\sim 50 \mu m$  is plotted as a function of normal translation distance. The solid line is the fitting using formula 3.1.

The signals were measured with a Hamamatsu R943-02 photomultiplier through a *Jarrell-Ash Monospec-18* monochrometer. During the experiments, all the reference signals were peaked up by translating the quartz crystal to the maximum intensity position. Later the sample second-order nonlinear optical signals were normalized using the quartz signals. During a normal SHG experiment, a SHG signal is at  $\sim 100$  photons/pulse and signal/background of  $\sim 100$ . The background signal was measured by blocking the laser beam and the value of signal/background was obtained by averaging over 5000 laser pulses. Further utilization of cooled PMT detection systems will increase the signal/background ratio. The spectral limitation arises from the quantum efficiency of the PMT tube, which is cut off after 900 nm. Cooled photodiode detectors will be the potential candidates in the near-infrared spectroscopy.

The reason for choosing  $\hat{y}$  cut quartz instead of  $\hat{z}$  cut quartz in our reference line can be explained as follows. The y-cut quartz is a birefringent crystal with  $D_3$  symmetry and carries two nonzero second-order nonlinear optical susceptibility  $\chi_{xyz}$  and  $\chi_{xxx}$ [25]. The y axis normal to the quartz surface. Along the y-direction the crystal does not have any optical activity. In another words, with linearly polarized fundamental lights, the SHG (SFG) lights are linearly polarized in  $\hat{x}$  direction. Both fundamental and SHG lights maintain linear polarizations. In contrast to y-cut quartz, both fundamental and SHG lights will not maintain their linear polarizations in the z-cut quartz. The linearly polarized light will be separated into left and right

circular polarized lights since the phase velocities of this two circular polarizations are not equal. As a result, the total SHG or SFG output fringes will not have the simple relation to the thickness of the quartz as shown in equation 3.1.

### 3.6 Electronic data acquisition system

The PMT output was sent to a *Stanford Research Systems* SR250 gated integrator (boxcar integrator). The boxcar is designed to recover fast analog signals from noisy background. It consists of a gate generator, a fast gated integrator, and exponential averaging circuitry. During experiments, the gate generator was triggered at  $20\text{Hz}$  externally by the Nd:YAG laser pulse through a fast photodiode and a frequency doubler[55]. The boxcar operated in toggle-mode. In the toggle-mode, the total output is the difference between the sampling gate and the background gate. In particular, with signals at  $10\text{Hz}$  and trigger signals at  $20\text{Hz}$ , the gated integrator integrated the input signal during the first gate period( $\sim 10\text{ns}$ ) during which the SHG signal is present; After  $50\text{ms}$ , the gated integrator integrated the background noise during the second gate period( $\sim 10\text{ns}$ ) while no SHG signal is present.

The gate integrator provide a DC voltage which is proportional to the average input signal during the sampling gate. Such sampling outputs allow the experimenter to do shot-by-shot analysis of the signal. Normally each data point was an average of 2500–5000 laser shots. The DC output can be directly read with an oscilloscope or a voltmeter. Finally it was digitized by a *Stanford Research* SRS245 A/D converter and recorded by a 486/66MHz computer through a *National Instrument* GPIB computer interface board. The software language *ASYST 4.0* was used to control all computer interfaces, stepping motors, and data acquisitions electronics. Some of the program codes are written in appendix I. Since many laser systems and electronic devices are operating in our laboratory now, all the signal cables need to be shielded.

### 3.7 Some linear optical experiments

In this section, we present a brief description of some linear optical spectroscopies which we undertook. Linear optical spectroscopy is a very useful method to probe the dispersion of dielectric properties and energy band profiles of bulk material. We measured the linear optical reflectivity as a function of *incident photon energy* ( $\hbar\omega$ ), which is a sensitive probe of the dispersion properties of the linear dielectric constant  $\epsilon(\omega)$ [43]. Our light source was a *Halogen* lamp and the incident photon energy was selected by a monochromator (see figure 3.8). The light was chopped and then illuminated the samples at  $45^\circ$  degree. The reflected light was detected by a silicon photodiode connected to a lock-in amplifier, and then recorded in a computer. The sample and reference detector were mounted on a translation stage with the translation axis normal to the incident light. At each light wavelength, the light intensity was calibrated according to the reference signal. A typical reflection spectrum from a undoped GaAs bulk sample is shown in figure 4.6. Our measurements show an increase in reflectivity when the incident photon energy is greater than the band gap, in good agreement with the theoretical calculations.

Another useful linear optical spectroscopy technique is the measurement of the superficial layer properties of multi-layer systems, such as thickness and dielectric constant. The interpretation of our second-order nonlinear optical results requires knowledge of the thickness of Au or As superficial films. By measuring the linear optical reflectivity as a function of *incident angle*, we are able to determine the thickness of superficial metal films on a GaAs(001) substrate (see figure 4.6). The linear optical reflectivity field  $E_R$  in an s-polarization configuration ( $E_I$  represents the incident field) from a medium-0/medium-1/medium-2 system can be written as (see section 4.5)

$$\frac{E_R}{E_I} = \frac{r_{01} + r_{12}e^{i\delta}}{1 + r_{01}r_{12}e^{i\delta}}$$

Here multi-reflections have been considered.  $r_{ij}$  represents the reflectivity from a

medium-i to a medium-j interface.

$$r_{ij} = \frac{(-n_j \cos \theta_i + n_i \cos \theta_j)}{(n_j \cos \theta_i + n_i \cos \theta_j)}$$

$n_i$  and  $n_j$  are the complex dielectric constants of medium-i and medium-j.  $\theta_i$  is the incident angles from medium-i to medium-j, and  $n_j \sin \theta_j = n_i \sin \theta_i$  (Snell's law). The phase difference  $\delta = \frac{4\pi d}{\lambda} \cos \theta_1 n_1$ , in which the  $d$  is the thickness of the medium-1. In such an experiment, an s-polarized monochromatic light from a *He - Ne* laser at 632.8 nm was incident on the sample. The sample sat at the center of a rotation stage, and the reflected light was detected by a photodiode (see figure 3.9). Finally the reflected intensity as a function of incident angle  $\theta_0$  was fitted by the least-square method to obtain the thickness of the medium-1 film.

### 3.8 Sample cooling system

Schematic drawing of our sampling cooling system is plotted in figure 3.10. The sample holder is made of copper with a cooling fluid (Ethylene Glycol) circling through it. The cooling fluid temperature is controlled by a *Neslab RTE-110* refrigerator from  $-30^{\circ}C$  to  $100^{\circ}C$ .

Sample is sealed inside a chamber in the copper block with an optical window in front of it. Dry Ar gas is filled in this chamber, and the whole sample holder is thermally isolated by plastic foam. Finally whole system is purged by dry nitrogen gas.

- |       |                          |   |                                     |
|-------|--------------------------|---|-------------------------------------|
| A,B   | Beamsplitter             | N | 90° Prism                           |
| C     | 90° Prism                | O | 90° Prism for side-pumped amplifier |
| D,E   | Cylindrical Lens         | P | Mirror for side-pumped amplifier    |
| F     | Amplifier Dye Cell       | Q | Lens for side-pumped amplifier      |
| G     | Grating                  | R | Output 90° prism                    |
| H     | Oscillator Dye Cell      | S | Compensator for preamp. cell        |
| I     | Oscillator Output Mirror |   |                                     |
| J     | Preamplifier Dye Cell    |   |                                     |
| K,L,M | Lenses                   |   |                                     |

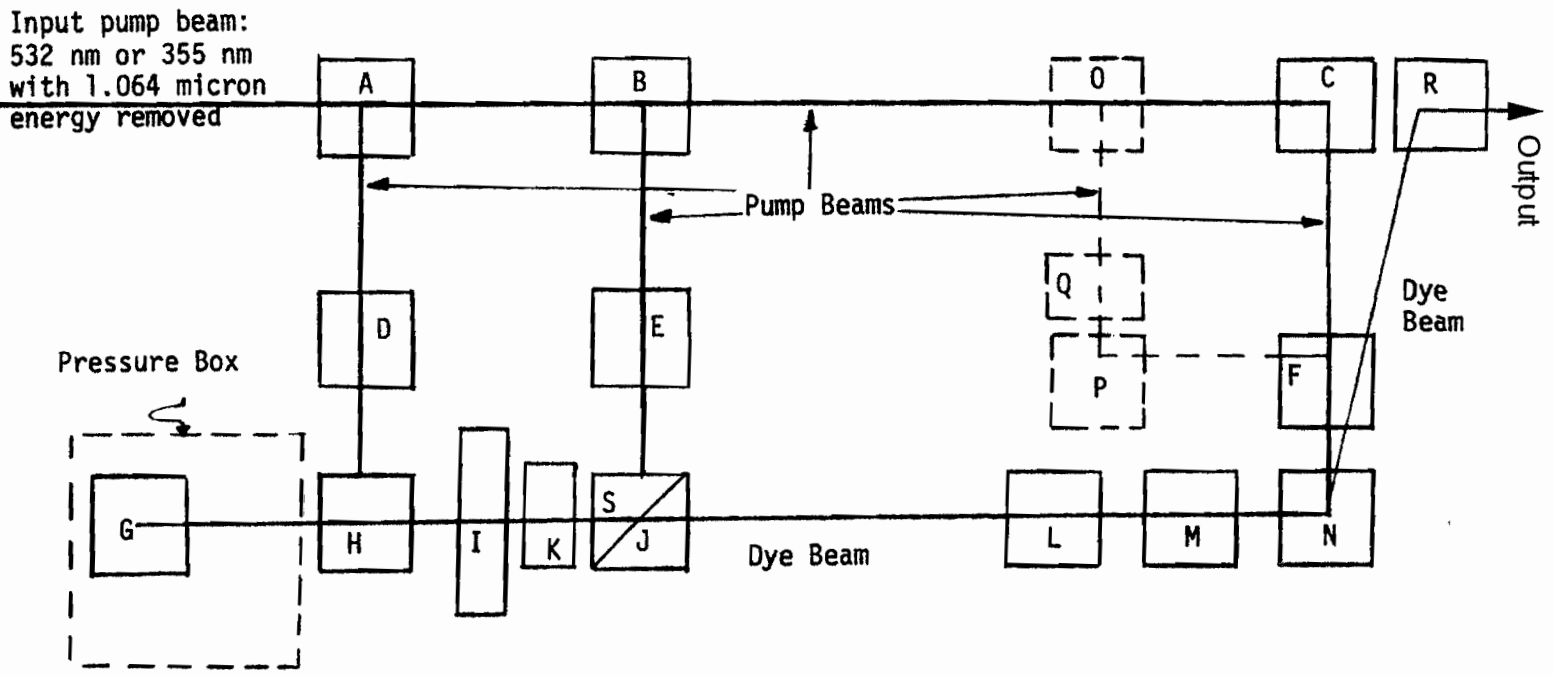


Figure 3.1: PDL-2 dye-laser layout.

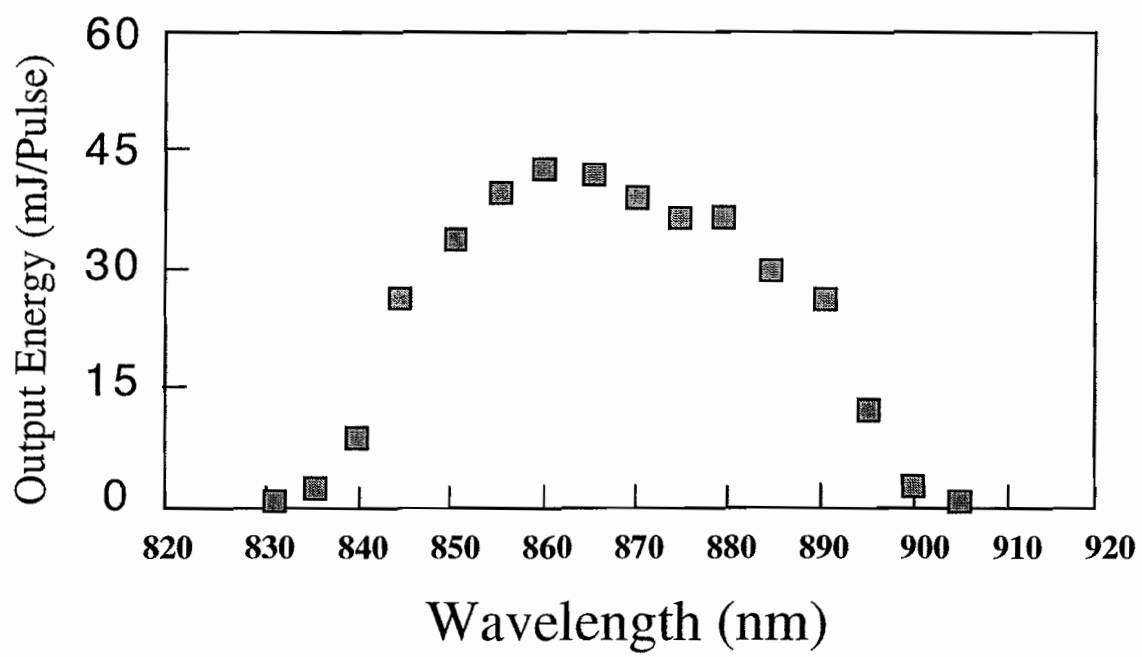


Figure 3.2: A typical dye-laser output power spectra for LDS867 dye.

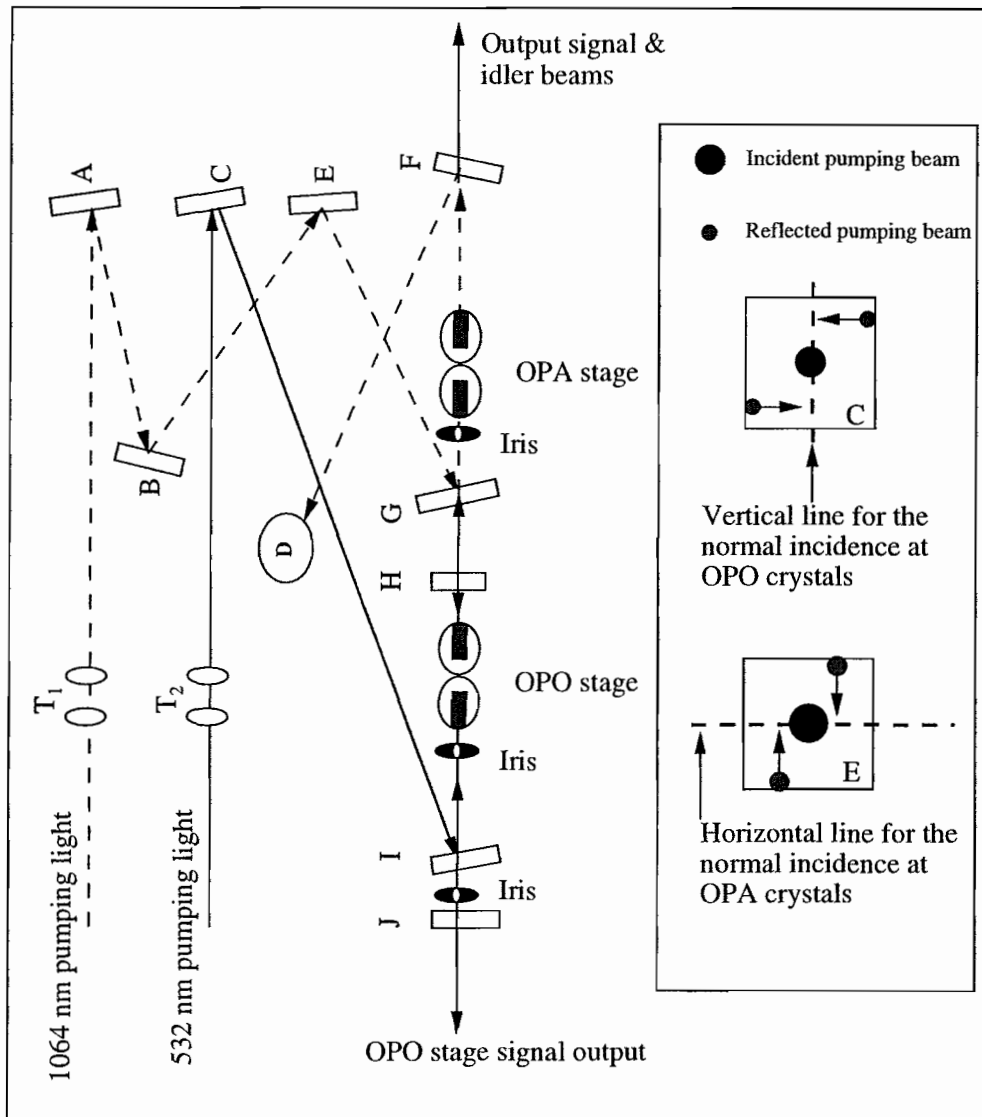


Figure 3.3: Schematic drawing of optical parametric oscillator OPO and optical parametric amplifier OPA. A, B, C, and E are high reflective mirrors for the pumping beams. D is beam-dumper for 1064 nm pumping light; H, I are transparent for IR light, but are highly reflecting at 532 nm. G is highly reflective at 1064 nm, but is transparent for IR light; J is transparent for signal beams at the OPO stage, but not for the idler beams;  $T_1$  and  $T_2$  are telescopes. Inlet shows reflected spots of pumping beam 532 nm (1064 nm) on mirror C (E), and two reflected spots correspond to two crystals in OPO (OPA) stage.

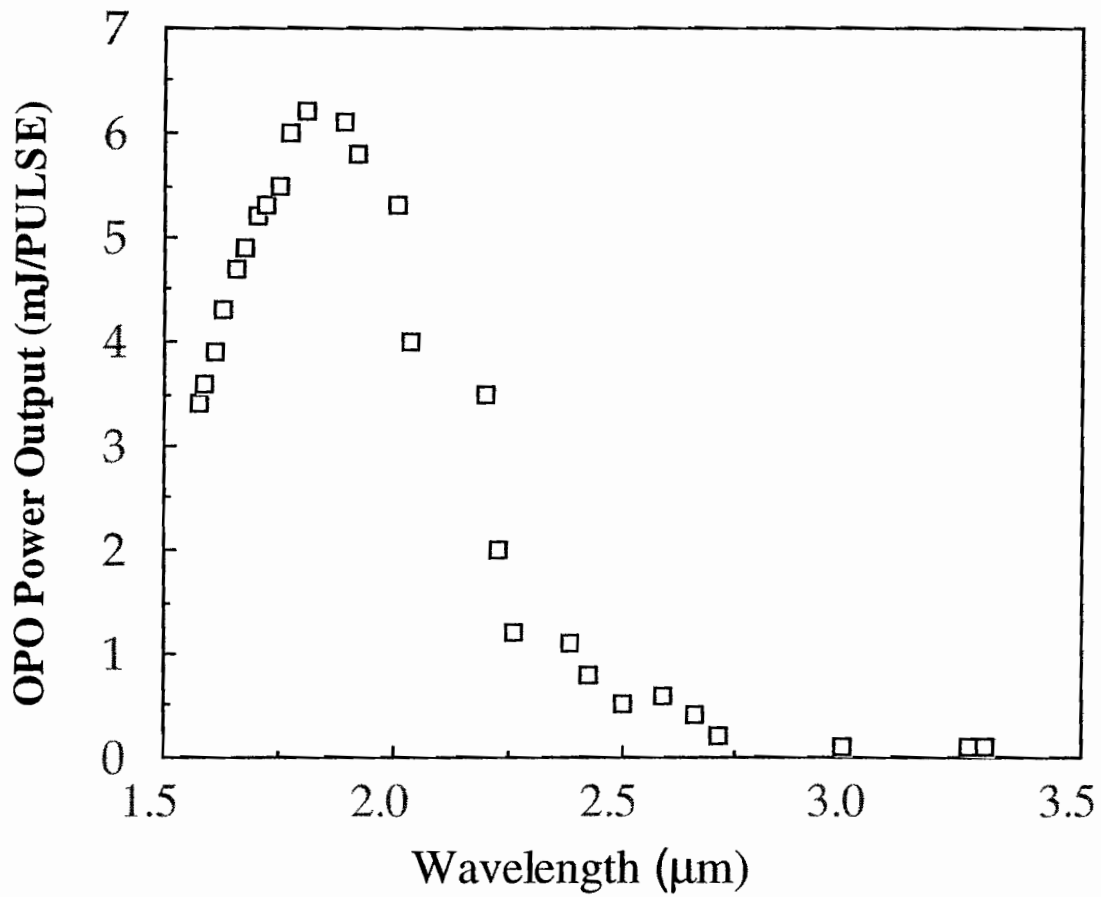


Figure 3.5: A typical Mirage3000 OPO output power spectrum while the pumping power of 532 nm (1064 nm) was at 70 mJ/pulse (280 mJ/pulse).

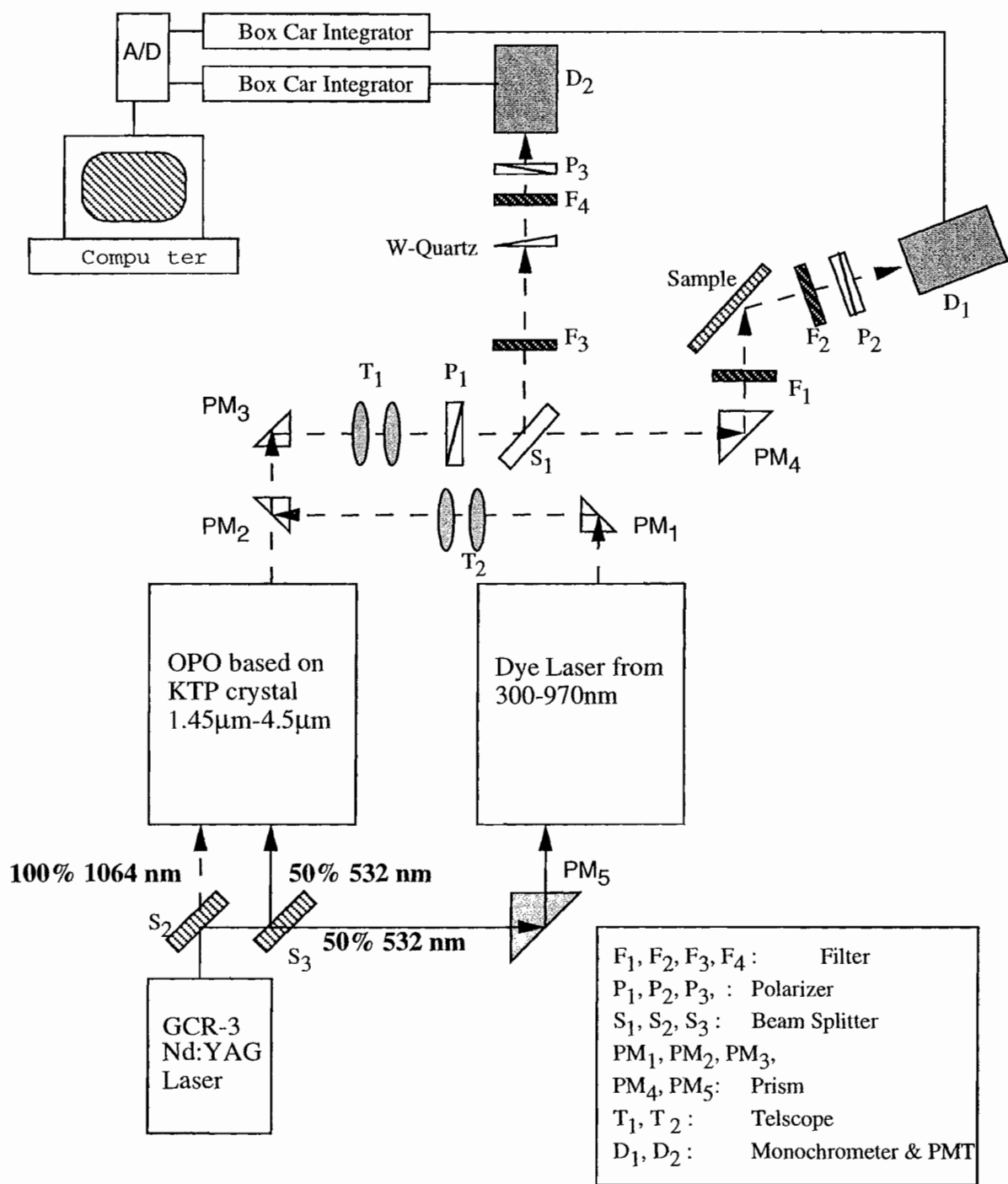


Figure 3.6: Schematic diagram of optical setups in SHG and SFG experiments.

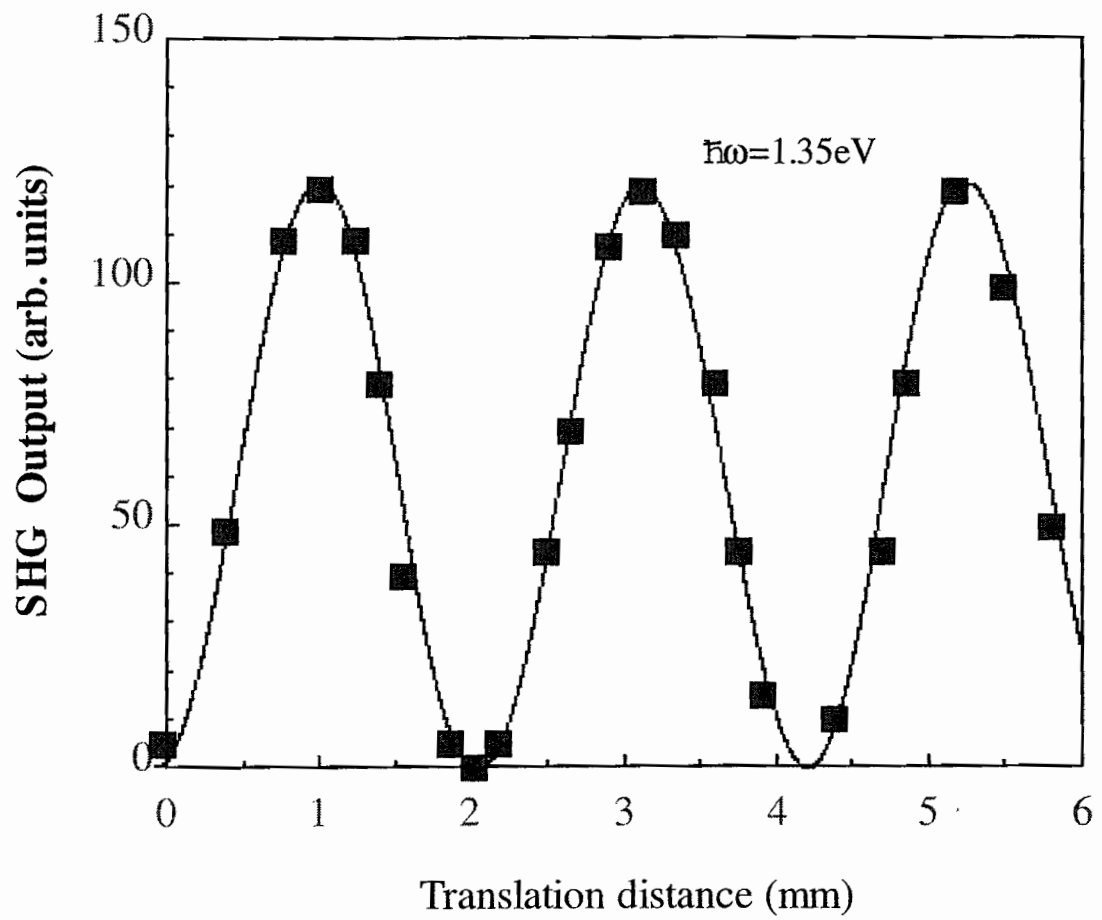


Figure 3.7: The transmitted SH intensity of a wedged quartz plate as a function of the translation distance.

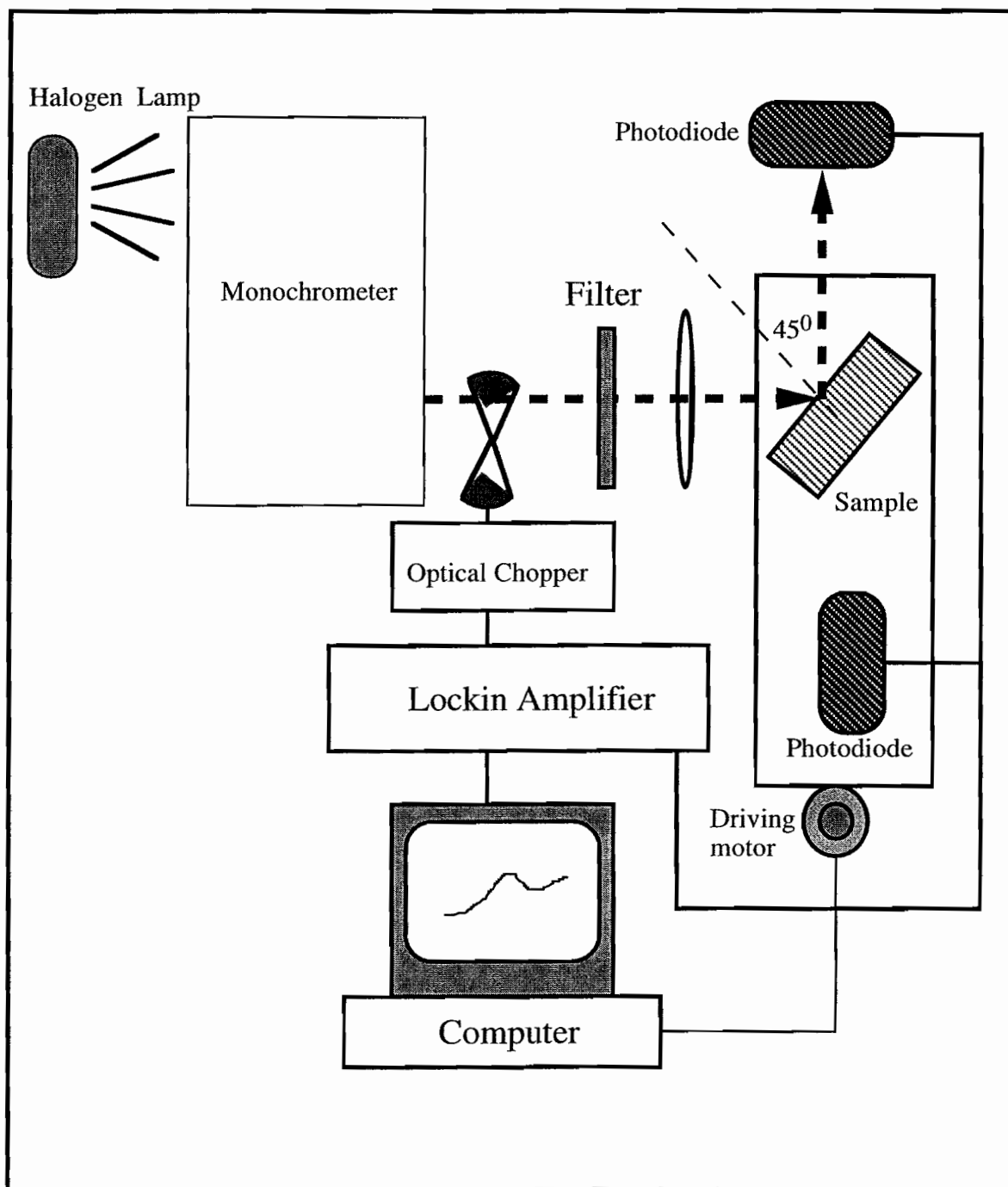


Figure 3.8: Linear reflectivity spectroscopy experimental setup.

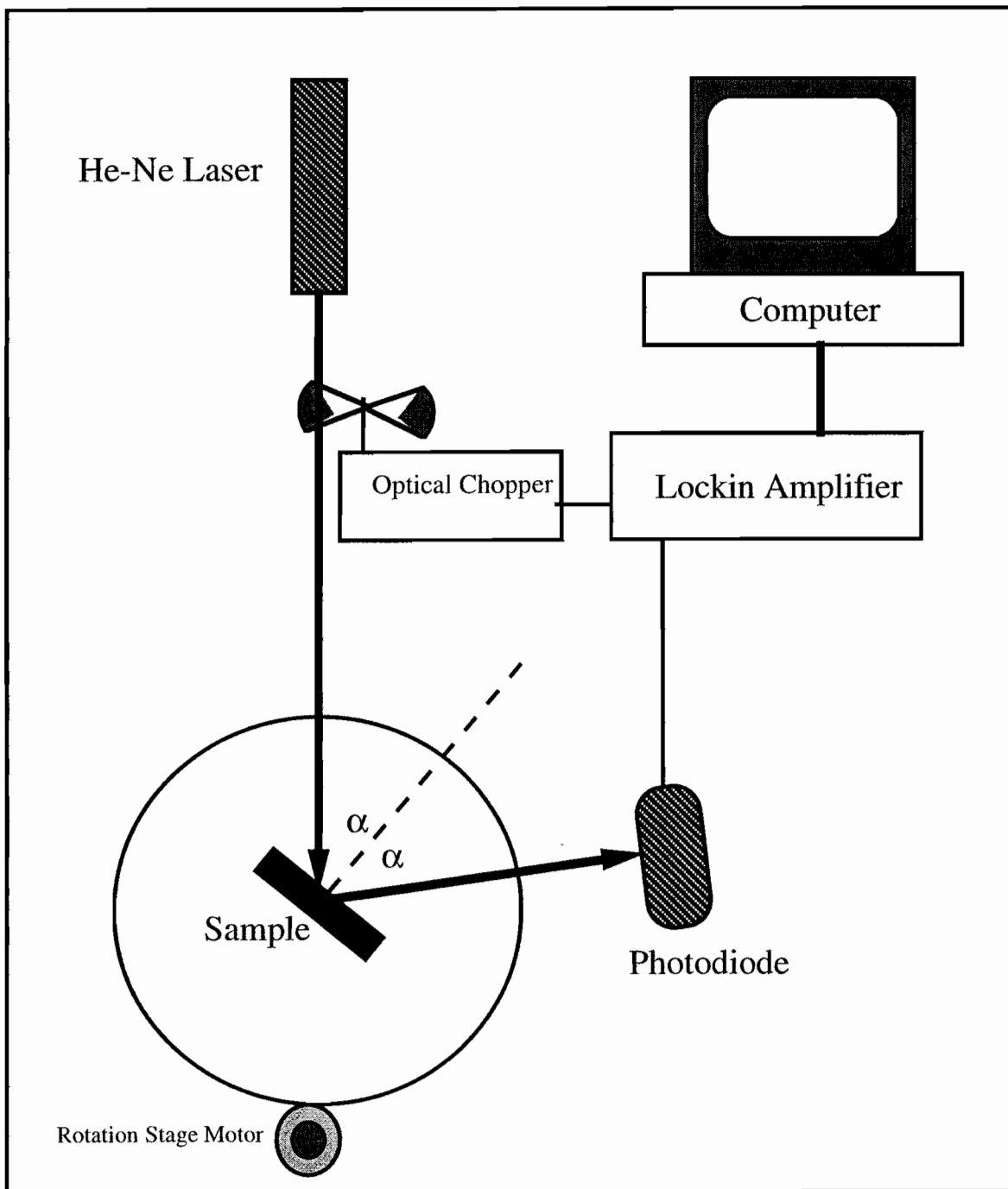


Figure 3.9: Experimental setup for the linear reflectivity as function incident angle experiments.

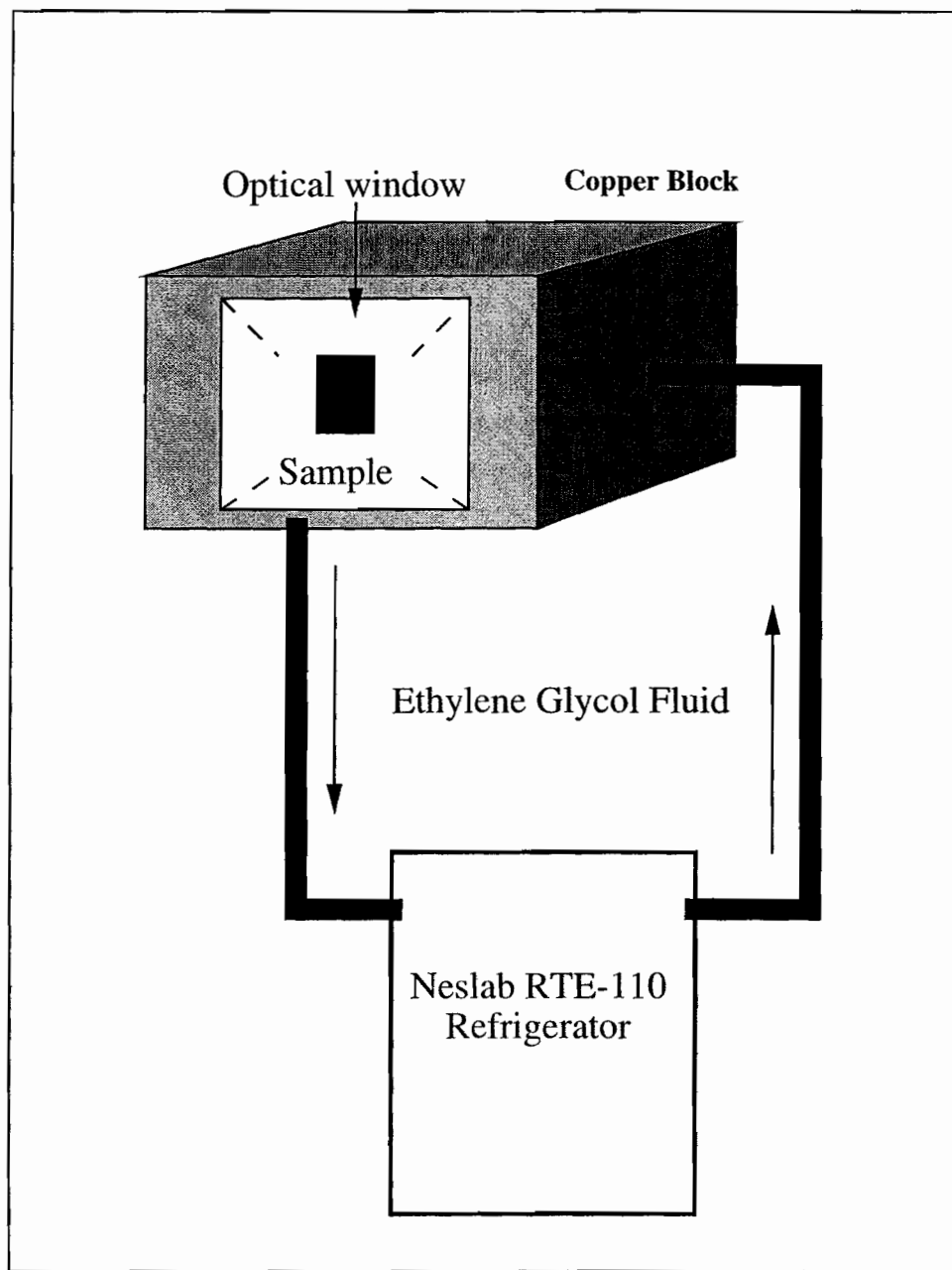


Figure 3.10: Schematic drawing of sample cooling system.

# Chapter 4

## GaAs and its interfaces

The concepts of this thesis are focused on the electronic properties of GaAs and its interfaces. Knowledge of sample and sample preparation is crucial for the interpretation of our experimental results. For example, the surface reconstruction of GaAs depends on the ratio of As:Ga during the growth. Different atomic ratios of As and Ga result in different atomic displacement-induced defects. One of our long range interests is to study the relation between sample preparation and the interface electronic structure. In this chapter, general properties of GaAs are briefly reviewed. Some concepts of GaAs bulk defects are introduced to further elucidate our investigation of the interface defects. Since the properties of GaAs depend largely on its growth conditions, our sample growth procedure is discussed in detail. Finally, general background information about GaAs related interfaces is presented.

### 4.1 Introduction to GaAs

#### 4.1.1 Structural and electronic properties

GaAs has a zincblende crystal structure. It possesses fcc translational symmetry with a basis of one GaAs molecule, one atom being at 000, and the other at  $\frac{1}{4}\frac{1}{4}\frac{1}{4}$  of the fcc unit cube (See Figure 4.1). “fcc” stands for face centred cubic. Some physical

properties of GaAs crystal are presented in table 4.1. In reciprocal space, the GaAs structure has bcc symmetry. Figure 4.2 exhibits the first Brillouin zone of GaAs.

The symmetry of bulk GaAs is  $\bar{4}3m$ . At a GaAs(001) surface, the bulk symmetry is broken, and surface symmetry is  $mm2$ . As discussed previously, the  $mm2$  symmetry axis  $\hat{x}''$  and  $\hat{y}''$  rotated by  $45^\circ$  about the  $\hat{z}$  axis ([001]) with respect to the bulk crystal axes  $\hat{x}'$  [100] and  $\hat{y}'$  [010]) (see figure 2.7).

GaAs is a direct band gap semiconductor with gap energy  $E_0 = 1.423$  eV[34]. The conduction band minimum and valence band maximum are situated at the  $\Gamma$  point in the Brillouin zone. Figure 4.3 shows the energy band profile of GaAs. Some electronic properties of GaAs are presented in Table 4.2[62].

The carrier transport properties of GaAs are determined by its scattering mechanisms which involve optical phonons, piezoelectric acoustic phonons and impurities[63]. Some typical values of carrier mobilities for GaAs are given in table 4.2[62] There have been many experiments carried out to study carrier transportation properties in the GaAs based quantum well structures ( $Al_{1-x}Ga_xAs/GaAs/Al_{1-x}Ga_xAs/\dots$ ). For example, the tunneling of carriers through the quantum-well barriers can be controlled by biasing electric field across the wells [36]; diffusion lengths of photoexcited free carriers in the two-dimensional well are longer than ones in the bulk due to separation of electrons and holes in different quantum-well layers [64]. In this thesis, we present measurements of minority carrier diffusion near the *surface* of GaAs;

### 4.1.2 GaAs bulk defects

Many impurity defect and native defect states exist in GaAs; as many as fifteen (twelve) electron (hole) traps have been identified[38]. The dominant midgap level electron trap, EL2, is believed to be a native point defect [66], and its energy level lies near the middle of the band gap. It is believed to play an important role in pinning the Fermi energy and is responsible for semi-insulating (SI) GaAs[67]. The high resistivity of SI GaAs is due to the Fermi level pinned at the EL2 midgap state.

One of the most intriguing properties of EL2 is the existence of a metastable state EL2\*. The EL2 states can be photoquenched into this metastable state EL2\* at low temperature, and recovered at high temperature ( $\sim 120^{\circ}K$ )[21, 66, 68]. For example, the EL2 optical absorption spectra can be bleached at low temperature ( $> 120^{\circ}K$ ) using a second pumping light ( $\hbar\omega > 1.0 eV$ ), which excites a neutral EL2 state to its metastable state EL\*; The “bleached” spectra recovers after sample heated above  $< 120^{\circ}K$  [21]. This type of behavior is the fingerprint of EL2 defects.

Most arguments attribute EL2 to a defect complex. For example, a common As antisite ( $As_{Ga}$ ) defect is ascribed to EL2 states. In this case, the As atom sits in the Ga site (see figure 4.4), and this defect can be neutral or charged. The metastable state EL2\* is attributed to the complex of  $As_{Ga}$  with a Ga vacancy  $V_{Ga}$ [68].

The optical transitions from the EL2 ground level to each of the  $\Gamma$ ,  $L$ , and  $X$  conduction band valleys have been demonstrated by deep-level optical spectroscopy (DLOS)[69, 70]. EL2 energy level was found around the middle of the band gap, and large optical transition cross sections were observed. However an isolated neutral EL2 level is theoretically believed to have  $A_1$  symmetry[68]. The direct transition from a localized  $A_1$  state to the conduction band minimum at  $\Gamma$  point is thus unlikely in the electric dipole approximation[68]. The large experimental cross section for optical transitions between the EL2 ground state and the conduction  $\Gamma$  band has been explained through indirect transitions by coupling of LO phonons[66]. Knowledge of these properties helps us to interpret our experimental results and relate our spectral features to proper states.

Two levels of  $As_{Ga}$  antisite states are found at  $0.75eV$  below the conduction band minimum and  $0.5eV$  above valence band maximum by electron paramagnetic resonance (EPR) [71]. All of the antisite and vacancy defect energy levels in GaAs bulk have been calculated in reference 6. These are plotted in figure 4.5. All energy levels in figure 4.5 correspond to simple isolated and localized defect models. The states measured in EPR differ about  $0.3\sim 0.4 eV$  as comparison to this simple

theoretical calculations. More sophisticated theoretical model may be needed to explain these differences. However this simple isolated, localized defect model can give us qualitative informations about these defect states. In the case of  $As_{Ga}$  defects, the filled  $s$ -like level represents an isolated neutral As antisite defect, and is associated to EL2 ground state with  $A_1$  symmetry; The empty level is a  $p$ -like state, and the dipole transition between this level and conduction band minimum is allowed. In the case of Ga antisite  $Ga_{As}$  defect, the Ga atom sits on the As atom site. The empty level of  $Ga_{As}$  defect state is also near the middle of band gap and is a  $p$ -like state [6]. Thus the dipole transition between this level and conduction band minimum is allowed.

### 4.1.3 General optical properties of GaAs

Numerous experiments have been performed in the study of the linear optical properties of GaAs. The dispersion properties of its optical dielectric constants for example, have been intensively studied. A comprehensive source of information about GaAs optical properties are to be found in references [62, 72, 73].

In order to understand the optical properties of GaAs, we must consider the selection rules which govern optical transitions. These selection rules depend solely on the electronic properties and structural symmetry of the medium. The symmetry of the GaAs crystal is represented by the symmetry group  $T_d$ , which is a summation of a series of symmetry operators  $E$ ,  $8C_3$ ,  $3C_2$ ,  $6\sigma_d$ , and  $6S_4$ . A direct product of  $T_d$  and spin space results in a  $\bar{T}_d$  symmetry group. Under such a symmetry group, the energy band states can be represented in an irreducible representation with particular basis functions[55]. In the electronic dipole approximation, the transition matrix at the direct band gap of GaAs is (see figure 4.6(a) )

$$M = \langle \Gamma_6^c | \vec{Q} | \Gamma_8^v \rangle \quad (4.1)$$

Here  $Q$  is the dipole moment operator, which may be represented by the symmetry group  $\Gamma_5$ . The symmetry selection rule tells us that  $M$  is zero unless  $\Gamma_6$  is contained

in  $\Gamma_5 \times \Gamma_8$ . A direct product table of  $\bar{T}_d$  is presented in Table 5.2.[74]. In this particular case,

$$\Gamma_5 \times \Gamma_8 = \Gamma_6 + \Gamma_7 + 2\Gamma_8,$$

and so optical transitions in the electric dipole approximation are allowed at the GaAs direct band gap.

The relation of the linear susceptibility to the energy band states can be written as

$$\chi_{ij}^{(1)}(\omega) = \frac{Ne^2}{\hbar} \sum_{ge} \left[ \frac{\langle g|Q_i|e\rangle\langle e|Q_j|g\rangle}{\omega + \omega_{eg} + i\Gamma} - \frac{\langle g|Q_i|e\rangle\langle e|Q_j|g\rangle}{\omega - \omega_{eg} + i\Gamma} \right]$$

where  $|g\rangle$  and  $|e\rangle$  are the ground and excited states, respectively. Studies of the dielectric constant as a function of frequency provide electronic energy level information. For example, linear dielectric constants dramatically increase for photon energies above the band gap ( $E_{eg} \sim 1.42 \text{ eV}$ ), as a result of resonances ( $\omega - \omega_{eg} \sim 0$  in the second term). Such an effect was seen in our linear optical reflectivity experiments (see figure 4.6 (b)) [72, 73].

A more accurate value of the GaAs band gap ( $E_0 = 1.42 \text{ eV}$  at  $300^\circ \text{K}$ ) was measured by photoreflectance experiments[75]. In photoreflectance experiment, the reflectance is measured as a function of coincident secondary light beam intensity, which modulates the built-in electric field near the surface[76, 77]. Modulation spectroscopy reveals sharp, well-resolved spectra which can be analyzed to yield material properties. Some photoreflectance spectra of GaAs are presented in references [75, 78].

#### 4.1.4 Nonlinear optical properties of GaAs

The dispersion properties of the second-order nonlinear optical susceptibility of GaAs were first measured by Chang, *et al* [79, 80]. Their results indicate that the second-order susceptibility is correlated to the electronic band structure. A one photon resonance has been assigned to the direct band gap ( $E_0$ ). Since then, a few related

experiments and theoretical calculations have been conducted by different groups[80, 81, 82]. The detailed second-order nonlinear optical susceptibilities of GaAs have been calculated from the band structure obtained by empirical methods[50]. On the other hand, studies of symmetry patterns of second-order nonlinear optical processes also reveal the spatial structure of GaAs[55, 83, 84].

With a zinc-blende structure, GaAs carries a single nonzero bulk second-order-susceptibility  $\chi_{zxy}^{(2)} = \chi_{xzy}^{(2)} = \chi_{xyz}^{(2)}$ , whose contribution to the output radiation is highly anisotropic. The orientation dependence of our SHG signal is illustrated in figure 2.4. We have performed frequency-dependent measurements to further elucidate both bulk and surface contributions (see section 2.4). Further details of the experiments are discussed in chapters 2 and 6.

As in linear optical processes, the external field can also modulate the second-order nonlinear optical susceptibility, whose general properties under a localized electric field were studied by inverse Franz-Keldysh mechanisms[85, 86]. Such a field effect arises from field induced symmetry breaking and band-bending. The localized field (e.g. depletion electric field) perturbs the existing second-order susceptibility tensor elements, and generates new second-order susceptibility tensor elements which are forbidden in the unperturbed medium[41]. In chapters 5 and 6, the effect of depletion electric field on second-harmonic generation in GaAs(001) are studied in detail.

## 4.2 MBE Growth Procedures

Since our interest is focused on the relation between the sample preparations and the interface electronic structures. Sample preparation is crucial for the interpretation of our experimental results. Commercial GaAs samples were poorly calibrated and were not grown by molecular-beam epitaxy (MBE) methods. Our focus has thus been entirely on MBE grown system. In this section, MBE growth procedures and

sample interfacial properties are reviewed. Samples were grown by Dr. W. M. Theis at Naval Air Warfare Center.

#### 4.2.1 MBE Growth of GaAs(001)

All samples studied here were grown on undoped GaAs substrates by molecular-beam epitaxy (MBE). MBE, one of the best crystal growth techniques. It allows layer by layer atomic growth. The great advantage of MBE is in its control of sample growth conditions. These are controlled by varying growth parameters, e.g., the molecular beam flux and substrate temperature. Therefore, MBE permits a finer control of the thickness of successive layers than either liquid phase epitaxy (LPE) or vapor phase epitaxy (VPE)[87]. A typical MBE system is comprised of the following components:

1. A UHV system, including a specimen exchange vacuum load-lock.
2. A heated substrate holder
3. A Multifurnace with shutters and baffles
4. Epitaxy control instrumentation (Beam flux detector)
5. Components for substrate cleaning (Heater, Ion sputtering gun)
6. Surface analytical instruments (Auger, RHEED, LEED, Mass spectrometer)

A schematic drawing of our MBE growth chamber is shown in figure 4.7. All our GaAs(001) samples were grown at a substrate temperature of  $580^{\circ}C$  with the background UHV chamber pressure at  $10^{-10}$  Torr. The total growth pressure was  $\sim 10^{-6}$  Torr. The As:Ga beam flux ratio was 4 : 1, for which GaAs grows about  $\sim 1\mu m/hour$ . The n-type (p-type) doping flux was supplied by a Si (Ge) beam and the doping levels were controlled by the effusion cell temperature. Finally, the doping levels were calibrated by Hall measurements[4]. Along the [001] direction, crystal planes are alternately occupied by cations and anions. Ideally terminated [001] surfaces would thus consist of either cations or anions and each surface atom would possess two dangling bonds.

However, in these experiments the GaAs(001) plane were not ideally terminated,

but rather exhibited various reconstructions, which reduce the number of dangling bonds by the dimerization of surface atoms. Experimentally, different reconstructions are found to be related to the ratio of Ga to As at the surface[88, 89]. For the As-rich growth conditions, the RHEED pattern indicates a  $2 \times 4$  surface reconstruction.

A typical  $2 \times 4$   $\beta$  phase surface reconstruction of a GaAs(001) surface is plotted in figure 4.8(a)[3]. The Ga-rich surface was grown by closing the As-beam shutter for 2 *seconds* at the end of the growth process, and the RHEED pattern indicates a  $4 \times 2$  surface reconstruction for our Ga-rich samples. A typical  $4 \times 2$  surface reconstruction of the GaAs(001) surface is plotted in figure 4.8(b)[3]. The ratio of As:Ga was 75% : 25% (25% : 75%) for the  $2 \times 4$  reconstruction( $4 \times 2$  surface reconstruction).

#### 4.2.2 MBE Growth of Metal:GaAs

The metal films were grown on well calibrated n-type and p-type MBE GaAs(001) substrates by molecular beam epitaxy. Since GaAs(001) exhibits a wide variety of surface reconstructions, RHEED measurements were performed on all samples before growth of the Au epitaxial film. The GaAs surfaces were either As-rich or Ga-rich; further details of the GaAs(001) growth process can be found in section 4.2.1. After the GaAs surface reconstruction was calibrated by RHEED, the sample was cooled down inside the UHV chamber for several hours. An  $80\text{\AA}$  epitaxial Au film was then grown on the GaAs(001) substrate at a surface temperature of  $\sim 400^\circ\text{C}$ . The growth rate of Au was around  $0.1\mu\text{m}/\text{hour}$ . The Au film was confirmed to be epitaxial by RHEED measurements.  $80\text{\AA}$  amorphous As films were also grown on GaAs(001). When such a sample is exposed to air, a fraction of the As film is converted into an oxide ( $\sim 40\text{\AA}$ ), but Auger spectroscopy confirmed that oxygen did not penetrate as far as the As:GaAs interface.

### 4.3 Linear optical measurements of the metal film thickness

A linear optical method was employed to measure the thickness of the metal superficial films. For a three slab system (e.g. air/Au/GaAs) (see figure 4.9), the total reflected s-polarized  $E_R$  can be related to the incident s-polarized  $E_I$  by

$$\frac{E_R}{E_I} = \frac{r_{01} + r_{12}e^{i\delta}}{1 + r_{01}r_{12}e^{i\delta}}$$

with

$$\delta = \frac{4\pi d}{\lambda} \cos\theta_1 n_1$$

Here,  $r_{01}$  represents the reflectivity amplitude at the air/Au interface, and  $r_{12}$  represents the reflectivity amplitude at the Au/GaAs interface.  $d$  is the thickness of the Au film. For s-polarized incident light, we find:

$$r_{01} = \frac{(-n_1 \cos\theta_0 + n_0 \cos\theta_1)}{(n_1 \cos\theta_0 + n_0 \cos\theta_1)}$$

$$r_{12} = \frac{(-n_2 \cos\theta_1 + n_1 \cos\theta_2)}{(n_2 \cos\theta_1 + n_1 \cos\theta_2)},$$

where  $n_0, n_1$ , and  $n_2$  represent the complex dielectric constants of air, Au, and GaAs respectively.  $\theta_0, \theta_1$ , and  $\theta_2$  represent the incident angles in the air, Au, and GaAs respectively. As part of these experiments, the linear reflectivity as a function of incident angle was measured. The light beam diameter is  $\phi = 1 \sim 2 \text{ mm}$ . By fitting for  $d$ , we found the thickness of the Au overlayer to be  $\sim 80 \text{ \AA}$  (see figure 4.10). The same method can also be used to measure the thickness of As film on GaAs. The fitting results are plotted in figure 4.11. Since the As overlayer is amorphous, the film is expected to be nonuniform. From the fits, we found that the As overlayer thickness is between  $50 \sim 100 \text{ \AA}$ .

## 4.4 General properties of GaAs based surfaces and interfaces

GaAs surfaces exhibit both intrinsic and extrinsic surface states. Generally extrinsic states refer to the impurity and defects induced states, and intrinsic surface states arise from the surface dangling bonds. Theoretical calculations show that no intrinsic surface bands of GaAs exist in the gap when the surface atoms relax from their normal bulk positions [90, 91, 92]. All occupied surface bands overlap with the bulk valence bands, and all unoccupied surface bands overlap with the bulk conduction bands [3, 93, 94].

On the other hand, the Fermi levels at GaAs surfaces and interfaces are pinned near the midgap (see figure 4.12)[96]. This suggests that a large density of extrinsic surface states ( $> 10^{12} \text{cm}^{-2}$ ) can be attributed to this pinning phenomenon[20]. The origin of these surface states is still only partially understood. Spicer, *et al.*, proposed a unified defect model which attributed these interface states to the existence of antisite defect states (e.g.  $As_{Ga}$ )[5, 6]. In contrast, Heine, *et al.* proposed that the interface states are due to metal-induced midgap states[8]. In this case, the wavefunctions of those metal electrons overlapping the semiconductor band gap, decay exponentially into the semiconductor. These tails form metal-induced interface states.

In addition, these interface states can arise from other mechanism such as interdiffusion and replacement between the metal overlayer atoms and the semiconductor substrates[97]. It has been pointed out that the Ga atoms are more likely to be involved in a replacement reaction with metal atoms in a Ga terminated surface, whereas the As terminated surface would stabilize the interface against such a replacement reaction[98]. In the case of our Ga-rich interface samples, replacement reactions could produce different interface structures and the formation of alloys in the interface layer[98]. As a result, additional interface states might arise[89] At

metal/semiconductor interface it is possible that all these mechanisms could affect the electronic properties at the interface. However, in some situations one of them may dominate above all others. In addition, because bulk symmetry is broken at the interface, and strong localized depletion electric field exists, the interface defects differ from the bulk defects. The interface defects are perturbed by localized field, and as a result its symmetry is perturbed.

There are very few direct spectroscopic measurements of these interface states. Some spectroscopic evidence for interface states has been derived from I-V/C-V curve experiments[95], cathodoluminescence spectroscopy (CLS)[24], inverse photoemission spectroscopy (IPS)[10], and ultraviolet-photoemission spectroscopy (UPS)[23]. But these spectra are very broad, and the measurements are not intrinsically sensitive to the buried interface. The lack of clean spectra from the buried interface makes it difficult to test microscopic models of the origin of these midgap states.

Length of side of unit cube	5.65325Å
Nearest-neighbor distance	2.44793Å
Crystal density	5.317g/cm <sup>3</sup>
Specific heat	0.327J/gK
Effective Debye temperature	360K
Static dielectric constant	12.85

Table 4.1: Some physical properties of GaAs at room temperature (300K)

Direct intrinsic gap $E_0(\Gamma_8^v - \Gamma_6^c)$	1.423 eV
$E_1(L_{4,5}^v - L_6^c)$	2.82 eV
$E_0'(\Gamma_8^v - \Gamma_7^c)$	4.5 eV
$E_2(X_7^v - X_6^c, X_6^v - X_6^c, X_7^v - X_7^c, X_6^v - X_7^c)$	5.0 eV
Electron mass at conduction band edge	0.0632 $m_0$
Heavy hole mass at valence band edge	0.5 $m_0$
Light hole mass at valence band edge	0.088 $m_0$
Electron drift mobility	8000cm <sup>2</sup> /Vs
Electron Hall mobility	9400cm <sup>2</sup> /Vs
Hole drift mobility	320cm <sup>2</sup> /Vs
Hole Hall mobility	400cm <sup>2</sup> /Vs

Table 4.2: Some electronic properties of GaAs at room temperature (300K)

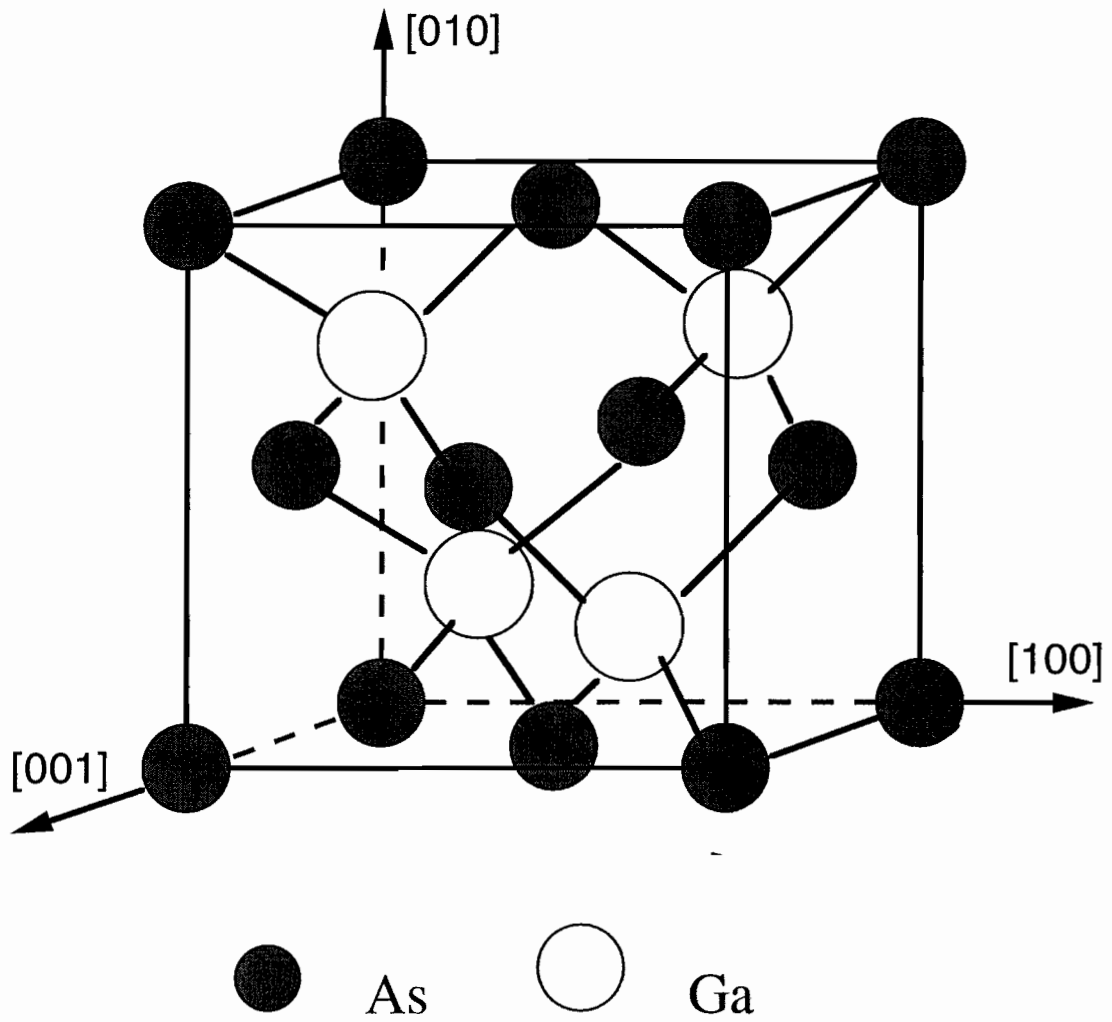


Figure 4.1: GaAs crystal structure. Lattice constants see table 4.1.

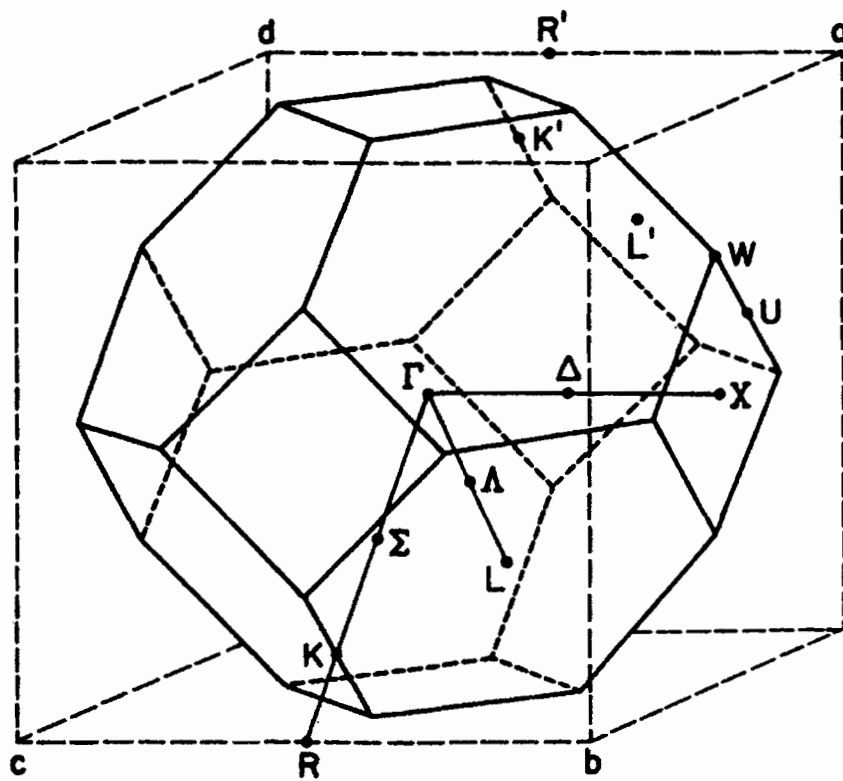


Figure 4.2: First Brillouin zone for the GaAs lattice.

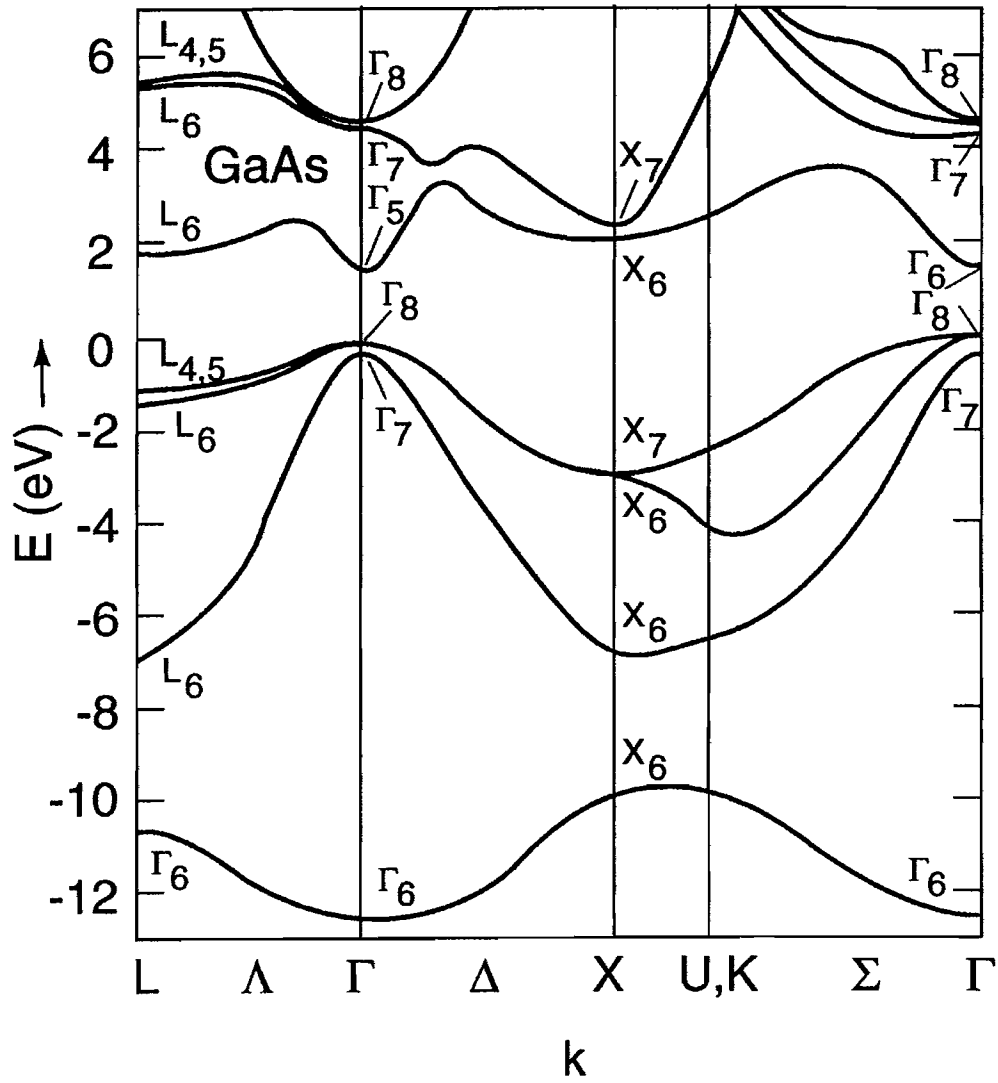


Figure 4.3: The electronic band structure of GaAs.

## As antisite ( $As_{Ga}$ )

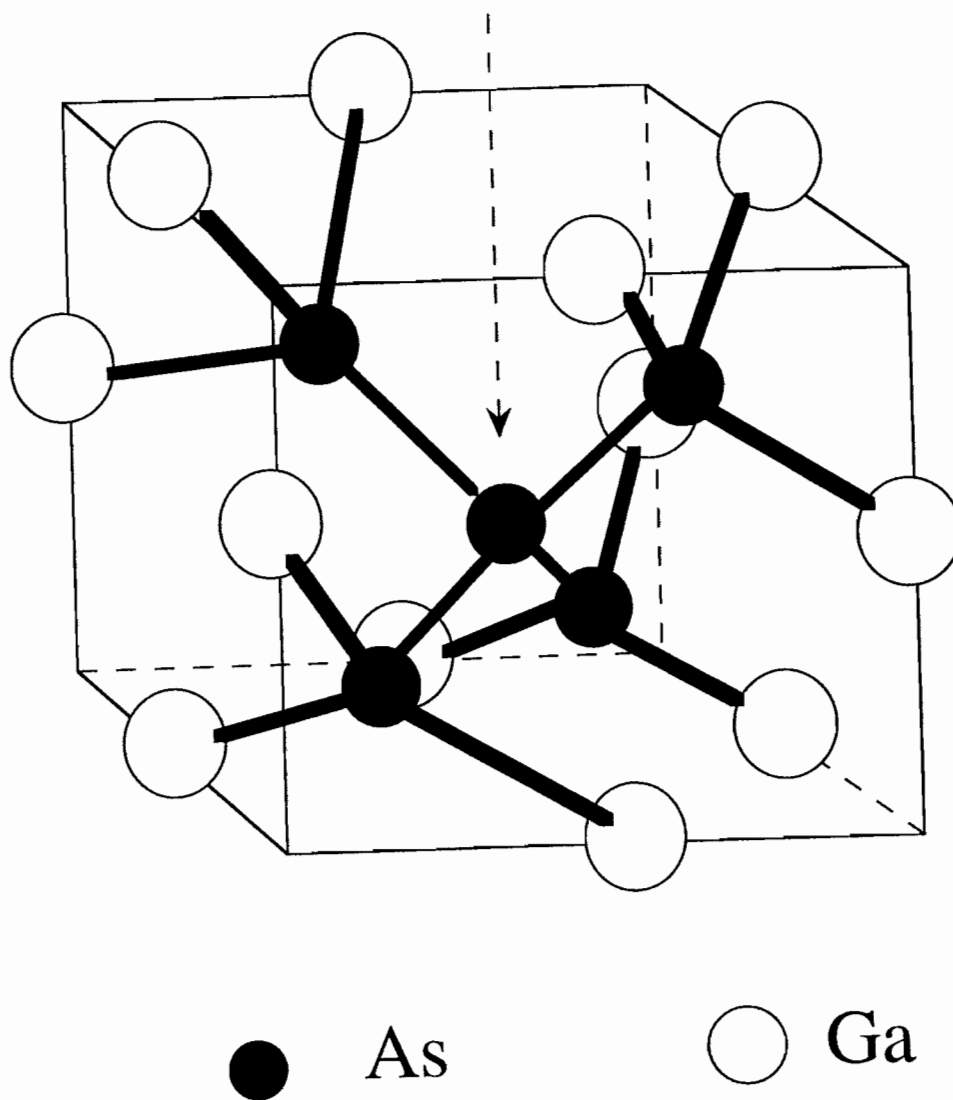


Figure 4.4: An isolated As antisite ( $As_{Ga}$ ) defect structure.

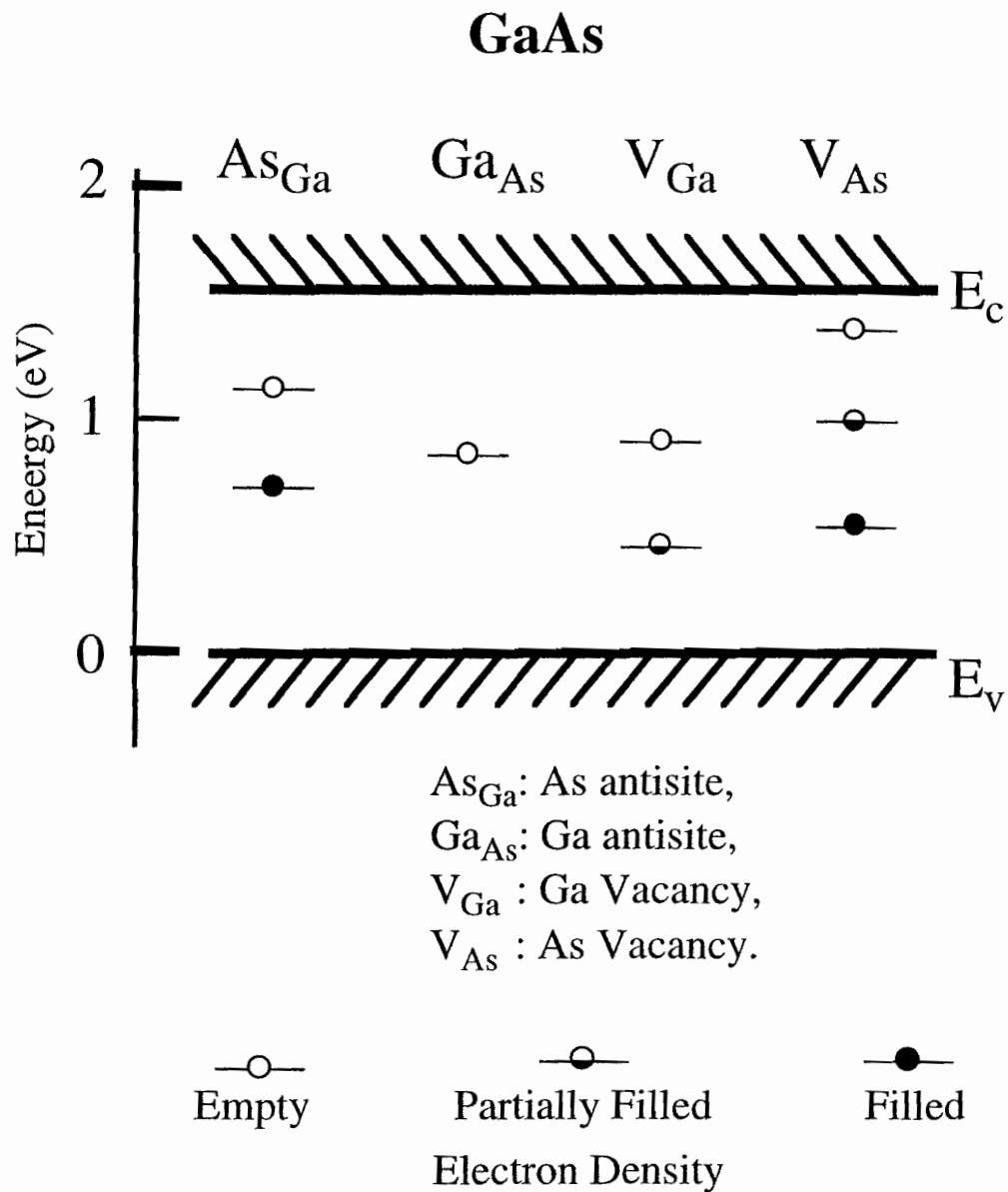


Figure 4.5: Theoretical calculations of the atomic displacement-induced defect state energy levels in GaAs bulk (from reference 6).

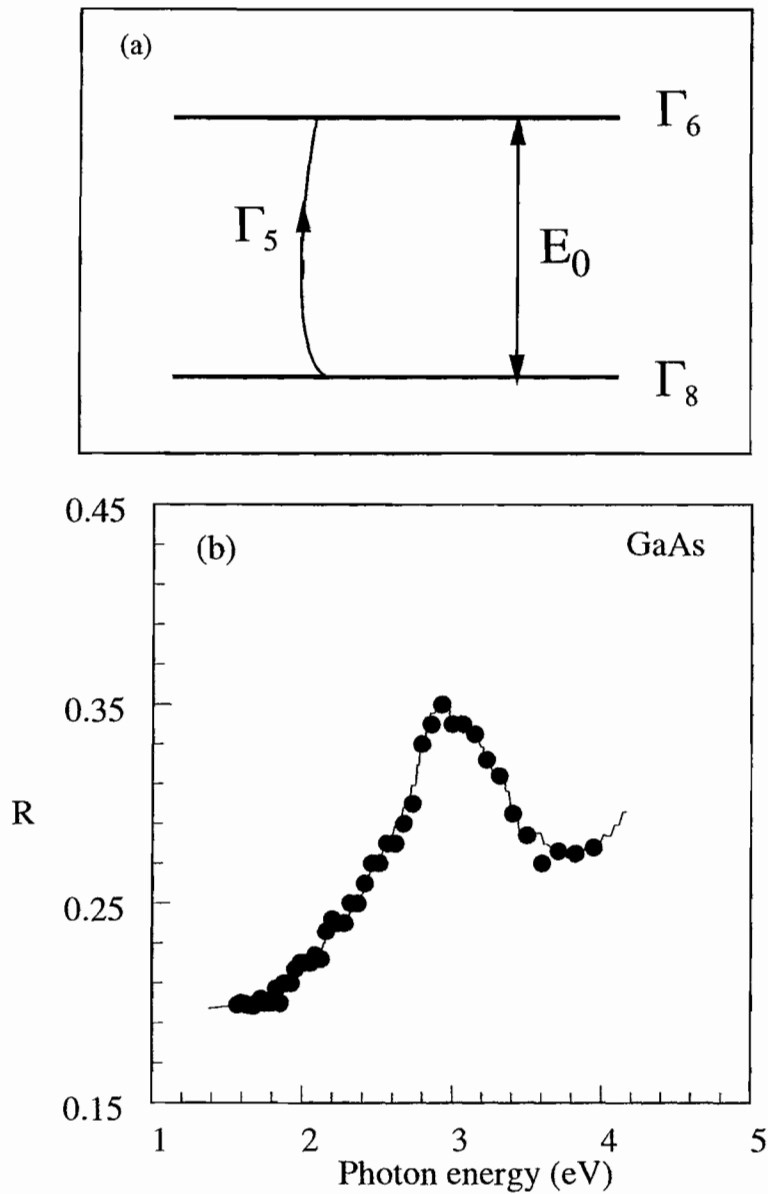


Figure 4.6: (a) Linear electric dipole transition at the direct band gap of GaAs. The dipole operator is represented by  $\Gamma_5$ . (b) Linear reflectivity  $R$  as function of the incidence photon energy from GaAs crystal. The light incident at angle  $45^\circ$ . The solid line is the theoretical calculation.

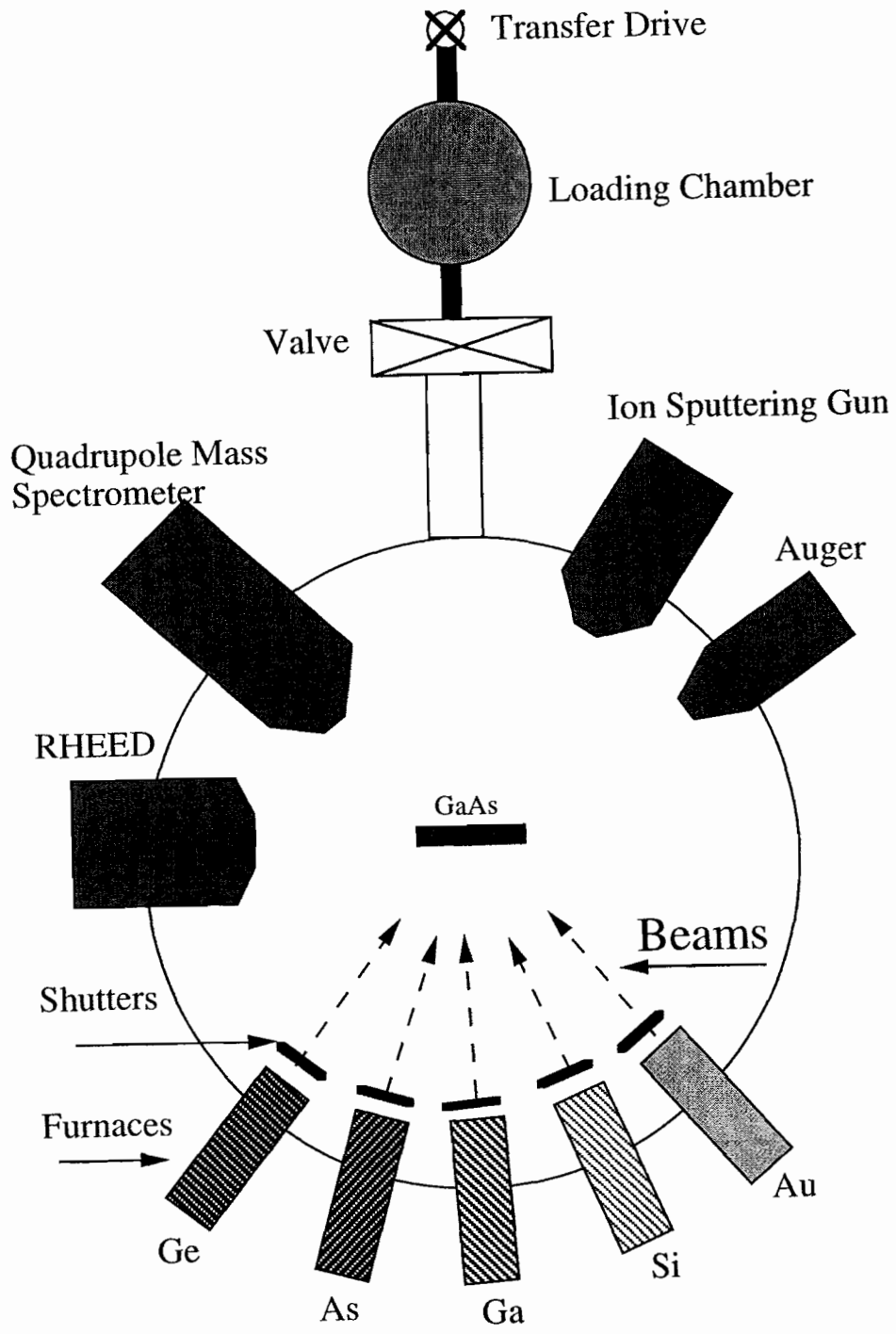


Figure 4.7: Schematic diagram of MBE growth chamber.

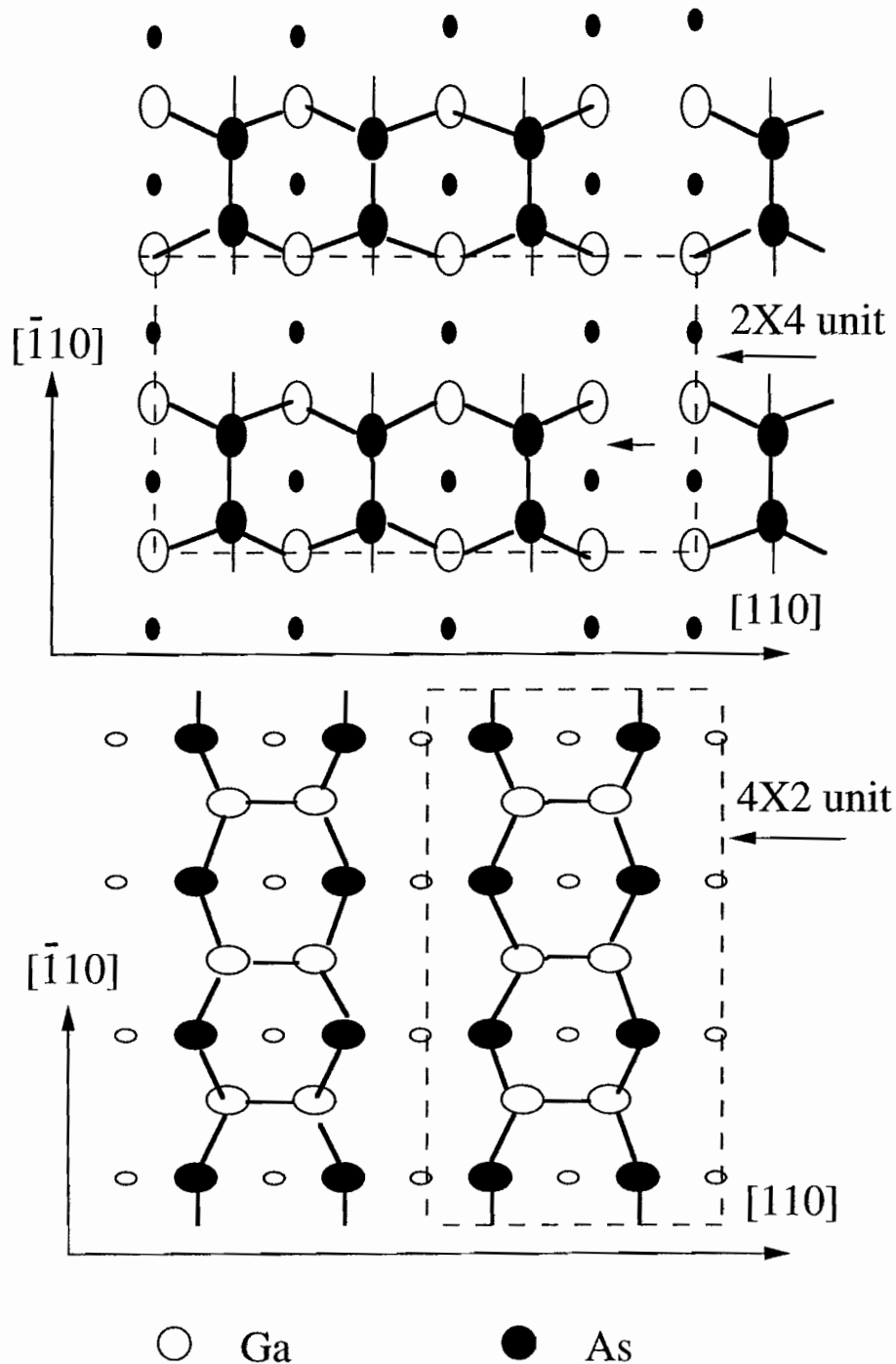


Figure 4.8: (a) One of the proposed  $2 \times 4$  reconstructions at GaAs surface. As atoms form the first layer; (b) One of the proposed  $4 \times 2$  reconstruction at GaAs surface. Ga atoms form the first layer.

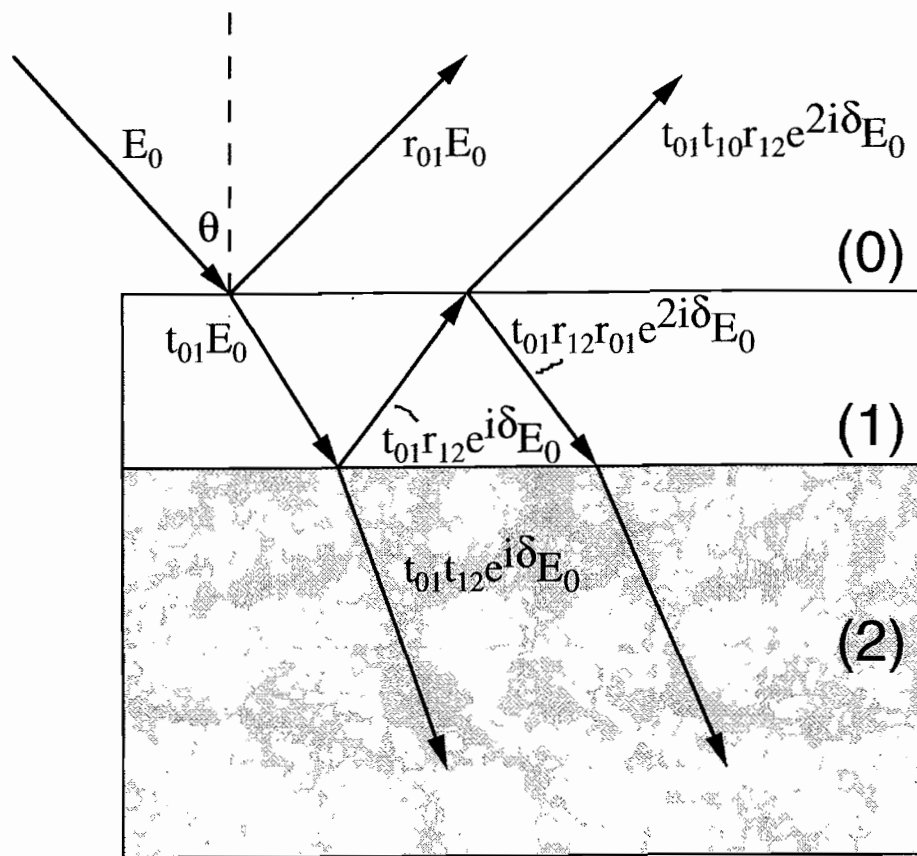


Figure 4.9: Linear reflection from two-slab system.

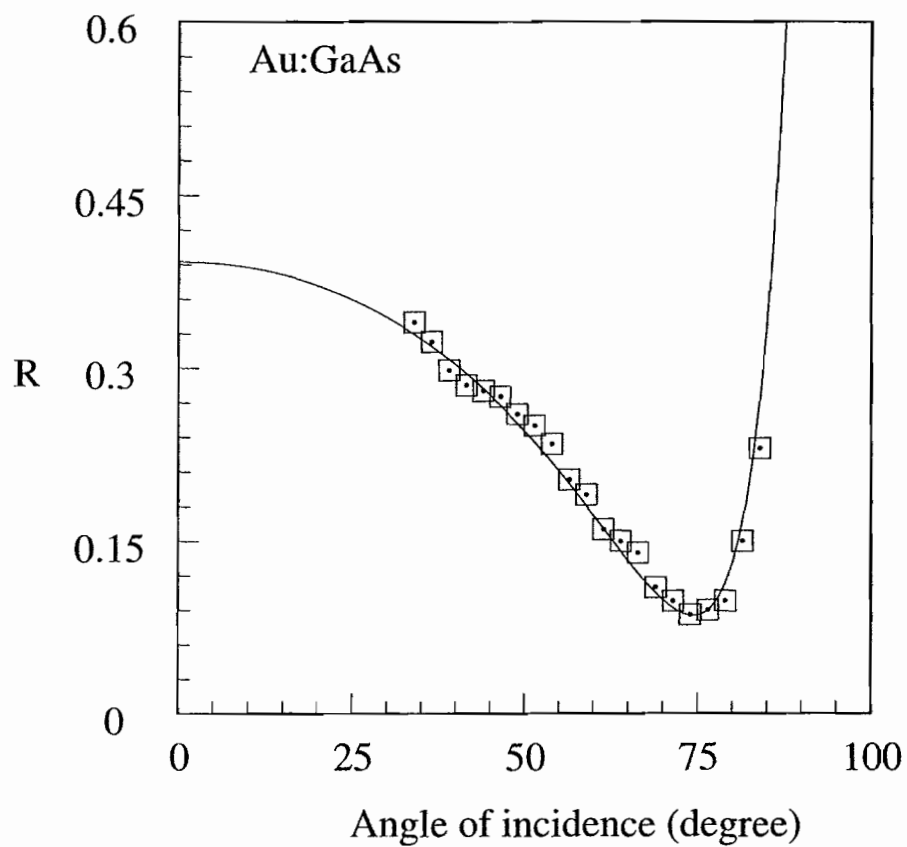


Figure 4.10: Linear reflectivity  $R$  as function of the incident angle for a Au:GaAs system. The solid line is the best fit to the Au layer thickness, which is  $80 \text{ \AA}$ . Incident light is at  $632.8 \text{ nm}$ .

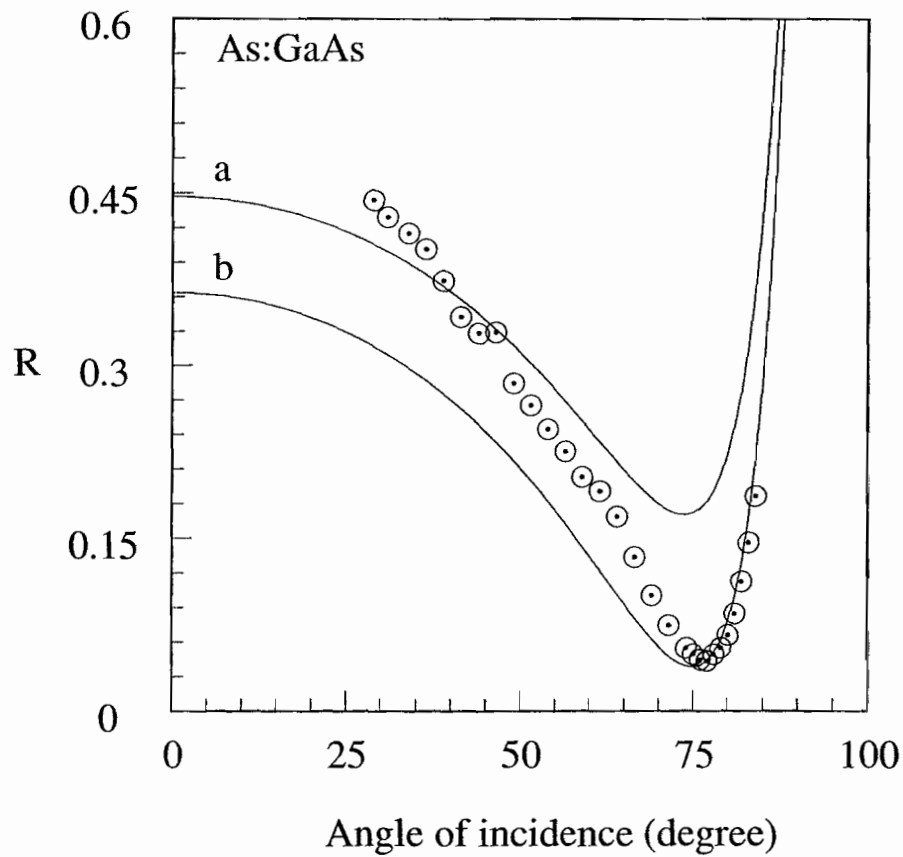


Figure 4.11: Linear reflectivity  $R$  as function of the incident angle for a As:GaAs system. The solid lines (a) and (b) represent two different As overlayer thicknesses in the theoretical calculation, i.e.  $d_a \sim 100\text{\AA}$ , and  $d_b \sim 50\text{\AA}$ . Since the As overlayer is amorphous, the film is expected to be nonuniform.

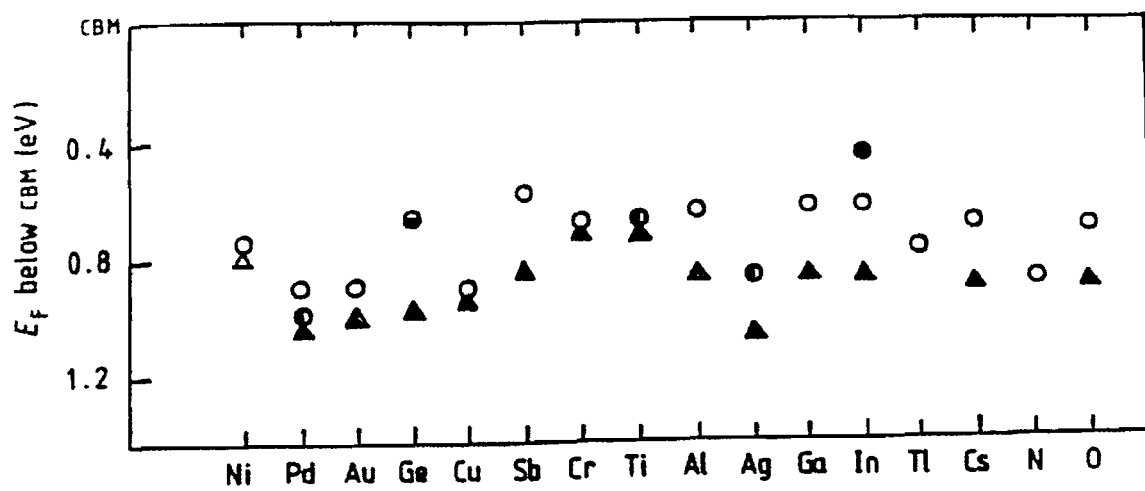


Figure 4.12: Fermi level pinning positions at different solid:GaAs interfaces. Circles represent n-type GaAs based interfaces; Triangles represent p-type GaAs based interfaces (from reference 95).

## Chapter 5

# Theory of field induced perturbation on the second-order susceptibility

Spatially extended space-charge layers are usually present near semiconductor surfaces. This behavior distinguishes semiconductors from metals. The space-charge region arises mainly from the existence of surface states. When these surface states become charged, charge neutrality requires the existence of a space-charge layer (*depletion region*) which penetrates from the surface into the semiconductor bulk. This charge distribution creates a strong depletion electric field, which generates a new band profile and changes the bulk symmetry in the depletion region. The accompanying localized electric field plays an important role in many semiconductor devices such as photodiodes and solar cells[4].

In the case of an isotropic medium, it is well known that an externally applied DC electric field breaks the isotropic symmetry, and leads to the enhancement of otherwise forbidden second-order nonlinear optical processes[57, 59]. The static electric fields within the surface depletion region of a semiconductor provides a naturally

occurring analogue of this effect. In this chapter, we calculate the depletion field induced perturbation on the second-order nonlinear susceptibility of GaAs(001) based on a simple three-band model.

## 5.1 The depletion field

The electric field  $E(z)$  and potential distribution  $\phi(z)$  in the depletion region depend on the doping density  $\rho$  and the surface charge density  $N_s$ . The form of these dependences can be obtained by solving the one-dimensional Poisson equation. Figure 4.1 shows the energy band diagram of an n-type semiconductor and the charge distribution. Assuming that the semiconductor is uniformly doped over entire crystal and all the donors are ionized, the Poisson equation can be written as

$$\frac{d^2\phi(z)}{dz^2} = -\frac{q}{\epsilon}[N_s\delta(z=0) + \rho + n(z) + p(z)] . \quad (5.1)$$

Here  $z = 0$  at surface,  $q = |e|$  is the unit charge and  $e$  is electron charge. Signs of the charges are carried with their densities. In the case of n-type semiconductor,  $N_s$  is negative, and  $\rho$  is positive.  $n(z)$  ( $p(z)$ ) is the free electron (hole) concentration inside the depletion region, which can be written:

$$n(z) = n_0 \exp\left(\frac{q\phi(z)}{kT}\right) \quad (5.2)$$

$$p(z) = p_0 \exp\left(-\frac{q\phi(z)}{kT}\right) \quad (5.3)$$

Here  $n_0$  ( $p_0$ ) represent the equilibrium electron (hole) concentration inside the neutral bulk region. The potential  $\phi(z = W) = 0$  in the neutral bulk region, where  $W$  is the depletion length. A closed form solution of this equation is impossible, so an additional assumption is made in this analysis called *the depletion approximation*. In this approximation the free carrier concentrations are assumed to fall abruptly from their equilibrium value in the bulk neutral region to a negligibly small value in the depletion region, i.e.,  $n(z \leq W) = 0$  and  $p(z \leq W) = 0$  [4]. Therefore we

can divide the semiconductor into a space charge region ( $0 \leq z \leq W$ ) and a neutral region devoid of any space charge ( $z \geq W$ ). Finally, the Poisson equation in the depletion region can be written as

$$\frac{d^2\phi(z)}{dz^2} = -\frac{q}{\epsilon}[N_s\delta(z=0) + \rho] . \quad (5.4)$$

Using the boundary condition  $\frac{d\phi}{dz} = 0$  at  $z = W$  we obtain the electric field  $E(z)$  in the depletion region;

$$\mathbf{E}(z) = -\frac{q\rho W}{\epsilon}\left(1 - \frac{z}{W}\right)\hat{z} . \quad (5.5)$$

The maximum electric field  $E_{max}(z=0) = -\frac{q\rho W}{\epsilon}\hat{z}$  is at the surface boundary. Here  $\epsilon$  is the dielectric constant of the medium. Because of charge neutrality, the total surface charge density  $|N_s| = \rho W$ . A second integration, with the boundary condition  $\phi(z=W) = 0$ , leads to the following relation;

$$\phi(z) = -\frac{q\rho W^2}{2\epsilon}\left(1 - \frac{z}{W}\right)^2 . \quad (5.6)$$

This indicates that the depletion field induced potential depends on the distance  $z$  parabolically. It reaches its maximum value  $\phi(z=0) = \Phi_{max}$  at  $z = 0$ .

$$\Phi_{max} = -\frac{q\rho W^2}{2\epsilon} . \quad (5.7)$$

$\Phi_{max}$  determines the band-bending amplitude and relies on the surface Fermi level pinning position [4]. In the case of n-type semiconductor, the potential energy of majority carrier (electron) is

$$V(z) = \frac{q^2\rho W^2}{2\epsilon}\left(1 - \frac{z}{W}\right)^2 .$$

Results for n-type semiconductor are plotted in figure 5.1.

Typically n-type (p-type) GaAs samples have a built-in potential of  $\sim 0.75$  V ( $\sim 0.5$  V) due to the surface Fermi level pinning [5]. Therefore samples with different doping densities can have the same  $V_{max}$ , with different depletion region widths and depletion field strengths;

$$E(z) = \sqrt{2\epsilon V_{max}|q\rho|}\left(1 - \frac{z}{W}\right) . \quad (5.8)$$

If the near surface region which we optically probe is thinner than the depletion length, i.e.,  $z \ll W$ , we can make the first order approximation to obtain  $E(z) \sim E_{max}(z=0) = \sqrt{2\epsilon V_{max}|q\rho|}$ . Experimentally the depletion length of our samples was between  $0.1 \mu m$  and  $3.0 \mu m$  depending on the doping levels, with the exception of the most highly doped samples. The SHG penetration depth of  $\sim 0.1 \mu m$  was substantially less than the sample depletion length. The assumption of a constant depletion field is essential for the simplification of our theoretical calculations in the following sections.

## 5.2 Depletion field induced perturbation on second-order susceptibilities

Because of surface charging, a strong electric field exists along the crystalline [001] direction near the GaAs(001) surface. As a result, the bulk symmetry in the depletion region is reduced from  $\bar{4}3m$  to  $mm2$ . In principle, all elements of  $\chi^{(2)}$  are perturbed by such a localized field. In this section we focus on the changes in the existing bulk nonlinear susceptibility  $\chi_{yxz}^{(2)}$ . The perturbation of other elements such as  $\chi_{zzz}^{(2)}$  will be presented in Appendix D. All of our calculations are based on the electric dipole approximation. The following analysis involves the application of group theory. Since it is impossible to present group theory in complete detail, I will simply explain the main results and provide key references.

### 5.2.1 The three band model in GaAs(001)

For our experiments the fundamental photon energy was chosen to be near the band gap of GaAs, so that the dominant contribution to the second-order susceptibility  $\chi_{yxz}^{(2)}$  arose mainly from transitions between the top valence band ( $|\Gamma_8 \rangle$ ) and the two lowest conduction bands ( $|\Gamma_6 \rangle$  and  $|\Gamma_7 \rangle$ ) at the  $\Gamma$  point in the Brillouin zone[50] (see figure 5.2). As a result, the second-order nonlinear optical process is dominated

by the three band states at the  $\Gamma$  point in the Brillouin zone. This basically is our *three-band model* approximation. These three band states will be the basis states for calculations of the field induced perturbations. The form of the three band state wavefunctions can be derived from their symmetries[100].

The GaAs is a zinc-blende crystal, whose properties are invariant under the symmetry operators  $E, 8C_3, 3C_2, 6\sigma_d$  and  $6S_4$  [48]. The set of these operators forms the group  $T_d = \{E, 8C_3, 3C_2, 6\sigma_d, 6S_4\}$ . This group is a closed set. However, its matrix representation is not unique; one can start with any representation, apply a similarity transformation (i.e.  $A' = T^{-1}AT$ , where  $T$  is a unitary matrix), and obtain a new representation. If, however, the group is represented by the traces of the matrices, called the character, this new representation is unique because the trace of a matrix remains unchanged under any similarity transformation. The character table of  $T_d$  is given in Table 5.1. Each row of the table is labeled with  $\Gamma_i$ , which is the character representation of the group.

In addition to the representation, the form of the basis functions of each representation is also an important factor. The usual choice for the basis functions is  $XYZ$ . The basis functions are not the exact mathematical expression of the wavefunction, but are rather a mathematical expression which transforms exactly with the same symmetry of the irreducible representation [100, 101]. A systematic way to describe basis function is with projection operators. This method is described in reference 74 and 101, and some basis functions for the  $T_d$  group are shown in Table 5.2.

A direct product of  $T_d$  and spin space results in a  $\bar{T}_d$  symmetry group. Therefore the wave functions of  $|\Gamma_6 \rangle$ ,  $|\Gamma_7 \rangle$ , and  $|\Gamma_8 \rangle$  are combinations of products of the spinor states ( $|\alpha \rangle$ ,  $|\beta \rangle$ ) and spatial functions, where  $|\alpha \rangle$  ( $|\beta \rangle$ ) represents spin up (down). The spatial functions of  $|\Gamma_6 \rangle$ ,  $|\Gamma_7 \rangle$ , and  $|\Gamma_8 \rangle$  have been given out in reference 98 and 99. Considering the spatial and spin space together, we get the general forms of these three states. The states  $|\Gamma_6 \rangle$  can be written as

$$\phi_{+\frac{1}{2}}^{(6)} = f|\alpha\rangle \quad (5.9)$$

$$\phi_{-\frac{1}{2}}^{(6)} = f|\beta\rangle \quad (5.10)$$

Here  $f$  is a scalar spatial function, and transforms as  $x^2 + y^2 + z^2$ . The subscripts represent the  $z$ -component ( $J_z$ ) of the angular momentum ( $J$ ). The states  $|\Gamma_7\rangle$  can be written as;

$$\phi_{+\frac{1}{2}}^{(7)} = \frac{1}{\sqrt{3}}[(X + iY)|\beta\rangle + Z|\alpha\rangle] \quad (5.11)$$

$$\phi_{-\frac{1}{2}}^{(7)} = \frac{1}{\sqrt{3}}[(X - iY)|\alpha\rangle - Z|\beta\rangle] \quad (5.12)$$

States  $|\Gamma_8\rangle$ ;

$$\phi_{+\frac{3}{2}}^{(8)} = \frac{1}{\sqrt{2}}(X + iY)|\alpha\rangle \quad (5.13)$$

$$\phi_{+\frac{1}{2}}^{(8)} = \frac{i}{\sqrt{6}}[(X + iY)|\beta\rangle - 2Z|\alpha\rangle] \quad (5.14)$$

$$\phi_{-\frac{1}{2}}^{(8)} = \frac{1}{\sqrt{6}}[(X - iY)|\alpha\rangle + 2Z|\beta\rangle] \quad (5.15)$$

$$\phi_{-\frac{3}{2}}^{(8)} = \frac{i}{\sqrt{2}}(X - iY)|\beta\rangle \quad (5.16)$$

Here  $X, Y, Z$  transform as the  $x, y, z$  components of a polar vector. All the functions are orthogonal to each other and normalized.

### 5.2.2 The perturbation of the three-bands at the $\Gamma$ point

Under the depletion field  $E_{depletion} = E\hat{z}$ , the three band states are perturbed, giving rise to mixtures of the states  $|\Gamma_6\rangle$ ,  $|\Gamma_7\rangle$ , and  $|\Gamma_8\rangle$ . For a dipole induced perturbation, the perturbation hamiltonian can be written as;

$$H' = \vec{Q} \cdot \vec{E}(z) \quad (5.17)$$

Here the  $Q$  is the dipole moment of the system. In the case of nondegenerate states, the perturbed wavefunction  $|\phi_n\rangle$  and energy  $E_n$  are generally written as;

$$|\phi_n\rangle = |\phi_n^0\rangle + |\phi_n'\rangle + |\phi_n''\rangle + \dots \quad (5.18)$$

$$E_n = E_n^0 + E_n' + E_n'' \dots \quad (5.19)$$

$$(5.20)$$

with

$$|\phi'_n\rangle = \sum_m \frac{|\phi_m^0\rangle \langle \phi_m^0 | H' | \phi_n^0 \rangle}{E_n^0 - E_m^0} \quad (5.21)$$

$$E'_n = H'_{nn} \quad (5.22)$$

$$E'_n = \sum_m \frac{|\langle \phi_m^0 | H' | \phi_n^0 \rangle|^2}{E_n^0 - E_m^0} \quad (5.23)$$

Here the summation is over all  $m$  states. In our case,  $m$  represents all three band states at the  $\Gamma$  point. In the case of degenerate eigenstates, we use degenerate perturbation theory to diagonalize the perturbation matrix.

Generally it is impossible to explicitly solve this perturbation problem with  $H' = \vec{Q} \cdot E(\vec{z})$ . Because the perturbation  $H'$  depends on spatial parameters  $(x,y,z)$  nonlinearly, integrations for perturbation matrices are more complicated. However, if our SHG photon escape depth is less than the depletion length, we can simplify our problem by assuming constant depletion field. Therefore the perturbation  $H'$  depends linearly on the position  $z$  via the dipole moment  $Q$ , (i.e,  $H' = \vec{Q} \cdot E_{max}(\vec{z} = 0)$ ). Finally the electric field  $E_{max}(\vec{z} = 0)$  can be treated as a constant and pulled out of the integral. Under such circumstances, the perturbation matrices among these band states are the same as dipole transition matrices and are governed by the dipole transition rule.

Calculation of the perturbation matrix requires knowledge of the selection rules for dipole transitions among these three states. The selection rule arises from the existence of a certain symmetry in the system. For example, in the case of a dipole transition from state  $|a\rangle$  to  $|b\rangle$ , the transition probability is proportional to the square of the magnitude of the matrix element

$$M_{ba} = \langle b | \vec{Q} | a \rangle \quad (5.24)$$

The wave function  $|a\rangle$  ( $|b\rangle$ ) belongs to the irreducible representation  $\Gamma_a$  ( $\Gamma_b$ ) of the symmetry group of the system. If the operator  $\vec{Q}$  belongs to the irreducible representation  $\Gamma_c$ , then the symmetry selection rule tells us that  $M_{ba}$  is zero unless  $\Gamma_b$  is

contained in  $\Gamma_c \times \Gamma_a$ . A direct product table of  $\bar{T}_d$  is presented in Table 5.3 and 5.4. As a result, the general dipole transition elements can be derived from the product tables.

Let us consider the general form of the dipole moment operator  $\vec{Q}$  which acts on our  $\bar{T}_d$  symmetry system. The dipole moment operator  $\vec{Q}$  belongs to the irreducible representation  $\Gamma_5$ . According to table 5.3 and 5.4, the direct product of  $\Gamma_5 \times \Gamma_6$  ( $\Gamma_5 \times \Gamma_7$ ) does not contain  $\Gamma_6$  ( $\Gamma_7$ ), which means that the interband dipole transition within  $\Gamma^{(6)}$  and  $\Gamma^{(7)}$  are zero ( $\langle \phi^{(6)} | Q | \phi^{(6)} \rangle = 0$  and  $\langle \phi^{(7)} | Q | \phi^{(7)} \rangle = 0$ ) [55]. These results mean that  $\langle \phi^{(6)} | H + Q | \phi^{(6)} \rangle$  and  $\langle \phi^{(7)} | H + Q | \phi^{(7)} \rangle$  are still diagonal under  $\times$  this dipole perturbation, where  $H$  is the unperturbed system Hamiltonian. Thus we can solve the first order perturbation on the  $\Gamma_6$  and  $\Gamma_7$  band states by using the nondegenerate perturbation formula [99].

In the case of the  $\Gamma_8$  state, the interband dipole transition is not zero ( $\langle \phi^{(8)} | Q | \phi^{(8)} \rangle \neq 0$ ), because;

$$\Gamma_5 \times \Gamma_8 = \Gamma_6 + \Gamma_7 + 2\Gamma_8$$

This means that for the dipole perturbation the matrix  $\langle \phi^{(8)} | H + Q | \phi^{(8)} \rangle$  is not diagonalized. Therefore we must treat the perturbation of state  $\Gamma_8$  with degenerate perturbation theory.

According to first order perturbation theory, the perturbed wavefunctions  $\phi^{(6)}$  ( $\phi^{(7)}$ ) for the  $\Gamma_6$  ( $\Gamma_7$ ) band states depend on the matrices  $\langle \phi^{(6)} | Q | \phi^{(7)} \rangle$  and  $\langle \phi^{(6)} | Q | \phi^{(8)} \rangle$  ( $\langle \phi^{(7)} | Q | \phi^{(6)} \rangle$  and  $\langle \phi^{(7)} | Q | \phi^{(8)} \rangle$ ). Details of the calculation are presented in Appendix A. The results are as follows;

$$\langle \phi^{(7)} | Q | \phi^{(6)} \rangle = \sqrt{2}d_0 \begin{pmatrix} \hat{z} & \hat{x} + i\hat{y} \\ \hat{x} - i\hat{y} & \hat{z} \end{pmatrix}$$

Here  $\hat{x}$ ,  $\hat{y}$ , and  $\hat{z}$  represent the dipole moment operator acting on different axes  $Q_x$ ,  $Q_y$ , and  $Q_z$ .  $d_0 = \frac{1}{\sqrt{6}} \int f Q_x X d\vec{r} = \frac{1}{\sqrt{6}} \int f Q_y Y d\vec{r} = \frac{1}{\sqrt{6}} \int f Q_z Z d\vec{r}$  represents the single nonzero dipole transition element in this system.

$$\langle \phi^{(6)} | Q | \phi^{(8)} \rangle = d_0 \begin{pmatrix} \sqrt{3}(\hat{x} + \hat{y}) & -2i\hat{z} & (\hat{x} - i\hat{y}) & 0 \\ 0 & i(\hat{x} + i\hat{y}) & 2\hat{z} & \sqrt{3}(\hat{x} - i\hat{y}) \end{pmatrix}$$

and

$$\langle \phi^{(7)} | Q | \phi^{(8)} \rangle = d'_0 \begin{pmatrix} -(\hat{x} - i\hat{y}) & 0 & \sqrt{3}(\hat{x} + i\hat{y}) & 2i\hat{z} \\ -2\hat{z} & i\sqrt{3}(\hat{x} - i\hat{y}) & 0 & -i(\hat{x} + i\hat{y}) \end{pmatrix}$$

Here the single nonzero dipole matrix element is  $d'_0 = \frac{-i}{\sqrt{6}} \int X Q_y Z d\vec{r} = \frac{-i}{\sqrt{6}} \int X Q_z Y d\vec{r} = \frac{-i}{\sqrt{6}} \int Z Q_y X d\vec{r} = \frac{-i}{\sqrt{6}} \int Z Q_x Y d\vec{r} = \frac{-i}{\sqrt{6}} \int Y Q_z X d\vec{r} = \frac{-i}{\sqrt{6}} \int Y Q_x Z d\vec{r}$  [100, 101]. The above formula yields the nonzero dipole transition matrix elements. We will utilize these results later when we calculate the second-order nonlinear susceptibilities  $\chi_{ijk}^{(2)}$ .

### 5.2.3 The mixture of states at the $\Gamma$ point

In our case, the depletion field is along the z-axis. The perturbation Hamiltonian  $H' = \vec{Q} \cdot \vec{E} = Q_z E$  depends only on  $Q_z$ , while  $E$  is treated as a constant. Only terms corresponding to the  $\hat{z}$  component in the above general transition matrices are considered. Thus,

$$\langle \phi^{(6)} | H' | \phi^{(7)} \rangle = \langle \phi^{(6)} | \vec{Q} \cdot \vec{E} | \phi^{(7)} \rangle = E \langle \phi^{(6)} | Q_z | \phi^{(7)} \rangle$$

$$\langle \phi^{(6)} | H' | \phi^{(8)} \rangle = \langle \phi^{(6)} | \vec{Q} \cdot \vec{E} | \phi^{(8)} \rangle = E \langle \phi^{(6)} | Q_z | \phi^{(8)} \rangle$$

$$\langle \phi^{(7)} | H' | \phi^{(8)} \rangle = \langle \phi^{(7)} | \vec{Q} \cdot \vec{E} | \phi^{(8)} \rangle = E \langle \phi^{(7)} | Q_z | \phi^{(8)} \rangle$$

Finally we find that all of the perturbation matrix elements depend linearly on the depletion electric field ( $E$ ). Utilizing first order perturbation theory, we find the states are mixed. As a result,  $|\phi_0^{(6)}\rangle_{+\frac{1}{2}}$  and  $|\phi_0^{(6)}\rangle_{-\frac{1}{2}}$  are modified as

$$|\phi^{(6)}\rangle_+ = ig_6 |\phi_0^{(8)}\rangle_{\frac{1}{2}} - h_6^* |\phi_0^{(7)}\rangle_{\frac{1}{2}} + |\phi_0^{(6)}\rangle_{\frac{1}{2}} \quad (5.25)$$

$$|\phi^{(6)}\rangle_- = g_6 |\phi_0^{(8)}\rangle_{-\frac{1}{2}} + h_6^* |\phi_0^{(7)}\rangle_{-\frac{1}{2}} + |\phi_0^{(6)}\rangle_{-\frac{1}{2}} \quad (5.26)$$

and the  $|\phi_0^{(7)}\rangle_{+\frac{1}{2}}$  and  $|\phi_0^{(7)}\rangle_{-\frac{1}{2}}$  become

$$|\phi^{(7)}\rangle_+ = -ig_7|\phi_0^{(8)}\rangle_{-\frac{3}{2}} + h_6|\phi_0^{(6)}\rangle_{\frac{1}{2}} + |\phi_0^{(7)}\rangle_{\frac{1}{2}} \quad (5.27)$$

$$|\phi^{(7)}\rangle_- = -g_7|\phi_0^{(8)}\rangle_{\frac{3}{2}} - h_6|\phi_0^{(6)}\rangle_{-\frac{1}{2}} + |\phi_0^{(7)}\rangle_{-\frac{1}{2}} \quad (5.28)$$

The coefficients  $(g_6, g_7, h_6)$  are derived from first-order perturbation theory.

$$g_6 = \frac{2d_0^*E}{E^6 - E^8} \quad (5.29)$$

$$g_7 = \frac{2d_0^*E}{E^7 - E^8} \quad (5.30)$$

$$h_6 = \frac{\sqrt{2}d_0E}{E^7 - E^6} \quad (5.31)$$

Here  $E^6, E^7,$  and  $E^8$  represent the energy levels of  $\Gamma^{(6)}, \Gamma^{(7)},$  and  $\Gamma^{(8)}$ .

In the case of the degenerate  $\Gamma_8$  states, we diagonalized the perturbation matrix in order to get first order perturbed states. A detailed calculation of this matrix under an arbitrary perturbation field has been presented in references 98 and 99. For simplicity, we need only consider the nondiagonalized matrix under a z-direction field perturbation, which can be written as

$$\langle \phi^{(8)} | Q_z | \phi^{(8)} \rangle = \begin{pmatrix} 0 & 0 & -i(d-d') & 0 \\ 0 & 0 & 0 & -i(d+3d') \\ i(d+3d') & 0 & 0 & 0 \\ 0 & i(d-d') & 0 & 0 \end{pmatrix}.$$

The elements  $d, d'$  are dipole transition elements and depend linearly on the depletion field  $E$ . By diagonalizing the matrix, we find that the top valence band state  $|\Gamma_8^{(0)}\rangle$  has been perturbed as

$$|\phi^{(8)}\rangle_1 = |\phi_0^{(8)}\rangle_{\frac{3}{2}} - q|\phi_0^{(8)}\rangle_{\frac{1}{2}} + q|\phi_0^{(8)}\rangle_{-\frac{1}{2}} + |\phi_0^{(8)}\rangle_{-\frac{3}{2}} \quad (5.32)$$

$$|\phi^{(8)}\rangle_2 = |\phi_0^{(8)}\rangle_{\frac{3}{2}} + q|\phi_0^{(8)}\rangle_{\frac{1}{2}} + q|\phi_0^{(8)}\rangle_{-\frac{1}{2}} - |\phi_0^{(8)}\rangle_{-\frac{3}{2}} \quad (5.33)$$

$$|\phi^{(8)}\rangle_3 = |\phi_0^{(8)}\rangle_{\frac{3}{2}} - q|\phi_0^{(8)}\rangle_{\frac{1}{2}} - q|\phi_0^{(8)}\rangle_{-\frac{1}{2}} - |\phi_0^{(8)}\rangle_{-\frac{3}{2}} \quad (5.34)$$

$$|\phi^{(8)}\rangle_4 = |\phi_0^{(8)}\rangle_{\frac{3}{2}} + q|\phi_0^{(8)}\rangle_{\frac{1}{2}} - q|\phi_0^{(8)}\rangle_{-\frac{1}{2}} + |\phi_0^{(8)}\rangle_{-\frac{3}{2}} \quad (5.35)$$

Here  $q = i\sqrt{\frac{d+3d'}{d-d'}}$ , which is independent of strength of the field. This suggests that under the first-order perturbation, the mixed states are independent of the depletion field magnitude. Therefore the ground states in second-order nonlinear optical transition processes can be treated as unperturbed states, i.e., the results are the same whether we choose the diagonalized wavefunctions (5.32-5.35) or the unperturbed wavefunctions (5.14-5.16) as our basis set.

#### 5.2.4 The perturbation of the second-order susceptibility

$$\chi_{yxz}^{(2)}$$

Generally second-order nonlinear optical processes are the summation of all possible multi-interband transitions. However, such complicated multi-transition processes can always be simplified by considering only the few these dominate resonance transition processes and treating the other nonresonance transition terms as a background. In particular, our pumping photon energy is near the band-gap of GaAs (see figure 5.2). As a result, the interband transitions are determined by the near one-photon resonance process at the  $\Gamma$  point of the Brillouin zone.

$$\chi_{ijk}^{(2)} : \Gamma_8 \xrightarrow{Q_k} \Gamma_6 \xrightarrow{Q_j} \Gamma_7 \xrightarrow{Q_i} \Gamma_8 \quad (5.36)$$

Here  $Q_i$ ,  $Q_j$ , and  $Q_k$  represent the dipole matrix elements for different polarizations. Utilizing the dipole transition matrix results in section 5.2.2, we calculated the non-zero transition paths of the near one-photon resonance processes in p-in/s-out configuration with the crystalline axis [100] sitting in the plane of incidence. In such case, crystal axes [100], [010], and [001] are the same as laboratory frame axes  $x$ ,  $y$ , and  $z$  respectively (see figure 5.3). Since we probed the bulk SHG contributions from  $\chi_{yxz}^{(2)} = \chi_{yzx}^{(2)}$ , the first step transition (from  $\Gamma_8$  to  $\Gamma_6$ ) involves either  $Q_x$  or  $Q_z$  electric dipole (see figure 5.3), and the last transition step (from  $\Gamma_7$  to  $\Gamma_8$ ) arises from electric dipole  $Q_y$ . The details of these calculations are presented in Appendix

Appendix C. Finally, the second-order perturbation term is:

$$\delta^2 \chi_{yxz}^{(2)} = \delta^2 \chi_{yzx}^{(2)} = \beta E^2 \quad (5.47)$$

with

$$\beta = \frac{4\sqrt{6}i}{(E^6 - E^8)(E^7 - E^6)} |d_0|^2 [-2|d_0|^2(d'_0 - d'^*_0) + d'^3_0 + |d'_0|^2 d'_0] \quad (5.48)$$

Since our fundamental photon energy is still below the band gap of GaAs, we consider our system a lossless medium, which means that the integrations inside the  $d_0$  and  $d'_0$ ,  $\int f Q_x X d\vec{r}$  and  $\int X Q_y Z d\vec{r}$ , are real positive numbers. Therefore the  $d_0$  ( $d'_0$ ) is purely real (imaginary) constant. As a result, the perturbation term  $\beta$  can be written as

$$\beta = -\frac{16\sqrt{6}}{(E^6 - E^8)(E^7 - E^6)} |d_0|^4 |d'_0|$$

Here  $\beta$  is a negative constant. By comparison with the original  $\chi_{yzx}^{(2),old}$ , the unperturbed second-order susceptibility can be written as

$$\chi_{yzx}^{(2),old} = -4i\sqrt{6}d_0^2 d'^*_0$$

Under the same lossless medium assumption,  $\chi_{yxz}^{(2),old}$  is a positive real constant.

$$\chi_{yxz}^{(2),old} = 4\sqrt{6}d_0^2 |d'^*_0|$$

Therefore the second-order perturbation  $\beta$  has a  $180^\circ$  phase difference with the original second-order susceptibility  $\chi_{yzx}^{(2),old}$ . This leads to a change in  $\chi_{yxz}^{(2)}$  that is *second-order* in  $E$ , i.e.

$$\chi_{yxz}^{(2),new} = \chi_{yzx}^{(2),new} = \chi_{yxz}^{(2),old} + \beta E^2 \quad (5.49)$$

Finally we find that the electric field induced perturbation will diminish the original nonzero second-order susceptibility  $\chi_{yzx}$ . We also examined corrections to other tensor elements of  $\chi^{(2)}$  which are initially zero in the electric dipole approximation (see Appendix D). We find that  $\chi_{zzz}^{(2)}$  is linearly proportional to the depletion electric field  $E$ .

### 5.3 SHG from the depletion region of GaAs

In the above section, we calculated the changes in the second-order susceptibility based on a three-level system. This result will elucidate the effect of depletion electric fields on harmonic generation in GaAs. The output SHG intensity is modified by an interference between the initial bulk second-order susceptibility  $\chi_{yzx}^{(2),old}$  and the small perturbation  $\delta^2\chi_{yzx}^{(2)}$  which depends quadratically on the depletion electric field. It can be written as

$$\frac{I^{2\omega}(E)}{(I^\omega)^2} \sim |\chi_{yzx}^{(2),old}|^2 + 2Re(\chi_{yzx}^{(2),old}\delta^2\chi_{yzx}^{(2)}) + |\delta^2\chi_{yzx}^{(2)}|^2 \quad (5.50)$$

Here  $I^\omega$  is the fundamental laser beam intensity, and  $I^{2\omega}(E)$  is the  $E$ -dependent SHG intensity. The lowest order change in SHG will depend linearly on the perturbation  $\delta\chi_{yzx}^{(2)} \sim \beta E^2$  and hence quadratically on  $E$ .

In general case,  $\chi_{yzx}^{(2),old}$  and  $\beta$  can be complex numbers. In such case, the dipole moments  $d_0$  and  $d'_0$  is

$$d_0 = |d_0|e^{i\phi} \quad (5.51)$$

$$d'_0 = |d'_0|e^{i\phi'}. \quad (5.52)$$

Here  $\phi$  ( $\phi'$ ) is the phase of the complex number  $d_0$  ( $d'_0$ ). Thus, the  $\chi_{yzx}^{(2),old}$  and  $\beta$  are given by Eq. 5.45 and 5.48

$$\chi_{yzx}^{(2),old} = -4i\sqrt{6}|d_0|^2|d'_0|e^{i(2\phi-\phi')} \quad (5.53)$$

$$\beta = \frac{4\sqrt{6}i}{(E^6 - E^8)(E^7 - E^6)}|d_0|^2[-4i|d_0|^2|d'_0|\sin\phi' + |d'_0|^3(e^{3i\phi'} + e^{i\phi'})] \quad (5.54)$$

As discussed previously, since the fundamental light energy is near but below the band gap, our system can be treated as an optical lossless medium. In such case  $d_0$  ( $d'_0$ ) is real (imaginary), which means that  $\phi = 0$  and  $\phi' = \frac{-\pi}{2}$  (see section 5.2.2). As a result, the  $\chi_{yzx}^{(2),old}$  ( $\beta$ ) is positive (negative). Therefore the field induced perturbation diminish the original second-order susceptibility  $\chi_{yzx}^{(2),old}$ .

In general cases, the  $\beta$  and  $\chi_{yz}^{(2),old}$  can have a phase difference  $\Phi$ , which is determined by the following formula

$$|\chi_{yz}^{(2),old}\beta|e^{i\Phi} = \frac{96|d_0|^4|d'_0|}{(E^6 - E^8)(E^7 - E^6)} e^{i(2\phi - \phi')}[-4i|d_0|^2|d'_0|\sin\phi' + |d'_0|^3(e^{3i\phi'} + e^{i\phi'})]. \quad (5.55)$$

All these calculations are based on three-level model and fundamental light energy is near the band gap. On the other hand, we must consider transitions among other energy bands when the near resonance condition is not satisfied. For example,  $\chi_{yz}^{(2)}$  may contain a summation of several different transition paths,

$$\begin{aligned} \chi_{ijk}^{(2)} : & \quad \Gamma_8 \xrightarrow{Q_k} \Gamma_6 \xrightarrow{Q_j} \Gamma_7 \xrightarrow{Q_i} \Gamma_8 \\ & + \Gamma_8 \xrightarrow{Q_k} \Gamma_7 \xrightarrow{Q_j} \Gamma_6 \xrightarrow{Q_i} \Gamma_8 \\ & + L_4 \xrightarrow{Q_k} L_6 \xrightarrow{Q_j} L_6 \xrightarrow{Q_i} L_4 \\ & + X_7 \xrightarrow{Q_k} X_6 \xrightarrow{Q_j} X_7 \xrightarrow{Q_i} X_7 \\ & + \dots \end{aligned} \quad (5.56)$$

Here X and L represent the transitions at the X and L points of the Brillouin zone respectively. In such cases, the field induced perturbation can no be explained by this simple three-level model.

The assumption of a constant depletion field largely simplified our theoretical calculations. Considering an nonconstant depletion field  $E(z)\hat{z}$ , all the first order perturbation coefficients ( $g_6, g_7, h_6$ ) are changed to (see section 5.2.3)

$$g_6 \sim \frac{\langle \phi^{(6)} | Q_z E(z) | \phi^{(8)} \rangle}{E^6 - E^8} \quad (5.57)$$

$$g_7 \sim \frac{\langle \phi^{(7)} | Q_z E(z) | \phi^{(8)} \rangle}{E^7 - E^8} \quad (5.58)$$

$$h_6 \sim \frac{\langle \phi^{(6)} | Q_z E(z) | \phi^{(7)} \rangle}{E^7 - E^6} \quad (5.59)$$

In this case, the perturbation matrix elements are not in the dipole approximation, and high-order z-dependent elements are involved. As a result, the mixture of states

at the  $\Gamma$  point becomes more complicated. For example, the mixed state  $|\phi_0^{(6)}\rangle_{+\frac{1}{2}}$  in Eq. 5.25 contains not only  $|\phi_0^{(8)}\rangle_{\frac{1}{2}}$ ,  $|\phi_0^{(7)}\rangle_{\frac{1}{2}}$ , and  $|\phi_0^{(6)}\rangle_{\frac{1}{2}}$ , but also all other states. More states mixture results in more transition paths in comparison of the results in constant field case. As a result complicated phase relation between the  $\chi_{yxz}^{(2),old}$  and  $\beta$  is expected.

In summary, our theoretical calculation indicates that second-order nonlinear susceptibility is perturbed by the depletion electric fields. If we modulate such a depletion field by a second light source (e.g. a lamp), the SHG signals will be very sensitive to variations in the field. The perturbation of SHG signals is directly related to the surface states' properties, such as surface trap lifetime and carrier diffusion properties. We also examined corrections to other tensor elements of  $\chi^{(2)}$  which are initially zero in the electric dipole approximation. In many cases the corrections  $\delta\chi^{(2)}$  (such as  $\delta\chi_{zzz}^{(2)}$ ), are proportional to  $E$ . However, because there is no interference term, these changes are much more difficult to detect. More data is presented in chapter 6.

$T_d$	$E$	$8C_3$	$3C_2$	$6S_4$	$6\sigma_d$
$\Gamma_1$	1	1	1	1	1
$\Gamma_2$	1	1	1	-1	-1
$\Gamma_3$	2	-1	2	0	0
$\Gamma_4$	3	0	-1	1	-1
$\Gamma_5$	3	0	1	-1	1

Table 5.1: Character table of  $T_d$

$T_d$	Basis functions
$\Gamma_1$	$x^2 + y^2 + z^2$
$\Gamma_2$	$x^4(y^2 - z^2) + y^4(z^2 - x^2) + z^4(x^2 - y^2)$
$\Gamma_3$	$2z^2 - x^2 - y^2, \sqrt{3}(x^2 - y^2)$
$\Gamma_4$	$x(y^2 - z^2), y(z^2 - x^2), z(x^2 - y^2)$
$\Gamma_5$	$x, y, z$

Table 5.2: Basis functions of  $T_d$

$\Gamma_1$	$\Gamma_2$	$\Gamma_3$	$\Gamma_4$	$\Gamma_5$	
$\Gamma_1$	$\Gamma_2$	$\Gamma_3$	$\Gamma_4$	$\Gamma_5$	$\Gamma_1$
	$\Gamma_1$	$\Gamma_3 + \Gamma_5$	$\Gamma_4$	$\Gamma_2$	$\Gamma_2$
		$\Gamma_1 + \Gamma_2 + \Gamma_3$	$\Gamma_4 + \Gamma_5$	$\Gamma_4 + \Gamma_5$	$\Gamma_3$
			$\Gamma_1 + \Gamma_3 + \Gamma_4 + \Gamma_5$	$\Gamma_2 + \Gamma_3 + \Gamma_4 + \Gamma_5$	$\Gamma_4$
				$\Gamma_1 + \Gamma_3 + \Gamma_4 + \Gamma_5$	$\Gamma_5$

Table 5.3: Direct product of  $T_d$

$\Gamma_6$	$\Gamma_7$	$\Gamma_8$	
$\Gamma_6$	$\Gamma_7$	$\Gamma_8$	$\Gamma_1$
$\Gamma_7$	$\Gamma_6$	$\Gamma_8$	$\Gamma_2$
$\Gamma_8$	$\Gamma_6$	$\Gamma_6 + \Gamma_7 + \Gamma_8$	$\Gamma_3$
$\Gamma_6 + \Gamma_8$	$\Gamma_7 + \Gamma_8$	$\Gamma_6 + \Gamma_7 + 2\Gamma_8$	$\Gamma_4$
$\Gamma_7 + \Gamma_8$	$\Gamma_6 + \Gamma_8$	$\Gamma_6 + \Gamma_7 + 2\Gamma_8$	$\Gamma_5$
$\Gamma_1 + \Gamma_4$	$\Gamma_2 + \Gamma_5$	$\Gamma_3 + \Gamma_4 + \Gamma_5$	$\Gamma_6$
	$\Gamma_1 + \Gamma_4$	$\Gamma_3 + \Gamma_4 + \Gamma_5$	$\Gamma_7$
		$\Gamma_1 + \Gamma_2 + \Gamma_3 + 2\Gamma_4 + 2\Gamma_5$	$\Gamma_8$

Table 5.4: Direct product of  $\bar{T}_d$

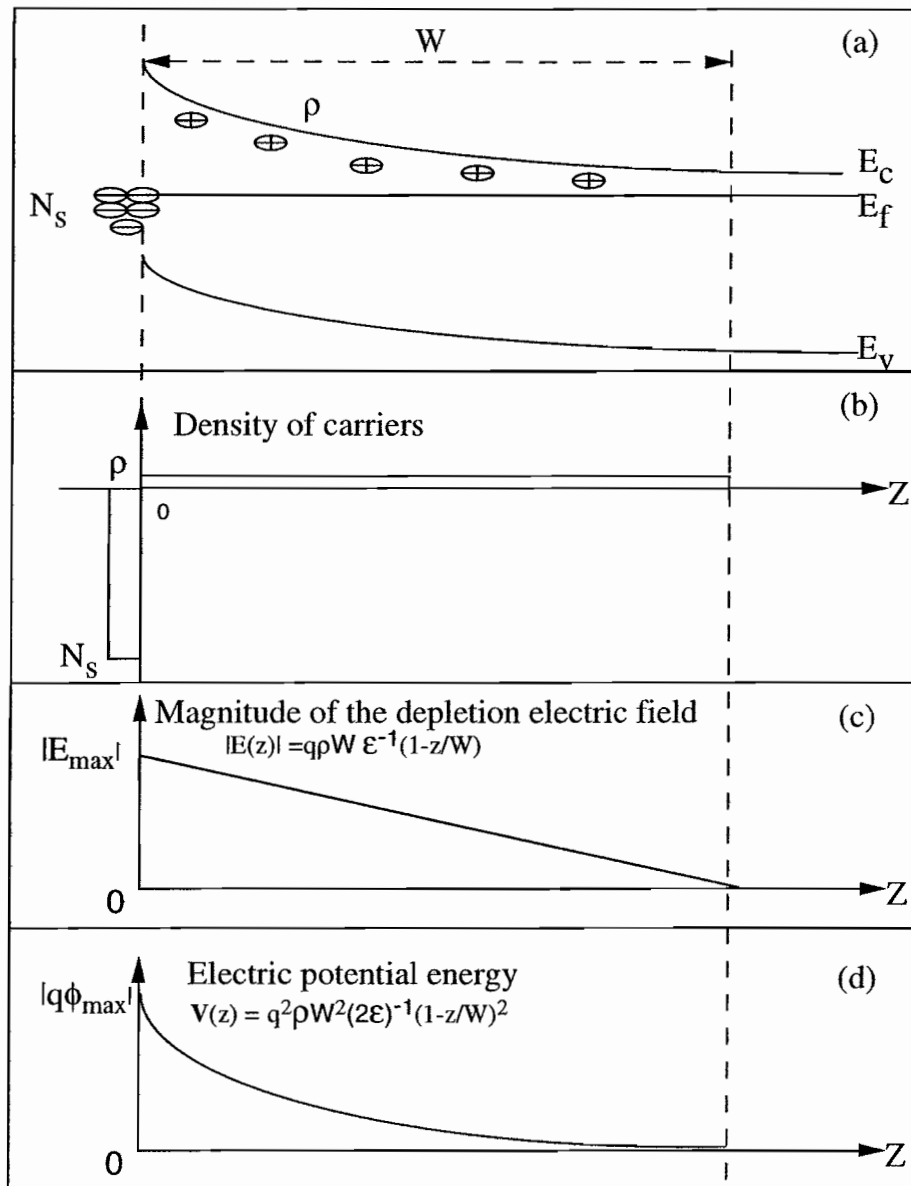


Figure 5.1: Schematic drawing of the band-bending profile for an n-type semiconductor within the depletion region.  $E_c$ ,  $E_v$ , and  $E_f$  represent conduction band, valence band, and Fermi level respectively.  $N_s$ ,  $\rho$  refer to surface charge density and ionized doping density respectively. More details are in text. By assuming the depletion approximation and a uniform doping density, the magnitude of the depletion electric field and the potential energy for electrons are plotted as a function of the distance from the surface.

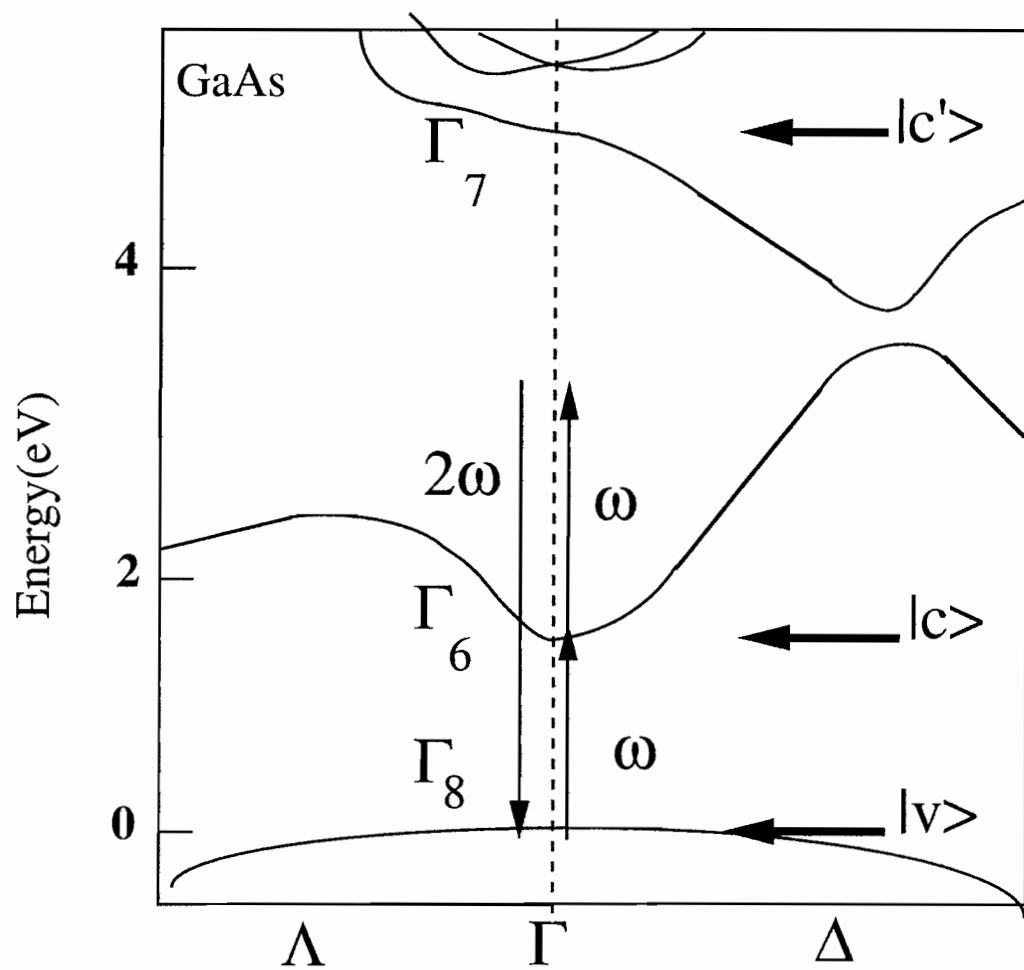


Figure 5.2: Schematic diagram of the second harmonic process at the  $\Gamma$  point of the Brillouin zone in GaAs. The fundamental photon energy is near the band gap energy, i.e.  $\hbar\omega \sim E_{\Gamma_6} - E_{\Gamma_8}$ .

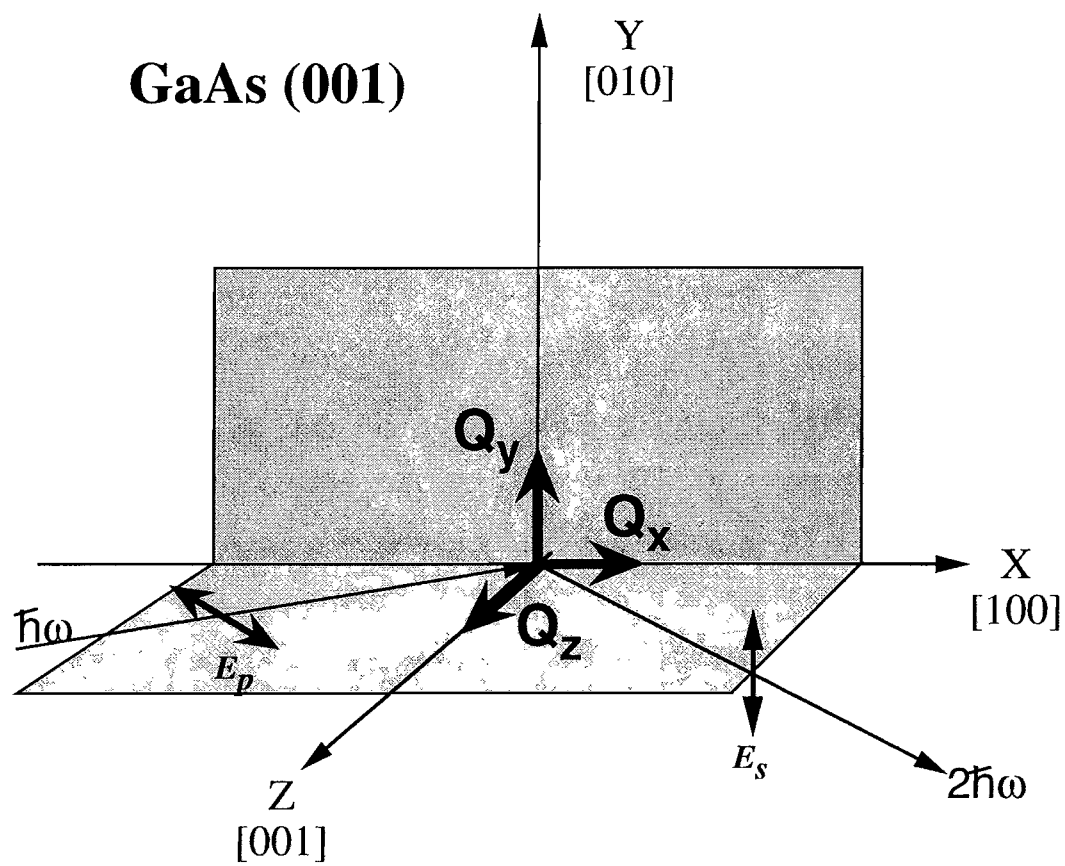


Figure 5.3: Schematic drawing of the electric dipole elements ( $Q_x$ ,  $Q_y$ ,  $Q_z$ ) with respect to the crystal orientation and light polarizations.

## Chapter 6

# Measurements of depletion electric field effects on SHG

Our experiments reveal that the dominant perturbation caused by the depletion electric field is on the *existing bulk* nonlinearity  $\chi_{yxz}^{(2)}$ . Through studies of  $\chi_{yxz}^{(2)}$  as a function of dopant type and concentration, we demonstrate that the bulk  $\chi_{yxz}^{(2)}$  is systematically reduced as a result of the depletion field, and that this diminution depends on the square of the near surface depletion field[40]. This is consistent with our theoretical calculations.

Furthermore, photomodulation-second-harmonic generation (PSHG) experiments reveal that  $\chi_{yxz}^{(2)}$  in *doped* GaAs can be *enhanced* by carrier excitation in the depletion region. Utilizing this technique, we have measured the surface minority trap lifetime. Finally, spatially separated second-harmonic generating and photocarrier-exciting light beams were employed to study transverse diffusion of carriers confined near GaAs(001) surfaces[41]. All of these experiments were performed on GaAs(001) samples with native oxide surfaces ( $\sim 50 \text{ \AA}$  in air).

## 6.1 SHG from the depletion region

In the p-in/s-out polarization configuration, with the crystalline [100] axis parallel to the plane of incidence[17], the output SHG intensity from  $\chi_{yxz}^{(2)}$  is maximized (see figure 6.1). More importantly, in this polarization configuration the detected SHG intensity is insensitive to the higher order contributions from the bulk magnetic dipole and electric quadrupole transitions[47]. The experimental details have been described in chapter 3. A 10 Hz Nd:YAG pumped dye laser was used as the fundamental light source for SH measurements. The photon energy of the fundamental laser beam was chosen to be near the band gap of GaAs so that the dominant contribution to the second-order susceptibility  $\chi_{yxz}^{(2)}$  arose mainly from transitions between the top valence band  $|v\rangle$  and the two lowest conduction bands  $|c\rangle$  and  $|c'\rangle$  at the  $\Gamma$  point in the Brillouin zone[50] (see figure 5.2).

GaAs(001) samples were doped with Si (n-type) and Be (p-type), and were grown on an undoped GaAs substrate by molecular-beam epitaxy. All samples were As-terminated and exhibited a  $2 \times 4$  RHEED pattern. Details of sample growth are presented in chapter 4. As is usually the case, surface defect electronic states (traps) pin the material Fermi level leading to near surface band bending[5]. This strong electric field is produced along the crystalline [001] direction. The depletion length of our samples was between  $0.1 \mu\text{m}$  and  $3.0 \mu\text{m}$  depending on the doping levels. With the exception of the most highly doped samples, the SHG penetration depth of  $\sim 0.1 \mu\text{m}$  was substantially less than the sample depletion length. The primary variation from sample to sample was the near surface depletion electric field,  $E$ , which scaled with doping density  $\rho$  (i.e.  $E \sim \sqrt{\rho}$ ).

The variation of SHG intensity at 2.68 eV as a function of doping density is displayed in figure 6.2. At this energy, the escape depth of a SHG photon is less than or comparable to the depletion width in all of our samples. Therefore, it is reasonable to assume that the detected SHG signal was generated within the depletion region. Since the fundamental light energy was below the band-gap of

GaAs, the depletion field modulation by the fundamental beam was small. Our data clearly demonstrates that the SHG intensity of both n- and p-type samples decreases as a function of increasing doping densities. This picture is in agreement with our theoretical expectations.

With the constant depletion field approximation, the electric field in the depletion region can be written

$$E = 4\pi\sqrt{(2\pi)^{-1}\epsilon\phi\rho/\epsilon},$$

where  $\epsilon$  is the dielectric constant of GaAs. The second-order susceptibility, perturbed by this depletion field, is of the form (see chapter 5),

$$\chi_{yxz}^{new} = \chi_{yzx}^{new} = \chi_{yxz}^{old} + \beta E^2 \quad (6.1)$$

Using Eq. 6.1 the relationship between the SHG intensity  $I_{2\omega}(E)$  and the doping density has the form:

$$I_{2\omega,0} - I_{2\omega}(E) \sim 2|\text{Re}(\chi_{yxz}^{old}\beta\rho)| = C\rho$$

Here  $I_{2\omega,0}$  is the SHG intensity in the limit of small  $\rho$  (i.e.  $I_{2\omega,0} \sim |\chi_{yxz}^{old}|^2|I_\omega|^2$ ), and  $C$  is a constant. The solid lines in figure 6.2 represent the best fits to our experimental results using this model with  $I_{2\omega,0}$  and  $C$  as free parameters. In figure 6.3, we demonstrate the linear (quadratic) relationship between the SHG intensity and dopant density (electric field) at low dopant concentration.

The deviations between our theoretical model and experimental results at high dopant density result from the fact that the SHG penetration depth is comparable to the depletion length, and thus the position dependence of the electric field must be considered. In addition, it is possible that the density of majority carriers in highly doped samples exceeded the maximum number density of surface states. In this case the electric field at the surface will reach a maximum value, independent of dopant density. Both effects produce a saturation of the reduction in SHG at high doping levels.

## 6.2 Photomodulation the depletion field

Since the changes in GaAs bulk SHG signals are produced via the strong electric field and band-bending near the surface, any perturbation of the depletion electric field should affect the SHG signal from this depletion region. We can accomplish this by weakly photoexciting carriers in the sample[103]. In our experiments the sample was illuminated by light from either a Tungsten lamp/monochromator or an  $Ar^+$  ion laser, *while the SHG experiment was in progress* (see figure 6.4). The photon energy of the photomodulation light was set at 2.72 eV where the absorption length ( $\sim 0.1 \mu m$ ) is within the depletion region[104]. Experimentally, an *enhancement* of the second-harmonic intensity has been observed for both n- and p-type samples as a result of light illumination (see figure 6.5).

The microscopic mechanism of enhancement in the photoexcitation-second-harmonic generation experiments can be described as follows. The linear photoexcitation creates electrons and holes in the depletion region. These carriers are separated by the built-in field and, as a result, partly neutralize the surface charge (see figure 6.6). This in turn decreases the depletion electric field and the band bending as follows,

$$\vec{E}_{on} = \vec{E}_0 + \delta\vec{E}$$

Here  $\vec{E}_0$  is the depletion field without photoexcitation light.  $\delta E$  is the variation of the depletion field generated by the photoexcitation light ( $\frac{\delta E}{E_{on}} < 0$ ). Thus  $|\delta\chi_{yxz}^{(2)}|$  becomes smaller, and the enhancement of the SHG signal can be written as

$$\begin{aligned} I_{2\omega,on} &= |\chi_{yxz,0} + \beta E^2|^2 I_\omega^2 & (6.2) \\ &= |\chi_{yxz,0} + \beta E_0^2 + 2\beta E_0 \delta E + \beta \delta E^2|^2 I_\omega^2 \\ &\sim |\chi_{yxz,0} + \beta E_0^2 + 2\beta E_0 \delta E|^2 I_\omega^2 \end{aligned}$$

Here  $I_{2\omega,on}$  is the SHG signal with the photoexcitation light illuminating the sample. Note, we neglect the higher order term  $\beta \delta E^2$ . Since the SHG signal  $I_{2\omega}$  without

photoexcitation light is

$$I_{2\omega} = |\chi_{yxz,0} + \beta E_0^2| I_{\omega}^2,$$

the variation in the ratio of SHG with the photoexcitation light is

$$\frac{I_{2\omega,on}}{I_{2\omega}} = |1 + \alpha \delta E|^2$$

with

$$\alpha = (2\beta E_0) / (\chi_{yxz,0} + \beta E_0^2).$$

Our experimental observations again confirm our theoretical model. The saturation of SHG enhancement with respect to photoexcitation intensity has been found for all of the samples. Qualitatively the saturation of SHG enhancement is expected to be related to the density of the surface states (traps) and their lifetime.

Furthermore, photoexcitation-second-harmonic generation as a function of the fundamental photon energy was studied (see figure 6.7). First, our spectrum reveals that the enhancement of SHG by photoexcitation light diminished when the fundamental photon is above the band gap. This effect can be explained as follows: When the fundamental photon energy is greater than the band gap, the electrons and holes can be excited by the fundamental SH light beam. As a result, depletion electric field and the band bending even without the photoexcitation light, are decreased. Since our fundamental light (10 Hz) fluence of  $\sim 5 \text{ mJ/cm}^2$  per pulse is much stronger than the saturation intensity of the photoexcitation light, the enhancement of SHG was already saturated without the photoexcitation light. Second, the spectrum shows that enhancements of SHG by photoexcitation light is weak as the fundamental photon energy moves away from the one photon resonance between the states  $\Gamma_8$  and  $\Gamma_6$ . We explain this effect as follows. In the theoretical calculations, the second-order nonlinear optical process is dominated by the three band states at the  $\Gamma$  point in the Brillouin zone. This is true only if the fundamental photon energy is near the band gap of GaAs. In that case, the dominant contribution to the second-order susceptibility  $\chi_{yxz}^{(2)}$  arises mainly from the transitions between the

top valence band  $|\Gamma_8\rangle$  and the two lowest conduction bands  $|\Gamma_6\rangle$  and  $|\Gamma_7\rangle$  at the  $\Gamma$  point in the Brillouin zone[50]. The other transitions may be considered to be background. However, this is not true when the fundamental photon energy differs from the band gap of GaAs. In the latter case all other terms at other points in the Brillouin zone must be considered in the field perturbation calculation.

### 6.3 Surface trap lifetime

We have performed time dependent measurements to follow the *decrease* of the SHG intensity after the photomodulation light is turned off. This is a direct measurement of the surface state (trap) *discharging* time[33]. Here *discharging* refers to the removal of minority carriers from the the surface traps. The measurements were carried out by illuminating the sample for at least 2 minutes, turning off the lamp, and monitoring the SH signal as a function of time.

A typical time-dependent SHG signal for a p-doped (n-doped)  $10^{16}/cm^3$  sample is plotted as a function of time in figure 6.8 (figure 6.9). The solid line is our best fit to the experimental results based on a simple carrier recombination and generation model which is described in Appendix E. The SHG signal as a function of time  $t$  is written as

$$I_{2\omega}(t) = (A + Be^{-\frac{t}{\tau}})^2$$

with

$$A = [\chi_{yxz,0} + \beta E_0^2] I_\omega$$

$$B = \frac{4\pi\beta E_0 P_0}{\epsilon} I_\omega.$$

Here  $I_\omega$  represents the fundamental SH light intensity, and  $\tau$  is the trap lifetime.  $P_0$  is the photoexcited surface minority carrier density when the sample was illuminated for a long time and then the photomodulating lamp source was turned off at  $t = 0$ . Although samples with different doping densities have much different depletion widths, all of our samples exhibit approximately the same discharging time ( $\sim 25$

seconds). Since the characteristic time for carrier trapping on the surface states is much longer than the time it takes a carrier to pass through the depletion region ( $\sim 10^{-8}$  second), this suggests that the surface recombination process is the slowest step in discharging traps on the surface. Thus the rate limiting step for discharging arises primarily from the surface trap lifetime. Our experimental results suggest that the surface trap lifetime is similar in all samples.

Microscopically minority carriers excited within the depletion region drift to surface, and are trapped quickly by interfacial defects in a time  $\tau_c$  ( $10^{-6}$  to  $10^{-10}$  seconds)[77]. Since the depletion field separates electrons and holes in space, the trapped photoexcited minority carriers has such a long lifetime at the surfaces. Before recombining and leaving the surface however, these carriers can be excited thermally from the traps into free carrier states near the surface.

The thin oxide film ( $\sim 50 \text{ \AA}$ ) are primarily composed of  $Ga_2O_3$  and a small amount  $As_2O_3$  [105], since  $As_2O_3$  is volatile in the air.  $Ga_2O_3$  has a band gap of 4.7 eV [106]. At  $Ga_2O_3$ :GaAs interface, the oxide layer acts as a quantum barrier for both electrons and holes (see figure 6.10) [105, 106, 107]. Therefore these photoexcited carriers which were trapped by surface states primarily localized at the GaAs side of the interfacial region.

In addition, these experiments indicated that we basically measured the surface trapped carriers with cw photomodulation light. If the photomodulation light is a short pulse ( $\sim ps$ ) which can excite large density of free carriers to modulate the surface band-bending during such short period, this depletion field modulation can also be probed by SHG techniques. In contrast to the cw modulation light, the modulation of the depletion field is a time-dependent modulation, and depends on photoexcited free carriers.

## 6.4 Surface minority carrier diffusion

In this section we present measurements of minority carrier diffusion near the *surface* of GaAs utilizing the PSHG technique [83]. Our measurements suggest that surface charge transport is isotropic and diffusive, with small diffusion coefficients relative to the bulk[4]. It is proposed that these differences arise via the effects of charge traps and near surface charge recombination. Further temperature dependent measurements indicate that charge traps play a prominent role in the diffusion of both holes and electrons.

### 6.4.1 Spatially separated photoexcitation and SHG experiments

In our experiment we do not use electrical contacts; instead we use spatially separated photocarrier exciting and second-harmonic generating (SHG) light beams to study charge transport (see figure 6.11). The cw laser beam creates surface charge by the photoexcitation and drift of minority carriers in the GaAs depletion field. This *additional* surface charge diminishes the depletion electric field within the excitation beam waist, and the depletion field outside the beam waist is modified due to diffusion of these carriers. A second, *spatially separated* SHG beam probes surface charge transport. We utilize the above photoexcitation-second-harmonic generation effect, whereby near-surface second harmonic generation in GaAs is modulated by surface charge density changes, to map out the spatial distribution of the photoexcited surface carriers. Because of the substantial band bending near the interface, the minority carriers are constrained to move near (within 10 nm) the surface plane of the sample[75] (see Appendix F). As mentioned before, the oxide layer acts as a quantum barrier for both electron and holes. Therefore diffusion takes place primarily in the GaAs side surface plane.

A dye-laser beam at 925 nm (1.34 eV), with  $\sim 50 \mu\text{m}$  sample spot size, was used

as the fundamental SHG generating source for these measurements. The energy per pulse was  $\sim 50 \mu J$ . An  $Ar^+$  ion laser operating at  $457nm$  ( $2.782 eV$ ), and with intensity of  $300\mu W/cm^2$ , was used as a cw photocarrier excitation beam. The transverse excitation beam profile on the sample was a narrow rectangle ( $\sim 2.5 cm$  long,  $\sim 4 mm$  wide) with sharp ( $\leq 50 \mu m$ ) edges on all sides. The long edge of the excitation beam was made parallel to the sample  $[010]$  axis.

Photoexcited carriers will diffuse out of this excitation region parallel to the GaAs surface plane. The geometry of the photoexcitation beam restricts the spatial charge variation to one dimension, i.e., normal to the photoexcitation beam line (see figure 6.11). We assume that charge motion is well approximated by a diffusion equation under these circumstances,

$$D_{eff} \nabla_x^2 \sigma - \frac{\sigma}{\tau} = 0$$

then the variation of the surface charge density,  $\sigma$  (photoexcitation generated minority carrier), as a function of distance,  $x$ , along the  $[100]$  axis ( $x = 0$  defines the edge of the photocarrier excitation beam) is given by,

$$\sigma(x) = \sigma_0 e^{-\frac{x}{L}}, \quad (x > 0) \quad (6.3)$$

Here the diffusion length  $L = \sqrt{D_{eff}\tau}$  depends on the effective carrier diffusion coefficient  $D_{eff}$ , and lifetime  $\tau$ , near the surface.  $\sigma_0$  is the photoexcited minority carrier surface density at the edge of the photoexcitation beam. In our analysis of the diffusion process, we make the standard electrical neutrality assumption[108]. That is, we neglect the effects of the internal electric field due to the photoexcited minority carriers (see Appendix G). Experimentally we checked this assumption by studying charge diffusion as a function of excitation beam width (which was varied from  $2 mm$  to  $5 mm$ ). By changing the beam width, we are effectively changing the transverse electric field due to minority carriers. No variation in diffusion was observed within our experimental error of  $\sim 2\%$ .

In this particular experiment, our GaAs(001) samples were doped with Si (n-type) and Be (p-type) at low density ( $10^{16}cm^{-3}$ ). The escape depth of the SHG

output photon at 2.68 eV was  $\sim 0.1 \mu m$ , less than the depletion width in all of our low doping samples, so we approximate the near surface depletion electric field as a constant over this escape depth. As a result of the minority carrier diffusion, the depletion electric-field *along* the [001] direction (normal to sample surface) is perturbed by the minority carriers, i.e.,

$$\delta\mathbf{E}(x) \sim \frac{\sigma(x)}{\epsilon}, \quad (x > 0). \quad (6.4)$$

Here  $\delta\mathbf{E}$  represents the change in depletion electric field due to photoexcited minority carriers. The variation of our SHG output intensity  $I_{2\omega,on}$  as a function of the distance,  $x$ , from the photoexciting beam edge can be written as [41];

$$\frac{I_{2\omega,on}}{I_{2\omega}} \sim |1 + \alpha' e^{-\frac{x}{L}}|^2$$

$$(x > 0)$$

$I_{2\omega,on}$  ( $I_{2\omega}$ ) represents the SHG intensity measured when the photoexciting beam is on (off).  $\alpha'$  is a constant that depends on dipole transition matrix elements and the unperturbed depletion electric field. Because the probe beam spot size is around  $50 \mu m$ , much less than the observed minority carrier diffusion *length*, the surface minority carrier density *within* the probe beam spot was approximately constant.

The observed variation of the SHG enhancement ( $I_{2\omega,on}/I_{2\omega}$ ) as a function of distance  $x$  from the excitation beam edge is plotted in figure 6.12 for an n-type sample and a p-type sample. The solid lines represent our best fits to the data. In the case of n-type (p-type) samples, the variation of surface charge density is due to photoexcited holes (electrons). In all cases, the diffusion model appears to account for our observations. The diffusion *length* of the electrons is larger than that of the holes. From a fit of the data we determined the hole (electron) diffusion *length*  $L_h$  ( $L_e$ ) to be  $2.83 \pm 0.09 \text{ mm}$  ( $7.01 \pm 0.13 \text{ mm}$ ) at room temperature. Interestingly, the observed surface diffusion lengths are at least one order of magnitude larger than pure bulk carrier diffusion lengths[4]. Further experiments revealed that the

photoexcited carrier diffusion processes were isotropic in the surface plane. For example, we rotated the sample through an angle  $\phi$  ( $0^\circ \leq \phi \leq 90^\circ$ ) about the [001] axis. No variation in diffusion was observed under these circumstances.

### 6.4.2 Mechanism for surface minority carrier diffusion

We considered three possible mechanisms for the surface carrier diffusion: (1) free carriers diffusing in near surface bands; (2) activated free carriers diffusing and trapping between bands and localized states (see figure 6.13 and 6.14); and (3) variable-range hopping (VRH) or fixed-range hopping (FRH) of trapped carriers. Several pieces of evidence enable us to rule out *pure* free carrier diffusion. First, the ratio of electron and hole surface diffusion coefficients derived from diffusion *length* and lifetime measurements, i.e.  $\frac{D_e}{D_h} \sim (\frac{L_e}{L_h})^2 \sim 6$ , is nearly three times smaller than the bulk ratio, ( $\frac{D_e^{bulk}}{D_h^{bulk}} \sim 22$ )[4].

Furthermore we measured these diffusion coefficients as a function of temperature from  $\sim 250 - 350 K$  for both n- and p-type samples. Typical SHG results at two different temperatures in n-type GaAs are plotted in figure 6.15. We observed an *increase* of the diffusion length at higher temperatures. This suggests that the surface carrier diffusion process is not a result of purely free carrier motion in the near surface bands, but is some sort of thermally activated process. Finally, since the surface acts like a *sink* for free minority carriers, it is unlikely that purely free carriers would exist near the surface for long periods of time[109].

A priori there are several mechanisms that can be invoked to explain our temperature dependent results. One possible mechanism for near surface minority carrier diffusion is an activated diffusion process which may involve free carriers. In such a model (see of figure 6.13), minority carriers excited within the depletion region drift to the surface, and are quickly trapped by interfacial defects in a time  $\tau_c$  ( $10^{-6}$  to  $10^{-10}$  seconds)[109]. Before recombining and leaving the surface however, these carriers can be excited thermally from the traps into free carrier states near the surface.

Let  $\tau_e$  represent the average time a trapped carrier resides in a trap before it is thermally excited into a surface free carrier state. Thermally excited free carriers will *diffuse* along the surface until they become trapped again (usually  $\tau_c \ll \tau_e$ ). The effective diffusion coefficient of the “quasi-free” carriers will depend on the trapping time ( $\tau_c$ ), the excitation time to reexcite thermally out of the trap ( $\tau_e$ ), and the scattering time of the free carrier in the near surface bands  $\tau_s$  (usually  $\tau_s \ll \tau_c$ ). A simple analysis demonstrates that the effective diffusion coefficient is (see Appendix H)

$$D_{eff} \sim (v_{free})^2 \frac{\tau_s \tau_c}{\tau_e + \tau_c}.$$

Here  $v_{free}$  is the free carrier velocity in the near surface bands.  $v_{free}$  depends on the effective mass of the near surface minority carrier. We see that the role of traps is primarily to *reduce* the amount of time an electron or hole spends as a free carrier. Since the SHG signal is only sensitive to the depletion electric field, carriers affect the SHG signal in the same way whether trapped or free. We anticipate that a substantial amount of trap excitation/deexcitation occurs during the carrier lifetime,  $\tau$ , near the surface. In the case of  $\tau_c \ll \tau_e$ , we expect  $v_{free} \sim \sqrt{T}$ , and  $\tau_s \sim T^m$  where  $m$  is a constant. The temperature-dependence of the effective diffusion coefficient in this model is of the form

$$D_{eff} = aT^n e^{(-E/kT)} \quad (6.5)$$

Here  $a$  and  $n$  are constants, and  $k$  is the Boltzman constant.  $E$  is the energy difference between trap states and the free carrier band (conduction band for p-type and valence band for n-type). Experimental data and fits for typical n-type GaAs are plotted in figure 6.16. In summary, using this model we found that  $n = -0.1$  ( $-0.04$ ), and  $E = 21meV$  ( $17meV$ ) for n-type (p-type) samples. Errors were  $\sim 5\%$ . This model suggests that shallow trap states just below the conduction band(p-type samples) or above the valence band(n-type samples) affect the carrier diffusion process.

### 6.4.3 Other possible diffusion processes

Let us consider the other possible diffusion process involving hopping of carriers from trap to trap. The most common theories of this sort are variable-range hopping (VRH) and fixed-range hopping (FRH) between localized traps [110]. In the case of variable-range hopping (VRH), the diffusion coefficient  $D_{eff}$  is predicted to be temperature-dependent and of the form

$$D_{eff} \sim e^{-(T_0/T)^s}$$

Here  $T_0$  is a positive constant. The exponent  $s$  is  $1/3$  ( $1/4$ ) in two-dimensional (three-dimensional) systems [111]. A plot of  $\ln(D_{eff})$  as a function of  $T^{-s}$  with  $s = 1/3$  for a typical n-type GaAs sample is shown in figure 6.17(a). The solid line is our best fit to the VRH model.

In the model of fixed-range hopping (FRH) model, the diffusion coefficient has the form

$$D_{eff} \sim e^{(-E/kT)}$$

A typical plot of  $\ln(D_{eff})$  as a function of  $T^{-1}$  for typical n-type GaAs is shown in figure 6.17(b). In this case we find the excitation energy  $E$  to be  $19 \text{ meV}$  ( $16 \text{ meV}$ ) for n-type (p-type) samples. The latter result gives an activation energy quite similar to our first model involving free carrier activation and trapping.

Our temperature-dependent data are insufficient to distinguish between the latter three possible carrier diffusion mechanisms, but clearly demonstrate that the *bulk free carrier* mechanisms are unlikely. Recalling the relationship between the diffusion length, the diffusion coefficient, and the carrier recombination time, i.e.

$$L = \sqrt{D_{eff}\tau}$$

we find that the effective diffusion coefficient is  $2 \times 10^{-2} \text{ cm}^2/\text{second}$  ( $3 \times 10^{-3} \text{ cm}^2/\text{second}$ ) for electrons (holes). By comparison, bulk GaAs at the same doping density has a the bulk diffusion coefficient,

$$D^{bulk} \sim (v_{free}^{bulk})^2 \tau_s^{bulk}$$

of  $220 \text{ cm}^2/\text{second}$  ( $10 \text{ cm}^2/\text{second}$ ) for electrons (holes)[4]. The bulk diffusion coefficient is three-orders of magnitude larger than the effective diffusion coefficients obtained near the surfaces. Furthermore, the ratio of electron and hole diffusion coefficients in the bulk is nearly 3 *times* larger than the ratio observed at the surface. Clearly near surface bands and surface traps play an important role in the carrier diffusion process. In the of activated free carrier diffusion model, the surface carrier diffusion process can involve extra, trap related time scales ( $\tau_c, \tau_e$ ) relative to bulk free carriers. The diffusion coefficients decrease as a result of the capture of free carriers by traps. On the other hand, either VRH or FRH might also account for the observed diffusion. All models suggest that shallow trap states play an important role in the diffusion process. However the common EL2 defect states are at the midgap, and are unlikely to be directly related to these shallow states. As mentioned in chapter 4, as many as fifteen (twelve) electron (hole) traps have been identified in GaAs [38]. Among them, possible shallow electron traps include EI2, EI3, EB8, EB9, EB10, EL11 and EL15 whose energy levels are  $\sim 0.18 \text{ eV}$  below the conduction band minimum, and possible shallow hole traps include HB6, HL6, HL7, HL11, and HL12 whose energy levels are  $\sim 0.30 \text{ eV}$  above the valence band maximum. Except HL12 due to Zn impurity, all of them are more or less associated to complicated complex defects such as  $As_x$ . Here  $As_x$  represent the As interstitial defects in which several As atoms form a cluster.

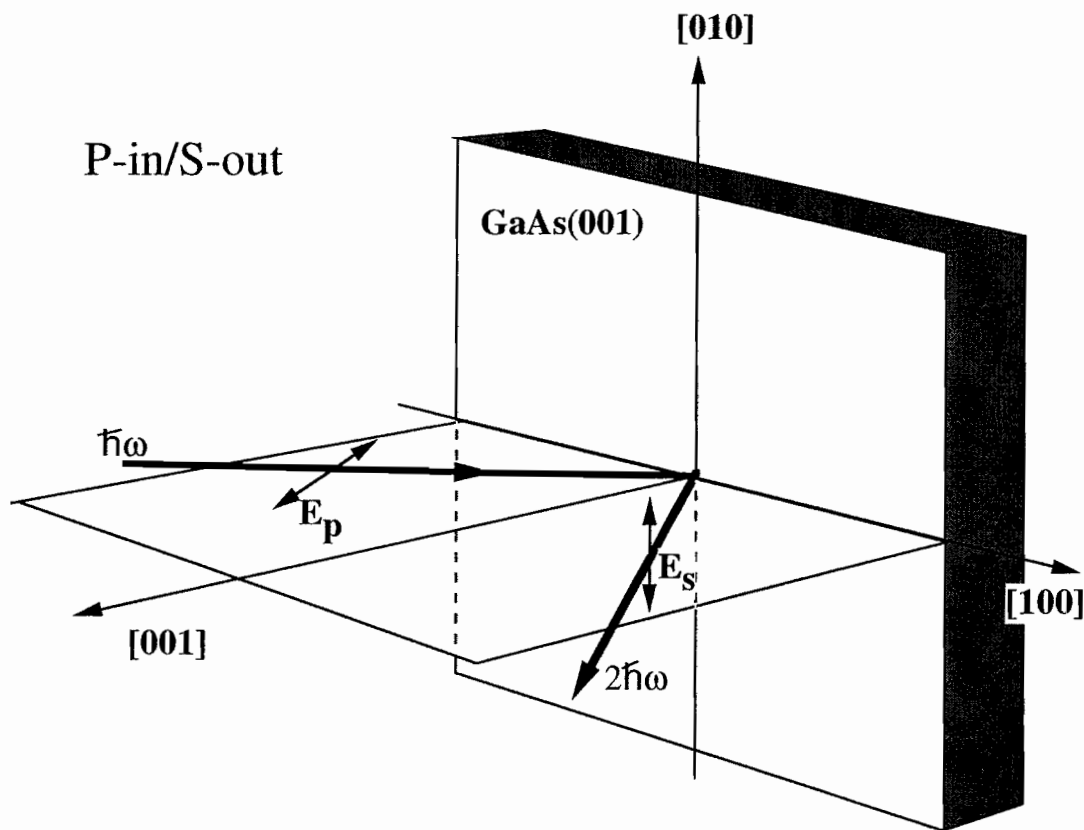


Figure 6.1: Schematic of the SHG experiment in p-in/s-out polarization configuration with crystalline  $[100]$  direction in the plane of incidence. The output SHG intensity is dominated by the contributions from  $\chi_{yxz}^{(2)}$ .

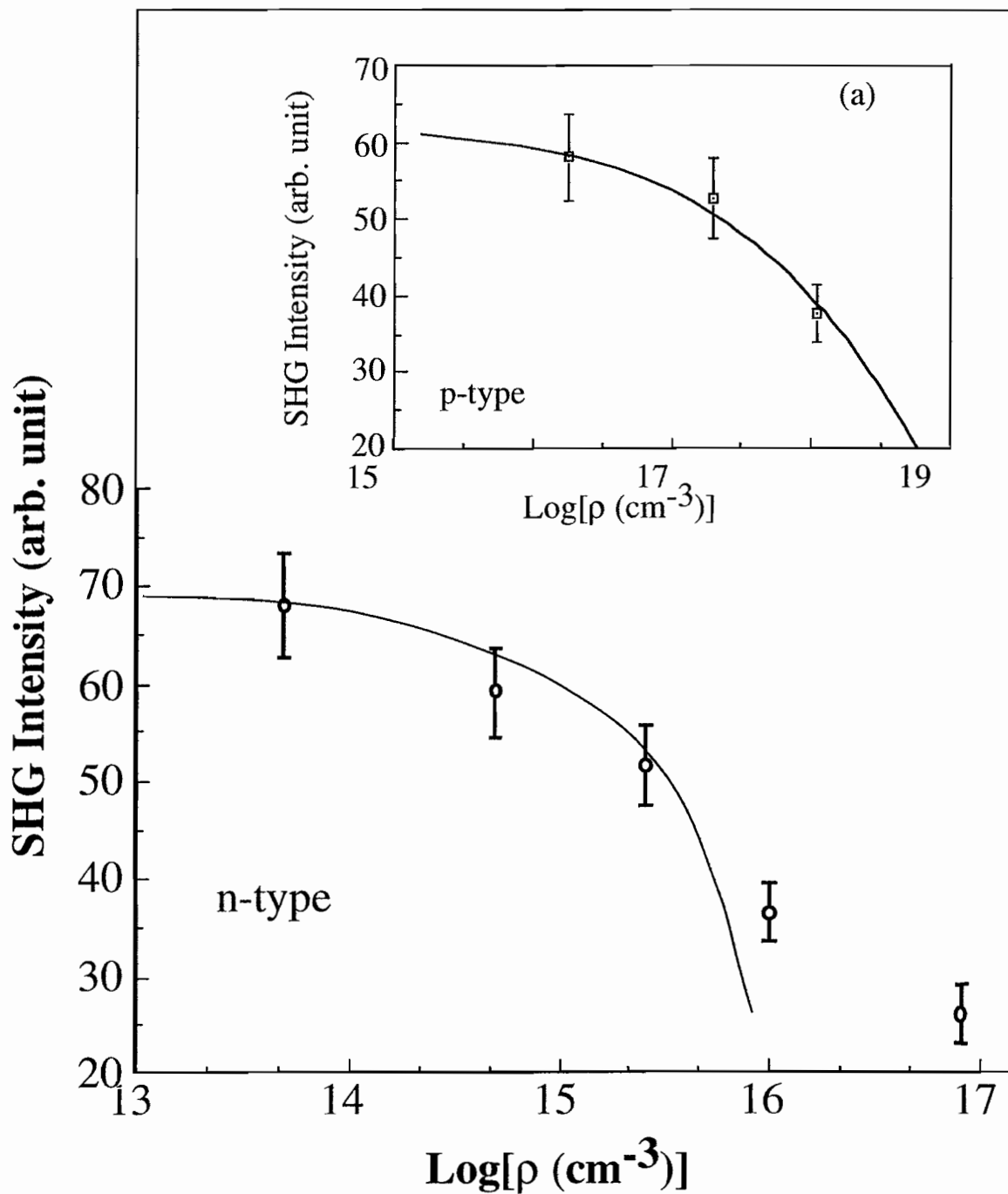


Figure 6.2: The variation of SH intensity at two-photon energy of 2.68 eV as a function of doping density. Both n- and p-type (see inset (a)) samples exhibit a reduction in SHG intensity as a function of increasing doping density. The solid lines are our theoretical fit to the data.

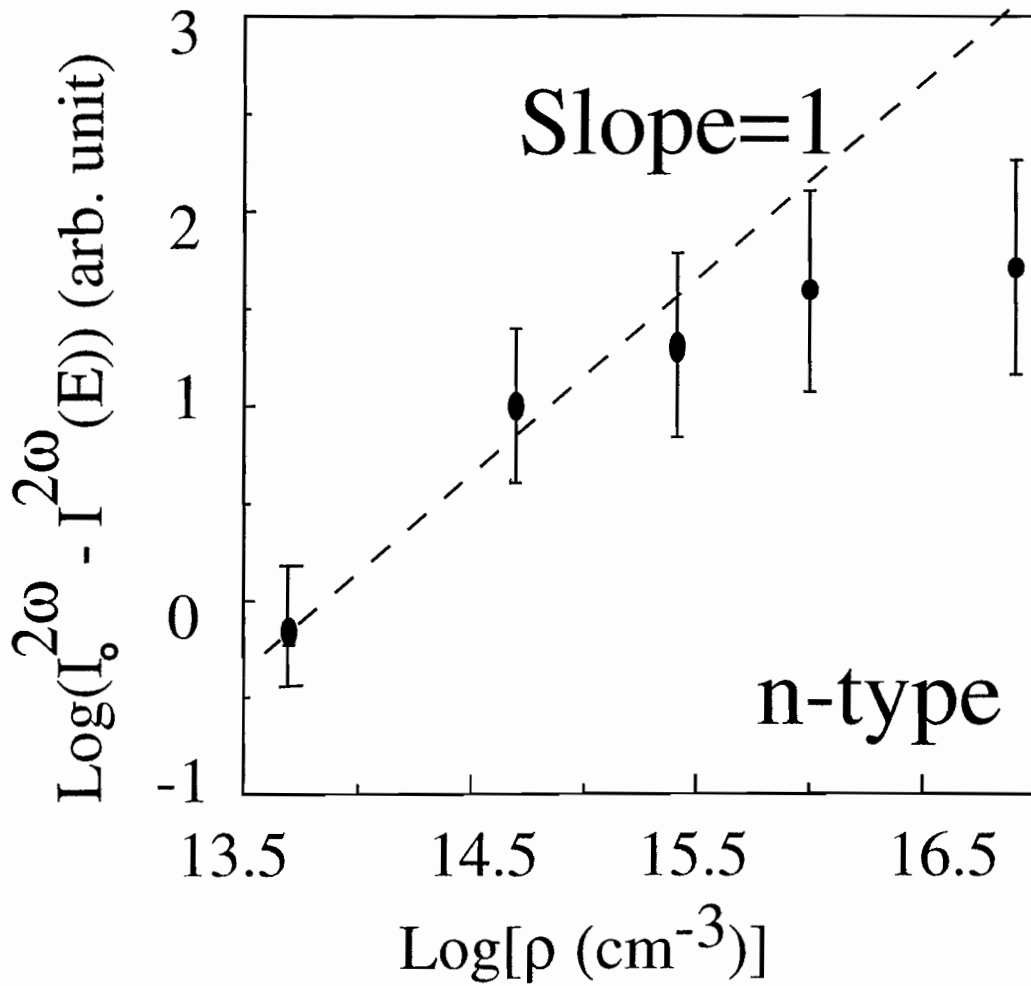


Figure 6.3: The plot of  $\log(I_0^{2\omega} - I^{2\omega}(E))$  as a function of  $\log(\rho)$  with SH fundamental photon energy at 2.68 eV. It clearly can be seen that the relationship between the SHG intensity and dopant density (electric field) is linear (quadratic) at the low dopant densities.

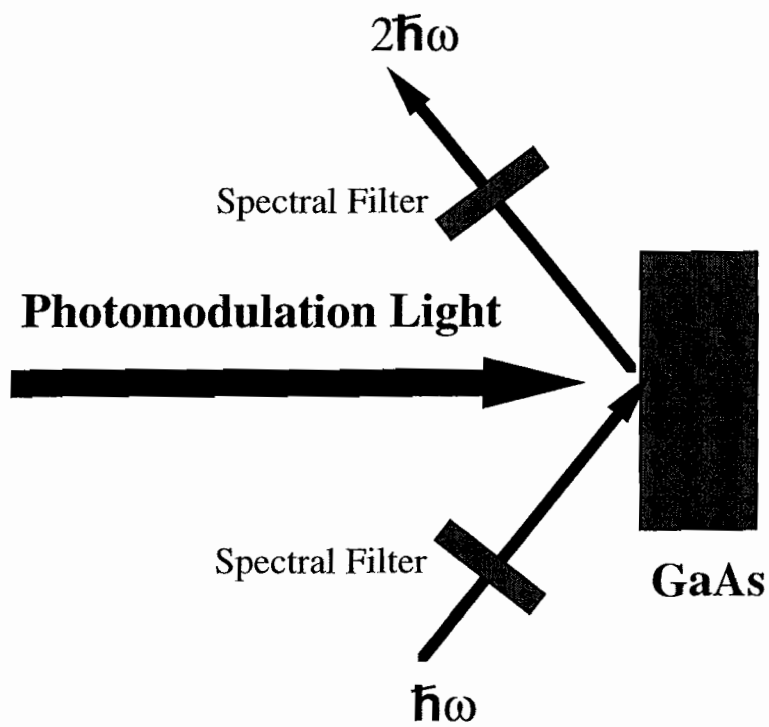


Figure 6.4: Schematic drawing of photomodulation second-harmonic generation (PSHG) experiment. In such PSHG experiments, light from an  $Ar^+$  ion laser illuminates the sample and modulates the band bending in the depletion region while the SHG experiment is in progress.

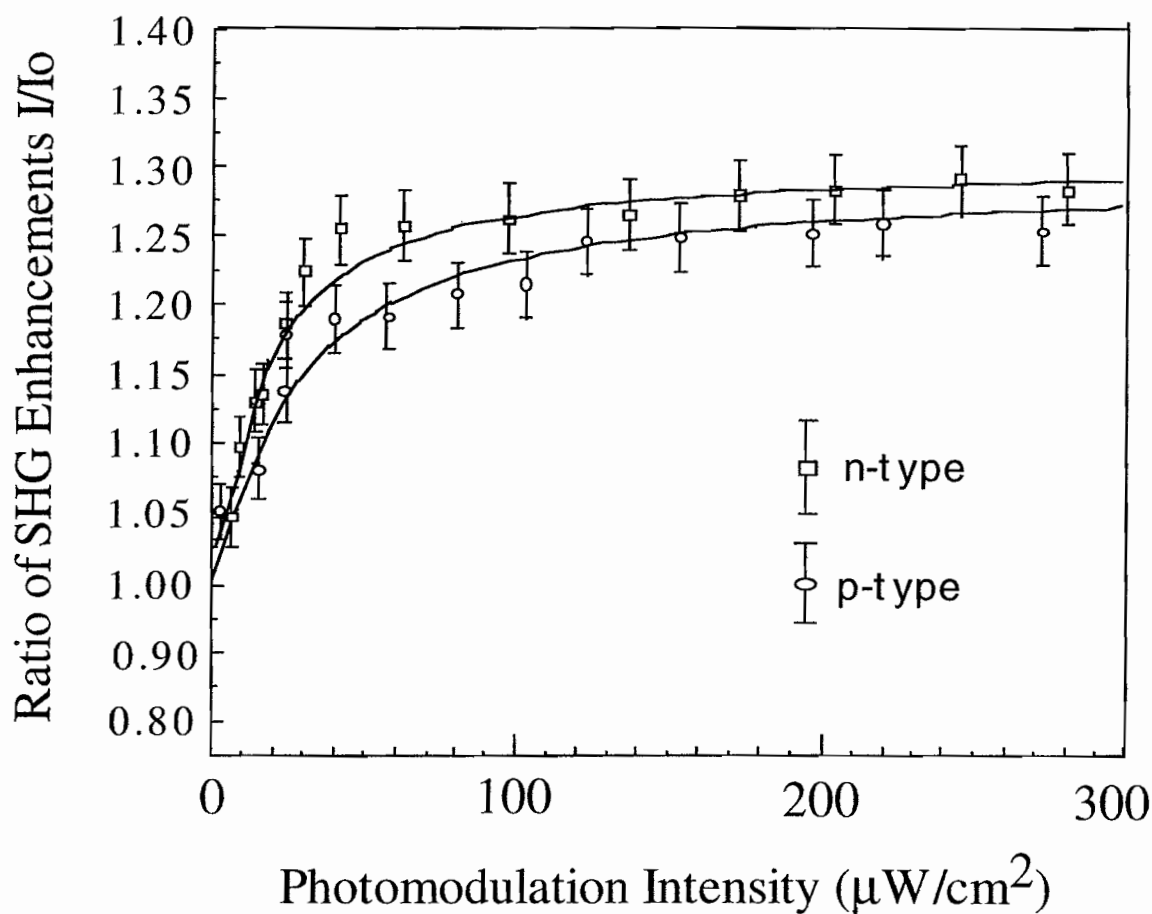


Figure 6.5: The enhancement of normalized SHG intensity at two-photon energy of 2.68 eV for two typical n-type ( $n=10^{16}/\text{cm}^3$ ) and p-type ( $p=10^{16}/\text{cm}^3$ ) samples as a function of the photoexcitation intensity. The solid lines are the theoretical fit to the data. The photon energy of the photomodulation light was 2.72 eV.

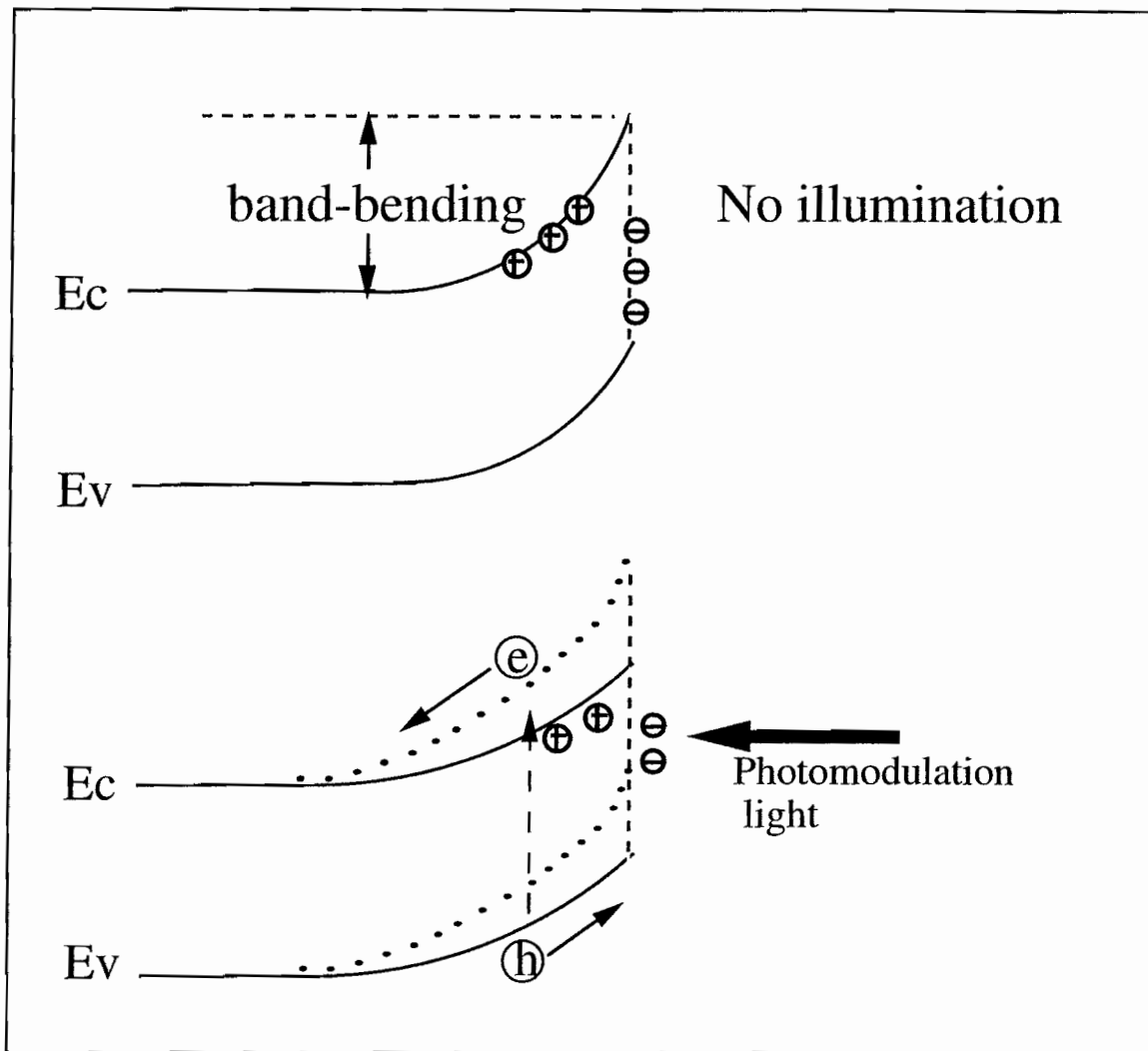


Figure 6.6: Schematic photomodulation of band-bending near surface. The linear photoexcitation creates electrons and holes in the depletion region. These carriers are separated by the built-in field and partly neutralize the surface charge. This in turn decreases the depletion electric field and the band bending.

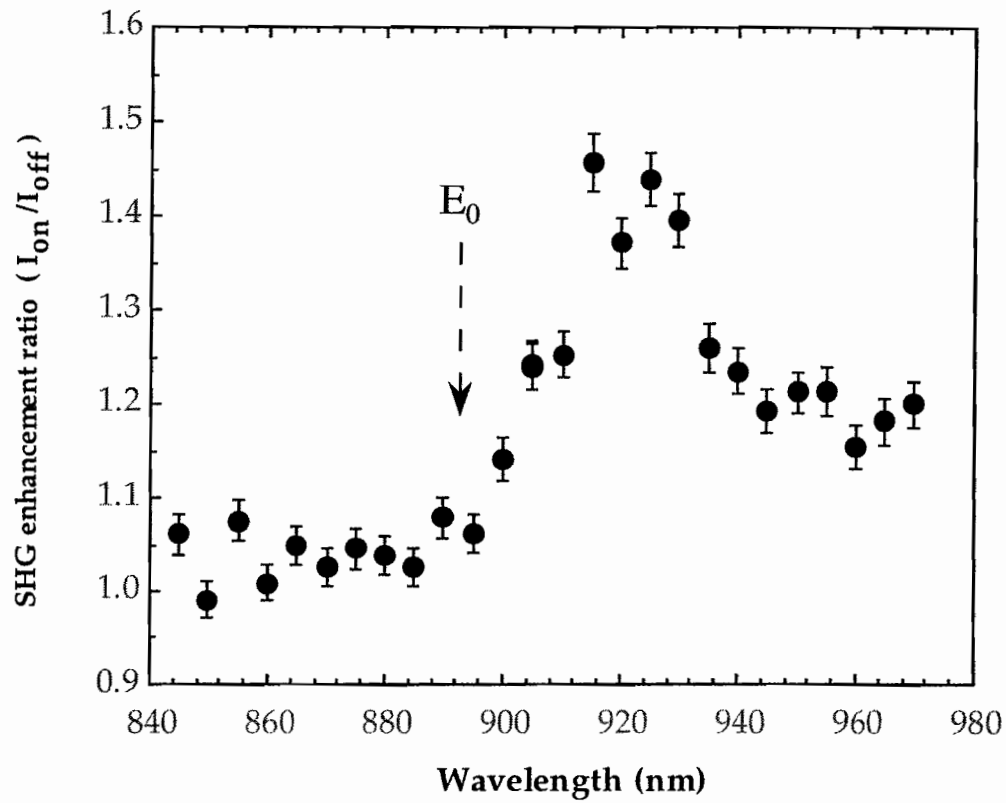


Figure 6.7: Enhancements of SHG ratio as a function of fundamental SH photon energies. The profile is same in n- and p-type samples.  $E_0$  refer to the GaAs band gap. The photon energy of the photomodulation light was 2.72 eV.

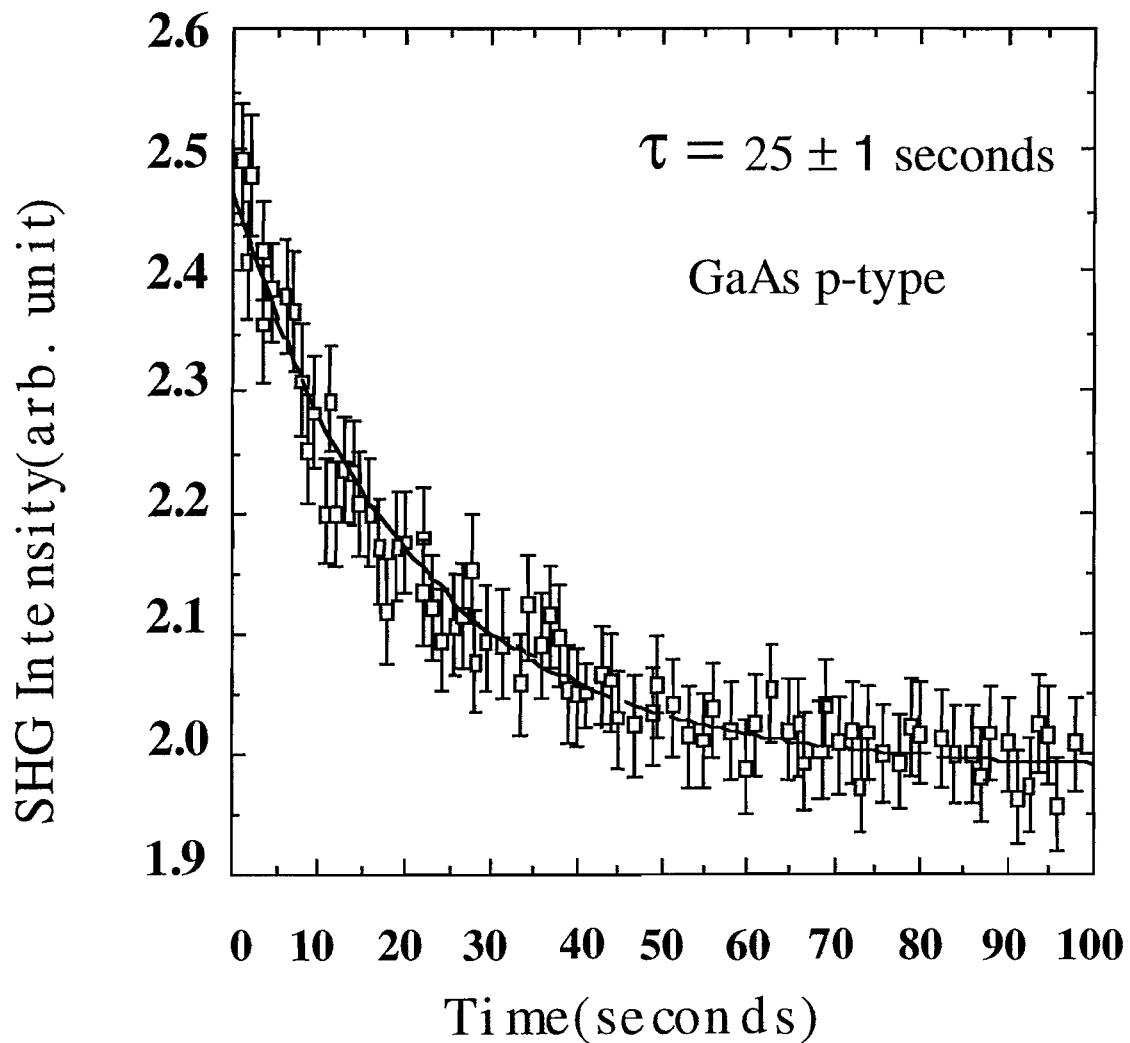


Figure 6.8: SH intensity from a typical p-type ( $\rho_p = 10^{16}/cm^3$ ) sample as a function of time after photomodulation light was turned off. From our theoretical fitting (solid line), the discharging time,  $\tau$ , of the surface traps is  $\sim 25 \pm 1$  seconds.

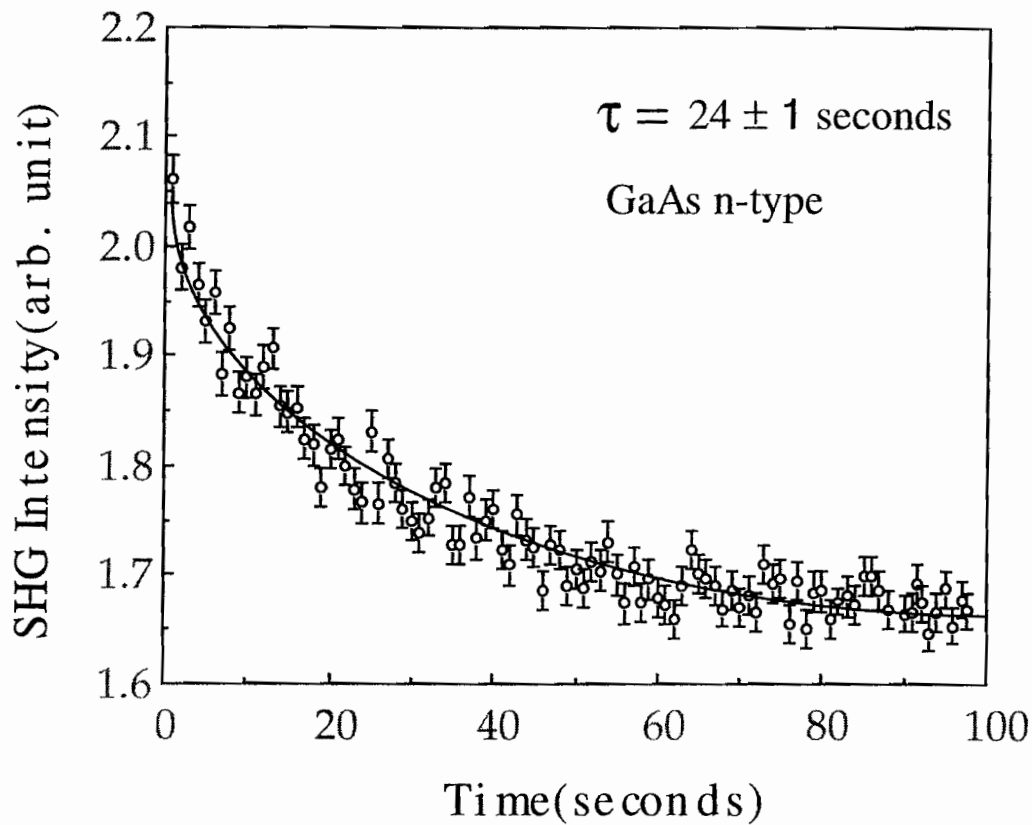


Figure 6.9: SH intensity from a typical n-type ( $\rho_n = 10^{16}/cm^3$ ) sample as a function of time after photomodulation light was turned off. From our theoretical fitting (solid line), the discharging time,  $\tau$ , of the surface traps is  $\sim 24 \pm 1$  seconds.

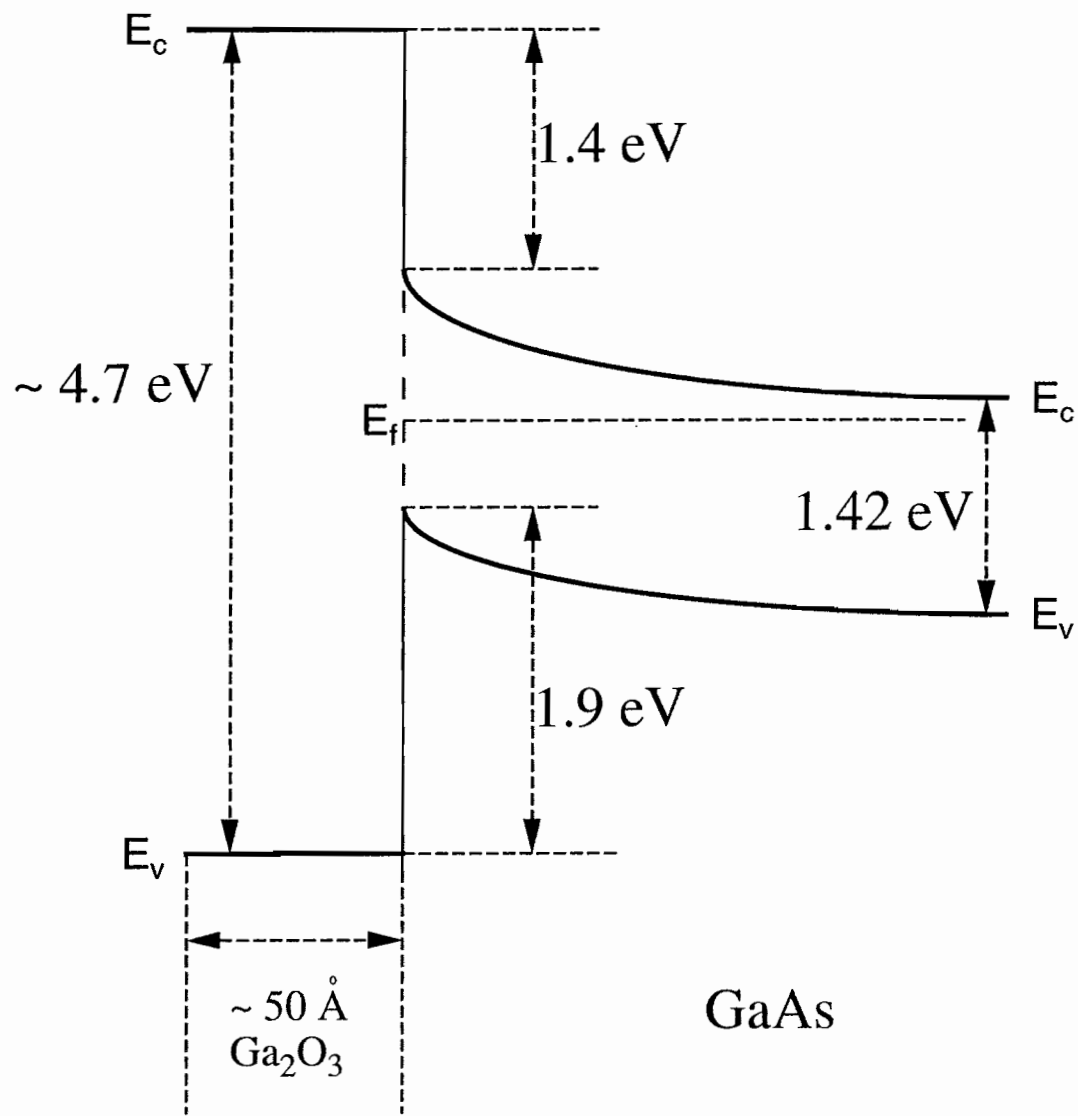


Figure 6.10: Schematic drawing of energy band profile at  $\text{Ga}_2\text{O}_3$  :  $\text{GaAs}$  n-type interface.

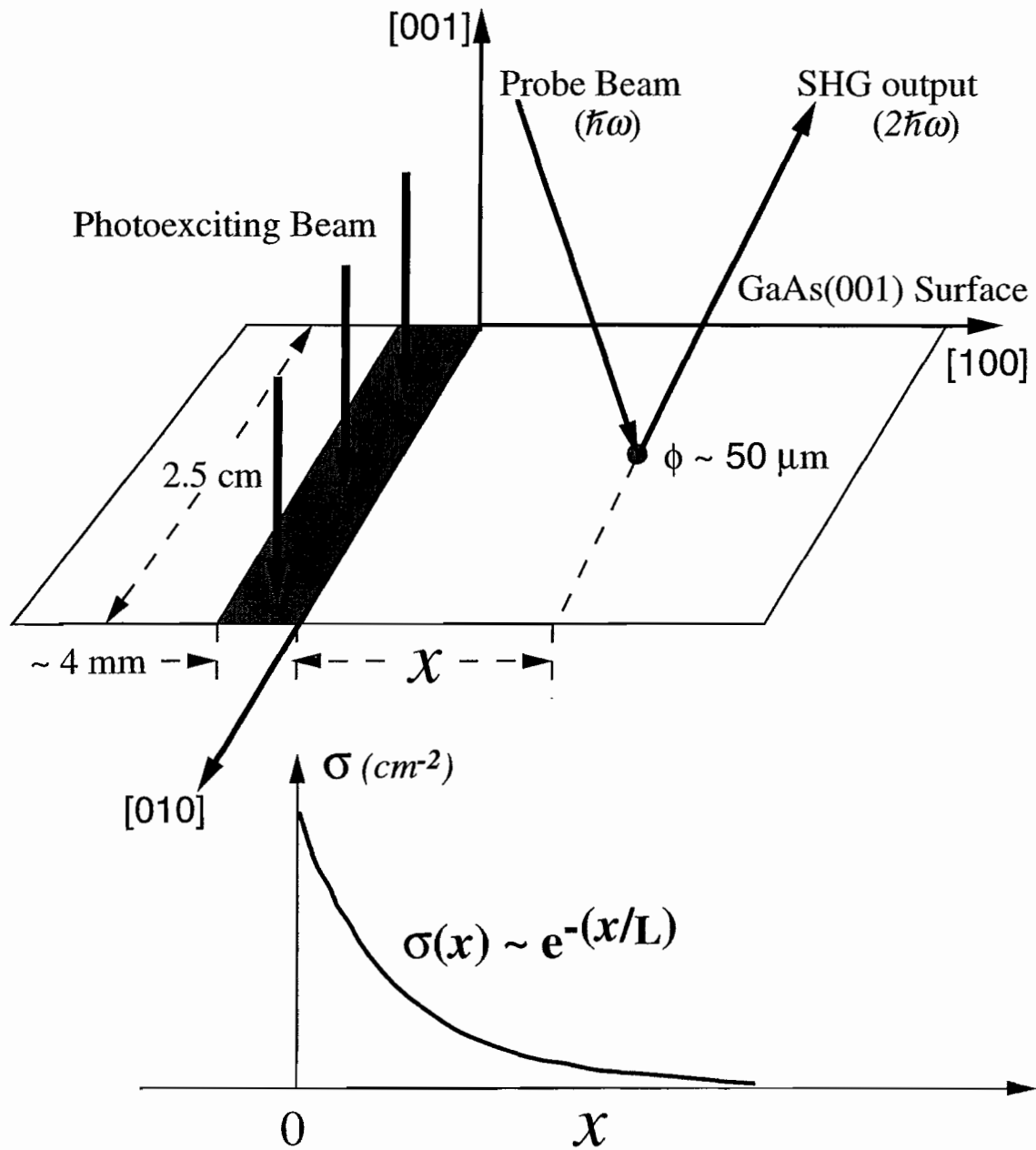


Figure 6.11: A 10 Hz Nd:YAG pumped dye laser, with  $\sim 50 \mu\text{m}$  sample spot size, was used as the fundamental probe light for the SHG measurements. An  $\text{Ar}^+$  ion laser was used as a cw photocarrier excitation beam, and its transverse beam profile on the sample was a narrow rectangle ( $\sim 2.5 \text{ cm}$  long,  $\sim 4 \text{ mm}$  wide) with sharp ( $\leq 50 \mu\text{m}$ ) edges on all sides. The long edge of the excitation beam was made parallel to the sample [010] axis. The photoexciting beam edge is at  $x = 0$ , and a schematic drawing of the photoexcited surface minority carrier density with diffusion length,  $L$ , is plotted as a function of the distance,  $x$ .

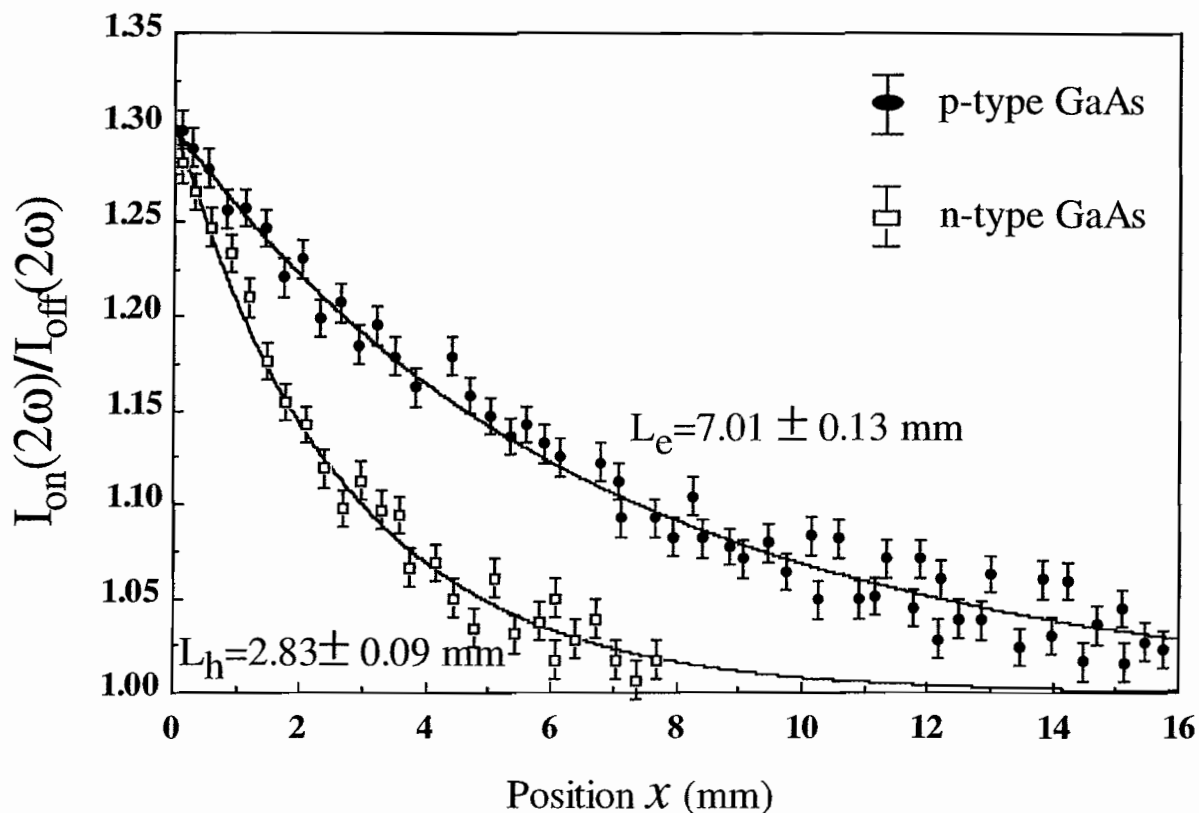


Figure 6.12: A typical digram of the variation of SHG output from n-type (p-type) GaAs plotted as a function of distance,  $x$ , from the photoexciting beam edge,  $x = 0$  at room temperature.  $I_{on}(2\omega)$  ( $I_{off}(2\omega)$ ) represents the SHG intensity when the photoexciting beam is on (off). The solid lines are our best fits. The error represents the standard deviation of multiple measurements on multiple samples. The hole (electron) diffusion length,  $L_h$  ( $L_e$ ), is  $2.83 \pm 0.09$  mm ( $7.01 \pm 0.13$  mm).

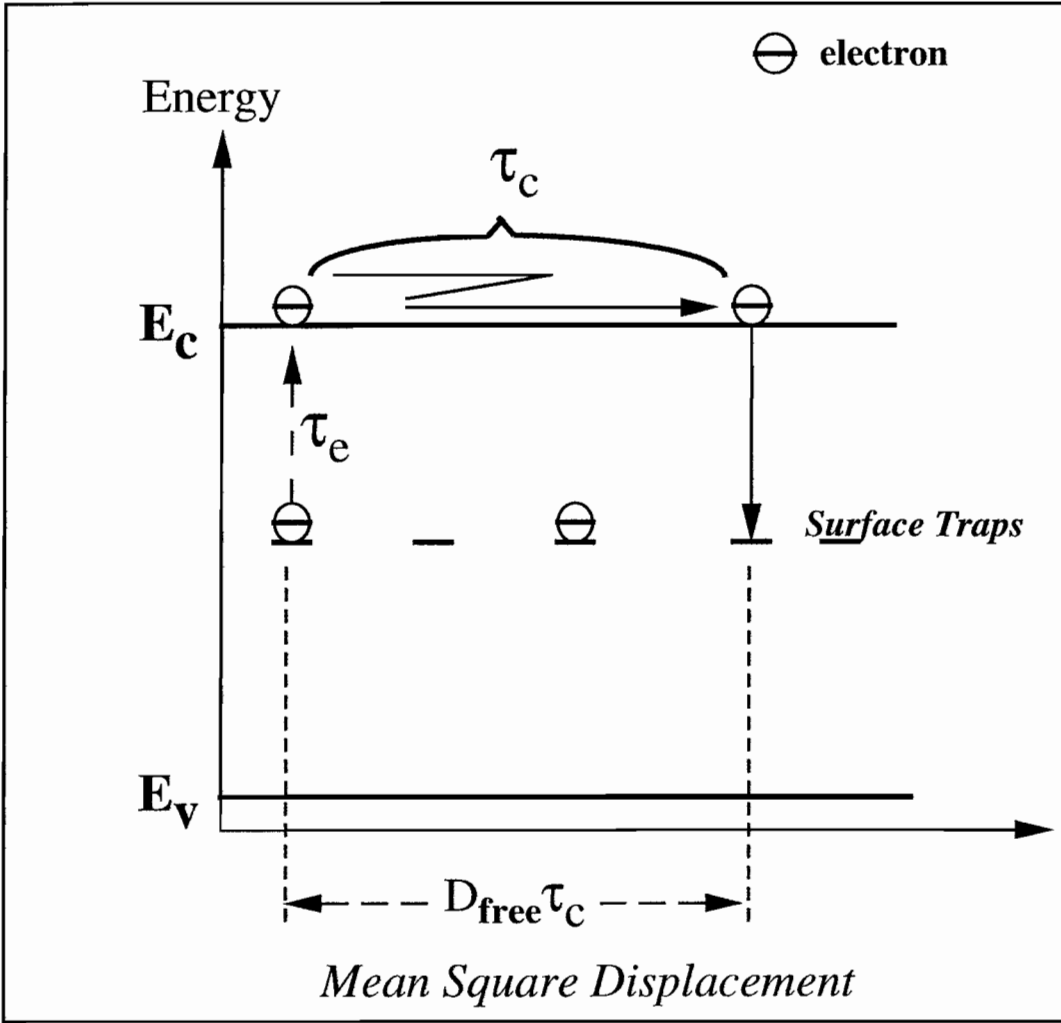


Figure 6.13: A schematic diagram of the energy and position of a minority carrier (p-type sample) that is excited, diffuses, and is then captured again.

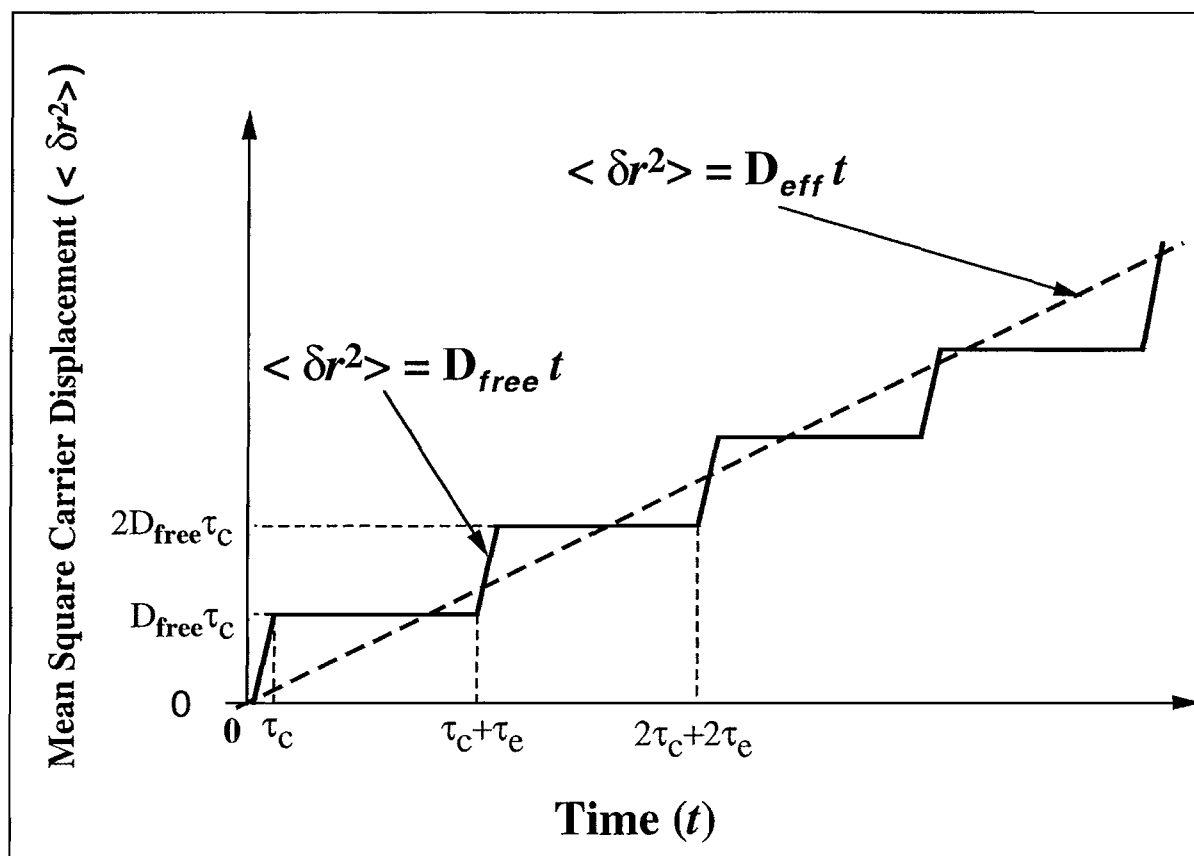


Figure 6.14: Schematic of the mean square displacement  $\langle \delta r^2 \rangle$  of the minority carrier as a function of time. The solid line indicates the carrier diffusion process with a free carrier diffusion coefficient  $D_{free}$  (large positive slope) and the carrier capture by traps for a time  $\tau_e$  (flat line). The dashed line (with relatively small positive slope) represents the effective diffusion process (with effective diffusion coefficient  $D_{eff}$ ) that we observed. Here  $\tau_c$  is the trapping time for the free carrier, and  $\tau_e$  is the time required for the carrier to become reexcited out of trap. Figures are intended to convey ideas and are *not* drawn to scale.

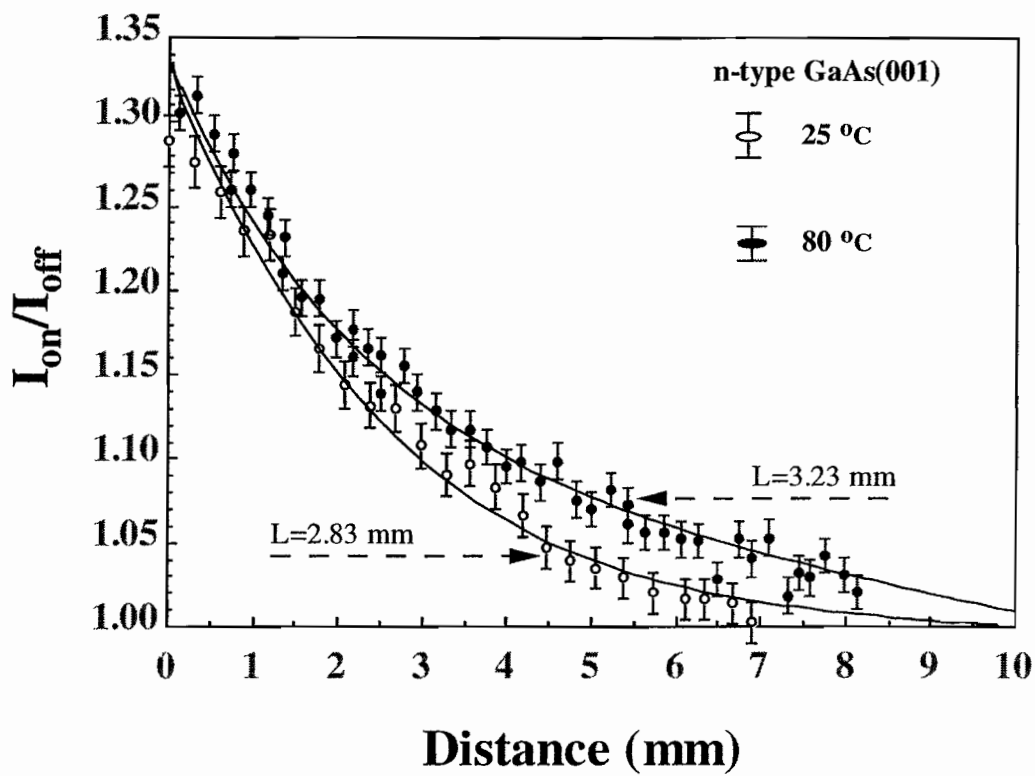


Figure 6.15: A typical SHG results at two different temperatures for n-type GaAs samples.

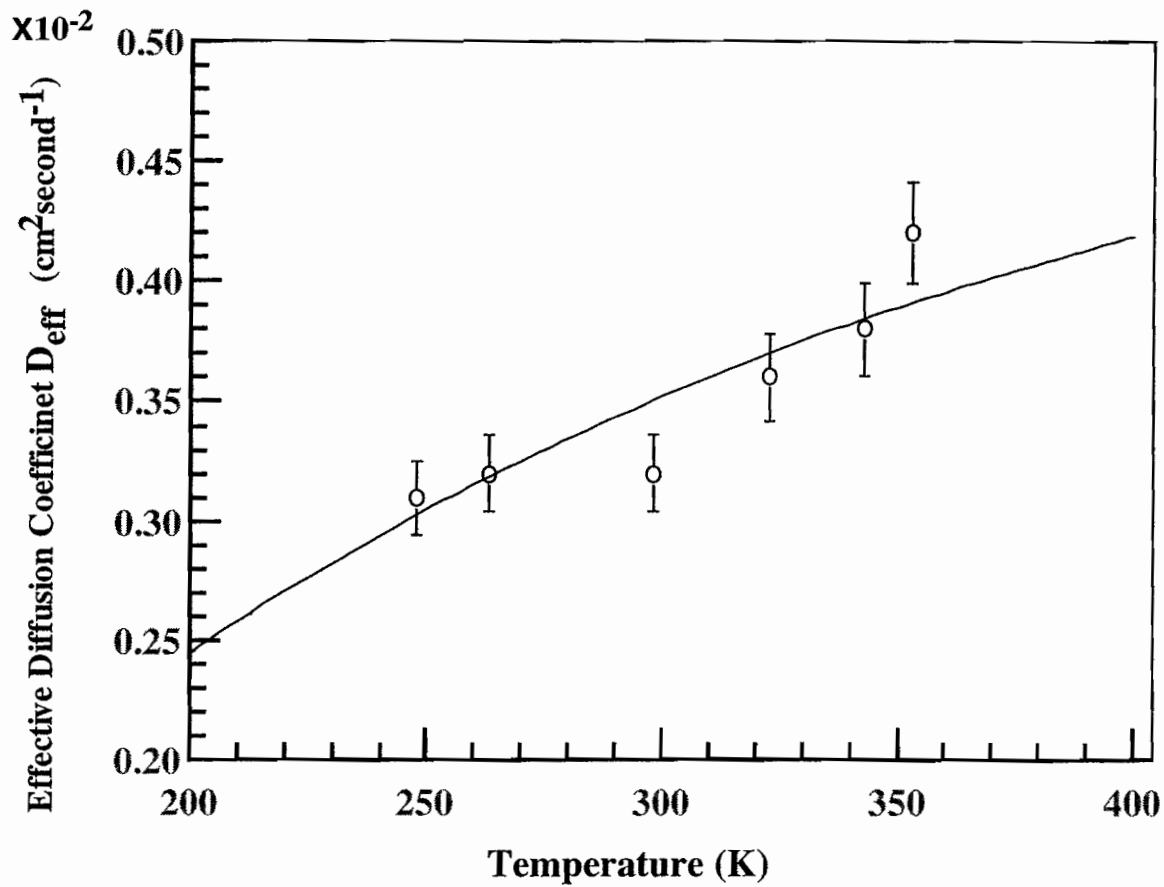


Figure 6.16: Diffusion coefficients as a function of temperature for a typical n-type GaAs sample. The solid line is our fitting according to activated free carrier diffusion model(see Figure 6.13).

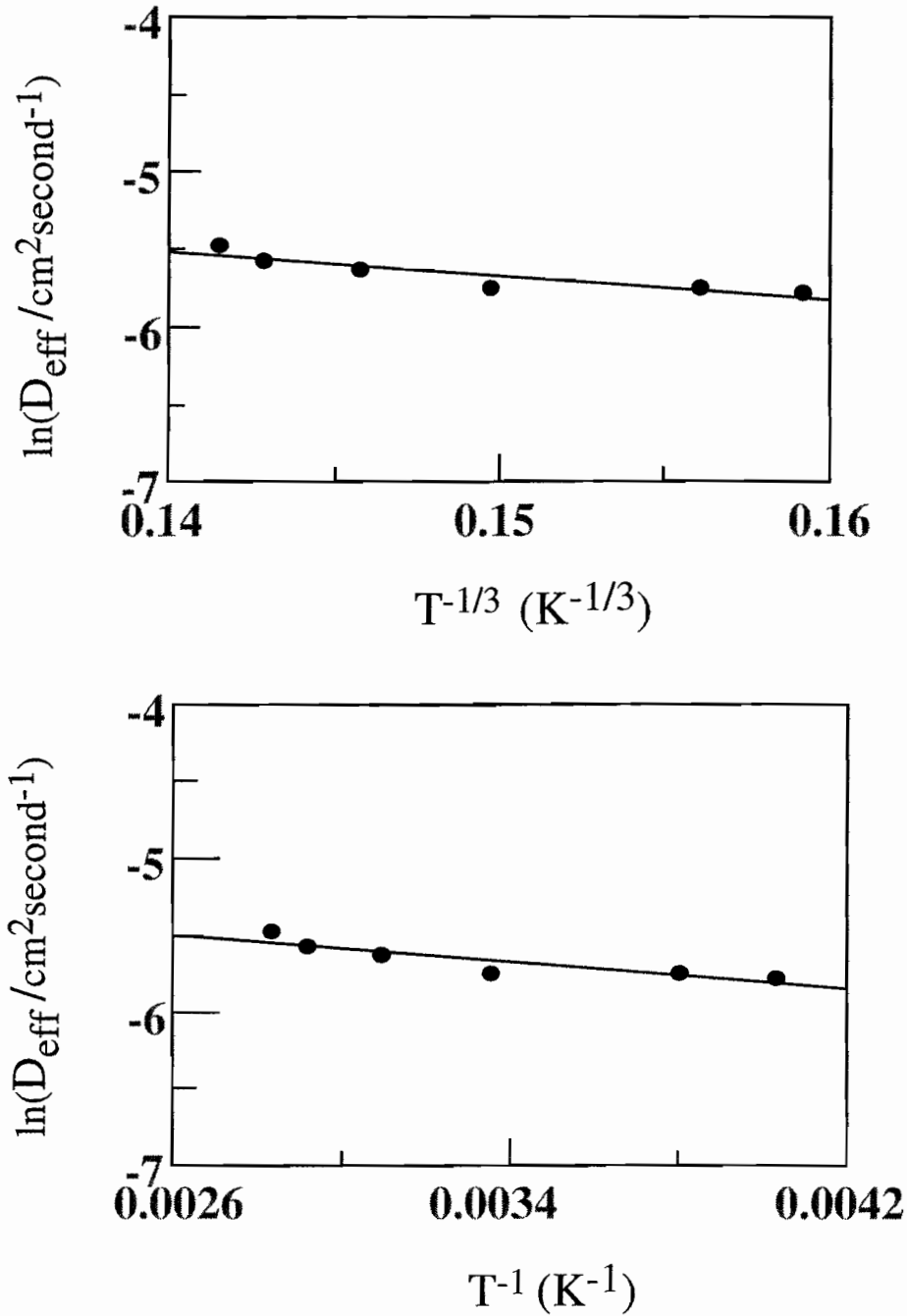


Figure 6.17: (a) shows  $\ln(D_{eff})$  as a function of  $T^{-1/3}$  for n-type GaAs. The solid line is a linear fit according to VRH model. Inset(b) shows  $\ln(D_{eff})$  as a function of  $T^{-1}$  for n-type GaAs. The solid line is a linear fit according to FRH model.

# Chapter 7

## Observation of midgap interface states at Metal:GaAs junctions by SHG and SFG

Electronic properties at buried solid:solid interfaces can depend on the existence of interface states. In this chapter, we utilize second-order nonlinear optical spectroscopies to probe the interface states at metal:GaAs junctions. We observe sharp SHG and SFG spectral features that provide compelling evidence for the existence of interface states just below the buried interface. The relationship between these interface states, interface preparation, and doping are discussed in detail.

### 7.1 Second-order nonlinear optical spectroscopies from Metal:GaAs interfaces

#### 7.1.1 SHG spectra from Au:GaAs (n-type) interfaces

We detected the interface SHG signals in the p-in/p-out configuration with the crystaline [100] axis oriented in the plane of incidence [83, 39]. The experimental setup for

these measurements were presented in chapter 3.  $80\text{\AA}$  Au (As) epitaxial (amorphous) films on n-type and p-type GaAs(001) surfaces were studied. The buried interfaces were either As-rich or Ga-rich as a result of different GaAs substrate growth conditions. Native oxide GaAs(001) samples were also studied. Further details of sample properties and growth conditions are described in chapter 4.

In figure 7.1, we exhibit measurements of interface SHG spectra from Au:GaAs n-type samples with different GaAs surface reconstructions (As-rich  $2\times 4$  and Ga-rich  $4\times 2$ ). We see that the interface spectra exhibit a single sharp peak at a one-photon energy of  $0.715\text{ eV}$  for the As-rich Au:GaAs n-type sample, and two closely spaced peaks for the Ga-rich Au:GaAs n-type sample. The solid line in the spectra from Ga-rich Au:GaAs n-type sample represents a best fit to the data using two Lorentzian lineshape functions. According to the fit, the SH peak positions are  $0.708 \pm 0.014\text{ eV}$  and  $0.731 \pm 0.014\text{ eV}$  respectively. We believe that the first peak in the SHG spectra at  $\sim 0.708\text{ eV}$ , has the same origin as the single sharp peak in the As-rich Au:GaAs n-type system, while the latter peak is a new feature resulting from the different interface preparation.

### 7.1.2 SFG spectra from Au:GaAs (n-type) interfaces

SHG spectral lines can be one-photon resonances, in which the incident photon energy ( $\hbar\omega$  equals) the transition energy between the two states involved, or two photon resonances, in which the output photon energy ( $2\hbar\omega$ ) equals the transition energy between the two states involved. Therefore we measured SFG spectra on the same systems to further characterize these resonances. The SFG spectra were obtained by irradiating the samples with mixture of the Q-switched Nd-YAG 1064 *nm* wavelength beam and an OPO tunable infrared beam at the same incidence angle and polarization.

The SFG spectra are shown in figure 7.2. The solid lines in the spectra from Ga-rich Au:GaAs n-type sample represent a best fit to the data using two Lorentzian

lineshape functions. According to the fitting, the SF peak positions are  $0.713 \pm 0.014$  eV and  $0.730 \pm 0.014$  eV respectively. The first peak in the SFG spectra at 0.713 eV is thought to be the same as the single sharp peak in the As-rich Au:GaAs n-type system. The resonance features in SHG and SFG spectra are matched to each other when the spectra were plotted as a function of *one-photon energy*. This indicates that all resonance features are one-photon resonances. Since the GaAs band gap is 1.42 eV, the resonance energy levels are all around the midgap. The bulk SHG  $\chi_{xyz}^{(2)}$  spectra have also been taken in the p-in/s-out polarization configuration[83]. Since bulk resonance features were not observed (see figure 7.3), our assignment of these features to interfaces in the system was further corroborated. We note that the SFG spectra are not as sharp as SHG spectra. This can be due to the following reasons; SHG processes are in double resonances due to the midgap states, however SFG processes are only in single resonance from the midgap states to the conduction band. In addition, sum frequency energy is far above the band gap, other sum frequency processes from other possible states will contribute to the total signal as a background. As a result, SFG spectra is not as sharp as SHG spectra.

### 7.1.3 One-photon resonance paths

There are two probable excitation paths that can be invoked to explain the one photon resonance (see figure 7.4). Each process starts in a different initial state. In one case the three-step process starts from the top of the valence band (see figure 7.4(a)), and in the other case the process starts from the interface midgap state (see figure 7.4(b)). Because the one-photon resonance energy is approximately half of the GaAs bandgap energy, double resonances arise in both cases, and SHG signals are stronger than SFG signals.

#### 7.1.4 SHG and SFG from Au:GaAs (p-type) interfaces

Because the two possible one-photon excitation paths begin in different initial states, variation of carrier density in these initial states should affect the interface resonance spectra. To test this hypothesis we took spectra from metal:GaAs (p-type) samples within the same spectral region. In our analysis, we assume that the energy levels at the interface are not changed by changes in bulk doping[67]. This assumption is plausible for atomic displacement-induced defect states. However, the carrier occupation density in these states will vary, since the Fermi level will shift with respect to the midgap levels. In the p-type metal:GaAs system these midgap states will become empty, as the Fermi level shifts towards the valence band maximum[24]. No resonance features were observed in p-type GaAs systems (see figure 7.5). These results suggest that the one photon resonances in metal:GaAs n-type samples are due to the resonant transition from the occupied midgap states to the conduction band minimum. As a result of the lower occupied midgap electron density in p-type systems, the resonance process originating from these midgap states was probably too weak to be detected. We conclude that the dominant three-step resonance processes starts from midgap interface states.

In addition, SHG and SFG spectra from native oxide GaAs (n-type) samples were also obtained within the same spectral region (see figure 7.6). Because oxygen atoms generally act as acceptors and metal atoms act as donors in GaAs[3], the occupied electron density in midgap states is expected to be lower than metal:GaAs n-type systems. Our spectra show no resonance features, which further confirms that one photon resonances of metal:GaAs n-type samples are due to the resonant transition from the occupied midgap states to the conduction band minimum.

### 7.1.5 SHG and SFG experiments on As:GaAs (n-type) samples

SHG and SFG experiments were also performed on As:GaAs(001) n-type samples within the same photon energy range. A similar single resonance feature around 0.715 eV was observed (see figure 7.7), and was confirmed to be a one photon resonance. Again in contrast to previous spectroscopic experiments[7, 10, 23, 24], all of the observed resonances are sharp, suggesting a narrow distribution of states at or just below the buried interface.

## 7.2 Higher order bulk and Au surface contributions

The interface signals in principle contain contributions from the front metal surface, and higher-order bulk nonlinearities. To examine the contributions from the Au surface, we measured SFG and SHG spectra from a thick Au-epitaxial film ( $\sim 5\mu m$ ) and found that SFG and SHG signals were below our noise level (see figure 7.7). Also, since the bulk nonlinear response of the Au epitaxial layer on GaAs(001) is expected to contribute in the same way in both n- and p-type GaAs systems, the fact that no resonance features were observed in Au:GaAs p-type systems effectively rules out possible contributions from bulk Au epitaxial films. The possibility of higher-order GaAs bulk contributions was also examined in the s-in/s-out and s-in/p-out polarization configurations. The bulk anisotropic contribution ( $\xi$ ) was below our noise level and the signal resulting from linear combinations of  $\gamma$  and  $\chi_{||\perp}^{(2)}$  was at least two orders of magnitude smaller than the interface signal (see figure 7.3). In addition, the higher-order bulk terms contribute in the same way to metal:GaAs and oxide:GaAs systems, and no resonances in oxide:GaAs systems were observed. In total, these findings rule out higher-order bulk contributions as sources of the

resonance features. The 0.715 and 0.731 eV resonance features most likely originate from the buried interface.

## 7.3 Nature of the midgap interface states

### 7.3.1 Atomic displacement induced defect states

Our second-order nonlinear optical spectral measurements of As-rich Au:GaAs and As:GaAs n-type samples possess a similar resonance at 0.715 eV, suggesting that the common interface state may be related to As atoms. On the other hand, the interface state at  $\sim 0.731$  eV was only found at the Ga-rich interface in Au:GaAs n-type systems. This suggests that this latter interface state is related to the presence of excessive Ga atoms at the interface.

These observations can be understood in the following context. Atomic displacements are produced at the buried interface. For example, a gradient in the chemical potential for As or Ga atoms can induce the migration of these atoms into the GaAs substrate. As a result of relative concentrations of As and Ga atoms during growth, we might expect the formation of As atom displacement induced defect states near the As-rich interface[67]. In this case the As atom sits in the Ga site in the interfacial region (see figure 7.8). Such an As atom displacement produces one of the primary defect states in GaAs [38, 112]. Its energy level is believed to lie near the middle of the band gap[67, 6]. The formation of Ga displacement-induced defect states are expected for the Ga-rich interface. In such a case, the Ga atom sits on the As atom site (see the figure 7.8). The Ga displacement defect state has been theoretically predicted to have an energy level near the middle of band gap [6]. All possible displacement defects in GaAs were calculated in reference [6] and plotted in figure 4.5.

We note that as many as fifteen (twelve) electron (hole) traps have been identified in GaAs [38]. The dominant electron trap, EL2, is believed to be a native defect [66],

and to play an important role in pinning the Fermi level [67]. Some of the interesting properties of EL2 are discussed in chapter 4. The As atom displacement induced defects  $As_{Ga}$  have been suggested to be associated with the EL2 state [67, 66, 68].

The lowest conduction band  $\Gamma_6$  has an s-like symmetry. As discussed previously in chapter 4, an isolated neutral  $As_{Ga}$  defect is a donor state ( $E \sim E_v + 0.5eV$ ), and has an s-like symmetry. Therefore the direct transition from a localized neutral  $As_{Ga}$  state to the  $\Gamma_6$  is unlikely in the electric dipole approximation [68]. However an  $As_{Ga}$  defect has an acceptor level ( $E \sim E_c - 0.75eV$ ), which has an p-like symmetry (see figure 4.5) [6], the direct transition between the acceptor state and the conduction band  $\Gamma_6$  is no longer forbidden. In the case of n-type GaAs, the Fermi level is pinned at this acceptor level [5], and the electron density at this level is high. Our results may arise through such a one photon resonance from this midgap acceptor state to the conduction band at the  $\Gamma$  point near the interface. The results are thus suggestive, but further considerations are required. Interestingly just as linear optical spectroscopic studies have provided important information about the energy levels and optical properties of deep-level traps [69], our nonlinear spectroscopy of these interface defect states may provide new information about the symmetry of these defects states near interfaces.

The formation of Ga displacement-induced defect states are also expected for the Ga-rich interface. In such a case, the Ga atom sits on the As atom site (see the figure 4.5 and figure 7.8). The Ga displacement defect  $Ga_{As}$  is an acceptor with a p-like symmetry, and it has been theoretically predicted to have an energy level near the middle of the band gap [6]. The transition from the  $Ga_{As}$  to the lowest conduction band  $\Gamma_6$  at the  $\Gamma$  point is allowed. Since the As displacement is among the most common defects in GaAs, the resonance state at 0.715 eV was still observed in the Ga-rich interfaces, albeit more weakly [112]. Qualitatively our spectra suggest that the ratio (peak height or integrated area) of the two resonance peaks (0.715 eV, 0.731 eV) can be related to the ratio of  $As_{Ga} : Ga_{As}$  at the interface. The interface

second-order susceptibilities  $\chi^{(2)}$  for these two defects can be written as [25]

$$\chi_{AsGa}^{(2)} \sim N_{AsGa} \beta_{AsGa}^{(2)} \quad (7.1)$$

$$\chi_{GaAs}^{(2)} \sim N_{GaAs} \beta_{GaAs}^{(2)} \quad (7.2)$$

$$(7.3)$$

Here  $N_{AsGa}$  ( $N_{GaAs}$ ) is the density of the  $AsGa$  ( $GaAs$ ) defect states.  $\beta_{AsGa}^{(2)}$  ( $\beta_{GaAs}^{(2)}$ ) is the second-order As (Ga) antisite polarizability. Therefore the resonance peak heights in the SHG spectra can be related to the ratio of  $AsGa : GaAs$ .

$$\frac{I_{AsGa}(2\omega_1)}{I_{GaAs}(2\omega_2)} = \left[ \frac{N_{AsGa} \beta_{AsGa}^{(2)}}{N_{GaAs} \beta_{GaAs}^{(2)}} \right]^2 \left[ \frac{I(\omega_1)}{I(\omega_2)} \right]^2 .$$

Here  $\omega_1$  and  $\omega_2$  represent resonance frequencies for the  $AsGa$  and  $GaAs$  states respectively.  $I(\omega_1)$  and  $I(\omega_2)$  are fundamental light intensities. In our case, the fundamental pumping lights  $I(\omega_1)$  and  $I(\omega_2)$  are equal, i.e.,

$$\left[ \frac{N_{AsGa} \beta_{AsGa}^{(2)}}{N_{GaAs} \beta_{GaAs}^{(2)}} \right]^2 = \frac{I_{AsGa}(2\omega_1)}{I_{GaAs}(2\omega_2)} .$$

Thus the ratio of  $AsGa : GaAs$  is related to the peak heights of two resonances at  $\omega_1$  and  $\omega_2$ . In particular, if we assume that  $\beta_{GaAs}^{(2)}$  equals  $\beta_{AsGa}^{(2)}$ , the ratio of  $AsGa : GaAs$  is  $\sim 1 : \sqrt{3}$  in Ga-rich interface samples. This type of analysis may prove to be a useful methodology for *in situ* chemical analysis during growth.

On the other hand, the  $AsGa$  defects are isotropically distributed in GaAs bulk, therefore the contribution of the second-order nonlinear process from these isotropically distributed states is forbidden (see chapter 2). In addition, the  $AsGa$  defects in bulk may primarily be at neutral ground state with s-like symmetry, since there does not exist a metal electron sea nearby to charge a neutral s-like  $AsGa$  defect up to a negatively charged p-like state (see chapter 4). The direct transition from this neutral s-like state to conduction band minimum at the  $\Gamma$  point is thus unlikely in the electric dipole approximation [68]. These is one of the reasons that no resonance features were observed in our GaAs bulk spectra. Since GaAs has an existing

nonzero bulk second-order susceptibility, SHG and SFG contributions from these defect states may be much smaller than the bulk  $\chi_{xyz}^{(2)}$ , this may be the other reasons that no resonance features were observed in our GaAs bulk spectra.

### 7.3.2 Some concerns about other defects states

Although the overall trends in these experiments are most easily understandable in terms of the different atomic displacements at the interface, we cannot eliminate all other possible mechanisms. In particular, microscopically there is also interdiffusion between metal overlayer atoms and the semiconductor substrate atoms [97]. In the case of our Ga-rich interface samples, replacement reactions could produce different interface structures and the formation of alloys in the interface layer [98]. As a result, an additional resonance might arise [89] and could explain some of our observations. However, interface states due to the reaction between metal atoms and Ga or As atoms are expected to be the same for n-type and p-type Au:GaAs systems. The fact that we do not see the resonance features in the Au:GaAs p-type systems minimizes the possibility of associating the resonances with new alloy states. While we cannot entirely rule out these possibilities, we believe the defect picture outlined above is the most plausible explanation of our observations when they are taken as a whole.

### 7.3.3 Depletion field effects

Let us consider the depletion field effects. The strong depletion electric field  $E\hat{z}$  will perturb the  $As_{Ga}$  defect states. Utilizing first order perturbation theory, the p-like  $As_{Ga}$  defect state  $|P_{As_{Ga}}\rangle$  is modified as

$$|P_{As_{Ga}}\rangle = |P_{As_{Ga}}^{old}\rangle + \sum_M \frac{\langle P_{As_{Ga}}^{old} | \vec{p} \cdot \vec{E} | M \rangle}{\Delta E_{MP}} |M\rangle$$

Here  $|M\rangle$  are excited states and  $\Delta E_{MS}$  is the energy difference between states  $|P_{As_{Ga}}\rangle$  and  $|M\rangle$ .  $p$  is dipole operator. In this case, the nonzero terms in

summation include s-like states in the dipole approximation. Therefore the p-like state  $|P_{AsGa}\rangle$  is mixed with the s-like ground state  $|S_{AsGa}\rangle$ .

$$|P_{AsGa}\rangle = |P_{AsGa}^{old}\rangle + \frac{\langle P_{AsGa}^{old} | p_z E | S_{AsGa}^{old} \rangle}{\Delta E_{SP}} |S_{AsGa}^{old}\rangle$$

In same way the s-like ground state  $|S_{AsGa}\rangle$  is also mixed with p-like state  $|P_{AsGa}\rangle$

$$|S_{AsGa}\rangle = |S_{AsGa}^{old}\rangle + \frac{\langle S_{AsGa}^{old} | p_z E | P_{AsGa}^{old} \rangle}{\Delta E_{PS}} |P_{AsGa}^{old}\rangle$$

The mixture of the states depends on the depletion field  $E$ . In chapter 5, we calculated the mixture of the conduction band states  $\Gamma_6$ .

$$\begin{aligned} |\Gamma_6\rangle_+ &= ig_6 |\phi_0^{(8)}\rangle_{\frac{1}{2}} + |\phi_0^{(6)}\rangle_{\frac{1}{2}} \\ |\Gamma_6\rangle_- &= g_6 |\phi_0^{(8)}\rangle_{-\frac{1}{2}} + |\phi_0^{(6)}\rangle_{-\frac{1}{2}} \end{aligned} \quad (7.4)$$

Here we only consider the conduction band minimum and valence band maximum at the  $\Gamma$  point. The interface second-order susceptibility  $\chi_{zzz}^{(2)}$  is determined by the second-order process at the  $\Gamma$  point of the Brillouin zone.

$$\chi_{zzz}^{(2)} : |P_{AsGa}\rangle \xrightarrow{Q_z} |\Gamma_6\rangle \xrightarrow{Q_z} |\Gamma_8\rangle \xrightarrow{Q_z} |P_{AsGa}\rangle \quad (7.5)$$

By summing up all paths, we derive the perturbation to first order in depletion field  $E$ .

$$\begin{aligned} \delta\chi_{zzz}^{(2)} &\sim \frac{\langle P_{AsGa}^{old} | p_z E | S_{AsGa}^{old} \rangle}{\Delta E_{SP}} \times \\ &[\langle S_{AsGa}^{old} | Q_z | \Gamma_8 \rangle \langle \Gamma_8 | Q_z | \Gamma_{(6)} \rangle_+ + \langle \Gamma_{(6)} |_+ Q_z | P_{AsGa}^{old} \rangle \\ &+ \langle S_{AsGa}^{old} | Q_z | \Gamma_8 \rangle \langle \Gamma_8 | Q_z | \Gamma_{(6)} \rangle_- - \langle \Gamma_{(6)} |_- Q_z | P_{AsGa}^{old} \rangle] \end{aligned} \quad (7.6)$$

Under the assumption of a constant depletion field,  $\delta\chi_{zzz}^{(2)}$  depends linearly on the depletion field  $E$ .

$$\delta\chi_{zzz}^{(2)} \sim \alpha E$$

with

$$\alpha = \frac{\langle P_{AsGa}^{old} | p_z | S_{AsGa}^{old} \rangle}{\Delta E_{SP}} \times$$

$$\begin{aligned}
& [ \langle S_{AsGa}^{old} | Q_z | \Gamma_8 \rangle \langle \Gamma_8 | Q_z | \Gamma_{(6)} \rangle_+ \langle \Gamma_{(6)} |_+ Q_z | P_{AsGa}^{old} \rangle \\
& + \langle S_{AsGa}^{old} | Q_z | \Gamma_8 \rangle \langle \Gamma_8 | Q_z | \Gamma_{(6)} \rangle_- \langle \Gamma_{(6)} |_- Q_z | P_{AsGa}^{old} \rangle ] .
\end{aligned}$$

The photoexcitation-second-harmonic generation experiments have been performed to check this field induced perturbation (see chapter 6). However, experimentally no effects of the second-harmonic intensity have been observed at these resonances for Au:GaAs n-type samples when the photoexcitation light illuminated samples. There are several mechanisms that can be invoked to explain this results. First, perturbation coefficient  $\alpha$  may be small between the localized defect states and the conduction and valence bands at the  $\Gamma$  point of the Brillouin zone in GaAs. Second, since the  $\chi_{zzz}^{(2)}$  is forbidden in bulk, and therefore there is no interference term as compared to the existing bulk  $\chi_{yzx}^{(2)}$  (see chapter 5). As a result, these changes are much more difficult to detect. In addition, in the Au:GaAs n-type system, the minority carriers (holes) drift to interface and recombine with metal electrons. This in turn does not affect the depletion electric field and the band bending.

### 7.3.4 Comparison with interfacial spectra by other techniques

There are a number of experimental observations consistent with the existence of midgap states in this system, however there are very few direct spectroscopic measurements of interface energy levels. Some spectroscopic evidence for interface states has been derived from cathodoluminescence spectra (CLS)[24], inverse photoemission spectra (IPS)[10], and ultraviolet-photoemission spectra (UPS)[23]. but these spectra are very *broad*, and the measurements are not intrinsically sensitive to the buried interface.

In contrast to the CLS, IPS and UPS measurements[24, 10, 23], *sharp* resonant features were observed in our SHG and SFG experiments. For instance, in the case of

ultraviolet-photoemission measurements at very low Au coverages on GaAs surfaces [23], the interface states became broadened when Au coverage increases from 0.1 monolayer to 0.35 monolayer (see figure 7.9). The possible mechanism is that the wavefunctions of metal electron overlap with the interface states [113]. With thick metal overlayer, the overlapping between the metal electron states and the interface states increases and the interface states were broadened. On the other hand, the very sharp spectra we observed suggest that the detected atomic displacement defects occur in bulk GaAs just far enough from the interface so that their interaction with the metal overlayer free electron states is weak.

In the case of cathodoluminescence spectra measurements, high energy electron ( $\sim keV$ ) beam incidenced on GaAs samples, all photon radition from the samples was recorded. By subatracting clean GaAs surface spectra from Au coated GaAs samples, the interface CLS was obtained. However the spectra contributions from the metal overlayer and GaAs bulk were not completely eliminated. In addiation, the luminescence can arise from states above the band gap and is not limited at the direct band gap region. As a result the spectra were broadened (see figure 7.10). In our SHG measurements, the intrinsic interface sensitivity of the second-order nonlinear optical spectroscopies enable us to suppress spectral contributions from the adjoining bulk media, resulting in more specific assignments of the spectral features, and a narrowing of the features by comparison to those observed with competing spectroscopies.

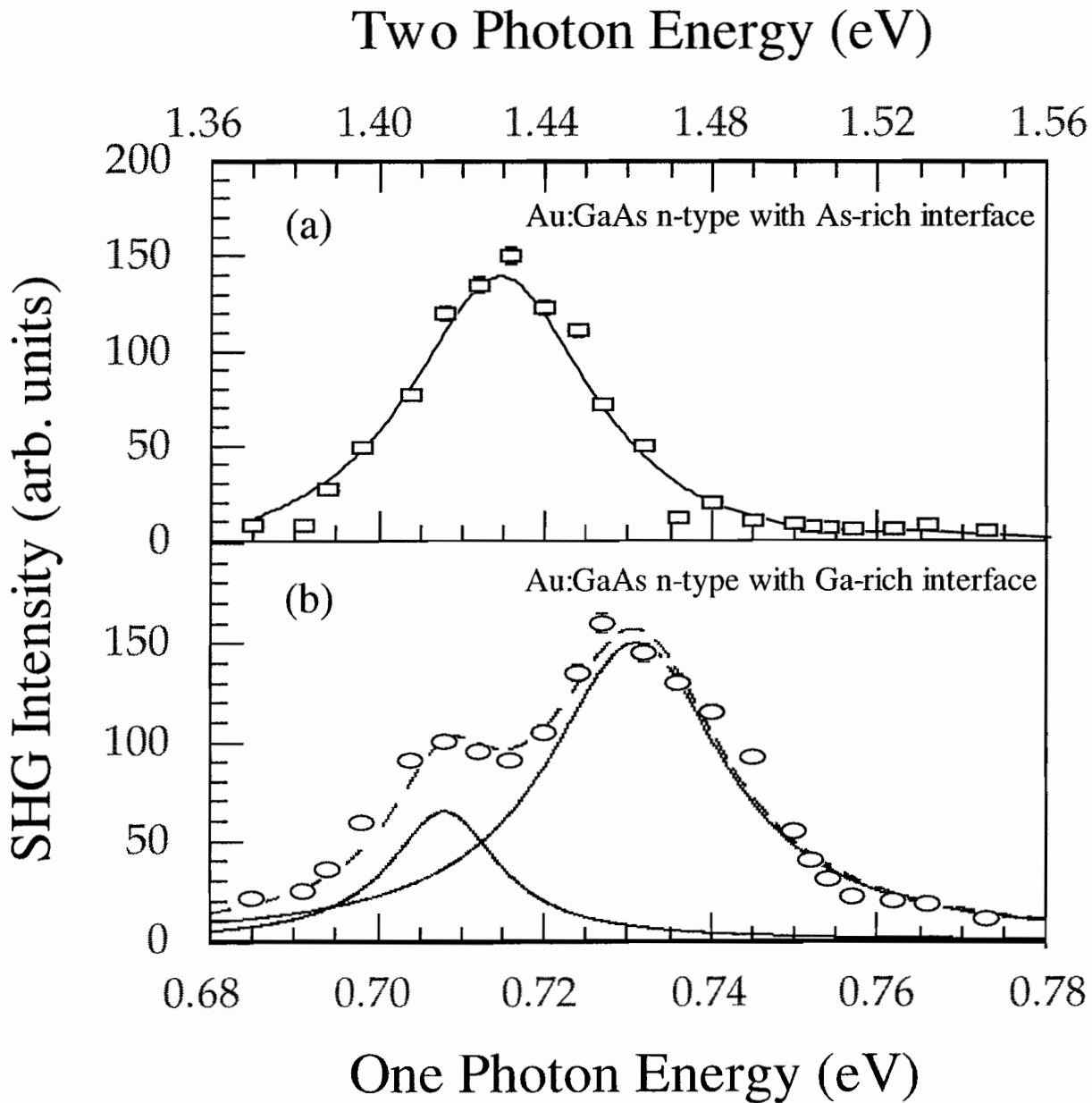


Figure 7.1: In p-in/p-out with  $\phi = 0$  configuration, (a) SHG spectrum from As-rich Au:GaAs n-type sample. The solid line is a guide for the eye; (b) SHG spectrum from Ga-rich Au:GaAs n-type sample. The two solid lines are fits using two Lorentzian line shape shape functions, and the dashed line is the combination of the two lines. The peak positions are estimated to be  $0.708 \pm 0.014$  eV and  $0.731 \pm 0.014$  eV respectively.

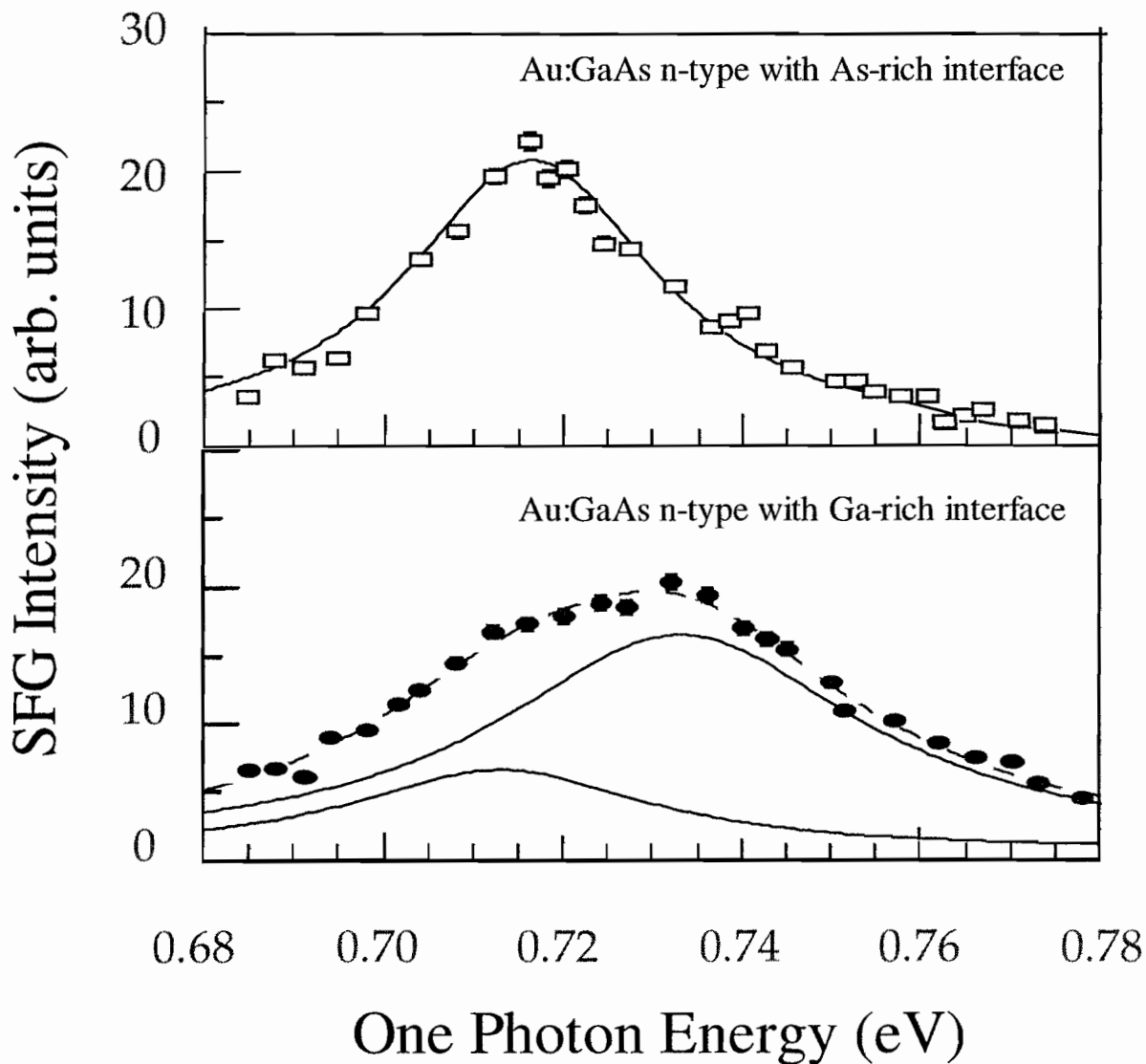


Figure 7.2: In p-in/p-out with  $\phi = 0$  configuration, SFG spectrum from an As-rich interface sample. The solid line is a guide for the eye; In the Ga-rich interface sample, the SFG spectrum was shown below. The two solid lines are fit using two Lorentzian line shape functions, and the dashed line is the combination of both lines. The peak positions are estimated to be  $0.713 \pm 0.014$  eV and  $0.730 \pm 0.014$  eV respectively.

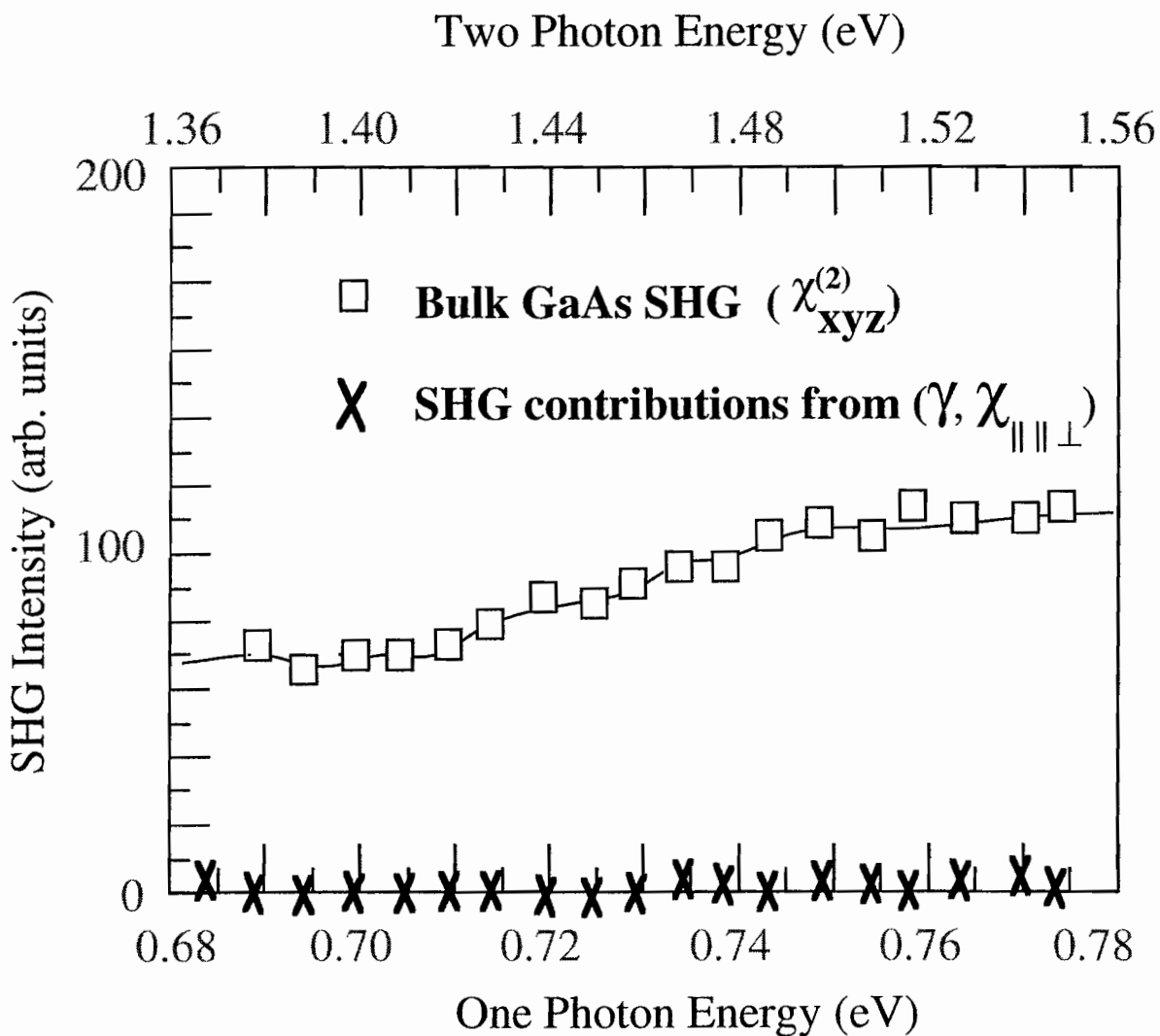


Figure 7.3: Bulk SHG spectra from the Au:GaAs n-type sample; the solid line is a guide for the eye. Both As-rich and Ga-rich interface samples have the same bulk spectra. No resonance features have been observed in the bulk SHG contribution. The SHG contribution from the linear combinations of higher-order bulk  $\gamma$  and surface  $\chi_{||| \perp}^{(2)}$  term was near the noise levels in both n- and p-type systems.

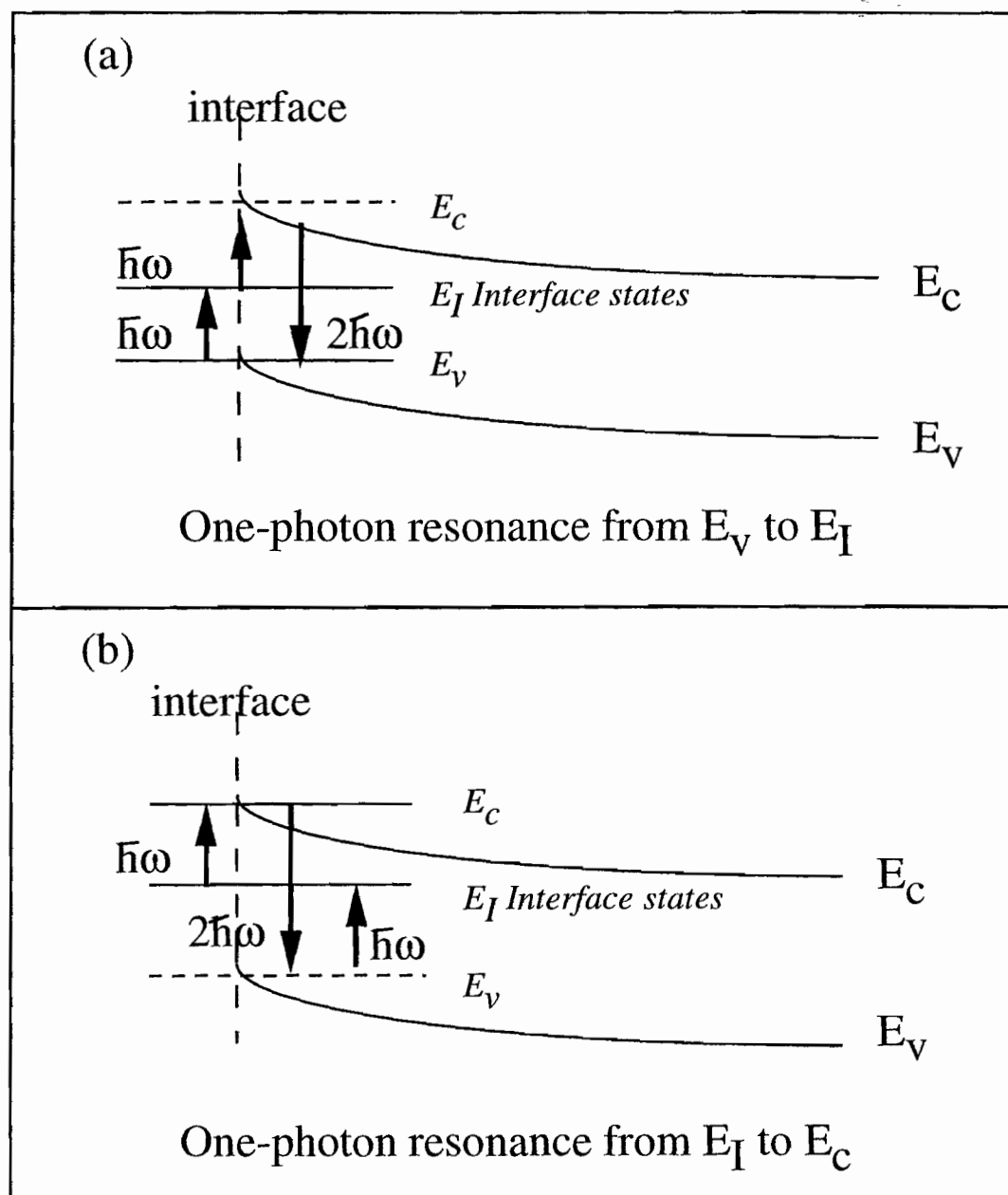


Figure 7.4: Schematic diagram of two probable three-step optical processes  $1 \rightarrow 2 \rightarrow 3$ . Here  $E_v$ ,  $E_I$ , and  $E_c$  represent energies of the valence band maximum, interface states, and conduction band minimum respectively. (a) The transition starts from valence band maximum. The three-step process is represented by  $E_v \xrightarrow{\hbar\omega} E_I \xrightarrow{\hbar\omega} E_c \xrightarrow{2\hbar\omega} E_v$ . (b) The transition starts from interface states. The three-step process is represented by  $E_I \xrightarrow{\hbar\omega} E_c \xrightarrow{2\hbar\omega} E_v \xrightarrow{\hbar\omega} E_I$ .

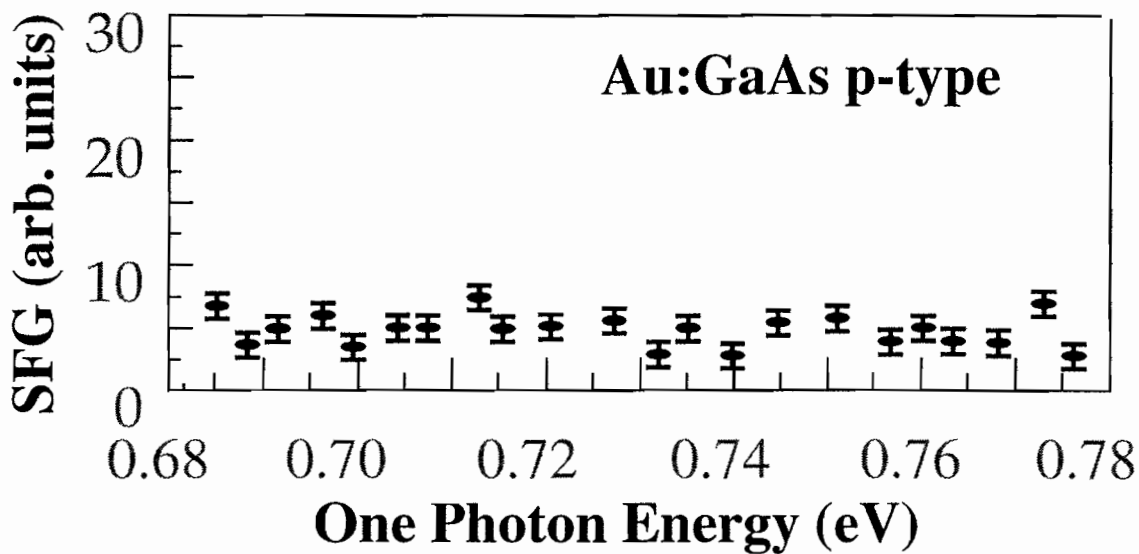
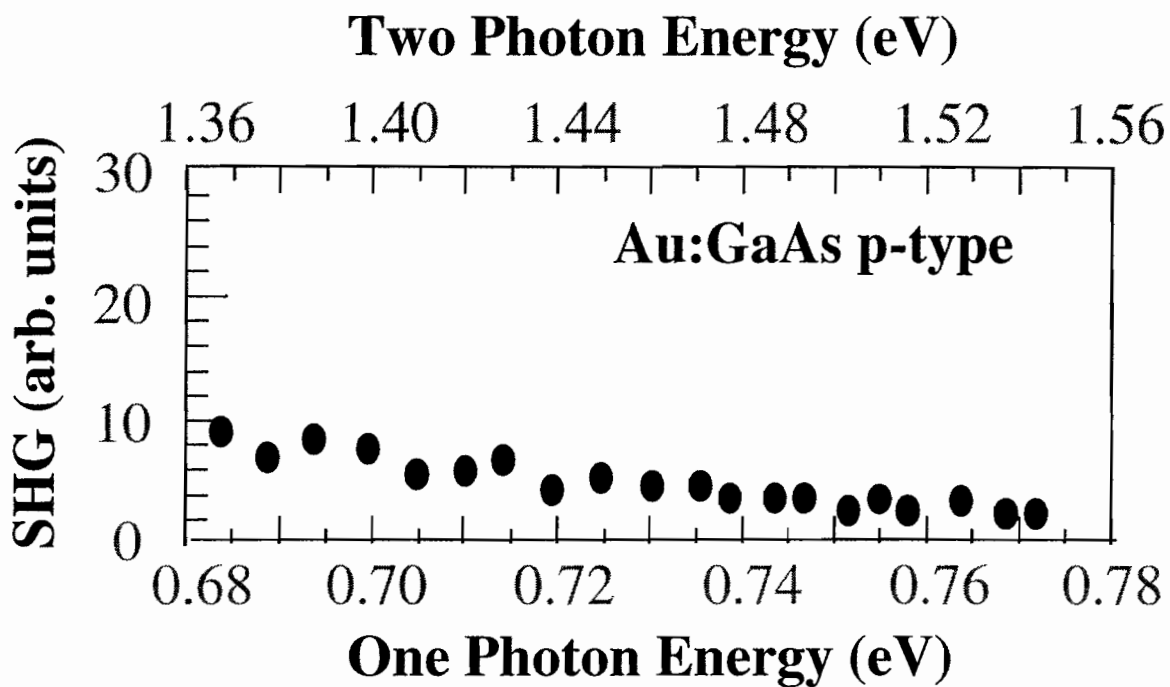


Figure 7.5: Interface SHG and SFG spectra from Au:GaAs p-type system, no resonance features were observed.

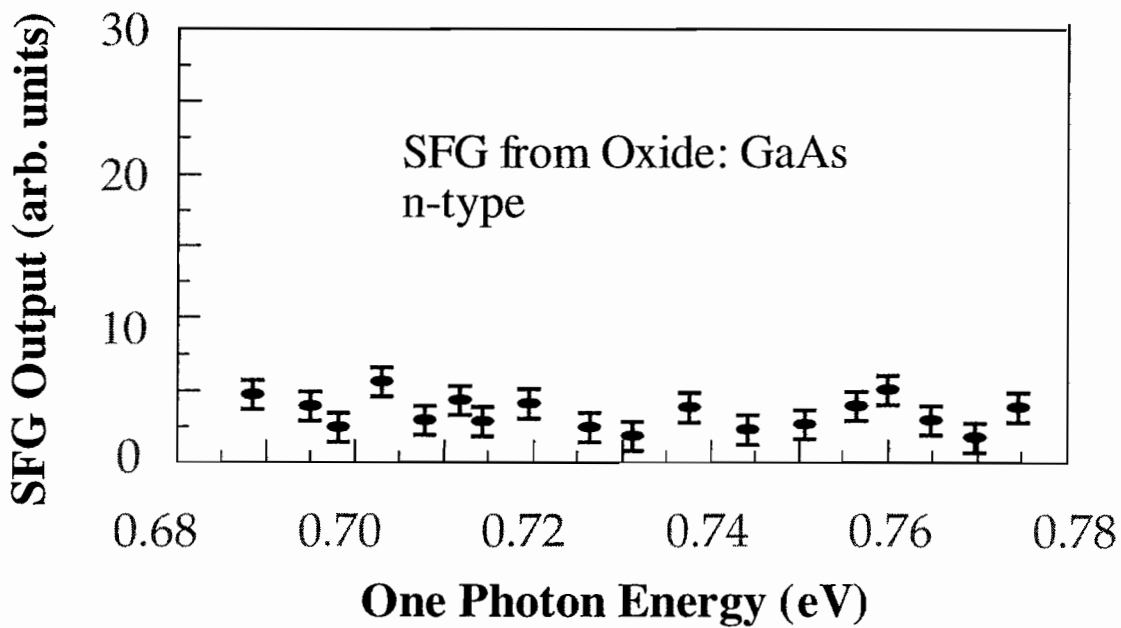
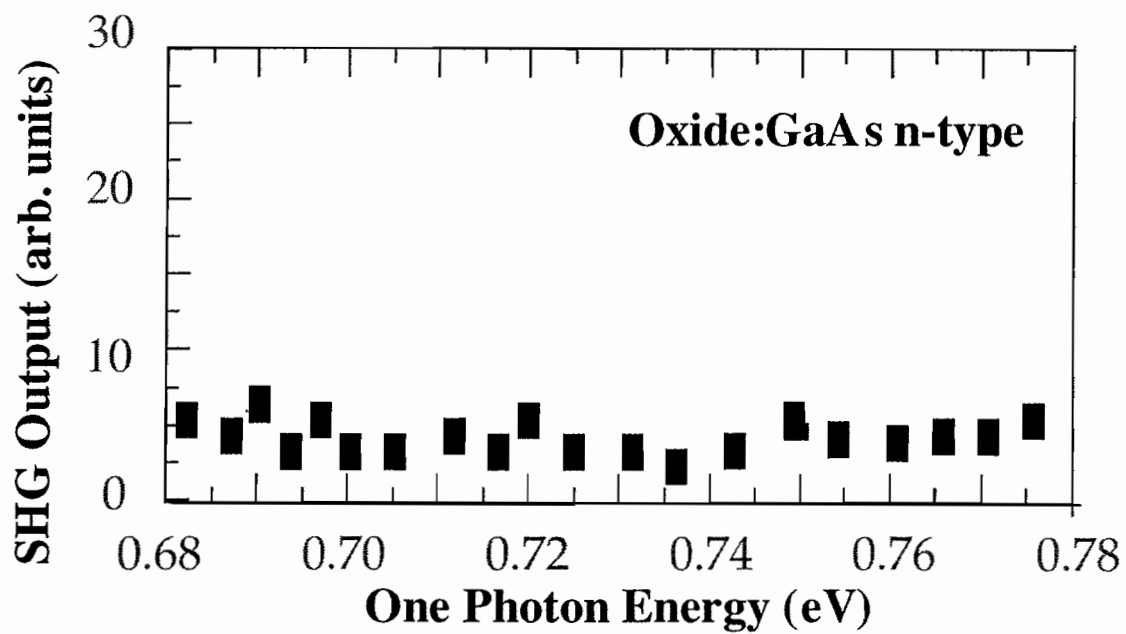


Figure 7.6: Interface SHG and SFG spectra from native oxide GaAs surface, no resonance features were observed.

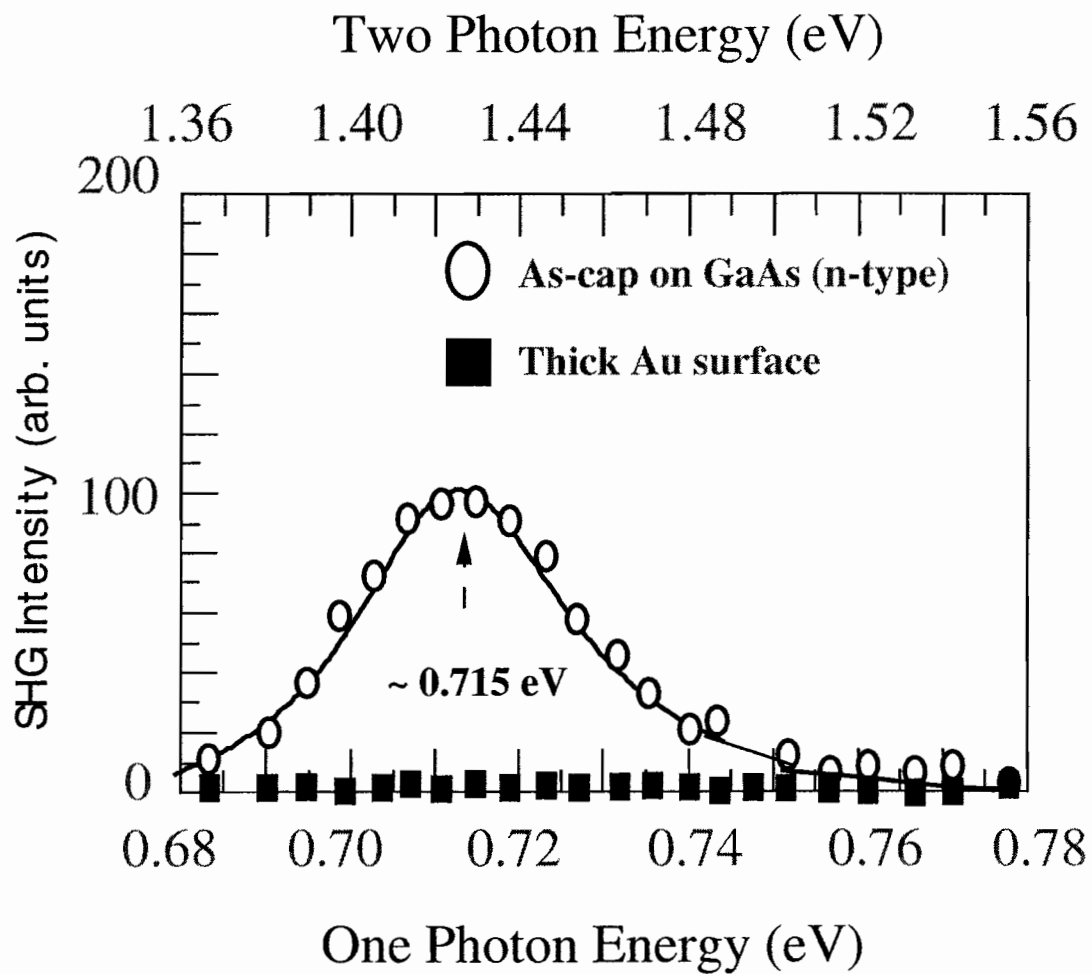


Figure 7.7: Interface SHG spectra from the As capped GaAs n-type sample; the solid line is a guide for the eye. The SHG from thick Au surface was at our noise level.

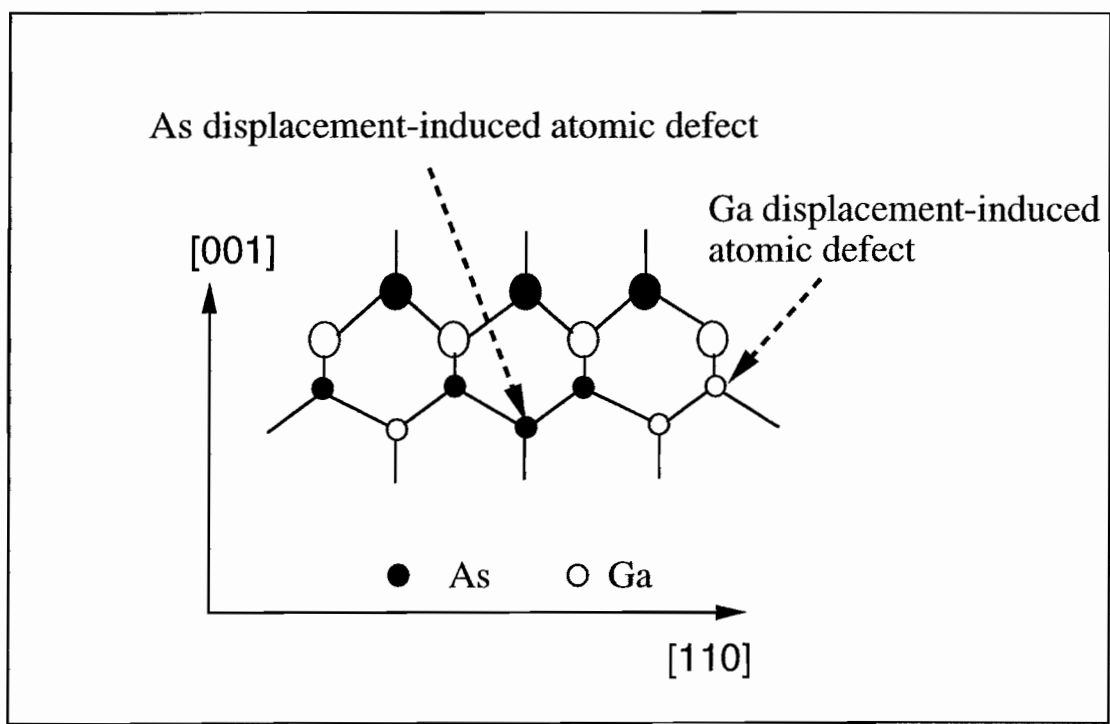


Figure 7.8: Schematic of As and Ga displacement defects.

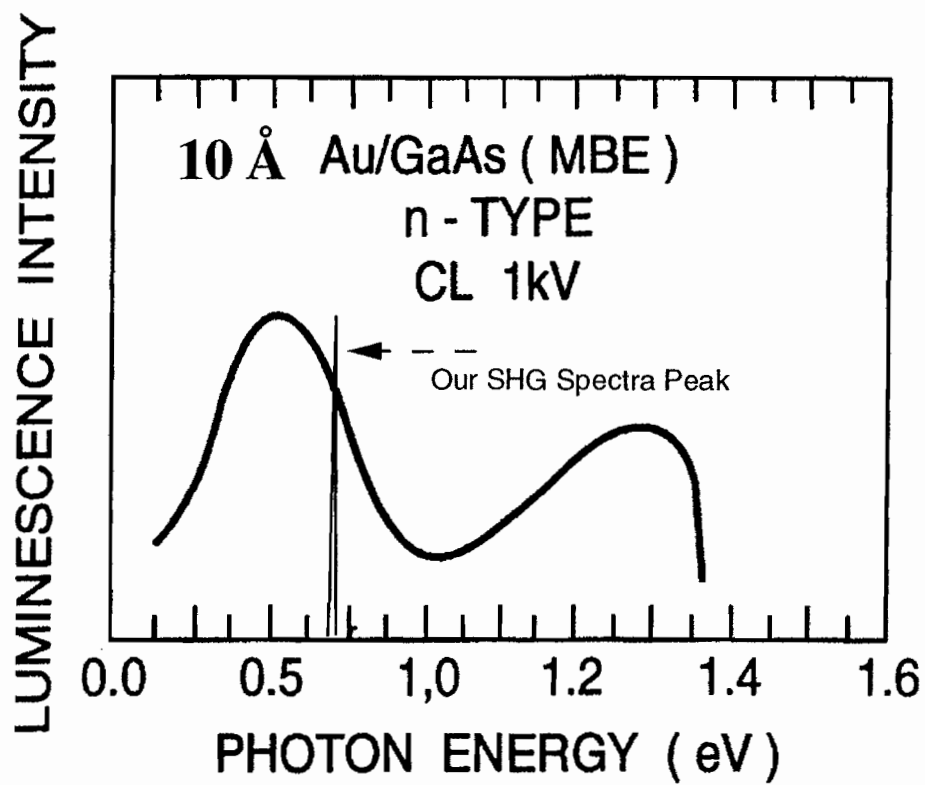


Figure 7.9: In comparison to cathodoluminescence spectra from 10 Å Au on GaAs (from reference 24), Our SHG reveals much sharp resonance feature.

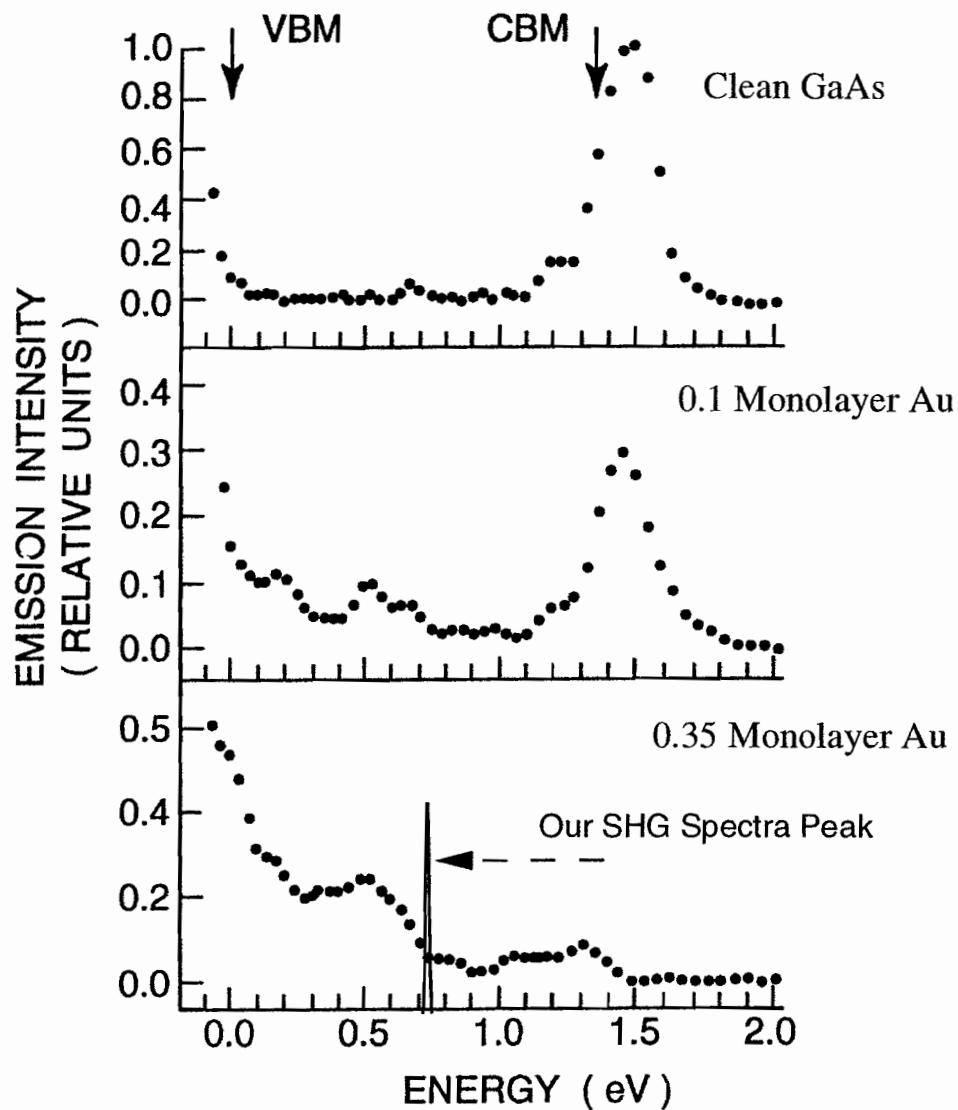


Figure 7.10: In comparison to ultraviolet-photoemission measurements at very low Au coverages on GaAs surfaces from reference 23, the interface states became broadened when Au coverage increases from 0.1 monolayer to 0.35 monolayer

# Chapter 8

## Conclusion

Second-order nonlinear optical spectroscopy has been used to probe the interface electronic structure of GaAs based thin films and interfaces. The nonlinear techniques presented here differ from conventional spectroscopic methods primarily as a result of their symmetry dependence and intrinsic interface sensitivity. In this thesis, one of our primary interests is to study the relation between the sample preparation and the interface electronic structure. We have found that second-order nonlinear optical spectroscopy is sensitive to a variety of *interfacial electronic* phenomena such as interface defect states, surface reconstruction of the buried GaAs, ratio of different atoms during the growth, and depletion electric fields.

Our observations provide strong evidence for the existence of atomic displacement-induced defect states at the buried metal:GaAs interface, and offer energy level information that can be used to check theoretical predictions about this class of interface state. In Au:GaAs n-type systems, we have observed two resonance features at 0.715 eV and 0.731 eV for the Ga-rich interface and one resonance feature at 0.715 eV for the As-rich interface. Similar single resonance features at 0.715 eV were observed in As:GaAs n-type samples, but were not present in oxide:GaAs and metal:GaAs p-type systems. All resonance features were confirmed to be one-photon resonances. After

consideration of various three-step optical processes, we conclude that the transitions originate from the midgap states. We suggest that the interfacial resonance features arise from the existence of atomic displacement-induced defect states near the junction.

Consider further the metal:GaAs p-type system. The electrons in the neutral s-like As antisite ground state (0.5 eV above the valence band maximum) can be discharged using highly p-doped GaAs samples. Since the dipole transition between the valence band maximum and the s-like As antisite ground state is allowed, the resonance ( $\hbar\omega \sim 0.5eV$ ) between the valence band maximum and the ground level s-like of As antisite state will be expected in such systems. To map out the whole range of states within the band gap, the spectral light needs to be tunable from infrared to mid-infrared. As a result, SHG photon energy will be within the infrared range, and the quantum efficiency of PMT can not cover this range. Therefore one solution is to upconvert the SHG signal to visible range through a nonlinear crystal by sum frequency. In such case, the spectral informations of the upconverting nonlinear crystal must be well studied in order to calibrate our signals. In addition, we had to consider the water absorption spectrum in the mid-infrared region ( $\sim 0.5eV$ ). The beam lines should be moisture-free. Due to the OH bonds inside the quartz crystal, we had to find another nonlinear crystal as our reference line. To increase the nonlinear optical signal, we can also utilize other infrared light sources such as free electron laser (FEL).

In the case of the native oxide GaAs system, we have studied depletion electric field induced effects on the existing bulk second-order nonlinear susceptibility  $\chi_{yz}^{(2)}$ , and provided information about surface states lifetimes and carrier transport along the surface of n- and p-type GaAs crystals. Our experiments reveal that the dominant perturbation caused by the depletion electric field is on the *existing bulk* nonlinearity  $\chi_{yz}^{(2)}$ . Through studies as a function of dopant type and concentration,

we demonstrate that the bulk  $\chi_{yxz}^{(2)}$  is systematically reduced as a result of the depletion field, and that this diminution depends on the square of the near surface depletion field. This is consistent with our theoretical calculations. Our measurements illustrate a potentially useful method to probe changes in symmetry and band bending in the near surface region of a semiconductor. This information is often of interest in materials and device applications.

In addition, the photomodulation-second-harmonic generation (PSHG) experiments reveal that  $\chi_{yxz}^{(2)}$  in *doped* GaAs can be *enhanced* by carrier excitation in the depletion region. By utilizing this technique, we measured the surface minority trap lifetimes. Our experimental results suggest that all of our samples exhibit approximately the same trap lifetime ( $\sim 25$  seconds). This suggests that the surface recombination process is the slowest step in discharging the traps on the surface. Finally, spatially separated second-harmonic generating and photocarrier exciting light beams were employed to study transverse diffusion of carriers confined near GaAs(001) surfaces. Our measurements suggest that surface charge transport is isotropic and diffusive, with diffusion coefficients small relative to the bulk. We present an activated free carrier diffusion model to explain our observations in which minority carriers diffuse and trap between surface free carrier bands and localized defect states. Knowledge about these quantities is essential for a full understanding of surface traps and charge transport at the surfaces and is of use in the analysis of transport in lower dimensional devices such as quantum well heterostructures.

The success of these experiments suggest that this technique has the potential to be a useful noncontact probe of interfacial electronic properties. By utilizing this technique, we can study crystal electronic and structural defects during sample growth. This might enable us to develop a microscopic understanding of the relationship between interface electronic structures and interface preparation, which in turn may help us to achieve better crystal growth conditions and design better electronic devices.

This technique can further be applied to the study of wide-gap semiconductors such as  $Al_xGa_{1-x}N$ .  $Al_xGa_{1-x}N$  is a compound semiconductor system with a tunable and direct band gap from 2 to 6.2 eV, which makes it ideal for optoelectronic devices in the visible and ultraviolet light region. One of its most important characteristics is its band-gap value. In this case, the symmetry sensitivity of second-order nonlinear optical processes enables us to suppress contributions from the adjoining substrate, resulting in more accurate measurements of the band gap. In addition, because there are very few lattice-matching substrates for this system, the electronic properties are largely affected by the substrates. The most widely used substrate is sapphire, which has a mismatch of 22% for InN, 14% for GaN, and 12% for AlN. Thus the interfacial junction suffers internal strains, and misfit dislocations are produced at the buried interface as a result of an abrupt strain relaxation. In such cases, interface SHG may reveal interface reconstructions, interface defect states, and the critical growth thickness. Besides the misfit dislocation induced defects at the interface, there are many other defects inside the bulk such as a N vacancy ( $V_N$ ) which is located at 30, 100, and 400 meV below the conduction band in GaN. These defects significantly affect the performance of wide-gap semiconductor based devices. For example, laser diodes degrade because the defects act as non-radiative recombination centers. By utilizing second-order nonlinear optical spectroscopy, we would separately identify the interface and bulk defects. Furthermore, we would study the relationship between the defect states and sample preparation to find the best crystal growth conditions.

# Appendix A

## The transition matrix using dipole operator $\vec{Q}$

In this appendix, based on our three-level model we calculate the electric dipole transition matrix between the top valence band ( $|\Gamma_8 \rangle$ ) and the two lowest conduction bands ( $|\Gamma_6 \rangle$  and  $|\Gamma_7 \rangle$ ) at the  $\Gamma$  point in the Brillouin zone.  $\phi_\nu^{(6)}$ ,  $\phi_{\nu'}^{(7)}$ , and  $\phi_\mu^{(8)}$  represent wavefunctions of  $|\Gamma_6 \rangle$ ,  $|\Gamma_7 \rangle$ , and  $|\Gamma_8 \rangle$  states respectively.

The calculation of the matrices  $\langle \phi_\nu^{(6)} | Q | \phi_{\nu'}^{(7)} \rangle$ ,  $\langle \phi_\nu^{(6)} | Q | \phi_\mu^{(8)} \rangle$ , and  $\langle \phi_{\nu'}^{(7)} | Q | \phi_\mu^{(8)} \rangle$  are fully based on group symmetry operations. Each wave function has its own symmetry group ( $\Gamma_6, \Gamma_7, \Gamma_8$ ) and can be expanded in certain basis functions, such as  $XYZ$  (see text). The basis functions are not the exact mathematical expression of the wavefunction, but a mathematical expression which transforms with exactly the same symmetry in the irreducible representation [100, 101]. The three state wave functions are shown in the text. All dipole transition elements are projected into the irreducible representations of  $\bar{T}_d$  and expanded by its eigenvector functions.

## A.1 $\langle \phi_{\nu}^{(6)} | Q | \phi_{\nu'}^{(7)} \rangle$

The wavefunction of  $\phi_{\nu}^{(6)}$  with its spatial part  $f_0(r)$  belongs to the  $\Gamma_1$  symmetry group. As a result,  $\langle \phi_{\nu}^{(6)} | Q | \phi_{\nu'}^{(7)} \rangle$  is zero unless product of  $Q | \phi_{\nu'}^{(7)} \rangle$  contains the eigenvector of  $\Gamma_1$ .  $Q | \phi_{\nu'}^{(7)} \rangle$  involves the spatial functions  $QX$ ,  $QY$ , and  $QZ$ , which can be written as nine functions

$$Q_x X, Q_y Y, Q_z Z, Q_x Y, Q_x Z, Q_y X, Q_y Z, Q_z X, Q_z Y$$

These nine wave functions can be projected into various irreducible representations of  $T_d$  according to Table 5.1 [100, 101]:

$$\Gamma_1 : \kappa_0 = Q_x X + Q_y Y + Q_z Z \quad (\text{A.1})$$

$$\Gamma_3 : \kappa_1 = 2Q_z Z - Q_x X - Q_y Y; \kappa_2 = \sqrt{3}(Q_x X - Q_y Y) \quad (\text{A.2})$$

$$\Gamma_4 : \kappa_{\xi} = \frac{1}{2}(Q_y Z - Q_z Y); \kappa_{\eta} = \frac{1}{2}(Q_z X - Q_x Z); \kappa_{\zeta} = \frac{1}{2}(Q_x Y - Q_y X) \quad (\text{A.3})$$

$$\Gamma_5 : \kappa_x = \frac{1}{2}(Q_y Z + Q_z Y); \kappa_y = \frac{1}{2}(Q_z X + Q_x Z); \kappa_z = \frac{1}{2}(Q_x Y + Q_y X) \quad (\text{A.4})$$

Here  $\Gamma_1, \Gamma_3, \Gamma_4$ , and  $\Gamma_5$  represent four different symmetry groups with their corresponding eigenvectors  $\kappa_0$ ;  $\kappa_1, \kappa_2$ ;  $\kappa_{\xi}, \kappa_{\eta}, \kappa_{\zeta}$ ; and  $\kappa_x, \kappa_y, \kappa_z$ . The nine functions can be expanded by the eigenvector functions of  $T_d$ .

$$Q_x X = \frac{1}{3}\kappa_0 - \frac{1}{6}\kappa_1 + \frac{1}{2\sqrt{3}}\kappa_2 \quad (\text{A.5})$$

$$Q_y Y = \frac{1}{3}\kappa_0 - \frac{1}{6}\kappa_1 - \frac{1}{2\sqrt{3}}\kappa_2 \quad (\text{A.6})$$

$$Q_z Z = \frac{1}{3}\kappa_0 + \frac{1}{3}\kappa_1 \quad (\text{A.7})$$

$$Q_x Y = \kappa_{\zeta} + \kappa_z \quad (\text{A.8})$$

$$Q_x Z = \kappa_y - \kappa_{\eta} \quad (\text{A.9})$$

$$Q_y X = \kappa_z - \kappa_{\zeta} \quad (\text{A.10})$$

$$Q_y Z = \kappa_{\xi} + \kappa_x \quad (\text{A.11})$$

$$Q_z X = \kappa_{\eta} + \kappa_y \quad (\text{A.12})$$

$$Q_z Y = \kappa_x - \kappa_{\xi} \quad (\text{A.13})$$

Here each function can have several different symmetry eigenvectors. From the above formulas, we can easily find the functions which contain the  $\kappa_0$  eigenvector of  $\Gamma_1$ . As a result, the nonzero matrix elements are;

$$d_0 = \frac{1}{\sqrt{6}} \int f Q_x X d\vec{r} = \frac{1}{\sqrt{6}} \int f Q_y Y d\vec{r} = \frac{1}{\sqrt{6}} \int f Q_z Z d\vec{r}$$

Thus the  $\langle \phi_\nu^{(6)} | Q | \phi_{\nu'}^{(7)} \rangle$  can be derived. For example

$$\langle \phi_{\frac{1}{2}}^{(6)} | Q | \phi_{\frac{1}{2}}^{(7)} \rangle = \frac{1}{\sqrt{3}} \int f Q_z Z d\vec{r}$$

Finally the matrix elements  $\langle \phi_\nu^{(6)} | Q | \phi_{\nu'}^{(7)} \rangle$  can be calculated.

$$\langle \phi^{(7)} | Q | \phi^{(6)} \rangle = \sqrt{2} d_0 \begin{pmatrix} \hat{z} & \hat{x} + i\hat{y} \\ \hat{x} - i\hat{y} & \hat{z} \end{pmatrix}.$$

Here  $\hat{x}$ ,  $\hat{y}$ , and  $\hat{z}$  represent the results of the dipole moment operator acting on different axes, i.e.,  $Q_x$ ,  $Q_y$ , and  $Q_z$ .

## A.2 $\langle \phi_\nu^{(6)} | Q | \phi_\mu^{(8)} \rangle$

The  $\langle \phi_\nu^{(6)} | Q | \phi_\mu^{(8)} \rangle$  can be derived by the same method employed for the  $\langle \phi_\nu^{(6)} | Q | \phi_{\nu'}^{(7)} \rangle$  matrix.  $Q | \phi_\mu^{(8)} \rangle$  also involves the spatial functions  $QX$ ,  $QY$ , and  $QZ$ , which can be written as nine functions as shown above. These nine wave functions can be projected onto various irreducible representations of  $T_d$ . The only wavefunctions of the  $Q | \phi_\mu^{(8)} \rangle$  which contain  $\kappa_0$  will form a nonzero product element with the wavefunction  $\phi_\nu^{(6)}$ .

The results are

$$d_0 = \frac{1}{\sqrt{6}} \int f Q_x X d\vec{r} = \frac{1}{\sqrt{6}} \int f Q_y Y d\vec{r} = \frac{1}{\sqrt{6}} \int f Q_z Z d\vec{r}$$

For example,

$$\langle \phi_{\frac{1}{2}}^{(6)} | Q | \phi_{\frac{3}{2}}^{(8)} \rangle = \frac{1}{\sqrt{2}} \int f Q(X + iY) d\vec{r} = \frac{1}{\sqrt{2}} (\hat{x} + i\hat{y}) \int f Q_x X d\vec{r}$$

As a result, the matrix element  $\langle \phi_{\frac{1}{2}}^{(6)} | Q | \phi_{\frac{3}{2}}^{(8)} \rangle$  is

$$\langle \phi^{(6)} | Q | \phi^{(8)} \rangle = d_0 \begin{pmatrix} \sqrt{3}(\hat{x} + \hat{y}) & -2i\hat{z} & (\hat{x} - i\hat{y}) & 0 \\ 0 & i(\hat{x} + i\hat{y}) & 2\hat{z} & \sqrt{3}(\hat{x} - i\hat{y}) \end{pmatrix}.$$

### A.3 $\langle \phi_{\nu'}^{(7)} | Q | \phi_{\mu}^{(8)} \rangle$

The product of  $Q|\phi_{\mu}^{(8)}\rangle$  contains the same spatial functions  $QX$ ,  $QY$ , and  $QZ$ , which can be written as nine functions as shown before. Now the spatial parts of  $\phi_{\nu'}^{(7)}$  contain  $X$ ,  $Y$ , and  $Z$ , which belong to the symmetry group  $\Gamma_5$ . As a result,  $Q|\phi_{\mu}^{(8)}\rangle$  must contain eigenvectors  $\kappa_x$ ,  $\kappa_y$ , and  $\kappa_z$  of  $\Gamma_5$  symmetry in order to have nonzero transition elements. In other words, only wavefunctions of  $Q|\phi_{\mu}^{(8)}\rangle$  which contain  $\kappa_{x,y,z}$  elements will form nonzero transition elements with the wavefunction  $\phi^{(7)}$ . By checking the nine functions in terms of irreducible representation  $T_d$  eigenvectors, we find that the nonzero matrix elements are

$$\begin{aligned} d'_0 &= -\frac{i}{\sqrt{6}} \int XQ_y Z d\vec{r} = -\frac{i}{\sqrt{6}} \int XQ_z Y d\vec{r} = -\frac{i}{\sqrt{6}} \int YQ_x Z d\vec{r} \quad (\text{A.14}) \\ &= -\frac{i}{\sqrt{6}} \int YQ_z X d\vec{r} = -\frac{i}{\sqrt{6}} \int ZQ_y X d\vec{r} = -\frac{i}{\sqrt{6}} \int ZQ_x Y d\vec{r} \end{aligned}$$

Therefore the matrix elements can be calculated as follows. For example,

$$\langle \phi_{\frac{1}{2}}^{(7)} | Q | \phi_{\frac{3}{2}}^{(8)} \rangle = \frac{1}{\sqrt{6}} \int ZQ(X + iY) d\vec{r} = \frac{1}{\sqrt{6}} (\hat{y} + i\hat{x}) \int ZQ_x Y d\vec{r}$$

Finally the whole matrix  $\langle \phi_{\nu'}^{(7)} | Q | \phi_{\mu}^{(8)} \rangle$  can be written as

$$\langle \phi^{(7)} | Q | \phi^{(8)} \rangle = d'_0 \begin{pmatrix} -(\hat{x} - i\hat{y}) & 0 & \sqrt{3}(\hat{x} + i\hat{y}) & 2i\hat{z} \\ -2\hat{z} & i\sqrt{3}(\hat{x} - i\hat{y}) & 0 & -i(\hat{x} + i\hat{y}) \end{pmatrix}.$$

# Appendix B

## Nonzero Electric Dipole Transition Paths

In this Appendix we calculate all possible electric dipole transition paths in the three level system to determine the nonzero second-order optical processes. In a p-in/s-out configuration with the crystal axis [100] in the plane of incidence, we probe the SHG contributions from the bulk second-order susceptibility  $\chi_{yxz}^{(2)}$  and  $\chi_{yzx}^{(2)}$ , where  $\chi_{yxz}^{(2)} = \chi_{yzx}^{(2)}$ . The interband transition is determined by a three-wave mixing process at the  $\Gamma$  point of Brillouin zone.

$$\chi_{yxz,yxz}^{(2)} \sim \Gamma_8 \xrightarrow{Q_z \text{ or } x} \Gamma_6 \xrightarrow{Q_x \text{ or } z} \Gamma_7 \xrightarrow{Q_y} \Gamma_8 \quad (\text{B.1})$$

Here  $Q_x$ ,  $Q_y$ , and  $Q_z$  represent the dipole matrix elements with different polarizations. The perturbed states have been given in the main text. The nonzero transition elements were been derived in Appendix A. For example, the transition

$$\Gamma_6(\nu = +) \xrightarrow{Q_y} \Gamma_8(\mu = \frac{3}{2})$$

can be written as

$$\begin{aligned} & \langle \phi_{\frac{3}{2}}^{(8)} | Q_y | \phi_+^{(6)} \rangle \\ &= \langle \phi_{\frac{3}{2}}^{(8)} | Q_y [ i g_6 | \phi_0^{(8)} \rangle_{\frac{1}{2}} - h_6^* | \phi_0^{(7)} \rangle_{\frac{1}{2}} + | \phi_0^{(6)} \rangle_{\frac{1}{2}} ] \end{aligned} \quad (\text{B.2})$$

$$= (d + d')g_6 + id'_0 h_6^* - \sqrt{3}id_0^*$$

Thus all the possible transition elements can be calculated and listed below; the nonzero transition paths in  $\langle \phi^{(6)} | Q_z | \phi^{(8)} \rangle$  are:

$$\Gamma_8(\mu = +\frac{3}{2}) \xrightarrow{Q_z} \Gamma_6(\nu = -) : -2h_6 d'_0 + i(d + 3d')g_6^* \quad (\text{B.3})$$

$$\Gamma_8(\mu = +\frac{1}{2}) \xrightarrow{Q_z} \Gamma_6(\nu = +) : -2id_0 \quad (\text{B.4})$$

$$\Gamma_8(\mu = -\frac{1}{2}) \xrightarrow{Q_z} \Gamma_6(\nu = -) : 2d_0 \quad (\text{B.5})$$

$$\Gamma_8(\mu = -\frac{3}{2}) \xrightarrow{Q_z} \Gamma_6(\nu = +) : -2id'_0 h_6 - (d + 3d')g_6^* \quad (\text{B.6})$$

The nonzero transition paths in  $\langle \phi^{(6)} | Q_x | \phi^{(8)} \rangle$  are:

$$\Gamma_8(\mu = +\frac{3}{2}) \xrightarrow{Q_x} \Gamma_6(\nu = +) : \sqrt{3}d_0 + d'_0 h_6 + idg_6^* \quad (\text{B.7})$$

$$\Gamma_8(\mu = +\frac{1}{2}) \xrightarrow{Q_x} \Gamma_6(\nu = -) : id_0 + i\sqrt{3}d'_0 h_6 - \sqrt{3}d'g_6^* \quad (\text{B.8})$$

$$\Gamma_8(\mu = -\frac{1}{2}) \xrightarrow{Q_x} \Gamma_6(\nu = +) : d_0 - \sqrt{3}d'_0 h_6 - \sqrt{3}id'g_6^* \quad (\text{B.9})$$

$$\Gamma_8(\mu = -\frac{3}{2}) \xrightarrow{Q_x} \Gamma_6(\nu = -) : \sqrt{3}id_0 - id'_0 h_6 + dg_6^* \quad (\text{B.10})$$

The nonzero transition paths in  $\langle \phi^{(7)} | Q_x | \phi^{(6)} \rangle$  are:

$$\Gamma_6(\nu = +) \xrightarrow{Q_x} \Gamma_7(\nu' = -) : \quad (\text{B.11})$$

$$-\sqrt{3}d'_0 g_6 - d_0 g_6 h_6^* + ig_6 g_7^* d^* + \sqrt{2}d_0^* h_6^* h_6^* + \sqrt{2}d_0 - \sqrt{3}d_0^* g_7^* - d_0^* h_6^* h_6^*$$

$$\Gamma_6(\nu = -) \xrightarrow{Q_x} \Gamma_7(\nu' = +) : \quad (\text{B.12})$$

$$\sqrt{3}d'_0 g_6 + d_0 g_6 h_6^* + ig_6 g_7^* d^* + \sqrt{2}d_0^* h_6^* h_6^* + \sqrt{2}d_0 + \sqrt{3}d_0^* g_7^* - d_0^* h_6^* h_6^*$$

The nonzero transition paths in  $\langle \phi^{(7)} | Q_z | \phi^{(6)} \rangle$  are:

$$\Gamma_6(\nu = +) \xrightarrow{Q_z} \Gamma_7(\nu' = +) : \quad (\text{B.13})$$



## Appendix C

# Depletion field $E\hat{z}$ effects on second-order Susceptibility $\chi_{yxz}^{(2)}$

In this appendix, we calculate the depletion field  $E\hat{z}$  effects on second-order susceptibility  $\chi_{yxz}^{(2)}$ . According to the results of appendix A and B, the perturbation of  $\chi_{yxz}^{(2)}$  and  $\chi_{yzx}^{(2)}$  can be derived in orders of  $E_z\hat{z}$ .

All possible transition paths for  $\chi_{yxz}^{(2)}$  or  $\chi_{yzx}^{(2)}$  are written down as follows:

$\chi_{yxz}^{(2)}$ :

$$|\phi_0^{(8)}\rangle_{\frac{3}{2}} \xrightarrow{Q_z} |\phi_0^{(6)}\rangle_- \xrightarrow{Q_x} |\phi_0^{(7)}\rangle_+ \xrightarrow{Q_y} |\phi_0^{(8)}\rangle_{\frac{3}{2}} \quad (\text{C.1})$$

$$|\phi_0^{(8)}\rangle_{\frac{1}{2}} \xrightarrow{Q_z} |\phi_0^{(6)}\rangle_+ \xrightarrow{Q_x} |\phi_0^{(7)}\rangle_- \xrightarrow{Q_y} |\phi_0^{(8)}\rangle_{\frac{1}{2}} \quad (\text{C.2})$$

$$|\phi_0^{(8)}\rangle_{-\frac{1}{2}} \xrightarrow{Q_z} |\phi_0^{(6)}\rangle_+ \xrightarrow{Q_x} |\phi_0^{(7)}\rangle_- \xrightarrow{Q_y} |\phi_0^{(8)}\rangle_{-\frac{1}{2}} \quad (\text{C.3})$$

$$|\phi_0^{(8)}\rangle_{-\frac{3}{2}} \xrightarrow{Q_z} |\phi_0^{(6)}\rangle_+ \xrightarrow{Q_x} |\phi_0^{(7)}\rangle_- \xrightarrow{Q_y} |\phi_0^{(8)}\rangle_{-\frac{3}{2}} \quad (\text{C.4})$$

$\chi_{yzx}^{(2)}$ :

$$|\phi_0^{(8)}\rangle_{\frac{3}{2}} \xrightarrow{Q_x} |\phi_0^{(6)}\rangle_+ \xrightarrow{Q_z} |\phi_0^{(7)}\rangle_+ \xrightarrow{Q_y} |\phi_0^{(8)}\rangle_{\frac{3}{2}} \quad (\text{C.5})$$

$$|\phi_0^{(8)}\rangle_{\frac{1}{2}} \xrightarrow{Q_x} |\phi_0^{(6)}\rangle_- \xrightarrow{Q_z} |\phi_0^{(7)}\rangle_- \xrightarrow{Q_y} |\phi_0^{(8)}\rangle_{\frac{1}{2}} \quad (\text{C.6})$$

$$|\phi_0^{(8)}\rangle_{-\frac{1}{2}} \xrightarrow{Q_x} |\phi_0^{(6)}\rangle_+ \xrightarrow{Q_z} |\phi_0^{(7)}\rangle_+ \xrightarrow{Q_y} |\phi_0^{(8)}\rangle_{-\frac{1}{2}} \quad (\text{C.7})$$

$$|\phi_0^{(8)}\rangle_{-\frac{3}{2}} \xrightarrow{Q_x} |\phi_0^{(6)}\rangle_- \xrightarrow{Q_z} |\phi_0^{(7)}\rangle_- \xrightarrow{Q_y} |\phi_0^{(8)}\rangle_{-\frac{3}{2}} \quad (C.8)$$

Each path can easily be derived by utilizing the results of Appendix B. In the case of  $\chi_{yxz}^{(2)}$ , for example, the contribution from a particular path in  $\chi_{yxz}^{(2)}$ , e.g.

$$|\phi_0^{(8)}\rangle_{\frac{3}{2}} \xrightarrow{Q_z} |\phi_0^{(6)}\rangle_- \xrightarrow{Q_x} |\phi_0^{(7)}\rangle_+ \xrightarrow{Q_y} |\phi_0^{(8)}\rangle_{\frac{3}{2}}$$

can be given by

$$\begin{aligned} \chi_{yxz}^{(2)} : & [-2h_6 d'_0 + i(d + 3d')g_6^*][\sqrt{3}d'_0 g_6 - d_0 g_6 h_6^* + i g_6 g_7^* d^* \\ & + \sqrt{2}d_0^* h_6^* h_6^* + \sqrt{2}d_0 + \sqrt{3}d_0^* g_7^* - d_0^* h_6^* h_6^*][-\sqrt{3}d' g_7 - i\sqrt{3}d_0^* h_6 - id_0^*] . \end{aligned} \quad (C.9)$$

Note,  $g_6$ ,  $g_7$ , and  $h_6$  are linearly dependent on the electric field  $E$  as derived in chapter 5. In this path, the zeroth order of  $\chi_{yxz}^{(2)}$  to the fields  $E$  is zero. We find to first order in  $E$ ,

$$\delta\chi_{yxz}^{(2)} : -\sqrt{2}id_0 d' (-2h_6 d'_0 + i(d + 3d')g_6^*)$$

For another path such as

$$|\phi_0^{(8)}\rangle_{\frac{1}{2}} \xrightarrow{Q_z} |\phi_0^{(6)}\rangle_- \xrightarrow{Q_x} |\phi_0^{(7)}\rangle_- \xrightarrow{Q_y} |\phi_0^{(8)}\rangle_{\frac{1}{2}} ,$$

the result is given by

$$\begin{aligned} \chi_{yxz}^{(2)} : & -2id_0[-\sqrt{3}d'_0 g_6 - d_0 g_6 h_6^* + i g_6 g_7^* d^* + \sqrt{2}d_0^* h_6^* h_6^* + \sqrt{2}d_0 - \\ & \sqrt{3}d_0^* g_7^* - d_0^* h_6^* h_6^*][-idg_7 + d_0^* h_6 + \sqrt{3}d_0^*] . \end{aligned} \quad (C.10)$$

In this path, the zeroth order of the field  $E$  is nonzero, and the unperturbed second-order susceptibility can be written as

$$\chi_{yxz}^{(2),old} : -2i\sqrt{6}d_0^2 d_0^*$$

We find to first order in  $E$ ,

$$\delta\chi_{yxz}^{(2)} : +6id_0 d_0^* (d'_0 g_6 + d_0^* g_7^*) - 2\sqrt{2}id_0^2 (-idg_7 + d_0^* h_6) .$$

In the same way, we can calculate the other two paths. Finally we sum over all four paths to get the final result for  $\chi_{yz}^{(2)}$ . We find to zeroth order in  $E$ , i.e., unperturbed,  $\chi_{yz}^{(2),old}$  is

$$\chi_{yz}^{(2),old} = -4\sqrt{6}id_0^2d_0'^*$$

In an optical lossless medium,  $\chi_{yz}^{(2),old} = -4i\sqrt{6}d_0^2d_0'^*$  is a real number as shown in the later discussion. We find that the first order contribution from  $E_z$  is zero.

$$\delta\chi_{yz}^{(2)} = 0$$

So the second-order perturbation must be considered. By using the result for  $g_6$ ,  $g_7$ , and  $h_6$  in chapter 5,

$$g_6 = \frac{2d_0^*E}{E^6 - E^8} \quad (C.11)$$

$$g_7 = \frac{2d_0'^*E}{E^7 - E^8} \quad (C.12)$$

$$h_6 = \frac{\sqrt{2}d_0E}{E^7 - E^6} \quad (C.13)$$

Here  $E^6$ ,  $E^7$ , and  $E^8$  represent the energy levels of states  $\Gamma^{(6)}$ ,  $\Gamma^{(7)}$ , and  $\Gamma^{(8)}$ , and  $E$  represents the depletion electric field along the  $\vec{z}$  direction. If we substitute the above result into the representation of the perturbation formula for  $\chi_{yz}^{(2)}$ , we get the nonzero second-order perturbation terms.

$$\begin{aligned} \delta^2\chi_{yz}^{(2)} = & \left\{ \frac{16\sqrt{3}}{(E^6 - E^8)(E^7 - E^8)} |d_0|^2 |d_0'|^2 (d + d^*) + \frac{8\sqrt{6}i}{(E^7 - E^6)^2} |d_0|^2 (d_0^2 d_0' - d_0'^2 d_0^*) \right. \\ & + \frac{4\sqrt{6}i}{(E^6 - E^8)(E^7 - E^6)} |d_0|^2 [-2|d_0|^2 (d_0' - d_0'^*) + d_0'^3 + |d_0'|^2 d_0'] \\ & + \frac{4\sqrt{6}i}{(E^7 - E^6)(E^7 - E^8)} |d_0|^2 d_0' (3|d_0|^2 + 2d_0'^*{}^2 + d_0'^2) \\ & \left. + \frac{16\sqrt{3}}{(E^7 - E^8)^2} |d_0|^2 d_0'^2 d_0 \right\} E^2 \end{aligned} \quad (C.14)$$

It indicates that the second-order perturbation exists. If we consider the following relations at the  $\Gamma$  point in the Brillouin zone of GaAs system (see table 4.2),

$$E^6 - E^8 \ll E^7 - E^6$$

$$E^7 - E^6 < E^7 - E^8,$$

we need consider only the largest perturbation term, which contains  $(E^6 - E^8) * (E^7 - E^6)$  in the denominators. Finally, we can get,

$$\delta^2 \chi_{yxz}^{(2)} = \beta E^2 \quad (\text{C.15})$$

with

$$\beta = \frac{4\sqrt{6}i}{(E^6 - E^8)(E^7 - E^6)} |d_0|^2 [-2|d_0|^2 (d'_0 - d_0'^*) + d_0'^3 + |d'_0|^2 d_0']$$

Now let us consider the form of these dipole transition elements in detail. From the text, we know that:

$$d_0 = \frac{1}{\sqrt{6}} \int f Q_x X d\vec{r}$$

$$d'_0 = \frac{-i}{\sqrt{6}} \int X Q_y Z d\vec{r}$$

In the case of optical lossless media, the integrals are real positive constants. Then we get

$$\beta = -\frac{16\sqrt{6}}{(E^6 - E^8)(E^7 - E^6)} |d_0|^4 |d'_0|$$

Therefore  $\beta$  is *negative*. By comparison with the original  $\chi_{yxz}^{(2),old}$ , the unperturbed second-order susceptibility is written as

$$\chi_{yxz}^{(2),old} = -4i\sqrt{6}d_0^2 d_0'^*$$

Similarly in the case of lossless media,  $\chi_{yxz}^{(2),old}$  is a real positive number.

$$\chi_{yxz}^{(2),old} = 4\sqrt{6}d_0^2 |d_0'^*|$$

Therefore the second-order perturbation  $\beta$  has a  $180^\circ$  phase difference with respect to the original second-order susceptibility  $\chi_{yxz}^{(2),old}$ . As a result, the electric field induced perturbation will diminish the nonzero second-order susceptibility  $\chi_{yxz}^{(2)}$ .

# Appendix D

## Depletion field $E\hat{z}$ effects on second-order Susceptibility $\chi_{zzz}^{(2)}$

In this appendix, we calculate the depletion field  $E\hat{z}$  effects on second-order susceptibility  $\chi_{zzz}^{(2)}$ . According to the results of appendix A and B, the perturbation of  $\chi_{zzz}^{(2)}$  can be derived in orders of  $E_z\hat{z}$ .

The  $\chi_{zzz}^{(2)}$  transition path can be written as

$$\chi_{zzz}^{(2)} : \Gamma_8 \xrightarrow{Q_z} \Gamma_6 \xrightarrow{Q_z} \Gamma_7 \xrightarrow{Q_z} \Gamma_8$$

The first and second transition paths have been given in Appendix B. We now turn our attention to the third path, i.e.

$$\Gamma_7 \xrightarrow{Q_z} \Gamma_8$$

To calculate the perturbation of  $\chi_{zzz}^{(2)}$  under an  $E\hat{z}$  field, we need to know the inter-band transition path in which the nonzero paths are

$$\Gamma_7(\nu = -) \xrightarrow{Q_z} \Gamma_8(\mu = +\frac{3}{2}) : -2d_0'^* \quad (D.1)$$

$$\Gamma_7(\nu = +) \xrightarrow{Q_z} \Gamma_8(\mu = +\frac{1}{2}) : -(d^* - d'^*)g_7 + 2id_0'^*h_6 \quad (D.2)$$

$$\Gamma_7(\nu = -) \xrightarrow{Q_z} \Gamma_8(\mu = -\frac{1}{2}) : -i(d^* - d'^*)g_7 - 2d_0'^*h_6 \quad (D.3)$$

$$\Gamma_7(\nu = +) \xrightarrow{Q_z} \Gamma_8(\mu = -\frac{3}{2}) : -2id_0'^* \quad (D.4)$$

Thus the nonzero paths for  $\chi_{zzz}^{(2)}$  are

$$|\phi_0^{(8)}\rangle_{\frac{3}{2}} \xrightarrow{Q_z} |\phi_0^{(6)}\rangle_- \xrightarrow{Q_z} |\phi_0^{(7)}\rangle_- \xrightarrow{Q_z} |\phi_0^{(8)}\rangle_{\frac{3}{2}} \quad (\text{D.5})$$

$$|\phi_0^{(8)}\rangle_{\frac{1}{2}} \xrightarrow{Q_z} |\phi_0^{(6)}\rangle_+ \xrightarrow{Q_z} |\phi_0^{(7)}\rangle_+ \xrightarrow{Q_z} |\phi_0^{(8)}\rangle_{\frac{1}{2}} \quad (\text{D.6})$$

$$|\phi_0^{(8)}\rangle_{-\frac{1}{2}} \xrightarrow{Q_z} |\phi_0^{(6)}\rangle_- \xrightarrow{Q_z} |\phi_0^{(7)}\rangle_- \xrightarrow{Q_z} |\phi_0^{(8)}\rangle_{-\frac{1}{2}} \quad (\text{D.7})$$

$$|\phi_0^{(8)}\rangle_{-\frac{3}{2}} \xrightarrow{Q_z} |\phi_0^{(6)}\rangle_+ \xrightarrow{Q_z} |\phi_0^{(7)}\rangle_+ \xrightarrow{Q_z} |\phi_0^{(8)}\rangle_{-\frac{3}{2}}. \quad (\text{D.8})$$

For example

$$|\phi_0^{(8)}\rangle_{\frac{3}{2}} \xrightarrow{Q_z} |\phi_0^{(6)}\rangle_- \xrightarrow{Q_z} |\phi_0^{(7)}\rangle_- \xrightarrow{Q_z} |\phi_0^{(8)}\rangle_{\frac{3}{2}}.$$

In such a particular transition path,  $\chi_{zzz}^{(2)}$  to first order in  $E_z$  is

$$\chi_{zzz}^{(2)} \Rightarrow \quad (\text{D.9})$$

$$\begin{aligned} & [-2h_6 d'_0 + i(d + 3d')g_6^*] [-2d_0 g_6 h_6^* + i(d^* \\ & + 3d'^*)g_6 g_7^* + \sqrt{2}d_0^* h_6^* h_6^* + 2d_0^* h_6^* g_7^* - \sqrt{2}d_0] [-2d_0^*] \\ & = 2\sqrt{2}d_0 d'^* [-2h_6 d'_0 + i(d + 3d')g_6^*]. \end{aligned}$$

By summing all four paths above, we get the complete form of  $\chi_{zzz}^{(2)}$  to first order perturbation

$$\begin{aligned} \chi_{zzz}^{(2)} &= 4\sqrt{2}d_0^2 [d_0^* h_6 + i(d^* - d'^*)g_7] \\ &+ 4\sqrt{2}d_0 d'^* [-2d_0^* h_6 + i(d + 3d')g_6^*]. \end{aligned} \quad (\text{D.10})$$

By using the result for  $g_6$ ,  $g_7$ , and  $h_6$  in chapter 5,

$$g_6 = \frac{2d_0^* E}{E^6 - E^8} \quad (\text{D.11})$$

$$g_7 = \frac{2d_0^* E}{E^7 - E^8} \quad (\text{D.12})$$

$$h_6 = \frac{\sqrt{2}d_0 E}{E^7 - E^6} \quad (\text{D.13})$$

Here  $E^6$ ,  $E^7$ , and  $E^8$  represent the energy levels of states  $\Gamma^{(6)}$ ,  $\Gamma^{(7)}$ , and  $\Gamma^{(8)}$ , and  $E$  represents the depletion electric field along the  $\vec{z}$  direction. In the case of our three-step process, we consider  $E^6 - E^8 \ll E^7 - E^6 < E^7 - E^8$  at the  $\Gamma$  point in the Brillouin zone of GaAs system. By substituting  $g_6$ ,  $g_7$ , and  $h_6$  in above formula and only keeping the largest perturbation term which contains  $E^6 - E^8$  in its denominator, we get,

$$\chi_{zzz}^{(2)} = \frac{8\sqrt{2}i(d + 3d')d_0^2 d_0'^*}{E^6 - E^8} E \quad (\text{D.14})$$

This clearly shows that  $\chi_{zzz}^{(2)}$  depends linearly on the depletion field to first order.

# Appendix E

## Surface trap lifetime

In this Appendix we present a simple model for calculating the SHG intensity as a function of surface trap lifetime in our time dependent photoexcitation second-harmonic generation experiments. Since the surface charge variation arises from the drift of photoexcited minority carriers, we can neglect the effect of the intrinsic free minority carriers whose density is smaller than the photoexcited minority carriers.

When a sample is illuminated by the photoexcitation light long enough for the carrier populations to reach steady state, the surface charge density  $\sigma_0$  (majority carrier) is reduced by a factor of  $P_0$ , which is the surface minority carriers density generated by the photoexcitation light. After the photoexcitation light is turned off, this minority carrier density satisfies the equation:

$$\frac{dP(t)}{dt} = -\frac{P(t)}{\tau}.$$

Here  $\tau$  represents the surface minority carrier's lifetime. With the boundary condition  $P(t = 0) = P_0$ , we get

$$P(t) = P_0 e^{-\frac{t}{\tau}}.$$

Therefore the total surface charge density (majority and minority) can be written as

$$\sigma(t) = \sigma_0 + P(t).$$

Here  $\sigma_0$  is the surface carrier density without photoexcitation light. According to the constant depletion field approximation (see chapter 5), the near surface depletion electric field can be written as

$$E(t) = E(0) + \frac{2\pi P(t)}{\epsilon}$$

with

$$E(0) = \frac{2\pi\sigma_0}{\epsilon}.$$

Here  $E(0)$  is the initial depletion electric field without photoexcitation light.

Thus the second-order susceptibility  $\chi_{yxz}^{(2)}$  is perturbed as follows:

$$\chi_{yxz}^{(2)}(t) = \chi_{yxz}^{(2),old} + \beta E^2(t).$$

Here  $\chi_{yxz}^{(2),old}$  is the unperturbed second-order susceptibility. By substituting for  $E(t)$ , we obtain the time dependent perturbation of the second-order susceptibility,

$$\chi_{yxz}^{(2)}(t) = \chi_{yxz}^{(2),old} + \beta[E^2(0) + \frac{4\pi P(t)E(0)}{\epsilon} + (\frac{2\pi P(t)}{\epsilon})^2].$$

Neglecting the higher order contributions, we find that

$$\chi_{yxz}^{(2)}(t) = \chi_{yxz}^{(2),old} + \beta E^2(0) + \frac{4\pi\beta E(0)P_0 e^{-\frac{t}{\tau}}}{\epsilon}.$$

The first and second terms represent the depletion field perturbed second-order susceptibility without photoexcitation light. The third term is the photoexcitation light induced perturbation. Finally the SHG signal is

$$I_{2\omega} = (A + B e^{-\frac{t}{\tau}})^2$$

with

$$A = [\chi_{yxz}^{(2),old} + \beta E^2(0)]I_\omega$$

$$B = \frac{4\pi\beta E(0)P_0}{\epsilon}I_\omega.$$

Here  $I_\omega$  represents the fundamental SH light intensity. When  $t = \infty$ , the SHG intensity is  $I_{2\omega} = [\chi_{yxz}^{(2),old} + \beta E^2(0)]^2 I_\omega^2$ .

# Appendix F

## Carrier boundary at GaAs surface

In this Appendix, we estimate the surface carrier boundary under a strong depletion field at GaAs surfaces. We suppose that the carrier was confined within a quantum well at the surface, with an infinite potential barrier at the vacuum side and a linear electric potential  $\phi = eEz$  at other side. The wave equation can be written as

$$-\frac{\hbar^2}{2m} \frac{\partial^2 \psi(z)}{\partial z^2} + eEz\psi(z) = \varepsilon\psi(z)$$

with boundary conditions

$$\psi(z = 0) = 0$$

$$\psi(z = \infty) = 0.$$

Here  $\hat{z}$  is normal to the surface,  $E$  is the depletion field and  $e$  is the electron charge. This equation is solved exactly in reference[99]. Its ground state has the form

$$\psi(z) \sim \left(\frac{x}{l} - 2\right)^{\frac{1}{4}} e^{-\frac{2}{3}\left(\frac{x}{l} - 2\right)^{\frac{3}{2}}}$$

with

$$l = \left(\frac{\hbar^2}{2me\varepsilon}\right)^{\frac{1}{3}}$$

Here  $l$  is the wavefunction decay length inside the bulk, and it gives the carrier confining scale at the surface. In the case of GaAs, the surface the electric field normal to the surface is  $\sim 10^5 V/cm$ , and the effective mass of the electron at the

bottom of the conduction band is  $m = 0.06m_e$ . Therefore the carrier confining boundary length is

$$l = \left(\frac{\hbar^2}{2me\epsilon}\right)^{\frac{1}{3}} \sim 10nm$$

As a result, the carrier is confined within 10 nm of the surface region.

# Appendix G

## Electrical neutrality assumption

In this appendix, we estimate the the internal electric field effects on the diffusion process. Because the carriers are charged, the internal electric field affects the diffusion process. Therefore, we had to consider both diffusion and drifting processes. On the other hand, when the drift length is less than the diffusion length, the electrical neutrality of carriers is a good assumption, and the drifting process can be neglected.. The drifting function of free carriers under an electric field  $E$  can be written as

$$\frac{\partial \sigma}{\partial t} = -\nabla \cdot j - \frac{\sigma}{\tau}$$

with

$$j = \mu \sigma E.$$

Here  $\sigma$  is the carrier density,  $\tau$  is the free carrier lifetime, and  $\mu$  is the carrier mobility. In our experiment, the drifting process can be treated as a one-dimensional steady state ( $\frac{\partial \sigma}{\partial t} = 0$ ) problem (see figure 6.8).

$$\mu E \frac{\partial \sigma}{\partial x} = -\frac{\sigma}{\tau}.$$

Here  $x$  is parallel to the surface and normal to the photoexcitation beam line. Finally the drifting formula for the carrier density is

$$\sigma(x) = \sigma_0 e^{-\frac{x}{\lambda}}$$

with

$$\lambda = \mu E \tau.$$

$\lambda$  is the drifting length. If we assume that the photoexcited minority carrier density is around  $10^{11} - 10^{12} \text{ cm}^{-2}$  at the surface, then the electric field component,  $E_x$ , along the surface  $\hat{x}$  direction in our experiment can be calculated (see figure 6.8). Since our diffusion length is about  $2 \text{ mm}$ , a typical electric field  $E_x$  at  $1 \text{ mm}$  away from the photoexcitation beam waist is

$$E_x \sim 10^3 - 10^4 \text{ V/cm}$$

If we assume that the surface free carrier mobility is close to its bulk free carrier value  $\mu \sim 10^3 \text{ cm}^2/\text{Vs}$  and the surface free carrier lifetime  $\tau \sim 10^{-9} \text{ s}$ , we obtain the drifting length

$$\lambda = 10^{-3} - 10^{-2} \text{ cm}$$

This drift length is less than our observed diffusion lengths. Therefore electric neutrality can be applied in our analysis.

# Appendix H

## Effective diffusion model

In this appendix, we derive effective diffusion formula based on our “quasi-free” carriers model (see figure 6.13), the minority carriers diffusion processes depend on the trapping time ( $\tau_c$ ), the time to reexcite thermally out of the trap ( $\tau_e$ ), and the scattering time of the free carrier in the near surface bands  $\tau_s$  (usually  $\tau_s \ll \tau_c$ ). Such a diffusion process can be treated as a random walk of the “quasi-free” carriers along the surface. The mean square distance  $\langle x^2 \rangle$  is

$$\langle x^2 \rangle = D_{surface} t_{effective}$$

with

$$D_{surface} = (v_{free})^2 \tau_s.$$

Here  $D_{surface}$  is the diffusion constant for the free carrier in the near surface bands, and  $t_{effective}$  is the “quasi-free” time when the carrier diffuses.  $v_{free}$  is the free carrier velocity in the near surface bands.  $t_{effective}$  can be written in terms of total time  $t$ , free time ( $\tau_c$ ) and trapped time ( $\tau_e$ ).

$$t_{effective} = \frac{\tau_c}{\tau_c + \tau_e} t.$$

Therefore the mean square walking distance is

$$\langle x^2 \rangle = (v_{free})^2 \tau_s \frac{\tau_c}{\tau_c + \tau_e} t.$$

Thus the effective diffusion constant is

$$D_{eff} = (v_{free})^2 \tau_s \frac{\tau_c}{\tau_c + \tau_e}.$$

# Appendix I

## Quick reference of computer codes

These codes are written in Asyst language.

: forget.me	to clear desk top.
: GPIB.INIT	
BUS.INIT	INITIALIZE BUS
SEND.INTERFACE.CLEAR	CLEAR THE BUS
REMOTE.ENABLE.ON	ALLOW DEVICES TO RESPOND
;	
:reset	Reset the whole systems
srs245	
" mr" gpib.write	
DEF.vuport	
forget.all	
load setup.asy	
load nonlinear.asy	
;	

```

: LOCAL.RESET                               Reset GPIB bus and SRS245
" mr" gpib.write
DEF.vuport
load setup.asy
;
: sh.st                                     show status of the positions of all motors
: set.st                                   set status and register the new
                                           positions for motors

: MOTORS.OFF                               turns off the current for all the motors
11 888 port.out
11 890 PORT.OUT
10 msec.delay;
: DM                                       Run dye motor
: SM                                       Run sample monochrometer
: RM                                       Run reference monochrometer
: QT                                       Run quartz motor
: tp                                       Take background data
:td TAKE.DATA                             Take data and subtract background
stablizer                                  Stablize box car
SAMP.NO 25 = IF
GR
THEN
SRS245                                    SRS245 is the computer interface
1 COUNTER :=
init.arrays                               initialize data array
BEGIN                                     loop over number of shots
chanell one == SAMPLE chanell two == REFERENCE
stack.clear

```

```

" scl,2:100" gpib.write
  120000 msec.delay
50 scan * msec.delay          wait till scan is over
Give.Nth.Shots
samp 12.0 ; if
refr 12.0 ; if
refr refr.pedestal - refr :=
samp samp.pedestal - samp :=      take away the background
samp samp.array [ counter ] :=   save it in samp.array
refr refr.array [ counter ] :=   save it in refr.array
  SAMP.NO 50 = IF
refr abs plot.array [ 1 ] :=
COUNTER COUNTER.ARRAY [ 1 ] :=
  " R " symbol
solid
counter.array plot.array Xy.data.plot
samp ABS plot.array [ 1 ] :=
COUNTER COUNTER.ARRAY [ 1 ] :=
solid
  " S " symbol
counter.array plot.array Xy.data.plot
  THEN
counter 1 + counter :=
then
then
samp.no 1 + counter =
UNTIL
" number of shots =====i" "type counter 1 - .

```

```
cr
" —" "TYPE cr
cr
1000 300 TUNE
" ?S" GPIB.WRITE "statu gpib.read          clear the bit
;
:sd                                           save the data
samp.array mean .
cr
refr.array mean .
cr
samp.array mean refr.array mean / 100 * .
;
```

# Bibliography

- [1] W. Schottky, *Z. Physik.* **113**, 367 (1939).
- [2] J. Bardeen, *Phys. Rev.* **71**, 717 (1947).
- [3] W. Mönch, "*Semiconductor Surfaces and Interfaces*", (Springer-Verlag, New York, 1993).
- [4] S. M. Sze, "*Physics of Semiconductor Devices*", (Wiley, New York, 1981).
- [5] W. E. Spicer, I. Lindau, P. Skeath, and C. Y. Yu, *J. Vac. Sci. Technol.* **17**, 1019 (1980); and W. E. Spicer, Z. Lilient-Weber, E. Weber, N. Newman, T. Kendelewicz, P. Cao, C. McCant, P. Miyano, and I. Lindau, *J. Vac. Sci. Technol.* **B6**, 1245 (1988).
- [6] R. E. Allen, and J. D. Dow, *Phys. Rev.* **B25**, 1423 (1982); R. E. Allen, O. F. Sankey, and J. D. Dow, *Surf. Sci.* **168**, 376 (1986).
- [7] R. M. Feenstra, A. Vaterlaus, J. M. Woodall, and G. D. Pettit, *Appl. Phys. Lett.* **63**, 2528 (1993).
- [8] V. Heine, *Phys. Rev.* **138**, A1689 (1965).
- [9] J. Tersoff, *Phys. Rev. Lett.* **52**, 465 (1984).
- [10] R. Ludeke and G. Landgren, *J. Vac. Sci. Technol.* **19**, 667 (1981).

- [11] F. J. Himpsel, U. O. Karlsson, J. F. Morar, D. Rieger and J. A. Yarmoff, Phys. Rev. Lett. **56**, 1497 (1986).
- [12] A. B. McLean and F. J. Himpsel, Phys. Rev. **B39**, 1457 (1989).
- [13] T. F. Heinz, F. J. Himpsel, E. Palange, and E. Burstein, Phys. Rev. Lett. **63**, 644 (1989).
- [14] R. People, K. W. Wecht, K. Alavi, and A. Y. Cho, Appl. Phys. Lett. **43**, 118 (1983).
- [15] L. Kassel, H. Abad, J. W. Garland, P. M. Racciah, J. E. Potts, M. A. Haase, and H. Cheng, Appl. Phys. Lett. **56**, 42 (1990).
- [16] M. S. Yeganeh, J. Qi, A. G. Yodh, and M. C. Tamargo, Phys. Rev. Lett. **68**, 3761 (1992).
- [17] M. S. Yeganeh, J. Qi, A. G. Yodh, and M. C. Tamargo, Phys. Rev. Lett. **69**, 3579 (1992).
- [18] R. B. Laughlin, J. D. Joannopoulos, and D. J. Chadi, Phys. Rev. **B21**, 5733 (1980).
- [19] W. Daum, H. J. Krause, U. Reichel, and H. Ibach, Phys. Rev. Lett. **71**, 1234 (1993).
- [20] B. L. Sharma, *"Metal-semiconductor Schottky Barrier Junctions and Their Applications"*, (Plenum Press, New York, 1984).
- [21] *"Semi-insulating III-V Materials"*, edited by D. C. Look and J. S. Blakemore, (Shiva Publishing Limited, England, 1984).
- [22] J. C. Brice, *"Crystal Growth Processes"*, (Halsted Press, New York, 1986).
- [23] R. Haight and J. Bokor, Phys. Rev. Lett. **56**, 2846 (1986).

- [24] R. E. Viturro, J. L. Shaw, C. Mailhiot, L. J. Brillson, N. Tache, J. McKinley, G. Margaritondo, J. M. Woodall, P. D. Kirchner, G. D. Pettit, and S. L. Wright, *Appl. Phys. Lett.* **52**, 5052 (1988).
- [25] Y. R. Shen, *"The Principles of Nonlinear Optics"*, (Wiley, New York, 1984).
- [26] H. W. K. Tom, T. F. Heinz and Y. R. Shen, *Phys. Rev. Lett.* **51**, 1983 (1983).
- [27] T. F. Heinz, M. M. T. Loy and W. A. Thompson, *Phys. Rev. Lett.* **54**, 63 (1985).
- [28] J. F. McGilp, and Y. Yeh, *Solid State Comm.* **59**, 91 (1986).
- [29] E. Ghahramani, D. J. Moss, and J. E. Sipe, *Phys. Rev. Lett.* **64**, 2815 (1990).
- [30] G. Lüpke, D. J. Bottomley, and H. M. van Driel, *Phys. Rev.* **B47**, 10389 (1993).
- [31] U. Emmerichs, C. Meyer, H. J. Bakker, H. Kurz, C. H. Biorkman, C. E. Shearon, Y. Mao, T. Yasuda, Z. Jing, G. Lucovsky, J. L. Whitten, *Phys. Rev.* **B50**, 5506 (1994).
- [32] L. L. Kulyuk, D. A. Shutov, E. E. Strumban, and O. A. Aktsipetrov, *J. Opt. Soc. Am.* **B8**, 1766 (1991).
- [33] M. S. Yeganeh, J. Qi, A. G. Yodh, and M. C. Tamargo, *J. Opt. Soc. Am.* **B10**, 2093 (1993).
- [34] M. Shur, *"GaAs Devices and Circuits"* (Plenum Press, New York, 1987).
- [35] C. Y. Chang and F. Kai, *"GaAs High-Speed Devices: Physics, Technology, and Circuit Applications"*, (Wiley, New York, 1994).
- [36] S. Adachi, *"GaAs and Related Materials : Bulk semiconducting and Superlattice Properties"* (World Scientific, Singapore, 1994).

- [37] S. Guha, H. Cheng, J. M. Depuydt, M. A. Haase, and J. Qiu, *Mater. Sci. Eng.-Solid States Mater. for Adv. Technol.* **B28**, 29 (1994).
- [38] G. M. Martin, A. Mitonneau, and A. Mircea, *Electron. Letters* **13** 191 (1977);  
A. Mitonneau, G. M. Martin, and A. Mircea, *Electron. Letters* **13** 666 (1977).
- [39] J. Qi, W. Angerer, M. S. Yeganeh, A. G. Yodh, and W. M. Theis, submitted to *Phys. Rev. Lett.*; J. Qi, W. Angerer, M. S. Yeganeh, A. G. Yodh, and W. M. Theis, *Quantum Electronics Laser Science, 1995*, Technical Digest **16**, 41 (OSA, Washington D.C., 1995).
- [40] J. Qi, M. S. Yeganeh, I. Koltover, A. G. Yodh, and M. W. Theis, *Phys. Rev. Lett.* **71**, 633 (1993).
- [41] J. Qi, W. Angerer, M. S. Yeganeh, A. G. Yodh and W. M. Theis, *Phys. Rev.* **B51**, 13533 (1995).
- [42] N. Bloembergen, *"Nonlinear Optics"*, (Benjamin, New York, 1965).
- [43] J. D. Jackson, *"Classical Electrodynamics"*, (Wiley, New York, 1975).
- [44] J. E. Sipe, D. J. Moss and H. M. van Driel, *Phys. Rev.* **B35**, 1129 (1987).
- [45] N. Bloembergen, R. K. Chang, S. S. Jha and C. H. Lee, *Phys. Rev.* **174**, 813 (1968).
- [46] J. A. Litwin, J. E. Sipe and H. M. van Driel, *Phys. Rev.* **B31**, 5543 (1983).
- [47] R. W. Boyd, *"Nonlinear Optics"* (Academic Press, San Diego, 1992).
- [48] G. Burns, *"Solid State Physics"* (Academic Press, Orlando, 1985).
- [49] A. Yariv, *"Quantum Electronics"* (Wiley, New York, 1988) Third Edition.
- [50] C. Y. Fong and Y. R. Shen, *Phys. Rev.* **B12**, 2325 (1975).

- [51] T. F. Heinz, H. W. K. Tom, and Y. R. Shen, *Phys. Rev.* **A28**, 1883 (1983).
- [52] T. F. Heinz, M. M. T. Loy, and W. A. Thompson, *Phys. Rev. Lett.* **54**, 63 (1985).
- [53] H. W. K. Tom, T. F. Heinz, and Y. R. Shen, *Phys. Rev. Lett.* **51**, 1983 (1983).
- [54] X. Xiao, X. D. Zhu, W. Daum, and Y. R. Shen, *Phys. Rev. Lett.* **66**, 2352 (1991).
- [55] M. S. Yeganeh, "*Ph.D. Thesis*", (University of Pennsylvania, 1992).
- [56] M. S. Yeganeh, J. Qi, J. P. Culver, A. G. Yodh, and M. C. Tamargo, *Phys. Rev.* **B46**, 1603 (1992).
- [57] R. S. Finn and J. F. Ward, *Phys. Rev. Lett.* **6**, 285 (1971).
- [58] P. Sitz and R. Yaris, *J. Chem. Phys.* **49**, 3546 (1968).
- [59] C. H. Lee, R. K. Chang, and N. Bloembergen, *Phys. Rev. Lett.* **5**, 167 (1967).
- [60] R. W. Terhune, P. D. Maker, and C. M. Savage, *Phys. Rev. Lett.* **8**, 404 (1962).
- [61] J. R. Heflin, "*Ph.D. Thesis*" (University of Pennsylvania, 1990).
- [62] J. S. Blackmore, *J. Appl. Phys.* **53**, R123 (1982).
- [63] C. M. Wolfe, C. E. Stillman, and W. T. Lindley, *J. Appl. Phys.* **41**, 3088 (1970).
- [64] P. L. Gourley, R. M. Bifeld, T. E. Zipperian, and J. J. Wiczer, *Appl. Phys. Lett.*, **44**, 983 (1984).
- [65] M. Toivonen, A. Salokatve, M. Jalonen, J. Nappi, H. Asonen, M. Pessa, R. Murison, *Electron. Lett.* **31**, 797 (1995).
- [66] G. A. Baraff and M. Schluter, *Phys. Rev.* **B45** 8300 (1992).

- [67] W. E. Spicer, T. Kendelewicz, N. Newman, R. Cao, C. McCant, K. Miyano, I. Lindau, Z. Lilient-Weber, and E. R. Weber, *Appl. Surf. Sci.* **33/34** 1009 (1988).
- [68] J. Dabrowski and M. Scheffler, *Phys. Rev.* **B40** 10391 (1989).
- [69] A. Chantre, G. Vincent, and D. Bois, *Phys. Rev.* **B23** 5335 (1981).
- [70] M. Kaminska, M. Skowronski, J. Lagowski, J. M. Parsey, and H. C. Gatos, *Appl. Phys. Lett.* **43**, 302 (1983).
- [71] E. R. Weber, H. Ennen, U. Kaufmann, J. Winscheif, J. Schneider, and T. Wosinski, *J. Appl. Phys.* **53**, 6140 (1982).
- [72] M. D. Sturge, *Phys. Rev.* **127**, 768 (1962).
- [73] H. C. Casey Jr., D. D. Sell, and K. W. Wecht, *J. Appl. Phys.* **46**, 250 (1975).
- [74] J. F. Cornwell, "*Group Theory In Physics*" (Academic Press, Orlando, 1984); B. S. Tsukerblat, "*Group Theory In Chemistry And Spectroscopy: A Simple Guide To Advanced Usage*" (Academic Press, San Diego, 1994).
- [75] J. L. Shay, *Phys. Rev.* **B2**, 803 (1970).
- [76] J. G. Gay and L. T. Klauder Jr., *Phys. Rev.* **172**, 811 (1968).
- [77] D. E. Aspnes, *Surf. Sci.* **37**, 418 (1973).
- [78] M. Olszakier, E. Ehrenfreund, and E. Cohen, *Phys. Rev.* **B43**, 9350 (1991).
- [79] R. K. Chang, J. Ducuing, and N. Bloembergen, *Phys. Rev. Lett.* **15**, 415 (1965).
- [80] F. G. Parsons and R. K. Chang, *Opt. Commun.* **3**, 173 (1971).
- [81] H. Lotem, G. Koren, and Y. Yacoby, *Phys. Rev.* **B9**, 3532 (1974).
- [82] D. Bethune, A. J. Schmidt, and Y. R. Shen, *Phys. Rev.* **B11**, 3867 (1975).

- [83] M. S. Yeganeh, J. Qi, J. P. Culver, A. G. Yodh, and M. C. Tamargo, *Phys. Rev.* **B49**, 11196 (1994).
- [84] M. S. Yeganeh, J. Qi, J. P. Culver, A. G. Yodh, and M. C. Tamargo, *Phys. Rev.* **B46**, 1603 (1992).
- [85] S. L. Chuang, S. Schmitt-Rink, B. I. Greene, P. N. Saeta, and A. F. J. Levi, *Phys. Rev. Lett.* **68**, 102 (1992).
- [86] X. C. Zhang, B. B. Hu, J. T. Darrow, and D. H. Auston, *Appl. Phys. Lett.* **56**, 1011 (1990).
- [87] *"Molecular Beam Epitaxy And Heterostructures"*, edited by L. L. Chang and K. Ploog, (Nijhoff, Boston, 1985).
- [88] J. H. Neave and B. A. Joyce, *J. Cryst. Growth*, **44**, 387 (1978).
- [89] H. H. Farrel, M. C. Tamargo, and J. L. de Miguel, *Appl. Phys. Lett.* **58**, 355 (1991); M. C. Tamargo, R. E. Nahory, B. J. Skromme, S. M. Shibli, A. L. Weaver, R. J. Martin, and H. H. Farrell, *J. Cryst. Growth*, **111**, 741 (1991).
- [90] J. R. Chelikowky and M. L. Cohen, *Phys. Rev.* **B13**, 826 (1979).
- [91] D. J. Chadi, *Phys. Rev.* **B19**, 2074 (1979)
- [92] J. E. Rowe, S. B. Christman, and G. Maragaritondo, *Phys. Rev. Lett.* **35**, 1471 (1975).
- [93] P. K. Larsen, J. F. van derVeen, A. Mazur, J. Pollman, J. H. Neave, B. A. Joyce, *Phys. Rev.* **B26**, 3222 (1982).
- [94] R. H. Williams, *J. Vac. Sci. Technol.* **18**, 929 (1981).
- [95] K. Maeda, H. Ikoma, K. Sato, and T. Ishida, *Appl. Phys. Lett.* **62**, 2560 (1993).
- [96] F. Flores and C. Tejedor, *J. Phys. C: Solid State Phys.* **20**, 145 (1987).

- [97] A. Hiraki, K. Shuto, S. Kim, W. Kammura, and M. Iwami, *Appl. Phys. Lett.* **31**, 611, (1977);
- [98] R. Ludeke and G. Landgren, *J. Vac. Sci. Technol.* **19**, 667 (1981).
- [99] A. H. Mavromatis, *“Exercises in Quantum Mechanics : A Collection of Illustrative Problems and Their Solutions”*, (D. Reidel, Boston, 1987);
- [100] S. Rodriguez, P. Fisher, and F. Barra, *Phys. Rev.* **B5**, 2219 (1972).
- [101] A. K. Bhattacharjee and S. Rodriguez, *Phys. Rev.* **B6**, 3836 (1972).
- [102] M. Tinkham, *“Group Theory and Quantum Mechanics”*
- [103] H. C. Gatos and J. Lagowski, *J. Vac. Sci. Technol.* **10**, 130 (1973).
- [104] S. D. Offsey, J. M. Woodall, A. C. Warren, P.D. Kirchner, T. I. Chappell, and G. D. Pettit, *Appl. Phys. Lett.*, **48**, 475 (1986).
- [105] C. W. Wilmsen, *“Physics and Chemistry of III-V Compound Semiconductor Interfaces”* (Plenum Press, New Yorkm 1985).
- [106] P. J. Harrop and D. S. Campbell, *Thin Solid Films*, **2**, 273 (1968).
- [107] C. C. Chang, P. H. Citrin, and B. Schwartz, *J. Vac. Sci. Technol.* **14**, 943 (1977).
- [108] J. P. Mckelvey, *Solid State and Semiconductor Physics*, (Harper & Row, New York, 1966).
- [109] D. E. Aspnes, *Surface Sci.* **132**, 406 (1983).
- [110] M. Pollak and B. Shklovskii, *“Hopping Transport in Solids”* (North-Holland, New York, 1990).
- [111] M. R. A. Shegelski, and R. Barrie, *Phys. Rev.* **B36**, 7549 (1987).

[112] C. Frigeri, J. L. Weyher, and H. C. Alt, *Phys. Status Solidi (a)* **138**, 657 (1993).

[113] R. Ludeke, G. Jezequel, and A. Taleb-Ibrahimi, *Phys. Rev. Lett.* **61** 601 (1988).